DETERMINATION OF STRUCTURAL MODELS OF THE COMPLEX BETWEEN ERYTHROCYTE BAND 3 AND ANKYRIN-R REPEATS 13-24

By

Sunghoon Kim

Dissertation

Submitted to the Faculty of the

Graduate School of Vanderbilt University

in partial fulfillment of the requirements

for the degree of

DOCTOR OF PHILOSOPHY

In

Chemical and Physical Biology

December, 2011

Nashville, Tennessee

Approved:

Charles R. Snaders

Hassane S. Mchaourab

Terry P. Lybrand

Phoebe L. Stewart

Borden D. Lacy

To my parents

and

To my wife and Claire

ACKNOWLEDGEMENTS

I would like to acknowledge all the people who have contributed to this dissertation and my graduate works at Vanderbilt. First of all, I must express my sincere gratitude to my mentor, Dr. Albert H. Beth, who has always been an amazing advisor and supporter to me. His profound insight and extensive knowledge not only guided me in the right direction in solving specific problems, but also encouraged scientific thinking and critical attitudes toward them. Dr. Eric J. Hustedt was my second mentor thoughout my graduate study. He taught me a lot of things on EPR from the basic theories to detailed techniques and without his guidance and expertise, I couldn't have made it. Also, I wish to thank another my advisor, Dr. Charles E. Cobb. His office has been open to me all the times and all the advices he gave me and discussions we made on the biochemical and physiological problems were pivotal to my works.

I feel fortunate to be able to have such a great thesis committee the advices and guidance from which was so supportive and helpful in my thesis project. All the meetings with my committee were truly encouraging and scientifically exciting experience to me. In particular, I would like to express my special thanks to Terry, who was not only one of my committee members, but also collaborator of my project. I appreciate the dedications from him and his lab members, especially Dr. Jarrod Smith, which significantly contributed to the molecular modeling part of my graduate works. Also, I am grateful to our colleague Dr. Hassane Mchaourab for all his concerns about my project and for his insightful and critical advices.

All the assistances and friendships from my lab members were another essential part of my graduate school experience. Suzanne Brandon was such a great assistant who provided me numeours protein samples and at the same fime a good friend who has cared my family and me in many aspects. It was really fortunate for me to have Dr. Nina Dixit as my colleague. The times we spent together in having discussions and performing experiments are precious moments to me.

Most of all, I have to acknowledge my family who always trust and support me throughout my whole life. My parents' love and prayer for me even across the see encourage me and with me all the time. My brother has been a confident supporter. Without their love, it would not be possible for me to be here.

Finally, any word can't express enough my love and gratitude toward my wife and my little one Claire. Nothing can substitute the sacrifice and dedication that my wife gave me during the last six years to support my graduate works in America. I would like to thank Claire for being here with me.

TABLE OF CONTENTS

LIST OF TABLES

LIST OF FIGURES

LIST OF ABBREVIATIONS

AE1	Anion exchanger1
AnkD34	Ankyrin-R repeats 13-24
ankD2	Ankyrin-R repeats 7-12
BMOE	Bis-maleimidoethane
CBD	Calcium binding domain
cdb3	Cytoplasmic domain of band 3
CD	Circular dichroism
cryo-EM	Cryo-electron microscopy
CW-EPR	Continuous wave – electron paramagnetic resonance
DEER	Double electron electron resonance
ENDOR	Electron nuclear double resonance
EPR	Electron paramagnetic resonance
ESEEM	Electron spin echo envelope modulation
FID	Free induction decay
FRET	Fluorescent resonance energy transfer
HE	Hereditary elliptocytosis
HS	Hereditary spherocytosis
HYSCORE	correlation spectroscopy
ITC	Isothermal titration calorimetry
MD simulation	Molecular dynamics simulation
MTSSL	1-oxyl-2,2,5,5-tetramethyl-3-pyrroline-3-methyl methanethio-sulfonate spin label
MBD	Membrane binding domain of ankyrin-R
NiEDDA	Nickel(II)-ethylenediaminediacetate

mw	Microwave
PELDOR	Pulsed electron double resonance
rf	Radiofrequency
SAXS	Small angle X-ray scattering
SDSL	Site-directed spin labeling
SDS-PAGE	Sodium dodecyl sulfate polyacrylamide gel electrophoresis
tdb3	transmembrane domain of band 3
TPX	trademark for polymethylpentene

CHAPTER I

INTRODUCTION

Rationale for the Dissertation Research

Since the beginning of modern physiology, human red blood cells have attracted many physiologists' interest due to its remarkable mechanical stability and deformability, which are essential in their survival during the circulation through the narrow capillaries. These unique physical properties can be explained by the presence of a mesh network of spectrin-based membrane skeleton, which lies right beneath the lipid bilayer and physically support it (reviewed in (Mohandas and Gallagher, 2008; Perrotta et al., 2008)). Each unit of the spectrin tetramer is linked to the lipid bilayer by means of the two major junctional complexes, one (the ankyrin complex) at the middle of spectrin dimer and the other (the 4.1R complex) at the junctional region between two spectrin dimers. Of those two vertical linkages, the ankyrin complex has a dominant role in determining erythrocyte membrane structure and its mechanical properties. Ankyrin-R forms a bridge between the the plasma membrane and membrane skeleton by directly interacting with cytoplasmic domain of the membrane protein band 3 and spectrin at two separate binding regions.

While the nature of the interaction between ankyrin-R and the spectrin tetramer has been elucidated by recent co-crystal structures (Stabach et al., 2009), the structure of the complex between the membrane binding domain (MBD) of ankyrin-R and the cytoplasmic domain of band 3 (cdb3) still remains unknown. The significance of this interaction can be manifested by a clinical condition called hereditary spherocytosis (HS). Mutation in cdb3 or the MBD of ankyrin-R that impairs the binding between these two proteins accounts for more than 60% of HS cases in North American and European populations (Eber and Lux, 2004).

Previous mutation studies defined two separate binding sites on the D2 and D34 subdomains of ankyrin-R, which showed distinct binding characteristics in terms of both pH- and salt-dependence (Michaely and Bennett, 1995). One ankyrin-R binds two band 3 dimers in the red blood cells and band 3 was found to be distributed between two subpopulations, dimer and tetramer in the ghost membrane preparations (Blackman et al., 1998; Casey and Reithmeier, 1991; Hanspal et al., 1998). Thus, one main question is whether the structure of the ankyrin complex is determined by the oligomeric state of cdb3 bound to ankyrin. Is it a dimer of dimers that bind to two distinct binding sites on ankyrin or alternatively, is it a tetramer as previously proposed (Michaely et al., 2002).

Depending on the cell type and isoform, ankyrins anchor many different membrane proteins to the spectrin-based cytoskeleton to form macromolecular complexes in diverse types of specialized membranes. The membrane proteins that are known to be associated with ankyrin include E-cadherin in epithelial cells (Kizhatil et al., 2007), the voltage-gated Na^+ channel in neuron (Lemaillet et al., 2003), the inositol 1,4,5-triphophate receptor (Mohler et al., 2004) and the Na^+/Ca^{2+} exchanger (Mohler et al., 2005) in cardiomyocytes as well as band 3 in erythrocytes. The ankyrin-mediated tethering of the membrane proteins to the cytoskeleton plays essential roles in cells from different tissues by contributing to membrane stability, the recruitment of cytosolic proteins and signaling complexes, and localization of receptors and channels in microdomains (Bennett and Baines, 2001). Therefore, elucidating the structure of the cdb3-ankyrin complex is of importance not only in understanding the molecular mechanism for a family of red cell disorders including HS, but also in gaining insight into the general nature of the spectrin-ankyrin based localization of the membrane proteins by providing a model system.

Since the co-crystal structure for the complex between cdb3 and the MBD-ankyrin-R is not available and the size of the complex exceeds the size limits for NMR studies, to obtain a high resolution structure from conventional biophysical techniques is formidable. This thesis work aims to determine the structure of the cdb3-AnkD34 complex at medium-resolution level

using SDSL-EPR techniques in conjunction with molecular modeling. Given that the crystal structures are currently available for the binding domain of each protein component, cdb3 and AnkD34, it is possible to probe any conformational change that may occur upon binding and to construct structural models using a range of constrains obtained from CW- and pulsed EPR measurements. Since intraprotein distance measurements indicated that the complex formation induces no significant conformational change in either protein, it was reasonable to perform rigid body docking using the ROSETTA docking algorithm to explore all possible conformational spaces and then filter the structural models that meet the full range of EPR-driven structural constrains such as spin label mobility, solvent accessibility, and interspin distances. This work shows that the inherent uncertainty in constraints which mainly originate from the flexible tether of the spin label relative to the proteins can be overcome by multiple and independent EPR data sets.

The same approach was employed in the second part of this thesis work as described in the Appendix. This work also utilized SDSL-EPR to determine structural features of the calcium binding domains of the Na^+/Ca^{2+} exchanger in cardiac myocytes (NCX1.1). NCX1.1 plays a crucial role in excitation-contraction (EC) coupling by extruding intracellular Ca^{2+} across the plasma membrane at the expense of Na^+ uptake using the electrochemical Na^+ gradient. This exchange activity returns the intracellular Ca^{2+} level, which is elevated by the Ca^{2+} signal cascade triggered by the action potential (Ca^{2+} transients), to the basal level after contraction. While no direct link between human *NCX1* gene variants and cardiac dysfunction has been identified to date, elevated Na^+/Ca^{2+} exchanger expression or activity has been associated with pathophysiological conditions in humans and animal models such as arrhythmia and heart failure (Sipido et al., 2000; Wang et al., 2001).

The exchange activity is totally reversible, depending on the Na^+ concentration gradient across the plasma membrane, and is modulated by the binding of regulatory Ca^{2+} to the calcium

binding domains which are located on the long cytosolic loop of NCX1. The calcium binding domains consist of a tandem array of two immunoglobulin-like domains, called CBD1 and CBD2. A collection of data from many functional analyses and structural studies unveiled the topology of the full length protein and the functional role of each separate domain. However, the molecular mechanism by which the ion exchange activity is modulated by regulatory Ca^{2+} binding to the two CBDs leading to an increase in Ca^{2+} extrusion is still unknown.

The structure of CBD12 shows similarities in many respects with a complex formed by a rigid body docking of two proteins, like the cdb3-AnkD34 complex. For example, the high resolution structures of each isolated domain, CBD1 and CBD2, were determined by X-ray crystallography and NMR studies. Both domains, which are linked with each other by a short and flexible linker, can form independent folding units. Furthermore, the data from this study indicated that the structures of the isolated domains of CBD1 and CBD2, which were previously determined by either X-ray crystallography (Chaptal et al., 2009; Besserer et al., 2007; Nicoll et al., 2006) or NMR studies (Hilge et al., 2006; Hilge et al., 2009) are well preserved in full length CBD12 within their central β-sheet regions. Thus, the structure of CBD12 was constructed in this work by determining the relative orientation of the two domains using multiple interdomain distance constraints. The effect of Ca^{2+} binding on the global structure of CBD12 was also determined to evaluate previously proposed structural models.

With the beginning of the post-genomic era, the number of protein structures that are experimentally determined is explosively increasing, and their functions are being explained at the molecular or even atomic levels based on their structures and functional analyses. Many of them found in databases (e.g., PDB) are recombinant proteins that were expressed as a small fragment or isolated domains due to the size limit or their unfavorable propensity for crystal formation. However, in many biological systems, macromolecular complexes are frequently found in diverse biochemical and physiological processes. These multi-component structures achieve the orchestration and fine tuning of the complex physiological processes, facilitate

biochemical machineries functioning in a concerted way as exemplified by the 'metabolon', or form structural frames of cells. Similarly, in some cases, a protein containing a combination of domains or modules, or a protein in oligomeric states can be regarded as a complex consisting of multiple domains or subunits. Therefore, 'assembling' is emerging as a common theme as we more and more commonly encounter multiprotein complexes or protein oligomers in important biological systems. From this point of view, SDSL-EPR can be a strong tool which can put the structures of the disparate pieces together and complete the whole picture of the complex systems, overcoming the limitations imposed on the other biophysical techniques. The dissertation works described in this thesis show how SDSL-EPR, especially DEER distance constraints, can be applied to construct structural models of a protein complex by determining the spatial arrangement of two protein components (Chapter III) and the structural models of a single protein by determining the relative orientation of two domains (Appendix Chapter).

Erythrocyte Membrane Skeleton

Mechanical Stability and Deformation of the Erythrocyte Membrane

The red blood cell is required to survive harsh environments during its journey through the narrow capillaries of the microvasculature where the cross-sections are less than its own diameter. In order to tolerate the applied shear stress inside the capillaries, erythrocytes undergo a large and reversible deformation with linear extensions of up to 250 %, which is seen in Fig. 1 which shows red blood cells traveling through capillaries with different diameters *in vivo* (Skalak and Branemark, 1969) and the ellipsoidal cells from flow-induced deformation *in vitro* (Mohandas and Gallagher, 2008).

A normal human erythrocyte is shaped as a biconcave disk with a volume of 90 fL and surface area of 136 μm^2. This unusual geometry of the cell gives rise to a 40% excess surface area

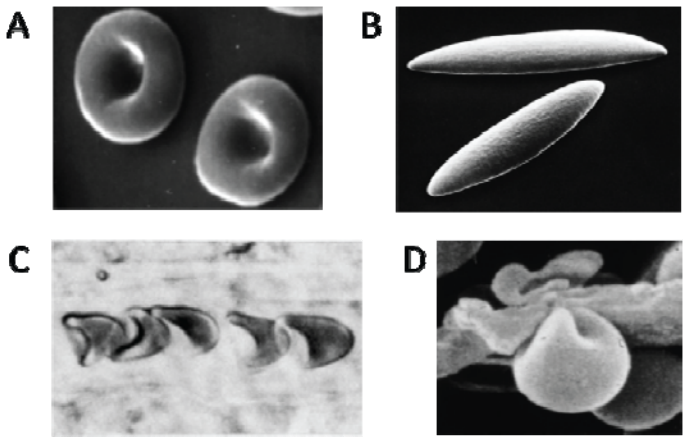

Figure 1. Deformability of red blood cells**.** A**, t**he precursor of the mature discoid red cell; B, **e**llipsoidal cells generated *in vitro* by flow-induced deformation of discoid cells; C, the parachute shape of red blood cells *in vivo* in a 7 μm diameter capillary; D, a red cell traversing from the splenic cord to the splenic sinus.

compared with a sphere of the same volume, which allows it to undergo extensive deformation without significant changes in its volume and surface area. In fact, even during deformation, the membrane surface area of the erythrocyte remains constant. This is essential given that a small change (3~4 %) in surface area is sufficient to induce cell lysis. Hence, the tight maintenance of the membrane surface area is essential in its survival throughout its 120-day average life span. The capability of erythrocytes to undergo deformation maintaining constant surface area is attributed to the presence of a 2-dimensional meshwork of spectrin-based membrane skeleton which lines the cytoplasmic surface of the plasma membrane and to the tethering of the lipid bilayer to this membrane skeleton through a set of junctional bridges. Two distinct multiprotein complexes have been identified as junctional contacts which form 'vertical' (normal to the membrane) linkages as illustrated in Fig. 2. At the first junctional sites, the cytoplasmic domain of the anion exchanger, also known as band 3, binds to ankyrin-R to form a bridge with the spectrin-based membrane skeleton by linking two structural entities directly. Protein 4.2 plays a critical role in stabilizing and regulating the protein-protein interaction between band 3 and

ankyrin-R. The key element involved in the other junctional complex, the 4.1R complex, is the interaction of glycoporin C with protein 4.1R, which in turn binds spectrin at a separate binding site to form a stable bridge with the aid of additional proteins. The details of the structural features of each constituent and their arrangements within each complex will be covered in the following section.

One of the most important properties of the erythrocyte membrane, its mechanical stability, allows the cell to resist external pressure and shear stress and to maintain its structural integrity during circulation. This unique property can be explained by the stability of spectrin-based membrane skeleton which is composed of stable tetramers of spectrin via lateral interaction between two spectrin dimers (Liu and Palek, 1980). The dimer-dimer interaction is dynamically regulated in response to the external forces imposed by deformation, maintaining a highly dynamic tetramer-dimer equilibrium within the membrane skeleton. An et al. has reported that

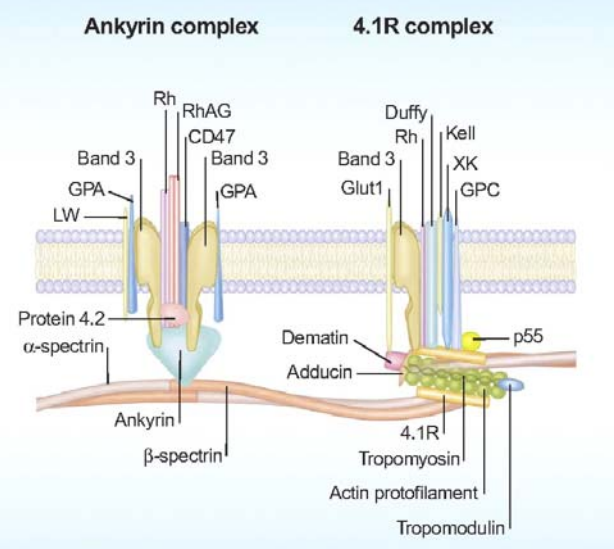

Figure 2. A schematic presentation of red cell membrane structure illustrating two major junctional multiprotein complexes with their constituents.

the loss of avidity of the dimer-dimer interaction resulted in decreased membrane mechanical stability (An et al., 2002). The distal end of the spectrin tetramer forms a junctional complex with F-actin and protein 4.1R, which also contributes to the membrane mechanical stability (An et al., 2005; Tchernia et al., 1981).

Besides mechanical stability, the modular structure of spectrin is also responsible for the high elasticity of the cell membrane although the structural identity for that feature remains ambiguous. The long filamentous spectrin dimer consists of 36 spectrin repeats, each of which acts as an independent folding unit with different melting temperatures (An et al., 2006a). The repeats with low stability have been observed to undergo unfolding under the mechanical stress in two different *in vivo* studies using mass spectroscopy (An et al., 2006a; Johnson et al., 2007) and atomic force spectroscopy (Rief et al., 1999). Currently, it is speculated that the fast folding-refolding cycle of the least stable repeats may contribute to the membrane elasticity together with the intrinsic flexibility due to its long modular structure.

Recently, the lipid bilayer itself is emerging as another important regulator for erythrocyte membrane stability via asymmetric distribution of phospholipids and its interaction with skeletal proteins. The outer monolayer exclusively contains phosphoatidylcholine and sphingomyelin while the inner monolayer includes most phosphatidylethanolamine, all phosphatidylserine (PS), and phosphoinositides (PI) (Zwaal and Schroit, 1997). Among these phospholipids, asymmetric distribution of PS and PI is of critical functional importance. For example, loss of asymmetry accompanying exposure of PS on the outer monolayer leads to phagocytosis by macrophages (Yasin et al., 2003) or adhesion of red cells to vascular endothelial cells (Setty et al., 2002). Furthermore, recent studies have suggested that PS and phosphatidyl-insitol-4,5-bisphosphate (PIP_2) can directly interact with cytoskeletal proteins such as spectrin and protein 4.1R, thereby modulating linkage of the plasma membrane to the membrane cytoskeleton (An et al., 2006b; Manno et al., 2002). Therefore, membrane phospho-lipids may also contribute to the mechanical stability of the red cell membrane.

Organization of the Erythrocyte Membrane Skeleton

Spectrin-based membrane skeleton The mesh network of spectrin tetramers provides the fundamental structural scaffold for the membrane skeleton. A main feature in spectrin structure is the tandem arrays of multiple spectrin repeats, 20 in α-spectrin and 16 in β-spectrin and each repeat is 106 amino acids long and forms a triple-helix bundle with two parallel and one antiparallel α-helices. α- and β-spectrin form an antiparallel heterodimer through strong lateral interactions between repeats 19 and 20 near the C-terminus of α-spectrin and repeats 1 and 2 near the N-terminus of β-spectrin. The spectrin tetramer, the major structural unit of the membrane skeleton, is formed by head-to-head interaction of two dimers, where a N-terminal solitary helix of the α-subunit from one dimer laterally interacts with 2 helices at the C-terminus of the β-chain from the other subunit to generate a stable triple-helical repeat (DeSilva et al., 1992; Speicher et al., 1993). While the ankyrin-binding site is located in the middle of the tetramer, F-actin and protein 4.1R form a multiprotein junctional complex at the distal end of the spectrin tetramer, which has a crucial role in increasing the membrane mechanical stability (Karinch et al., 1990). The effect of protein 4.1R on the stability of the F-actin-spectrin interaction becomes evident when the binding affinity of two proteins in the ternary complex ($K_d \approx 10^{-15}$ M) is compared with that in the binary complex of F-actin and spectrin ($K_d \approx 10^{-5}$ M)(Morris and Lux, 1995). Currently, a set of additional proteins including tropomyosin, tropomodulin, and adducin are known to be associated with this complex to further stabilize the structure of the complex and maintain the appropriate length of actin filaments (Bennett and Baines, 2001).

Ankyrin Complex Two transmembrane proteins, Band 3 and RhAG (Rh-associated glycoprotein) link the lipid bilayer to the membrane skeleton through the interaction of their cytoplasmic domains with ankyrin-R. Even though a number of membrane and cytosolic proteins are involved in the formation of a multiprotein complex, the band 3-ankyrin-R interaction is

central to the organization of the ankyrin complex and has provided a good model system for membrane structure studies. More comprehensive descriptions on this binary complex will be provided in the next section. Rh blood group antigens, Rh and RhAG, were also found to be associated with ankyrin (Endeward et al., 2008). A Tetramer composed of two Rh and two RhAG subunits forms a functional unit in the ankyrin complex and their C-terminal cytosolic domains interact with the D2 domain (repeats 6-12 of the membrane binding domain) of ankyrin-R (Nicolas et al., 2003). The morphological abnormalities of Rh-null erythrocytes, associated with the primary defects of Rh or RhAG, imply an importance of the association of the Rh complex to the membrane skeleton (Huang et al., 1999). Protein 4.2 is another member of the ankyrin complex which associates with both band 3 (Korsgren and Cohen, 1986) and ankyrin-R (Korsgren and Cohen, 1988) and stabilizes the interaction between the two proteins (Rybicki et al., 1996). The observation of spherocytosis caused by the mutation of protein 4.2 at its N-terminal region (Gallagher and Forget, 1997) and the diminished levels of protein 4.2 induced by

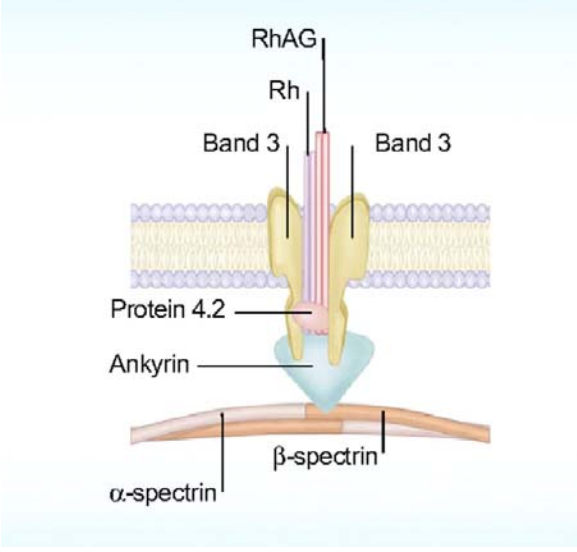

Figure 3. Structure of the ankyrin junction that links cytoskeleton to the lipid bilayer.

point mutations at various sites on the cytosolic domain of cdb3 (cdb3) (Jarolim et al., 1992) demonstrate the functional importance of protein 4.2 in the assembly of junctional proteins. The association of protein 4.2 with the erythrocyte membrane has been observed to be strengthened with protein modifications such as myristoylation and palmitoylation at specific sites of protein 4.2 (Bhattacharyya et al., 1999).

4.1R Complex Protein 4.1R, an essential constituent in the spectrin-4.1R-actin complex that is formed at the distal end of the spectrin tetramer, provides a docking site for the cytosolic domain of glycophorin C (GPC) to form the second class of junctional complexes. p55, a member of MAGUK (membrane associated guanylate kinase homologues), stabilizes the interaction between GPC and protein 4.1R by forming a stable ternary complex (Marfatia et al., 1994) with both proteins. GPC and p55 are missing in $4.1R^{-/-}$ mouse red cells (Shi et al., 1999) and much reduced in human 4.1R-deficient red cells (Reid et al., 1990). Besides, at least three other membrane blood group proteins, XK, Rh, and Duffy are associated with protein 4.1R providing further bridging interactions to the junctional complex though their relative contributions are not yet clear. Additionally, two other actin-binding proteins, adducin and dematin, are also known to stabilize this vertical linkage by directly binding band 3 and Glut1 (Khan et al., 2008; Salomao et al., 2008).

Inherited Red Cell Disorders

Inherited red cell disorders with impaired membrane and cell function can be categorized into two classes. The first group of conditions includes hereditary spherocytosis (HS), hereditary elliptocytosis (HE), hereditary ovalocytosis, and hereditary stomatocytosis where defects in the constituents in the junctional complexes or skeletal proteins due to mutations cause altered membrane structure. The second group features altered cell function resulting from mutations in

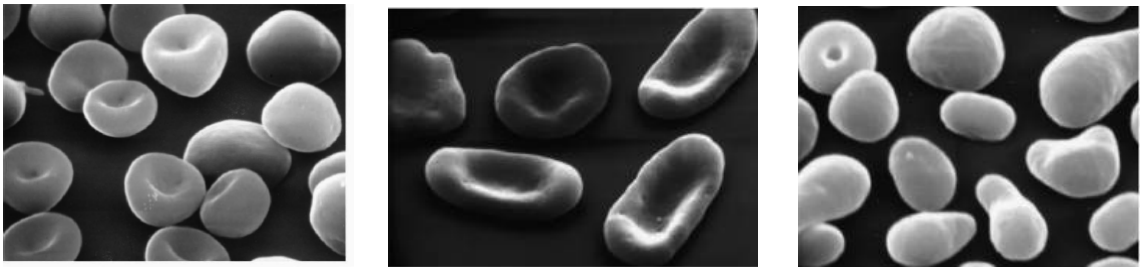

Figure 4. Red cell morphology. Hereditary spherocytosis (HS; left panel); nonhemolytic hereditary elliptocytosis (HE; middle panel); elliptocytes, poikilocytes, and fragmented red cells in hemolytic HE (right panel).

globin genes which includes sickle cell disease, Hb SC disease, Hb CC disease, and thalassemias. A common feature of red cells in all of these conditions is decreased cell deformability and each of them can be characterized by its abnormal morphology in peripheral blood smears. Among them, HS and HE have been most extensively studied and their mechanistic and molecular basis is well defined; however, for the other conditions, causative factors and mechanisms underlying the abnormal cell physiology still remain unidentified at the molecular level.

Hereditary spherocytosis HS refers to a group of heterogeneous inherited anemias that is characterized by the spherical shape of erythrocytes on a peripheral blood smear. It occurs in all ethnic groups, but is particularly common in northern European populations with an incidence rate of 1 in 3000 (Gallagher and Jarolim, 2005). The clinical manifestations of HS are highly variable ranging from mild to very severe hemolysis with anemia, jaundice, splenomegaly, reticulocytosis, and gallstones. Decreased membrane surface area and the resultant change in cell shape from biconcave disc to sphere is a common feature in all forms of HS. The spherocytes with reduced deformability are selectively trapped in the spleen, undergo splenic conditioning resulting in further loss of membrane, and are finally eliminated from the circulatory system (Gallagher and Jarolim, 2005). Splenic conditioning provides an unfavorable milieu to the

abnormal erythrocytes, which includes low pH, high macrophage contact, low glucose concentration, and high oxidant concentration. This elimination process in the spleen is the main severity of anemia by decreasing the survival of spherocytes.

Reduced membrane surface area in HS is ascribed to the weakened vertical linkages between the lipid bilayer and the membrane skeleton. Defects in genes encoding any of the protein components in the ankyrin complex (band 3, RhAG, ankyrin, protein 4.2, or spectrin) and the resultant deficiency in the corresponding protein lead to HS. Ankyrin deficiency is the most common cause of HS in northern European populations accounting for approximately 50-60% of cases (Eber and Lux, 2004). Ankyrin mutations cause both dominant and recessive disease that range from clinically mild to severe depending on the extent of membrane loss (Delaunay, 2007; Eber et al., 1996). Since ankyrin provides the main membrane binding site for the spectrin-based membrane skeleton, ankyrin deficiency is strongly coupled to a reduction in spectrin assembly in the membrane despite normal levels of spectrin (Hanspal et al., 1991).

While hereditary spherocytosis caused by α-spectrin mutations is recessive, mutations in β-spectrin give rise to dominant inheritance due to the 3-4 fold higher expression level in α-spectrin compared with β-spectrin (Wong et al., 2004). β-spectrin is known to be responsible for 15-30 % of cases of hereditary spherocytosis in the northern European population. Patients with β-spectrin deficiency have mild to moderately severe disease. α-spectrin defects account for about 5 % of cases, but typically lead to severe anemia.

Band 3 deficiency accounts for approximately 20-35 % of HS patients, presenting from mild to moderate anemia with dominant inheritance. Only 20-30 % of patients show a reduction in band 3 in SDS-PAGE analysis, which implies there is partial compensation by wild-type allele in trans for the mutated allele (Dhermy et al., 1997). Currently, over 40 different band 3 mutations have been identified from the gene (SLC4A1) which correspond to a range of mutant proteins associated with HS with mutations widely spread out in both cytoplasmic and transmembrane domains of the protein (Wrong et al., 2002).

Recessive HS resulting from homozygous mutations in the protein 4.2 gene (*EPB42*) is prevalent in Japan (Yawata et al., 2000), but is rare in other populations. The cell membranes from this condition show nearly complete absence of protein 4.2. To date, a series of protein 4.2 mutations have been identified in association with HS. While some mutations lead to premature termination of translation, the others have been found to generate mutant proteins with a single amino acid substitution which impair the ability to bind to the cytoplasmic domain of band 3 (Toye et al., 2005).

Absent or markedly reduced Rh or RhAG expressions result in mild to moderate hemolytic anemia. Rh deficiency accounts for less than 1 % of HS patients. In addition to the typical features of spherocytosis, Rh null erythrocytes show increased osmotic fragility and

Table 1. Clinical and molecular characterization of molecular defects that cause hereditary spherocytosis

Proteins	Patients with HS	Heredity	Prevalent mutations	Protein reduction	Disease severity	Peripheral blood smear
Ankyrin-1	USA and Europe, 40-65%; Japan, 5-10%	AD, AR, de novo	AD or de novo: null mutation; AR: missense and promoter mutation	Spectrin and ankyrin -R, 15-50%	Mild to moderate	Spherocytes
Band 3	20-35%	AD	Functionally null mutation	Band 3, 15-35%	Mild to moderate	Spherocytes, occasional mushroom-shaped or pincered cells
α-spectrin	< 5%	AR	α-LEPRA allele and null mutation	α-spectrin, 50-75%	Severe	Spherocytes, contracted cells, and poikilocytes
β-spectin	15-30%	AD, de novo	Null mutation	β-spectin, 15- %40	Mild to moderate	Spherocytes, 5-10% acanthocytes
Protein 4.2	USA and Europe < 5%; Japan, 45-50 %	AR	Missense (prevalence of 4.2 Nippon)	Protein 4.2, 95-100%	Mild to moderate	Spherocytes, ovalostomatocytes

AD=autosomal dominant; AR=autosomal recessive; HD=hereditary spherocytosis; LEPRA=low-expression allele Prague.

dehydration which is manifested by reduced cell cation and water content and increased cell density (Cartron, 2001).

Hereditary Elliptocytosis HE is easily characterized by the presence of elliptically shaped red cells on peripheral blood smear. It is a relatively common red blood cell disorder with worldwide distribution, but is more prevalent in malaria endemic regions such as West Africa where its prevalence reaches up to 2 % of the population. The majority of HE, which is heterozygous for an elliptocytic variant, is asymptomatic but approximately 10 % of patients with homozygous or compound heterozygous for HE variants suffer from mild to severe anemia. This abnormal morphology and mechanical property of cells in HE come from the mechanically unstable membrane, which results in progressive transformation of cell shape, membrane fragmentation, and reduction in membrane surface area. Therefore, the severity of the disease has a strong correlation with the extent of decrease in membrane mechanical stability (Lane et al., 1987). The underlying molecular mechanism for decreased membrane stability in HE is a loss of 'horizontal' linkages in the membrane skeleton mainly due to defects either in spectrin dimer-dimer interactions or in the spectrin-actin-4.1R junctional complex. Defects in any of the protein components involved in lateral linkages in the membrane skeleton are the main cause of HE.

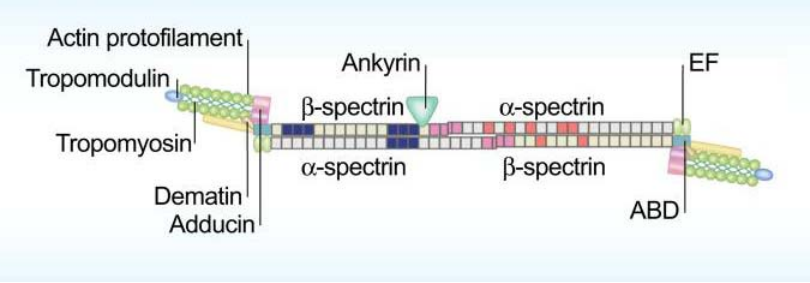

Figure 5. Horizontal linkages in the structure of the spectrin-based cytoskeleton

The primary cause of HE is α-spectin defects which account for 65 % of cases. The most frequent mutation in α-spectrin is missense mutations in the N-terminal region that is directly involved in the spectrin dimer-dimer interaction (Gallagher, 2004). Defects in β-spectrin also present in 30 % of HE cases. Mutations in β-spectin which are involved in loss of spectrin self-association include point mutations and truncations in the C-terminus. Most cases of HE from spectrin mutations show decreased spectrin self-association, the level of which shows a strong correlation with clinical severity. Defects in 4.1R contribute to only 5% of HE cases (Gallagher, 2004), which leads to a weakened spectrin-actin junctional complex and subsequently to decreased membrane mechanical stability.

Structure and Function of Anion Exchanger 1

Topology and function of the AE1 transmembrane domain

The transmembrane domain of AE1 (residues 361-911; tdb3) is functional in anion transport either when isolated from the cytosolic domain by proteolysis (Grinstein et al., 1978) or when expressed from a recombinant construct (Lepke et al., 1992), showing that it is structurally and functionally independent of the cytosolic domain. The primary biological function of tdb3 is to catalyze the one-for-one exchange of two monovalent anions, chloride and bicarbonate, in opposite directions across the red blood cell membrane. The passive exchange of these anions is essential to the disposal of carbon dioxide and pH homeostasis in the body. The discovery that stilbenedisulfonates are potent competitive inhibitors of band 3-mediated anion transport provided a tool to gain insight into the mechanism of the transport process (Cabantchik and Rothstein, 1972; Passow, 1986). A body of evidence from kinetic studies using competitive inhibitors and ^{35}Cl NMR revealed that band 3 is an alternating site transporter possessing a single transport site that is alternately exposed to opposite sides of the membrane (Falke and Chan,

1985; Jennings, 1982) confirming the early proposed ping-pong mechanism (Falke and Chan, 1985; Gunn and Frohlich, 1979).

Biophysical data from CD and NMR studies have shown that the transmembrane domain of band 3 is almost entirely helical (Gargaro et al., 1994; Popov et al., 1997). Due to its large size and difficulty in obtaining crystals suitable for high resolution diffraction studies, detailed structural information on tdb3 has remained ambiguous. Hydropathy analysis of amino acid sequence combined with some experimental data from covalent labeling studies, proteolysis, and antibody epitope mapping have lead to the model containing 14 membrane spans (Tanner, 1993; Vince and Reithmeier, 1996). However, a later study using scanning N-glycosylation mutagenesis (Popov et al., 1997) and cysteine scanning (Zhu et al., 2003) proposed a different model with 12 membrane spans. The main topological difference between the two models is seen in a 70 residue long fragment of the C-terminal region, raising a possibility of structural heterogeneity in this region.

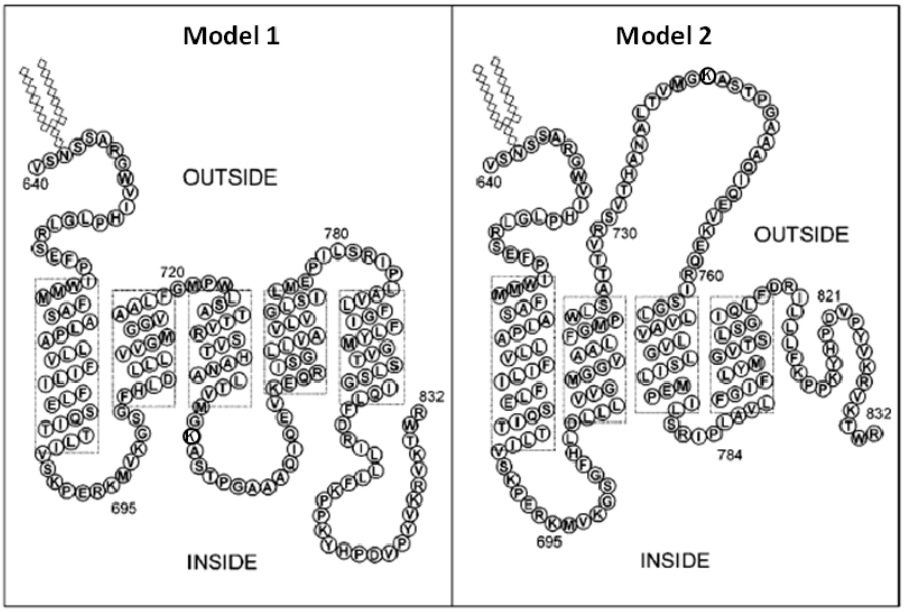

Figure 6. Two alternative models for the topology of the AE1 transmembrane domain

Notably, the isolated segment spanning this C-terminal region was sufficient to insert into the microsomal membrane by itself and when it was co-expressed in *Xenopus* oocyte with the remainder of the protein, transport activity was restored to the normal level (Groves and Tanner, 1995). Taken together with the presence of the signal sequences required for proper membrane insertion and targeting to the plasma membrane (Okubo et al., 1997), it is speculated that the C-terminal region of tdb3 is of structural and functional importance. Likewise, the N-terminal region encompassing the first transmembrane domain (TM1) was also shown to be associated with membrane targeting and transport activity of tdb3 in a more recent mutation study (Kanki et al., 2003). A set of specific mutants of an N-terminal fragment which has mutations within the residues involved in Southeast Asian ovalocytosis (residues 400-408) impaired membrane insertion of TM1 both *in vivo* and *in vitro*. Furthermore, deletion of the cytoplasmic surface sequence (G^{381}LVRD) abolished chloride transport indicating that this sequence is essential in anion transport of tdb3. A low resolution (20Å) EM image from two dimensional crystals (Wang et al., 1993; Wang et al., 1994) and NMR structures for a set of isolated fragments (Askin et al., 1998; Gargaro et al., 1994) have been previously reported. Recent cryo-EM image analysis of tubular crystals of tdb3 yielded a 3D image of the tdb3 dimer in the inhibitor-stabilized outward-open conformation at 18 Å resolution (Yamaguchi et al., 2010), but a higher resolution structure for the whole domain of tdb3 is still unknown.

Structure and function of the cytoplasmic domain of AE1

The cytoplasmic domain of band 3 serves as an organizing center to recruit various cytoplasmic proteins such as glycolytic enzymes (Campanella et al., 2005), hemoglobin (Walder et al., 1984; Waugh and Low, 1985), hemichromes (Waugh and Low 1985), and tyrosine kinase $p72^{syk}$ (Harrison et al., 1994). At least 5 glycolytic enzymes including glyceraldehyde-3-phosphate dehydrogenase (GAPDH), aldolase, phospho-fructokinase (PFK), lactate dehydro-genase (LDH), and pyruvate kinase (PK) were observed to bind to the N-terminal region of cdb3

to form a macrocomplex. The cdb3 recognition sites of GAPDH, aldolase, and PFK contain two consensus binding motifs ($D^{6}DYED^{10}$ and $E^{19}EYED^{23}$) and are clustered along the narrow segment (residues 1-23) of the unstructured N-terminal region of cdb3 (Chu and Low, 2006).

The current view on the functional implication of this macrocomplex assumes the formation of a 'metabolon', which provides two advantages for red cell metabolism; (i) increase in the efficiency of glycolysis through the channeling of substrates throughout the reaction pathway (ii) compartmentalization of generated ATP for the direct consumption by ion channels on the membrane without release into the cytoplasm (Campanella et al., 2005). It is interesting to note that the assembly of glycolytic enzymes on cdb3 is sensitive to the oxygenation state of the cell and tyrosine phosphorylation on the N-terminal region of cdb3. Recent studies showed that binding of deoxygenated hemoglobin or tyrosine phosphorylation by $p72^{syk}$ on the N-terminus of cdb3 lead to dissociation of glycolytic enzymes, strongly suggesting there might be regulatory mechanisms of the glycolytic machinery on the inner surface of the membrane by oxidative stress (Chu, Breite et al. 2008) or red cell senescence processes (Chu et al., 2008; Ding et al., 1996; Pantaleo et al., 2009). The observation of this glycolytic assembly in murine erythrocytes and of its dissipation in erythrocytes from band 3 knockout mice suggests that this could be a general phenomenon for all mammalian erythrocytes (Campanella et al., 2008). Another example of metabolon formation in red cells is seen in the cytoplasmic C-terminal tail of tdb3. Carbonic anhydrase II which catalyzes conversion of carbon dioxide to bicarbonate has been observed to bind a short acidic motif ($LD^{887}ADD$) on the C-terminal region of tdb3 (Vince and Reithmeier, 2000). The interaction of these two proteins involved in bicarbonate metabolism is speculated to facilitate and regulate the flow of bicarbonate across the membrane (Reithmeier, 2001).

The low pH (pH 4.8) crystal structure of the cdb3 dimer has been determined at 2.6 Å resolution as shown in Fig. 7 (Zhang et al., 2000). The core domain of each cdb3 monomer forms a tightly packed globular structure spanning residues 55-290. The dimerization arm of cdb3 (residues 314-344) extends away from the core domain and interdigitates with the equivalent part

of the second monomer to give a tightly interlocked dimer structure. The presence of a cluster of 9 leucine residues provides an extensive network of hydrophobic interaction contributing to the stabilization of dimer structure. Two important domains involved in the association with various binding partners, N- and C-terminal region of cdb3 (residues 1-54 and 357-379, respectively), were missing or poorly defined by electron density, suggesting that they are in a structurally dynamic or heterogeneous state. This finding agreed with the solution structure obtained from a recent SDSL-EPR study (Zhou et al., 2005) where spin labeling at both the N- and C-terminal regions, resulted in fast and unrestricted motion which is characteristic for unstructured protein.

One of the longtime intriguing questions about cdb3 structure is its reversible pH-dependent conformational equilibrium in solution. A body of evidence from various biophysical studies (Appell and Low, 1981; Low, 1986; Thevenin et al., 1994) revealed that cdb3 can exist in three distinct conformations along the wide range of pH (pH 4~10) with transitions at pH 7.2 and

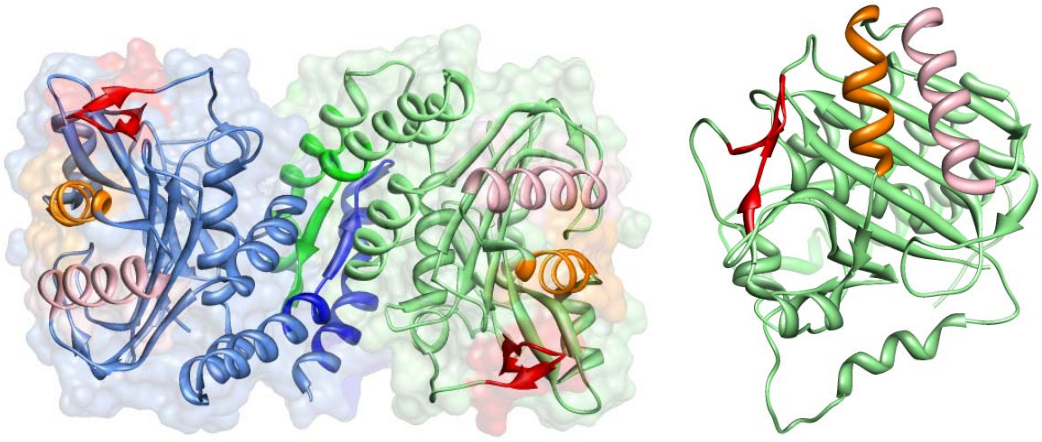

Figure 7. Crystal structure of the cdb3 dimer. Top view of a cdb3 dimer (left panel) and the peripheral surface of one monomer were illustrated in a ribbon presentation. Two monomers were colored in skyblue and pale green. The dimerization arms from each monomer were highlighted in green and blue, α-2 helix in pink, α3-helix in orange and β6/β7 hairpin loop in red. The unstructured N- and C-terminal regions are missing in the crystal structure.

9.2. Especially, the sedimentation experiment exhibited approximately a 10 Å increase in hydrodynamic radius with increasing pH (Low et al., 1984). Based upon the crystal structure, the conformational change observed at high pH was hypothesized to be involved in an outward movement of peripheral domains away from the dimerization arms to form an extended form of the dimer. Even though pH-driven conformational changes of cdb3 may not be relevant *in vivo* since variations in intracellular pH in normal erythrocytes is less than a tenth pH unit, it cannot be excluded that the conformational equilibrium of cdb3 might be controlled by other physiological triggers such as interaction with its binding partners (Zhou and Low, 2001). When the solution structure of cdb3 at neutral pH was extensively probed by SDSL-EPR (Zhou et al., 2005), the global structure determined by crystallography at low pH was found to be retained well, indicating the crystal structure is likely to be the physiologically relevant form of cdb3.

AE1 and Hereditary Spherocytosis

HS associated with AE1 is inherited dominantly and is generally milder than HS caused by ankyrin or spectrin mutations. AE1 deficiency accounts for approximately 30 % of HS cases in European patients (Jarolim et al., 1996). To date, more than 55 band 3 gene mutations have been identified, most of which are missense or frameshift mutations. Many of the mutations that are localized in the transmembrane domain involve highly conserved arginine residues as demonstrated by R490C, R518C, R760Q, R808C, R808H and R870W (Dhermy et al., 1997). These mutations in the transmembrane domain appear to impair co-translational insertion of band 3 into the membranes of the ER during protein synthesis or to reduce protein stability. Mutations in the cytosolic domain of band 3 can interfere with its binding to other membrane skeletal proteins such as ankyrin and protein 4.2. For example, three cytosolic domain mutations associated with HS, E40K (Band 3 Montefiore; (Rybicki et al., 1993), G130R (Band 3 Fukuoka; (Inoue et al., 1998), and P327R (Band 3 Tuscaloosa; (Jarolim et al., 1992) show normal AE1 content in the cell. Instead, these mutations are associated with significant decreases in the protein

4.2 content. Biophysical characterization of these mutants revealed that the overall structure and stability of wt-cdb3 are maintained in all three variants (Bustos and Reithmeier, 2006). Consistently, a structural study using EPR also demonstrated that the P327R mutation results in a subtle change in the local structure of the cdb3 dimer only near the mutation site (Zhou et al., 2007).

Structure and Function of Ankyrin-R

The ANK repeat and ankyrin protein family

Repeat proteins form one of the most abundant protein classes that mediate various protein-protein interactions involved in a number of physiological and cellular processes which includes cytoskeleton integrity, membrane protein targeting, cell-cell signaling, transcription and cell-cycle regulation, cell and tissue development, and inflammatory response etc. (Main et al., 2003; Mosavi et al., 2004). Their most prominent structural feature is that they contain relatively short (typically 20-40 amino acid residues long), repeating motifs which function as building blocks that stack side by side to form non-globular, modular structures. Unlike other protein-protein interaction domains, these modular structures typically recognize neither specific amino acid sequence nor structural motif. Instead, a tandem stack of repeating units provides an elongated binding interface and the variations in interacting surface residues (hot spots) determines the specificity for binding.

The ankyrin-Repeat (ANK), a motif of 33 amino acid residues, is the second most frequent repeating module found in protein databases. Although ANK proteins are present across all forms of life including the viral genome, the majority are found in eukaryotes indicating their critical role in modulating diverse signaling pathways necessary to evolve more complicated multi-cellular organisms (Marcotte et al., 1999). While the proteins with up to 34 ANKs have

been found by genome analysis, most of ankyrin proteins contain 4~7 ANK motifs. Consistent with the observation of no single ANK repeat in nature, an isolated ANK was shown to be unable to form a stably folded structure (Mosavi et al., 2002).

Despite a few exceptions of insertion in the long loop region, most of ANK repeats maintain a canonical helix-turn-helix-β-haripin/loop conformation. As shown in Fig. 8, two α-helices in the same repeat are arranged in an antiparallel fashion and the longer outer helix from the preceding repeat and the shorter inner helix from the next repeat are linked by the long hairpin loop which extends outward from the α-helices forming an approximately right angle with the helix axis. Multiple ANK repeat units stack together to form an elongated helix bundle, which exhibits a slight curvature mainly due to the differences in the lengths as well as in the extents in the interrepeat packing interactions between two α-helices. Each repeat is rotated 2–3º counterclockwise from the preceding repeat and hence 32 repeats can complete a single superhelical turn with a radius of 35 Å (Michel et al., 2001).

ANK repeats contain a set of key residues and sequence motifs which are well conserved in most ankyrin proteins which are critical in maintaining its characteristic topology. ANK consensus sequences obtained from statistical analyses shown in Fig. 8 (Kohl et al., 2003; Mosavi et al., 2002) highlights those residues and sequences. The two conserved sequences, α-TPLH motif (positions 4–7) from the inner helix and a (V/I)VX(L/V)LL motif (positions 17-22; X is any hydrophilic residue) from the outer helix are the primary contributors to the network of hydrophobic interactions which stabilize the extended helix bundles that constitute the main backbone of ANK proteins. To the contrary, the stability of the β-hairpin loop and its expansion to a β-sheet are ascribed to numerous hydrogen bonds between non-hydrophobic resides which are rich in the long loop region. It is notable that the β-hairpin loop domain is relatively flexible in size and conformation and consists of much less conserved residues as is evident in Fig 8. Given that one of the common features throughout all structures of ANK protein complexes determined to date is the direct involvement of β-hairpin loops in the binding, the residue

variations in β-hairpin positions are speculated to provide binding specificity for a range of diverse binding partners despite the high degeneracy in modular structure of ANK repeats (Li et al., 2006).

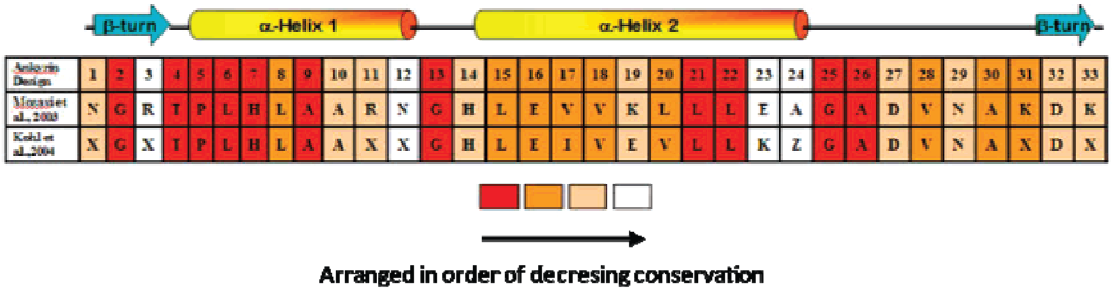

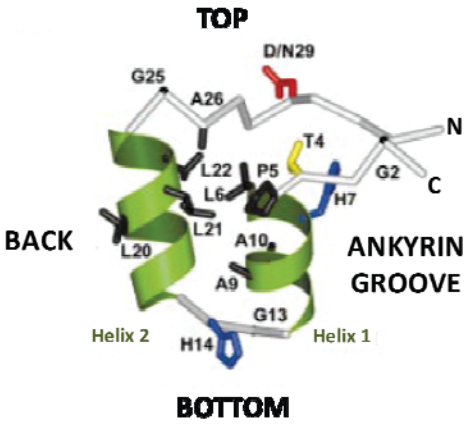

Figure 8. The top panel shows the consensus sequences of the ANK repeat as defined by Mosavi et al. (Mosavi et al., 2002) and Kohl et al. (Kohl et al., 2003). The schematic representation of the secondary structures corresponding to this sequence is presented above the sequences. The conservation level of each sequence is color-coded. The consensus sequence from Kohl et al. includes an X that denotes any amino acid except C, G, and P and a Z that can be a H, N, or Y. The left panel illustrates the structure of the typical ANK repeat with the highly conserved residues.

Ankyrins and ankyrin binding proteins

Ankyrins are a family of adaptor proteins that have the potential to link various membrane proteins to the spectrin-based membrane skeleton. In the mammalian genome, three distinct genes encoding ankyrins (ANK1, ANK2, and ANK3) have been identified. Corresponding polypeptides are designated as ankyrin-R (R for restricted, also called ankyrin 1), ankyrin G (G for giant, also called ankyrin 2), and ankyrin B (B for broad, also called ankyrin 3),

respectively. These isoforms share a similar domain structure which consists of four conserved domains: N-terminal membrane-binding domain, central spectrin-binding domain, and C-terminal regulatory domain and death domain. Ankyrin genes are expressed and processed through alternative splicing in a tissue-dependent and developmentally regulated fashion, giving rise to a large number of isoforms that utilize different combinations of functional domains (Bennett and Baines, 2001). While the canonical ankyrins including ankyrin-R in human erythrocytes have 190~220 kDa Mw, alternative splicing produces multiple isoforms with different sizes in all three ankyrin classes. A small isoform of ankyrin-R (20-26 kDa), which lacks both the membrane-binding and spectrin-binding domain is enriched in M and Z lines of skeletal myofibrils in the sarcoplasmic reticulum. The truncated forms of ankyrin G missing all or portions of their membrane-binding domain are found in Golgi and lysosomal membranes. The distribution pattern of these small ankyrins strongly suggests their distinct function in the cytoplasm. To the contrary, ankyrin G and B exhibit giant isoforms whose Mw is up to 480 kDa. One of the common structural features seen in these giant ankyrins is that they contain long inserted sequences between the membrane-binding and death domain forming an extended random coil. Based upon the observation that ankyrin isoforms containing this tail domain are highly localized in axons, the tail domain is hypothesized to have a role in axonal targeting of giant ankyrins.

The membrane binding domain of ankyrins provides a docking platform for a range of structurally diverse and sequence-unrelated integral membrane proteins to coordinate various tissue- and cell-specific physiological functions. These membrane proteins can be roughly categorized into three groups based on their fundamental functions and are listed in Table 2 below.

The L1 CAM family of cell adhesion molecules (L1, neurofascin, Nr-CAM, Ng-CAM) is the major class of ankyrin-binding proteins in the vertebrate nervous system. In axon initial segments and nodes of Ranvier, the 480/270 kDa isoform of ankyrin G anchors neurofascin to β-spectrin (Davis et al., 1996). On the other hand, ankyrin G showed the ability to form voltage-

gated Na^+ channel clustering in the same membrane domain. Targeted knockout of ankyrin G leads to loss of the ability to fire action potentials and clustering of voltage-gated Na^+ channels and neurofascin at the axon initial segments of Purkinje neurons in mice (Jenkins and Bennett, 2001) and cultured hippocampal neurons (Yang et al., 2007). KCNQ2/3 channels, which colocalize with voltage-gated Na^+ channels and modulate its activity at nodes of Ranvier and axon initial segments, also showed the ability to bind ankyrin G to form the a multiprotein complex (Pan et al., 2006; Rasmussen et al., 2007).

Another good example of ankyrin-mediated formation of functional membrane domains can be seen in microdomains of cardiomyocyte T-tubules where a set of membrane transporters coordinate synchronous waves of calcium release and uptake. Several lines of evidence indicate that ankyrin B colocalizes both the Na^+/Ca^{2+} exchanger (NCX1) and Na^+/ K^+ ATPase in the plasma membrane and is in association with the IP3 receptor in the sarcoplasmic reticulum (Mohler et al., 2005). Reduced expression of Ankyrin B has lead to the selective loss of NCX1 and Na^+/ K^+ ATPase as well as IP3 receptor in cardiomyocytes (Mohler et al., 2005; Mohler et al., 2003). These observations strongly suggest the plausible functional coupling between two transporters resulting from ankyrin B-dependent colocalization. In a different type of microdomain of T-tubules, ankyrin G binds Nav1.5 and is required to the targeting of the channel protein (Mohler et al., 2004).

In addition, E-cadherin, a key cell adhesion molecule in the lateral membrane of epithelial tissues, dystrophin-dystroglycan complex at costameres in skeletal muscle and cardio-mytocytes, and clathrin are known to require association with ankyrins for their normal trafficking and function (Bennett and Healy, 2009).

Even though all the proteins mentioned above have been evolved independently with neither sequence nor structural homology among them, it is intriguing to note that many of them show one shared feature. For many ankyrin-binding proteins, their binding sites are observed or

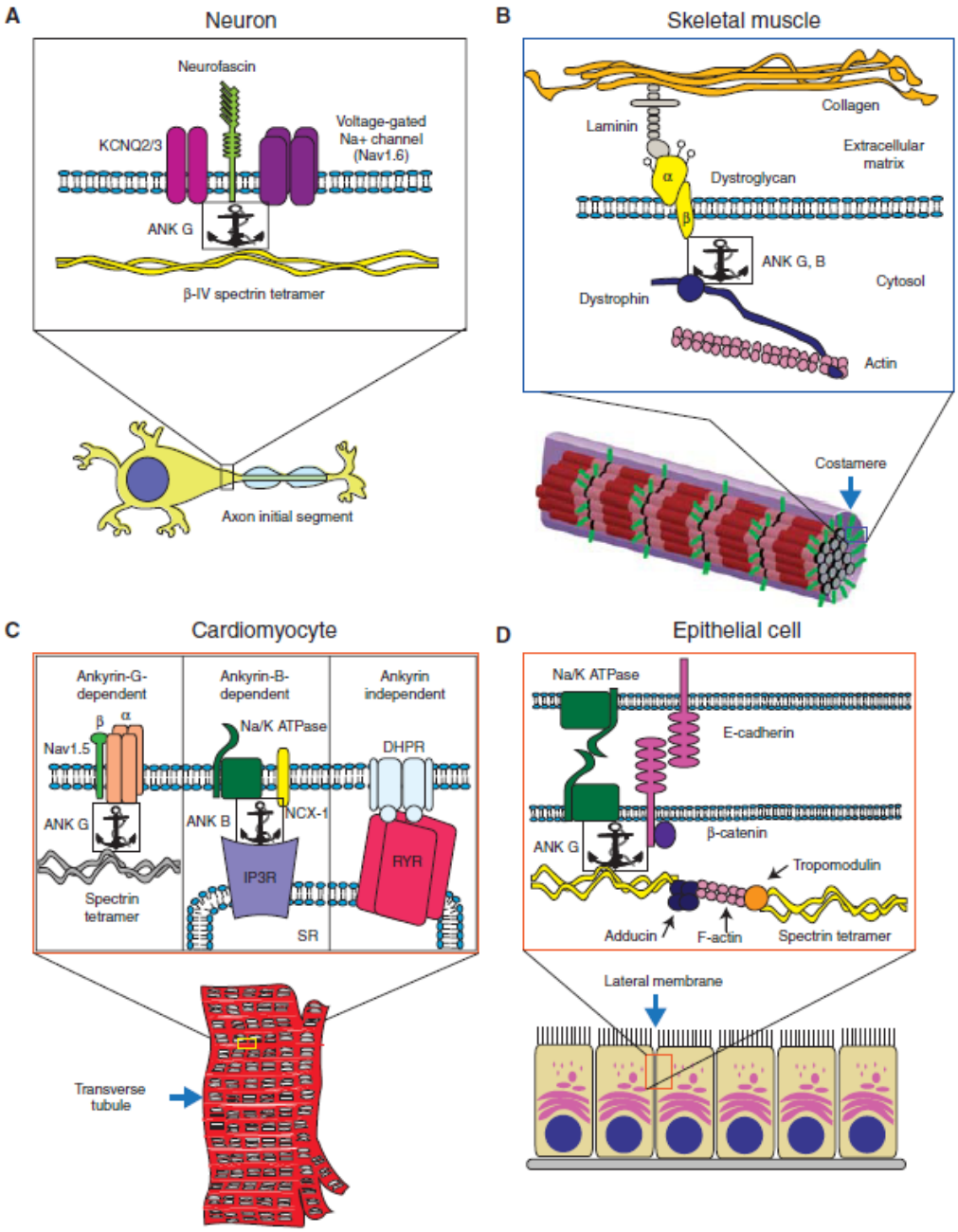

Figure 9. Macromolecular complexes organized by ankyrins and spectrins in diverse types of specialized membranes. (A) Ankyrin-G forms a complex with β-IV spectrin, neurofascin (a cell adhesion protein), and ion channels (KCNQ2/3 and voltage-gated sodium channel) at axon initial segments in Purkinje neurons. (B) In costameres of skeletal muscle, ankyrins-B and -G cooperate to target and stabilize key components of the dystroglycoprotein complex. At the membrane, ankyrin-G binds to dystrophin and β-dystroglycan. (C) In cardiomyocyte transverse tubules, ankyrins-B and -G coordinate separate microdomains. Ankyrin-B binds Na^+/K^+ ATPase, Na^+/Ca^{2+} exchanger (NCX1), and the inositol triphosphate receptor (IP_3R). Ankyrin-G forms a complex with Nav1.5 and spectrin. (D) Ankyrin-G in epithelial lateral membrane assembly.

Ankyrin-G binds to E-cadherin, β-2 spectrin, and the Na^+/K^+ ATPase. Spectrins are connected via F-actin bridges bound to α/γ-adducin and tropomodulin.

predicted to reside on the extended peptides with no secondary structure (Bennett and Healy, 2009). For these proteins, binding through unstructured domains is expected to provide their binding partners more functional versatility and variable binding affinity, enabling them to adapt to rapidly changing physiological demands.

Table 2. Ankyrin binding proteins

Ion channels and pumps	Cell adhesion molecules	Cellular transport
Anion exchanger	L1-CAM family	Tubulin
Na^+/K^+ ATPase	CD44	Clathrin
Voltage-gated Na channel	E-cadherin	
Na^+/Ca^{2+} exchanger	Dystroglycan	
KCNG2/3		
Rh antigen		
IP3 receptor		
Ryanodine receptor		

Unlike globular proteins, ANK proteins with modular structures lack long range-tertiary interactions. They are stabilized by intra-repeat interactions or inter-repeat interactions with neighboring repeats. This unique structural aspect raised many interesting questions with regards to protein folding issues. Surprisingly, most folding studies using various ANK proteins showed a two-state folding pathway (folded or unfolded state) with no observation of a partially folded intermediate, and a highly cooperative transition between them (Mosavi et al., 2002; Tang et al., 1999; Zeeb et al., 2002; Zhang and Peng, 2000; Zweifel et al., 2003). This observation strongly

implies the existence of long range coupling between the sparse repeats, which can affect the entire molecule. However, in other kinetic folding studies using human p16 and p19, members of the INK4 tumor suppressor family (Tang et al., 1999; Zeeb et al., 2002), and Notch ANK domain (Mello et al., 2005; Zweifel and Barrick 2001), partially folded intermediates were detected. The manipulation of ANK proteins such as insertion or truncation of a whole unit showed that each repeat in the protein has a distinct stability and folding equilibrium. In the case of p16, two ANK repeats at the C-terminus was found to fold first with higher stability and form a scaffold to facilitate the folding of the other repeats (Zhang and Peng, 2000; Zweifel and Barrick, 2001).

Structure of human erythrocyte ankyrin-R

Human erythrocyte ankyrin-R is a member of the canonical ankyrin (190 ~ 220 kDa) which consists of four distinct domains: a membrane-binding domain, a spectrin-binding domain, a death domain and a regulatory domain. The spectrin-binding domain contains a small subdomain, ZU5-ANK (homologous protein to ZO-1, a tight junction-associated protein, and Unc5, the netrin receptor), which interacts with repeat 13 to 15 of βI-spectrin. Recently, a crystal structure of this protein complex has been determined and the nature of the mutations associated with these proteins has been examined at atomic resolution (Ipsaro and Mondragon, 2010).

Figure 10. Multidomain structure of ankyrin-R. The N-terminal membrane-binding domain consists of 4 independently folded subdomains denoted D1-D4, each of which contains 6 ANK repeats.

Death domains were first reported in proteins such as Fas and tumor necrosis factor receptors that participate in apoptosis pathways. They possess the ability to interact with related death domains in other proteins. These findings lead to the assumption of the involvement of the death domain in self-association or interaction with other protein, but which ones remains to be elucidated. The C-terminal regulatory domain has been observed to modulate the binding affinity of the protein for both AE1 and spectrin (Davis et al., 1992; Hall and Bennett, 1987), but the mechanism underlying the regulatory activity is not defined yet.

The N-terminal membrane-binding domain (residues 1-826) is comprised of 24 ANK repeats and can be divided into four subdomains D1 through D4 based upon proteolytic maps, each of which contains the basic folding unit of 6 ANK repeats (Michaely and Bennett, 1993). The membrane-binding domain of Ankyrin-R is known to recruit two band 3 dimers with two separate binding sites interacting with the cytoplasmic domains of band 3. The details of this protein-protein interaction will be described in the next section.

The crystal structure of AnkD34 (repeats 13 through 24) from human ankyrin-R has been determined at neutral pH (Michaely et al., 2002). The structure of each individual repeat was found to feature the typical 'L'-shaped ANK repeat as described earlier. The 12 ANK repeats stack side by side to form a 125 Å long, left-handed super helix with 13° of pitch. This curvature of the repeat stack is primarily determined by the relative side chain volumes of residues that form the helical bundle cores, such as the residues at positions 10, 17, and 18 of each repeat. The residues from equivalent positions in each repeat form four distinct surfaces of overall structure: i) a concave 'bottom' surface (positions 13-16); ii) a concave 'groove' surface (positions 1, 3, 11, 12, and 32); iii) a convex 'back' surface (positions 19, 23, 24); and iv) a convex 'top' surface (positions 27, 29, 31, and 33) as shown in Fig 8. Each of four surfaces from individual repeats forms an extended and continuous surface along the superhelical axis in the whole molecule. In particular, the concave bottom and groove surfaces are predicted to provide multiple, but disparate binding interfaces for various binding partners such as the clathrin heavy chain, AE1,

Na^+/K^+ ATPase, L1 family of cell adhesion molecules and voltage-gated Na^+ channels (Michaely and Bennett, 1995; Michaely et al., 1999; Thevananther et al., 1998).

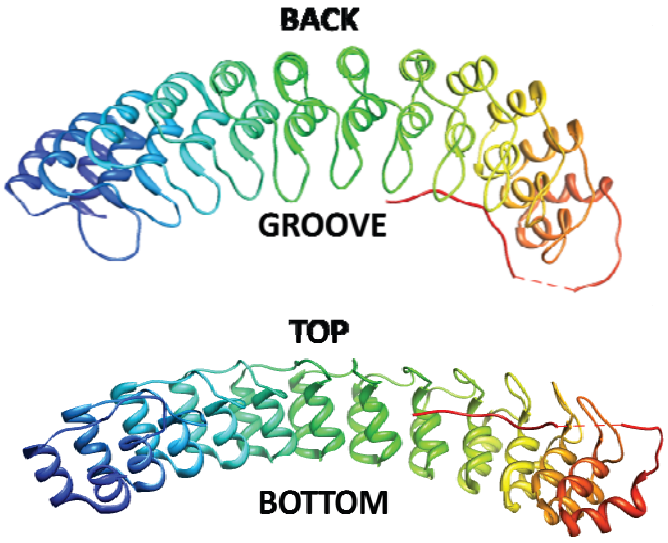

Figure 11. The crystal structure of AnkD34 which contains 12 ANK repeats. The juxtaposition of the long β-hairpin loops forms the β-sheet-like 'top' surface. The concave groove surface consists of inner helices and β-hairpin loops and the convex backbone surface is formed by outer helices.

Interaction between cdb3 and AnkD34

The association of cdb3 with ankyrin-R has been one of the most intensively studied protein-protein interactions due to its importance in contributing to the structural integrity of the erythrocyte membrane. Most of the previous efforts have been devoted to identifying the critical structural entities of each protein which mediate this interaction. Even though early studies with different approaches generated conflicting results on the binding interface of cdb3, general consensus has been reached that the putative central hinge (the β6/β7 hairpin loop) and the acidic

N-terminal tail of cdb3 are the regions which are essential for ankyrin binding. Competition assays using monoclonal antibodies raised against peptides encompassing the hinge region (residues 175-186) showed that these antibodies could block ankyrin binding (Davis et al., 1989; Willardson et al., 1989). Analyses of a series of chimeric constructs also revealed that a fragment containing the hinge region (residues 155~195) are necessary for binding (Ding et al., 1996). Furthermore, ankyrin has been observed to protect the cdb3 hinge from tryptic cleavage (Willardson et al., 1989). A recent *in vivo* study where transgenic mice expressing a deletion mutant of cdb3 which lacks the β6/β7 hairpin loop have lead to spherocytosis with decreased ankyrin binding demonstrated the importance of this loop in the interaction between cdb3 and ankyrin (Stefanovic et al., 2007).

Evidence from additional studies suggested that the N-terminal region of cdb3 might also be involved in ankyrin binding. The finding that kidney cdb3 which lacks the N-terminal region (residues 1-65) exhibits no affinity for ankyrin (Ding et al., 1994; Wang et al., 1995). Inhibition of tyrosine phosphorylation on the N-terminus of cdb3 upon binding ankyrin and reduction in binding affinity caused by antibodies against the N-terminus of cdb3 further supported the hypothesis that the N-terminus of cdb3 might be another ankyrin docking site for ankyrin-R (Willardson et al. 1989).

Several lines of evidences suggest that two cdb3 dimers are associated with the full length membrane binding domain of one ankyrin in the complex (Casey and Reithmeier, 1991a; Thevenin and Low, 1990; Van Dort et al., 1998) although there has been a report that the dimer is sufficient for ankyrin binding (Pinder et al., 1995). It is not known if a true tetramer of cdb3 is the preferential form that binds ankyrin or if ankyrin-Recruits two cdb3 dimers in a sequential manner. Currently, both hypotheses are equally plausible based upon the previous study on cdb3 binding sites of ankyrin where binding assays using a series of truncated mutants of ankyrin identified two separate cdb3 binding sites, one on repeats 7-12 (AnkD2) and the other on repeats 13-24 (AnkD34) with positive cooperativity between them (Michaely and Bennett, 1995).

Interestingly, these two sites exhibit totally different binding characteristics. Binding to AnkD2 has been observed to be highly salt and pH dependent with a higher affinity ($K_d \approx 10$ nM), strongly implying that this interaction could be mediated by electrostatic interactions. To the contrary, binding to AnkD34 is likely to depend on hydrophobic interactions since it displays no sensitivity to salt concentration or pH and exhibits lower binding affinity ($K_d \approx 40$ nM). The isolated fragment of either AnkD3 or AnkD4 lost its binding affinity when separately expressed. It is interesting that this latter binding interaction requires an abnormally long equilibrium time (longer than 10 hours), implying that some conformational changes in either protein might be involved in this binding event.

Based upon all the available structural information including the crystal structures and the plausible binding interfaces of both proteins, a working structural model for cdb3-AnkD34 complex has been proposed by Michaely and coworkers (Michaely et al., 2002) as shown below.

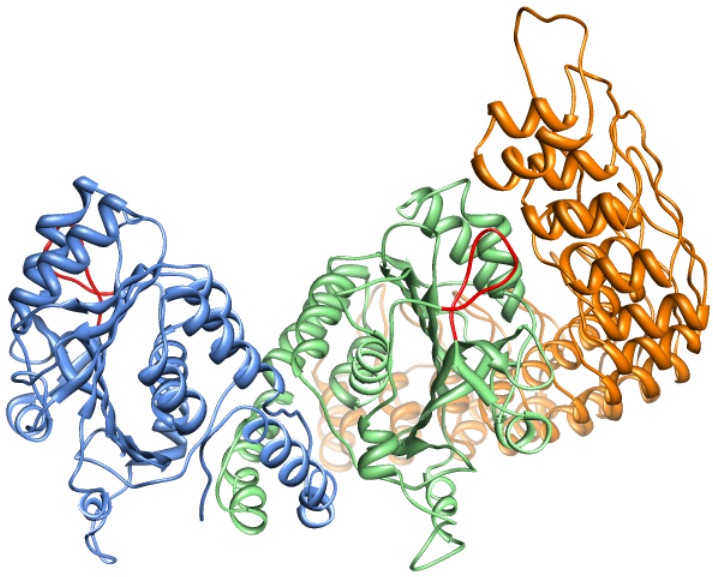

Figure 12. Hypothetical structural model of cdb3·AnkD34 complex proposed by Michaely et al. (Michaely et al., 2002). Note that peripheral domains of cdb3 including the β6/β7 hairpin loop (shown in red) directly interact with the concave groove region of AnkD34 (orange).

The two main features in this model are; i) ankyrin forms complex with cdb3 through its concave groove region composed of long hairpin loops and inner helices as seen in many other ankyrin complexes, ii) the β6/β7 hairpin loop of cdb3 makes direct contact with ankyrin on the binding interface. The studies in Chapter III utilize site-directed spin labeling in combination with modern EPR methods to test and refine this working structural model.

CHAPTER II

ELECTRON PARAMAGNETIC RESONANCE SPECTRSCOPY

Principles of Electron Paramagnetic Resonance

Zeeman Interaction

Spins are magnetic moments that are associated with angular momentum. An atom or molecule will possess a permanent magnetic dipole moment only if it has nonzero electronic (or total) angular momentum **J** which corresponds to the vectorial sum of spin angular momentum **S** and orbital angular momentum **L**. The primary and secondary quantum numbers for total angular momentum, j and m_j can be defined, for example, in a one electron system which has l and s = 1/2, as

$$j = l \pm 1/2 \qquad \text{and} \qquad m_j = j, j\text{-}1, \cdots, -j\text{+}1, -j$$

From these quantum numbers, the total angular momentum, J, and its z direction component, J_z, is given by

$$|J| = \sqrt{j(j+1)}\hbar, \qquad \text{and} \qquad J_z = m_j\hbar$$

In quantum theory, the magnetic moment of a particle with mass m and charge q in an electronic state specified by the quantum numbers **L**, **S**, and **J** is

$$\mu = g\beta\mathbf{J} = |\gamma|\hbar\ \mathbf{J}$$

where g is the spectroscopic splitting factor also called the Zeeman factor and $\hbar$ is h/(2π) = 1.054 × 10^{-34} Js (h is the Planck constant). The proportionality constant $\gamma = q/(2m)$, which is called the magnetogyric ratio, converts angular momentum to magnetic moment. When a single (unpaired) electron is placed in an external magnetic field B applied along the z direction, the component μ_z of the magnetic moment is given by

$$\mu_z = -g_e\beta_e m_s = \gamma_e \hbar m_s$$

where g_e is 2.00232 for a free electron, β_e is the Bohr magneton equal to 9.274×10^{-24} JT^{-1}, and γ_e is the electron magneto-gyric ratio. The spin quantum number, m_s is ±1/2 for an electron. The interaction energy (Zeeman energy) of the magnetic moment with an external field B of uniform intensity B_0 is calculated by the Hamiltonian

$$\mathrm{H_s} = -\mu \cdot \mathbf{B} = g_e\beta_e M_s \mathrm{B_0} = \pm\frac{1}{2} g_e\beta_e \mathrm{B_0}$$

The degeneracy of the electron spin states characterized by the quantum number, M_s = ±1/2 is lifted by the application of an electromagnetic field B_1 of the appropriate frequency ν and the energy required for the transitions between the spin levels thus are

$$\Delta E = g_e\beta_e \mathrm{B_0} = h\nu$$

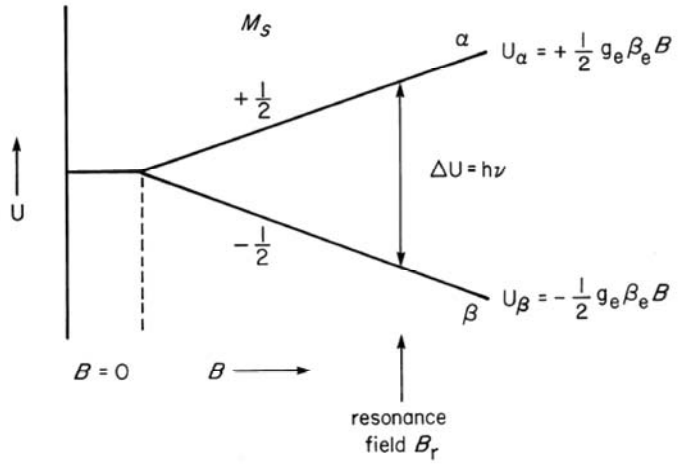

Figure 13. The energy diagram illustrating the transitions of spin states during the EPR experiment (a) and the resultant EPR spectrum (b).

The g-value of a bound electron generally exhibits some deviation from g_e that is mainly due to interaction of the spin with orbital angular momentum of the unpaired electron (spin-orbit

coupling) which arises from the electromagnetic field effects provided by the other nearby electrons and nuclei in the magnetic species. In general these fields provide an anisotropic environment, and one should thus expect the g factor to be anisotropic.

As the orbital angular momentum is associated with a molecular coordinate frame and the spin is quantized along the magnetic field (z axis of the laboratory frame), the g-value depends on the orientation of the molecule with respect to the field. This anisotropy can be described by a second rank tensor with three principal values, g_{xx}, g_{yy}, and g_{zz}. The corresponding principle axes can be determined by a proper transformation (diagonalization) of the laboratory axis using the unitary matrix $\boldsymbol{L}$.

$$\boldsymbol{LgL}^{-1} = \boldsymbol{g}_{diagonal} = \begin{bmatrix} g_{xx} & 0 & 0 \\ 0 & g_{yy} & 0 \\ 0 & 0 & g_{zz} \end{bmatrix}$$

In solution states where molecules tumble with a rotational diffusion rate that is much higher than the differences of the electron Zeeman frequencies between different orientations, the g-value is orientationally averaged and only its isotropic value is observed as

$$g_{iso} = (g_x + g_y + g_z)/3$$

The g anisotropy can be resolved in solid samples more clearly, but in a differential manner with dependence on degree of symmetry. Unpaired electron species placed in an isotropic medium with high symmetry, such as a cubic crystal, provide g-values that are of a scalar constant. As for crystalline systems which contain randomly oriented samples relative to the external field, however, the g factor is markedly dependent on the relative orientations and each component of the principle axis is empirically obtained from the line position. A uniaxial sample with a symmetry axis belongs to a special case and its g_{eff} is given by the following equation.

$$g_{eff} = \left(g_{\perp}^2 sin^2\theta + g_{\parallel}^2 cos^2\theta\right)^{-1/2}$$

where θ is the angel between the external field **B** and the symmetry axis.

For a nitroxide, the axis directions of the g-tensor are oriented relative to the molecular frame as illustrated in Fig. 14. These axes are chosen so that the corresponding principal g-values obey the relation $g_x > g_y > g_z$. Thus, the z axis of magnetic tensor (z_m) lies along the axis of the p_z orbital of the nitrogen, the x_m axis is perpendicular to z_m and lies approximately along the N-O bond direction, and the y_m axis is perpendicular to these.

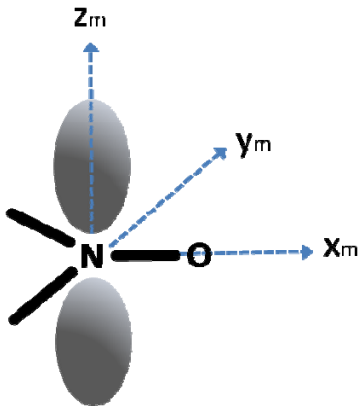

Figure 14. Directions of the principal g axes are oriented relative to the nitroxide molecular frame.

Nuclear Hyperfine Interaction

The electron spin magnetic moment interacts with the magnetic moments of nuclei possessing nonvanishing nuclear spin angular momentum such as nitrogen (I_N=1) to split each energy level of the electron spin into sublevels. Isotropic hyperfine interaction can be regarded as contact interaction between unpaired electrons in s orbitals and nuclei. By virtue of the spherical symmetry of s orbital, this hyperfine interaction is isotropic and its Hamiltonian is described as

$$H_{iso} = (8\pi/3)\, g_e \beta_e g_n \beta_n |\Psi(0)|^2 \boldsymbol{S}\cdot\boldsymbol{I} = A_0 \boldsymbol{S}\cdot\boldsymbol{I}$$

The factor $A_0 = (8\pi/3) g_e \beta_e g_n \beta_n |\Psi(0)|^2$ is an isotropic hyperfine (coupling) constant and this term is also called the "Fermi contact interaction". The second term, anisotropic hyperfine interaction is derived from the dipolar couplings between two particles and dependent on the length and orientation of the vector that connects them.

$$\mathsf{H}_{dip} = -g_e \beta_e g_n \beta_n \left\{ \frac{(\boldsymbol{I}\cdot\boldsymbol{S})r^2 - 3(\boldsymbol{I}\cdot\boldsymbol{r})(\boldsymbol{S}\cdot\boldsymbol{r})}{r^5} \right\}$$

$$= -g_e \beta_e g_n \beta_n \begin{bmatrix} \boldsymbol{S}_x & \boldsymbol{S}_y & \boldsymbol{S}_z \end{bmatrix} \cdot \begin{bmatrix} \left\langle \frac{r^2 - 3x^2}{r^5} \right\rangle & -\left\langle \frac{3xy}{r^5} \right\rangle & -\left\langle \frac{3xz}{r^5} \right\rangle \\ -\left\langle \frac{3xy}{r^5} \right\rangle & \left\langle \frac{r^2 - 3y^2}{r^5} \right\rangle & -\left\langle \frac{3yz}{r^5} \right\rangle \\ -\left\langle \frac{3xz}{r^5} \right\rangle & -\left\langle \frac{3yz}{r^5} \right\rangle & \left\langle \frac{r^2 - 3z^2}{r^5} \right\rangle \end{bmatrix} \cdot \begin{bmatrix} \boldsymbol{I}_x \\ \boldsymbol{I}_y \\ \boldsymbol{I}_z \end{bmatrix}$$

$$= \boldsymbol{S} \cdot \mathbf{A}_{\mathbf{dip}} \cdot \boldsymbol{I}$$

where < > means integration over the spatial coordinates and **r** is the distance vector. The matrix representation of $\mathbf{A}_{dip}$ is a tensor and its diagonal sum (trace) vanishes ($\mathbf{Tr}[\mathbf{A}_{dip}] = 0$). Thus the hyperfine spin Hamiltonian can be summarized as a combination of 'isotropic' and 'anisotropic' hyperfine interactions:

$$\mathsf{H}_{hf} = A_0 \boldsymbol{S}\cdot\boldsymbol{I} + \boldsymbol{S}\cdot\mathbf{A}_{dip}\cdot\boldsymbol{I} = \boldsymbol{S}\cdot\mathbf{A}\cdot\boldsymbol{I}$$
$$\mathbf{A} = A_0 + \mathbf{A}_{\mathbf{dip}}$$

The principal axis directions of the **A** tensor are specified using the Euler angles, referred to as the "magnetic tilt" angles. This set of angles, $\Omega_m = (\alpha_m, \beta_m, \gamma_m)$ defines the orientation of principal axes of the **A** tensor relative to the ***g*** tensor. In practice, **A** axes are usually assumed to coincide with the ***g*** axes with tilt angles of zero; however, the nitroxide in six-membered rings shows a small rotation in the x-y plane due to the twisted boat configuration of the ring.

Sensitivity of EPR experiment

When electromagnetic radiation induces a transition between different energy levels in a given quantum mechanical system, absorption or emission of a photon occurs. The experiment detects net absorption, i.e., the difference between the number of photons absorbed and the number emitted. Since absorption is proportional to the number of spins in the lower level and emission is proportional to the number of spins in the upper level, net absorption is proportional to the difference:

$$\text{Net absorption} \propto N_- - N_+$$

The ratio of populations at equilibrium is governed by the Boltzmann distribution:

$$N_+/N_- = \exp(-\Delta E/kT) = \exp(-g\beta_e B/kT)$$

Under the normal range of temperature and magnetic fields, the exponent is very small and the exponential can be accurately approximated by the expansion $e^{-x} \approx 1 - x$. Thus

$$N_+/N_- \approx 1 - g\beta_e B/kT$$

$$N_- - N_+ = N_-[1 - (1 - g\beta_e B/kT)] = Ng\beta_e B/2kT$$

This expression tells us that EPR sensitivity is improved with the higher magnetic field. Since the field at which absorption occurs is proportional to microwave frequency, in principle sensitivity should be greater for higher frequency K- or Q-band spectrometer than for X-band. However, practically, the need for small sample volume in K- or Q-band spectrometers cancels the advantage of a more favorable Boltzmann factor.

Spin relaxation

The magnetic moment in the static magnetic field undergoes a precessional motion around the field at the Larmor frequency $\omega_L = \gamma H$ and this motion is described by

$$\vec{T} = \vec{\mu} \times \vec{B} = \frac{d}{dt}\vec{J}$$

where $\vec{T}$ is a torque applied on a magnetic moment and $\vec{J}$ is the angular momentum of the spin. This relationship can be rewritten with regard to macroscopic the magnetization vector:

$$\frac{d}{dt}\vec{M} = \gamma\vec{M} \times \vec{B}$$

In the presence of a static magnetic field $\vec{B}_0$ along the z axis ($B_z = B_0$, $B_x = B_y = 0$), three Cartesian components of the magnetization vector can be given as:

$$M_x(t) = M_x(0)\cos(\omega_0 t)$$

$$M_y(t) = M_x(0)\sin(\omega_0 t)$$

$$M_z(t) = M_z(0)$$

The built-up of the macroscopic magnetization of the sample in a magnetic field requires energy exchange with motional degrees of freedom of the surroundings of the spin. Such energy exchange causes a relaxation of the M_z component of the magnetization vector towards its equilibrium value M_0 with time constant T_1, which is called longitudinal relaxation. The equilibrium values of the transverse components of the magnetization vector are $M_x = M_y = 0$. Transverse relaxation towards these equilibrium values does not necessarily require energy exchange with the surroundings. It can arise from energy exchange between spins in the same ensemble. In solutions, spin-spin relaxation is a dominating process that leads to transverse relaxation. However, since both spin-spin and spin-lattice relaxation contribute to transverse relaxation, it is in general characterized by a time constant T_2.

Bloch proposed a set of phenomenological equations to describe the dynamic behavior of interacting nuclear spins. The Bloch equation is basically the torque equation of motion with the relaxation term, **R**:

$$d\boldsymbol{M} / dt = \gamma\left(\boldsymbol{H} \times \boldsymbol{M}\right) + \boldsymbol{R}$$

$$\boldsymbol{R} = \left(-\frac{M_x}{T_2}, -\frac{M_y}{T_2}, -\frac{M_z - M_0}{T_1} \right)$$

In order to obtain the steady-state solutions, the rotating coordinates with frequency of ω can be employed to translate the magnetization to the in-phase and out-of phase components of the oscillating field, B_1, as

$$M_x(t) = u\cos\omega t + v\sin\omega t\,, \qquad M_x(t) = u\sin\omega t - v\cos\omega t$$

Presuming the steady-state conditions, $du/dt = dv/dt = dM_z/dt = 0$, one obtains the solutions:

$$u = M_0\omega_1 \frac{\Omega_0 T_2^2}{1 + \Omega_0^2 T_2^2 + \omega_1^2 T_1 T_2}$$

$$v = -M_0\omega_1 \frac{T_2}{1 + \Omega_0^2 T_2^2 + \omega_1^2 T_1 T_2}$$

$$M_z = M_0 \frac{1 + \Omega_0^2 T_2^2}{1 + \Omega_0^2 T_2^2 + \omega_1^2 T_1 T_2}$$

where ω_1 is the frequency of the off-resonance irradiation and $\Omega_0 = \omega_0 - \omega_1$. Since the average rate at which energy is absorbed per unit sample volume from the H_1 field depends on the out-of–phase component, *v*, *v*-mode is called the absorption mode while *u*-mode is called dispersion mode. In resonant condition ($\Omega_0 = 0$), M_y is proportional to the equilibrium magnetization M_0, and for $\omega_1^2 T_1 T_2 \ll 1$, is also proportional to ω_1. If this condition is violated, M_y grows less than linearly with ω_1, which is called a saturation effect and $\omega_1^2 T_1 T_2$ is the saturation factor. By avoiding the saturation effect, the Lorentzian lineshape from the magnetic resonance can be given by

$$L(\Omega_0) = M_0\omega_1 \frac{T_2}{1 + \Omega_0^2 T_2^2}$$

The actual lineshape obtained from the experiment has a form:

$$L(H) = \frac{I}{1 + \left[\left(H - H_0\right)/\left(\Delta \mathrm{H}_{1/2} / 2\right)\right]^2}$$

which contains the absorption line intensity, I, and the line-width, $\Delta H_{1/2}$, which corresponds to $\Delta\omega_{1/2}$. These parameters are related to T_2 with the equations, $\Delta\omega_{1/2} = 2/ T_2$ or $\Delta H_{1/2} = 2/\gamma T_2$. Since EPR spectra are recorded in a derivative line shape, the peak-to-peak line width, ΔH_{pp} can be utilized to obtain T_2 from the following equation:

$$\Delta H_{pp} = 2/\sqrt{3}\gamma T_2$$

Spin dynamics

In most SDSL applications, it is the motion of the spin label side chain that is of primary interest, as it is the side chain dynamics that is most sensitive to tertiary contacts and local structure of the protein. The lineshape of the EPR spectrum does not only depend on static interactions in the paramagnetic sample, but on dynamic processes on the timescale of the EPR experiment as well. These time-dependent terms are represented by the perturbing Hamiltonian, $\mathsf{H}'(t)$, to the Zeeman term, $\mathsf{H}_0 = g\mu_B \boldsymbol{S} \cdot \boldsymbol{B}_0$ which is time-independent. The EPR timescale is determined by the spectral anisotropy, $\Delta\omega$, i.e., the maximum difference between resonance line positions when the orientation of the molecule is varied. The most important and most visible dynamic process in solutions or membranes observable by EPR is the rotational diffusion of paramagnetic species. This rotational diffusion motion is a random process, and its timescale is characterized by the rotational correlation time τ_C. Nitroxides in different dynamic states (τ_C) thus give rise to their characteristic lineshapes as shown in Fig. 15. By comparing the speed of the rotational diffusion to the spectral anisotropy ($\Delta\omega/\tau_C$), four dynamic regimes with distinct types of EPR spectra can be distinguished (Fig. 16).

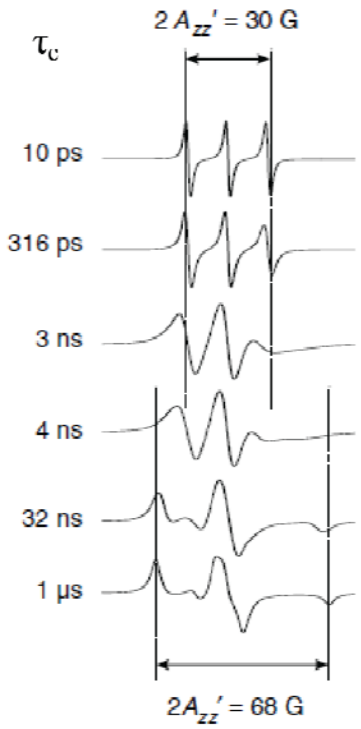

Figure 15. Simulated nitroxide spectra at different rotational correlation times τ_c.

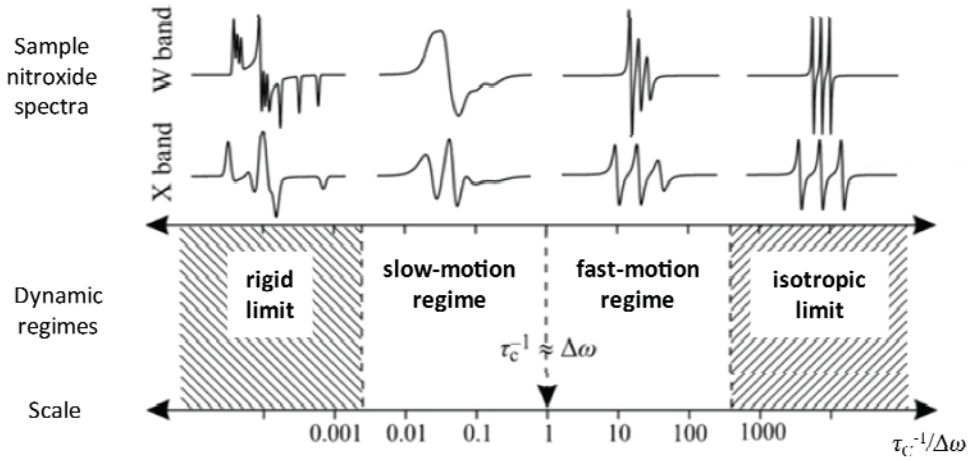

Figure 16. Schematic representation of the timescale of rotational dynamics accessible by CW-EPR. The four dynamic regimes are divided along the increasing where is the rotational correlation time and Δω is the spectral anisotropy. The borders between the four regimes are only approximate.

Isotropic limit paramagnetic molecules are tumbling extremely fast, so that any anisotropic property is completely averaged out. Only the isotropic parts of all interactions are observable such as the isotropic *g* factor and *A* constants. Spectral line intensities and widths are identical for all transitions.

Fast-motion regime The fast-motional regime for a spin system is defined as a stochastic process for which the anisotropic part of the spin Hamiltonian, $H_1(t)$, is effectively averaged out. This condition can be defined as

$$|H_1(t)|\tau_C/\hbar \leq 1$$

In this regime the EPR spectrum of a ^{14}N (I=1) nitroxide spin label consists of three equally spaced lines, and the only spectral manifestation of stochastic tumbling of the nitroxide is in broadening of the EPR lines. The homogeneous line width $\Delta H_{pp}(m_I)$ of each nitrogen hyperfine transitions m_I in the fast-motional regime can be expressed in terms of spectral parameters a, b, and c:

$$\Delta H_{pp} = a + bm_I + cm_I^2$$

$$a = 2J_1^{DD}(\omega_n) + \frac{2}{3}J_0^{DD}(\omega_0) + 4J_2^{DD}(\omega_0) + \frac{8}{3}J_0^{GG}(0) + 2J_1^{GG}(\omega_0)$$

$$b = \frac{16}{3}J_0^{DG}(0) + 4J_1^{DG}(\omega_0)$$

$$c = \frac{8}{3}J_0^{DD}(0) - J_1^{DD}(\omega_n) + 2J_1^{DD}(\omega_0)$$

These spectral parameters contain contributions of several modified spectral densities arising from rotational modulation of the anisotropic part of the nitrogen hyperfine tensor $\boldsymbol{A}$ (J^{DD}), the electronic $\boldsymbol{g}$-matrix (J^{GG}), and the correlated effect of both tensors (J^{DG}). In these equations ω_0 and ω_n are the electronic and nuclear resonant frequencies and the subscript identifies the net change in ($m_s + m_I$), where m_S and m_I are the z component quantum numbers of the electronic spin and nuclear spin, respectively (Budil, 1993).

Slow-motion regime As the rotational motion slows down further, the symmetric Lorentzian lines broaden substantially, become asymmetric and distort, and gradually converge to rigid-limit powder line shapes, revealing the full anisotropy of the underlying magnetic interactions. There are two major approaches that are adopted to calculate the EPR spectrum of a paramagnetic species reorienting on the slow-motional time scale. One approach is the trajectory method, which utilizes the time-dependent trajectories of axes that are fixed in the nitroxide frame. The trajectories can be generated either by simulating them using single-particle Brownian dynamics, or by obtaining them directly from a MD simulation. The other approach was developed by Freed and coworkers based on the stochastic Liouville equation (SLE)(Schneider, 1989). In this approach, the electronic and nuclear spins are treated quantum mechanically while the reorientational motion is treated classically using parameters describing rotational diffusion motion of paramagnetic species. For most of spin labeled biological samples, the MOMD (microscopic order-macroscopic disorder) model can be conventionally applied to simulate the EPR spectrum. The model assumes that the spin probe undergoes microscopic molecular ordering with respect to a local director that is determined by ordering potential; however, the local directors are randomly oriented in the laboratory frame (Budil et al., 2006). The physical origin of the ordering potential is the constrained local dynamics of spin label either by the tether bond or by interaction with neighboring side chains. A set of parameters that define rotational diffusion motion of the spin label is obtained from non-linear least square fitting of the experimental spectrum, including correlation time (τ) and order parameter (S^2).

Rigid limit The paramagnetic molecules are immobilized with no rotational motion. The EPR spectra reveal the full anisotropy of all interactions. This is a typical spectral pattern for powder materials, glasses, and frozen solutions at low temperatures. The simulation of rigid-limit spectra generally requires two separate stages: i) determination of positions, intensities, and widths of all resonance lines for each orientation, and ii) construction of the total spectrum by summing or

iteratively processing the obtained line information. To compute the resonance field positions for a given orientation of the paramagnetic molecule, explicit analytical formulae based on second-order perturbation theory or the adaptive modeling of the energy levels are commonly employed (Stoll, 2003).

Pulsed EPR

In an external magnetic field, electron spins can assume either a parallel orientation (α state) or an antiparallel orientation (β state). The β state, which is lower in energy, has a larger population than the α state as a consequence of the Boltzmann distribution and this forms a macroscopic magnetization M in the direction parallel to B_0. The behavior of this magnetization during a pulsed EPR experiment can be easily described using a coordinate system which rotates with the frequency ω_{mw}. Under this rotating frame, the mw field can be decomposed into two circularly polarized components. The component with the same rotational direction with coordinate system becomes time-independent and assumed to be parallel to the x-axis of the rotating frame. Application of a short intense mw pulse causes rotation of the magnetization M_z through the flip angle $\beta = \gamma_e B_1 t_p = \omega_1 t_p$, in the yz plane, where γ_e is the gyromagnetic ratio of the electron spin, B_1 is the field intensity of the mw pulse, and t_p is the pulse duration. If the resonance condition $\omega_{mw} = \gamma_e B_0$ is exactly fulfilled, the magnetization stays along the y-axis after the pulse. However, if the Larmor frequency ω_0 does not exactly match the microwave frequency ω_1, the magnetization vector starts to precess about the z-axis with the frequency $\Omega = \omega_0 - \omega_1$. The oscillating signal, which decays due to transverse relaxation or inhomogeneous line broadening, is called the free induction decay (FID). By performing a Fourier transformation (FT) into the frequency domain one obtains the spectrum, consisting of a peak at the frequency Ω

.

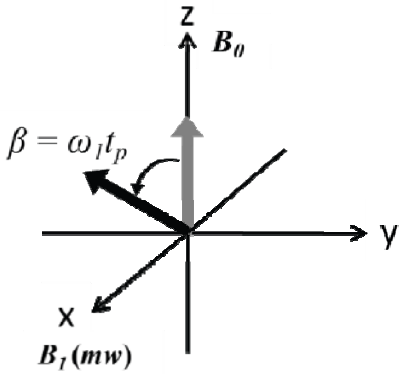

Figure 17. Tilt of magnetization vector on the yz plane by tilt angle β upon the application of *mw* pulse B_1 along the x axis.

In contrast to rf pulses in NMR, mw pulses cannot usually excite the entire spectrum at once. For this reason, pulsed EPR is somewhat less sensitive than CW-EPR for many applications and manipulation of the spin dynamics is less effective than in pulsed NMR. Much faster relaxation rates are also a big problem for pulsed EPR versus NMR, causing a loss of information by the deadtime. Nonetheless, pulsed EPR allows for a better separation of different interactions in the spin Hamiltonian, or detection of different types of spin relaxation mechanisms, compared with CW-EPR. Separation of interactions allows for precise measurements of the small interactions of the observed electron spin with remote spins in the presence of line broadening due to larger contributions from **g** tensor and hyperfine **A** tensor anisotropy. The separation of different contributions from spin relaxation relies on echo experiments. Spin echoes are also the basis for almost all other pulsed EPR experiments since the free induction signal induced by a single pulse usually decays within a time that is shorter than the receiver deadtime after that pulse. The simplest echo experiment is the two-pulse or Hahn echo experiment, which consists of a first pulse with flip angle $\pi/2$, a delay τ, and a second pulse with flip angle π. The first pulse converts the longitudinal magnetization of the spins to transverse magnetization.

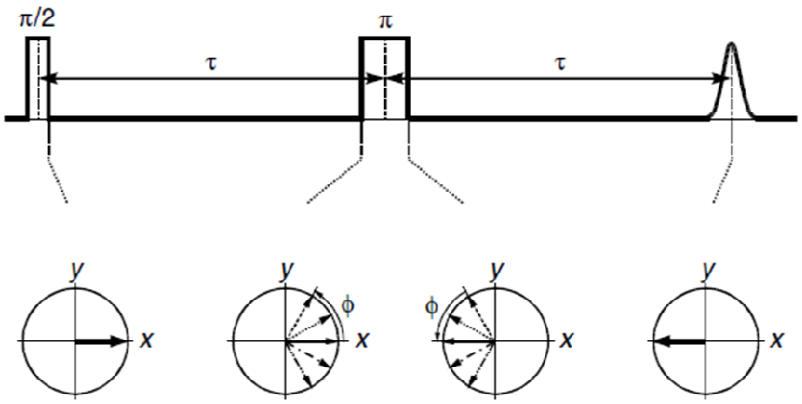

Figure 18. Pulse sequence for the two pulse echo experiment (top) and the evolution of the magnetization vectors corresponding to spin packets with difference resonance offsets Ω. (bottom)

Magnetization within each spin packet with equal resonance frequency decays by transverse relaxation with time constant T_2. The following π pulse inverts the phase of each spin packet cancelling the phase differences generated by transverse magnetization and leads to coherence of spin packets. This coherence corresponds to the observable FID signal after the first pulse with attenuation of the signal amplitude by a factor of exp $(-2\tau/T_2)$.

Various pulsed EPR experiments allow distance information to be extracted from a two spin system with a wide range of interspin distances as summarized in Table 4. Pulsed EPR experiments for the measurement of long interspin distances include single-resonance techniques such as saturation recovery and T_m measurement, double-resonance techniques (pulsed electron double resonance [PELDOR]), and double quantum coherence (DQC). Saturation recovery and T_m measurements utilize the effect of dipolar coupled fast-relaxing spins on the longitudinal or transverse relaxation rate of slow-relaxing spins (reviewed in (Eaton, 2000)). In typical applications, the slow-relaxing spin can be an amino acid radical (tyrosyl radical) or a spin label, and a metal center serves as the fast-relaxing spin. The double resonance technique, PELDOR is represented by 4-pulse DEER experiments, and will be more comprehensively discussed in the next section. In the DQC measurement, evolution of the electron spin coherences that is typically

generated by a 6-pulse sequence is selectively detected and the dipolar interaction between a pair of spin labels is extracted. DQC can excite almost all spins with strong microwave pulses, which give rise to a high sensitivity. Moreover, it suppresses complicating features due to correlations between orientations of the magnetic tensors of the nitroxide and the inter-radical vector, and unwanted artifacts can be filtered (Borbat and Freed, 2000). However, it has an ESEEM effect for relatively short distances and needs a complex phase cycle and precise pulse angles (Borbat et al., 2002) to eliminate the unwanted echo.

Short-range distance measurements involves electron-nuclear hyperfine interactions between paramagnetic transition metal ions or radicals and NMR nuclei such as ^{1}H, ^{2}H, ^{13}C, ^{14}N, ^{15}N, and ^{17}O. In both frequency-domain ENDOR and time-domain ESEEM and HYSCORE spectroscopy (Lakshmi and Brudvig, 2001; Prisner et al., 2001), spin-coupled nuclear transitions are monitored through the observation of the paramagnetic electron spins. ENDOR is a double resonance technique with high spectral resolution that allows the measurement of small hyperfine couplings. Pulsed ENDOR at high frequency can be used to obtain orientation selection of the Zeeman interaction for spin centers with small g anisotropy as well as distance measurements. It is applicable to the determination of substrate binding geometry and orientation of the hyperfine tensor within the molecular frame. ESEEM utilizes the spin echo technique to overcome the inhomogeneous broadening of EPR resonances and the unresolved nuclear hyperfine couplings. Typically, ESEEM experiments are performed with a two-pulse Hahn echo or a three-pulse stimulated echo pulse sequence measured as a function of the echo interval (t) or the interpulse separation (T). HYSCORE is a two-dimensional version of ESEEM spectroscopy that can be used to obtain correlations between nuclear transitions to facilitate the detection and assignment of nuclear hyperfine couplings.

Table 3. Pulsed EPR techniques that allow distance measurements over the various ranges.

Pulsed Technique	Type of interaction	Types of spins	Distance range (Å)
Saturation recovery	Electron-electron exchange and dipolar couplings	Observed spin: amino acid radical or spin label Relaxation enhancer: metal center	~ 40
T_m measurement	Electron-electron exchange and dipolar couplings	Observed spin: amino acid radical or spin label Relaxation enhancer: metal center	~ 30
PELDOR	Electron-electron dipolar couplings	Radical pairs	~ 60
DQC	Electron-electron dipolar couplings	Radical pairs	~ 60
ENDOR	Electron-nuclear hyperfine couplings	Electron spin interacting with nuclear spin	~ 4-5
ESEEM	Electron-nuclear hyperfine couplings	Electron spin interacting with nuclear spin	~ 4-6

Application of SDSL-EPR in Protein Structure

Side chain mobility

Among the most informative and simplest types of information that can be extracted from an EPR spectrum are parameters that reflect spin label motion. Conventional, X-band EPR spectra are sensitive to rotational motion in the range of 0.1 to 100 ns. Specialized techniques such as saturation transfer (ST) EPR can extend the motional sensitivity to the millisecond timescale and are useful for determining the tumbling rate of the spin-labeled protein as a whole or of a protein domain in a supramolecular complex (Fajer, 2000).

The relationship between side chain mobility and protein structure has been explored in detail for T4 lysozyme (Hubbell et al., 1996; McHaourab et al., 1996). The overall mobility of the spin label is determined by a combination of (i) motion of the label itself relative to the protein backbone, (ii) fluctuations of the α-carbon backbone, and (iii) rotational motion (molecular tumbling) of the entire protein or peptide (Columbus and Hubbell, 2002). For proteins with molecular weights greater than ~150 kDa or proteins in macromolecular assemblies, the overall

tumbling rate of the complex is too slow to affect the conventional EPR spectrum. However, for proteins of less than ~150 kDa, rotational diffusion of the protein can influence the observed spectrum. This can be simply overcome by increasing solution viscosity with additional solutes, such as sucrose or glycerol (e.g., (McHaourab et al., 1997))

Local fluctuations of the α-carbon backbone can also contribute to spin label mobility. To study backbone dynamics by SDSL, the flexibility of the spin label side chain can be eliminated by using MTSSL derivatives where the 4'-hydrogen is replaced with bulky substituents such as methyl or phenyl groups (Columbus et al., 2001). Additionally the effects of backbone fluctuations can be manifest via comparison of sites in similar environments where side chain flexibility is expected to be sequence-independent, as seen in the case of the α-helical zipper domain of the yeast transcription factor GCN4 (Columbus and Hubbell, 2004).

In β-sheet proteins the situation is somewhat more complex, with spin label motion being influenced by location within the β-sheet (i.e., edge vs internal strand) and interactions of side chains with neighboring strands even though the allowed conformational space is much narrowed compared with α-helical structure (Hubbell et al., 2000; Lietzow and Hubbell, 2004). Local secondary structure influences the spin label mobility somewhat, far more significant effects are seen at sites where the spin label is in tertiary contact with other side chains in the local environment. Spin labels at tertiary contact sites show relatively slow motions, and sites buried within the core of a protein often approach the rigid limit.

One of the main parameters for examining relative mobility in a semi-quantitative way is the inverse width of the center line, $\Delta H_{pp}(0)^{-1}$. Since linewidth increases with decreasing motion, taking the inverse width gives an empirical parameter that is proportional to motion. The inverse width of the center line can also be normalized to provide a scaled mobility parameter, M_S (Hubbell et al., 2000), as given by:

$$M_S = \left[\frac{\Delta H_{pp}(0)^{-1} - \Delta H_{pp}(0)^{-1}(i)}{\Delta H_{pp}(0)^{-1}(m) - \Delta H_{pp}(0)^{-1}(i)} \right]$$

where $\Delta H_{pp}(0)^{-1}$(m) and $\Delta H_{pp}(0)^{-1}$(i) are the inverse widths of the center line for the most mobile and most immobile sites in a given system, respectively. Alternatively, the spectral second moment, $<H^2>$, reflects the breadth of the EPR spectra (Slichter, 1980) and is given by

$$\left\langle H^2 \right\rangle = \frac{\int \left(B - \left\langle H \right\rangle\right)^2 S(B) dB}{\int S(B) dB},$$

which is defined based on the first moment $\left\langle H \right\rangle = \int BS(B)dB / \int S(B)dB$, where B is the magnetic field, and *S(B)* is the absorption spectrum of the spin-labeled protein. Like $\Delta H_{pp}(0)$, the inverse of $<H^2>$ is used as a mobility parameter since $<H^2>$ increase as the correlation time of the nitroxide reorientational motion is reduced. In the presence of multicomponent spectra $\Delta H_{pp}(0)^{-1}$ is dominated by the fast motional component while the second moment is biased toward the slow motional component. As shown in Fig. 19, the plot of the inverse of the second moment, $<H^2>^{-1}$, versus the inverse of the central line width, $\Delta H_{pp}(0)^{-1}$, extracted from the experimental data reveals the correlation of this plot with the topographical region of the protein that bears the spin label.

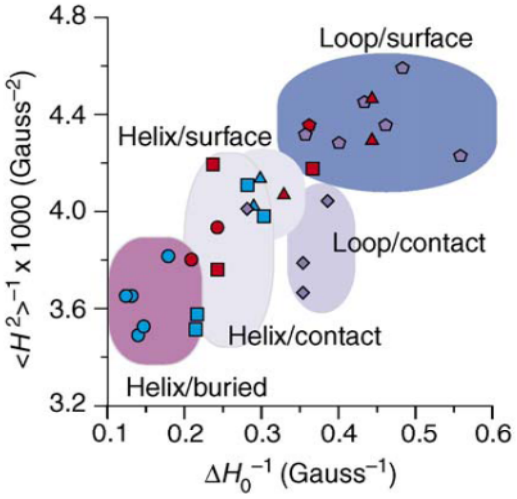

Figure 19. Reciprocal plot of the second moment ($<H^2>$) of the EPR spectrum versus central line-width ($\Delta H_{pp}(0)$) (Fanucci and Cafiso, 2006). Points represent analyzed spectra for 30 singly labeled R1 mutants of annexin 12 (Isas et al., 2002), and indicate the correlation between these spectral parameters and regions of secondary structure and tertiary contact.

A different set of parameters is used to characterize the spin label mobility in the slow motional regime. Such spectra are characterized by features corresponding to spin labels aligned with their z-axis either parallel to the external magnetic field, separated by $2T_{\|}$ or perpendicular to the external field, separated by $2T_{\perp}$. Spin label motion is typically modeled as rotation within a cone about the z-axis (i.e., the nitrogen p-orbital). The amplitude of the motion is described by an order parameter, S:

$$S = \frac{1}{2}(3\langle cos^2\theta\rangle - 1)$$

where $\langle cos^2\theta\rangle$ is the time-averaged value for the angle of deviation of the nitroxide z-axis. For EPR spectra with distinct $T_{\|}$ and $T_{\perp}$ features, the order parameter can be given as:

$$S = \left[\frac{\left(T_{\|}' - T_{\perp}'\right)}{(T_{\|} - T_{\perp})x_1}\right]\left[\frac{a_N(x_1)}{a'_N}\right]$$

where primes indicate experimental values and x_1 indicates values from single-crystal or powder spectra. The nitrogen isotropic hyperfine coupling constant, a_N, is given by $1/3\left(T_{\|}' + 2T_{\perp}'\right)$ from the experimental spectra.

Solvent accessibility

The power saturation technique takes advantage of the fact that certain reagents are paramagnetic and affect the relaxation rate of the spin label. The accessibility of the nitroxide toward those reagents selectively partitioning in different environments defines the topology of the natural side chain with respect to the protein/water/membrane boundaries. Thus, the Heisenberg exchange frequency (W_{ex}) of the nitroxide with a paramagnetic exchange reagent has a direct correlation with the solvent accessibility of the nitroxide in a given system.

The collision between a nitroxide and a relaxation enhancer leads to variations in T_1 (spin-lattice relaxation time) or T_2 (spin-spin relaxation time) of a spin label bound to a protein. If

the longitudinal relaxation time of the reagent is shorter than the encounter complex lifetime ($T_1 < t_c$), the Heisenberg exchange give rise to equal changes in T_1 and T_2:

$$W_{ex} = \Delta\left(\frac{1}{T_1}\right) = \Delta\left(\frac{1}{T_2}\right)$$

For a bimolecular encounter between a nitroxide moiety in solution (N) and an exchange reagent (R) the Heisenberg exchange frequency experienced by the nitroxide is given as

$$W_{ex} = k_{ex}C_R$$

where k_{ex} is the exchange constant and C_R is the concentration of the reagent (R).

For a single homogeneous Lorentzian line the peak-to-peak amplitude of the first derivative absorption spectrum, Y', has the form

$$Y' \propto \frac{H_1}{\left(1 + H_1^2\gamma^2 T_1 T_2\right)^{3/2}} = \frac{\Lambda\sqrt{P}}{\left(1 + \Lambda^2 P\gamma^2 T_1 T_2\right)^{3/2}}$$

where H_1 is the microwave magnetic field in Gauss, γ is the gyromagnetic ratio of the electron, and Λ is the correction factor. Y' is proportional to $\sqrt{P}$ for low microwave power and to $1/P$ for higher power. Saturation occurs when the amplitude of the signal deviates from the square root dependency on power because the relaxation rate of the spin system is not fast enough to absorb more power. An easily extractable parameter, $P_{1/2}$ which is defined as the mw power at which the signal amplitude reaches half of the theoretical value reachable in the absence of saturation:

$$Y'(P_{1/2}) = \frac{\Lambda\sqrt{P_{1/2}}}{2}$$

The expression of $P_{1/2}$ for a homogeneous line can then be written as

$$P_{1/2} = \frac{\left(2^{2/3} - 1\right)}{\Lambda^2\gamma^2 T_1 T_2}$$

The fitting equation can be derived from the above equation as

$$Y' = \frac{I\sqrt{P}}{\left(1 + (2^{\varepsilon} - 1)P/P_{1/2}\right)^{\varepsilon}}$$

with adjustable parameters of I, ε, and $P_{1/2}$.

In the presence of exchange paramagnetic reagents colliding with the nitroxide, variations in the relaxation times of the nitroxide are reflected in changes of $P_{1/2}$ values.

$$\Delta P_{1/2} = P_{1/2}^{R} - P_{1/2}^{0} \propto \frac{1}{T_1^R T_2^R} - \frac{1}{T_1^0 T_2^0} \propto \frac{W_{ex}}{T_2^0}$$

Under the condition of $T_2 << \tau_C$, T_2 is not affected by the relaxation enhancer and $T_2^R \cong T_2^0$. For different spin labels with comparable T_2, $\Delta P_{1/2}$ reflects the relative collision frequency. Thus, to eliminate the dependency on T_2, $\Delta P_{1/2}$ values are normalized with ΔH_0 (Farahbakhsh et al., 1992), thus leading to

$$\Delta P_{1/2}^{'} = \frac{\Delta P_{1/2}}{\Delta H_0} \propto W_{ex}$$

The relaxation enhancing reagents can be divided into two groups based upon their propensity for solvent partitioning. While oxygen is small and hydrophobic so that it is preferentially distributed in the center of lipid bilayer or hydrophobic pockets of proteins, nickel compounds such as nickel (II) ethylenediaminediacetate (EDDA) or chromium oxalate (CROX) are water soluble and are dominantly located in the solvent phase. NiEDDA is neutral and therefore does partition slightly into bilayers and hydrophobic regions, but CROX is negatively charged and is strictly found in the aqueous phase.

The accessibility measurement can be useful in determining the secondary structure of proteins when a series of consecutive sites along the primary sequence is measured. In the case of a peripheral α-helix, every 3 or 4 residues would be highly exposed to the solvent due to a periodicity of 3.6 residues per turn and consequently show high NiEDDA accessibility while the sites on the other side of the helix which would be buried against the protein exhibit low $\Delta P_{1/2}$ values for both NiEDDA and oxygen. Similarly, β-strands give a periodicity pattern of 2.0, and unstructured regions will show no regular periodicity. The application of solvent accessibility in

probing the secondary structure, tertiary structure and protein folding can be seen in the structural studies on water soluble proteins such as α-crystallin (Berengian et al., 1997) and voltage dependent potassium channel KvAP (Cuello et al., 2004).

For integral membrane proteins or membrane-associated peptides, the depth of a given spin label side chain within a lipid bilayer can be determined using accessibility data. This is an extremely useful technique for positioning protein or peptide segments within the lipid bilayer (e.g.,(Hubbell et al., 1998; Isas et al., 2002; Perozo et al., 2001)). The membrane depth of spin label side chains facing the membrane can be measured based on the following equation (Altenbach et al., 1994)

$$\Phi = \ln\left[\frac{\Delta P_{1/2}(O_2)}{\Delta P_{1/2}(NiEDDA)}\right]$$

The variation in the concentrations of oxygen and NiEDDA within the membrane bilayer has been shown to form inversely proportional gradients; oxygen concentration is greatest at the center of the bilayer and decreases toward the membrane surface whereas NiEDDA shows the greatest concentration at the surface of the bilayer and decreases to zero in the center of the bilayer. Φ can then be calibrated to each particular membrane system using lipid-analogue spin labels that reside at known bilayer depths. The accessibility measurements obtained for each lipid label are plotted against their known depths to yield a depth calibration equation:

$$\text{Depth (Å)} = m\Phi + b$$

Conformational changes in dynamic processes like receptor activation and channel gating are another main field that can be probed by accessibility measurement as shown in G protein coupled receptor rhodopsin (Farrens et al., 1996), pH-gated K^+ channel KcsA (Perozo et al., 1999), mechanosensitive channel MscL (Perozo et al., 2002), and multidrug transporter MsbA (Dong et al., 2005).

Inter-spin distance measurement

Short distance measurement by CW-EPR

The spin Hamiltonian for a pair of dipolar coupled nitroxides is given by

$$\mathsf{H} = \beta_e H_0 \cdot \mathbf{g}^1 \cdot \hat{S}^1 + \beta_e H_0 \cdot \mathbf{g}^2 \cdot \hat{S}^2 - \omega_n (I_z^1 + I_z^2) + \gamma_e \hat{I}^1 \cdot \mathbf{A}^1 \cdot \hat{S}^1 + \gamma_e \hat{I}^2 \cdot \mathbf{A}^2 \cdot \hat{S}^2 + \hat{S}^1 \cdot \mathbf{D} \cdot \hat{S}^2 + J\hat{S}^1 \cdot \hat{S}^2$$

where $\mathbf{g}^1$ and $\mathbf{g}^2$ are g tensors of nitroxide 1 ($\hat{S}^1$) and nitroxide 2 ($\hat{S}^2$) with external magnetic field (H_0), ω_n is the Larmor frequency of the nitrogen nucleus (I_z^1 and I_z^2), $\mathbf{A}^1$ and $\mathbf{A}^2$ are the hyperfine tensors, **D** is the dipolar coupling tensor, and *J* is the scalar exchange coupling constant. The dipolar coupling tensor, D, can be expressed with regard to the spin-spin vector, ***R***, by

$$D = \frac{\gamma_e^2 \hbar}{|\boldsymbol{R}|^3}\left(1 - 3\cos^2\theta\right)$$

where θ is the angle between the DC magnetic field and the interspin vector, ***R***. The principal axes of the g- and A-tensors of a spin label are essentially coincident and are well defined within the molecular frame of the nitroxide, with $\boldsymbol{g}_{xx}$ along the N-O bond and $\boldsymbol{g}_{zz}$ perpendicular to the planar nitroxide. Since the unpaired electron is assumed to be localized at the center of the N-O bond, which is a good approximation for distances longer than 1nm, the dipolar coupling tensor can then be described by the point-dipole approximation, where the **D** tensor is axially symmetric, with the principal z-axis of the diagonalized **D**-tensor aligned with the interspin vector. For spin labels on biomacromolecules, through-bond exchange couplings *J* are not significant for internitroxide distances greater than 10 Å compared to dipolar couplings (Luckhurst, 1976) and are neglected in normal circumstances.

An internitroxide distance in the range of 10-20 Å leads to dipolar splitting of 7~55 G in a CW-EPR spectrum. The dipolar couplings in this range are partially averaged by rotational diffusion, with correlation times on the order of 1-10 ns, which corresponds to the intermediate motional regime. Thus, analyses of the short interspin distance should adopt different approaches

based upon the motional regime to which a given spin system belongs and the contribution of global tumbling motion of protein.

When both spins are rigidly bound and statically ordered on the protein of which the global rotational correlation time is greater than 1μs, the motional averaging effects on dipolar couplings will disappear. Consequently, the unique values for internitroxide distance and the relative orientation of two nitroxides can be determined by rigorous numerical spectral analysis where the EPR spectrum that best fit the data is explored for a set of parameters that defining the distance and relative orientation of two nitroxides. One representative case study has been presented by Hustedt and coworkers in a study of ^{15}N-spin labeled coenzyme NAD^+ bound to tetrameric glyceraldehydes-3-phosphate dehydrogenase. For such a complex the spin labels adopt unique conformations and remain virtually immobilized with respect to the protein. The interspin distance and the angles that determine the relative orientation of the spin pair was simultaneously fit to the multifrequency EPR data collected at X-, Q-, and W-band by global analysis which performs simultaneous nonlinear least-squares analysis of multiple data sets.

Another case in which interspin distance can be reliably measured involves statically disordered spin pairs in the absence of any rotational diffusion effect on the EPR timescale. In this situation, the orientations of both dipolar coupling and magnetic tensors from the spin pair are assumed to be isotropic. Thus, the EPR spectrum for two dipolar coupled equivalent spins will be powder-pattern absorption spectrum known as a Pake pattern (Pake, 1948). Rabenstein and Shin (Rabenstein and Shin, 1995) has developed the Fourier deconvolution method which is based on the assumption that the biradical spectrum, Π(B) is the convolution of the dipolar broadening function, D(r,B) and the monoradical spectrum, *S(B)*:

$$\Pi(B) = \int_{-\infty}^{\infty} S(B')M(r, B'-B)dB', \qquad M(B) = \sum_{r} P(r)D(r, B)$$

where *M(B)* is the weighted sum of the *D(r,B)* over the distribution of the distances *P(r)*. The convolution of two functions in real space is given in Fourier space as $\Pi^*(\omega) = S^*(\omega) \cdot M^*(\omega)$. M(B) is then obtained from the inverse Fourier transform of $\Pi^*(\omega)/S^*(\omega)$:

$$M(B) = \frac{1}{\sqrt{2\pi}} \int_{-\infty}^{\infty} \exp(2\pi i \omega B) \frac{\Pi^*(\omega)}{S^*(\omega)} d\omega$$

In a model system of a set of doubly spin labeled peptides, the deconvolution method accurately measured the interspin distance in the range of 8-25 Å. In an independent study, Steinhoff and coworkers obtained a distribution in interspin distance by averaging a Pake pattern function over a Gaussian distribution (Steinhoff et al., 1997). They performed nonlinear least-squares analysis for the spectra obtained from the convolution model to determine the mean distance and width of the Gaussian distribution that best fit experimental spectrum. Further justification of this approach has been provided using insulin as a model and by comparing interspin distances between nitroxides from ESR and the available crystal structure of insulin.

Even with successful applications in many studies, the convolution approach has some intrinsic limitations in the accuracy of measurement. Its theoretical basis depends on two assumptions: i) the dipolar broadening function can be treated as a Pake pattern by neglecting the g- and A-tensor anisotropies. ii) the relative orientation of two nitroxides and the orientation of the interspin vector with respect to the nitroxides are isotropically distributed. However, these assumptions need to be corrected or treated more carefully in application to real biological systems. Typically, g- and A-tensor anisotropies are equal to or larger than the dipolar splitting for interspin distances in the range of 10-20 Å, leading to deviations from the Pake pattern even in ideal system (Hustedt and Beth, 1999). Moreover, most systems will have some restrictions in the relative orientations of two spin labels imposed by attachment to the protein backbone or side chain interactions. Recently Hustedt et al. developed the tether-in-a-cone model to overcome these limitations and to treat the side chain motion of a nitroxide more realistically (Hustedt et al., 2006). This model allows restricted spatial distribution of each unpaired electron by localizing

side chain dynamics to a cone which has a specific orientation and width rather than isotropic distribution. Spectral simulations and applications to T4 lysozyme have shown that more ordered spin systems (i.e. cones with narrower width), can provide a more detailed and accurate description of the relative geometry of a spin pair and the interspin distance distribution compared with the convolution approach.

The last case to be considered involves the systems of a spin pair where both the nitroxide side chains and the protein are in a highly dynamic state on a timescale to which linear EPR is sensitive. Since data analysis methods for this case are still in progress, many of these applications can be solved with the convolution methods after conversion to the second case by slowing the dynamics of side chain and global tumbling, which is typically done by lowering temperature or increasing viscosity of the media (Steinhoff et al., 1997). The fast motion regime is defined as a stochastic process for which the anisotropic part of the time-dependent spin Hamiltonian is effectively averaged out. Thus, for many practical applications the interspin distance could be assumed to be time-independent and then the only stochastic mechanism that could average the dipolar field would be reorientation of the interspin vector in the magnetic field arising from global tumbling of a spin labeled macromolecule in solution. If global tumbling of the macromolecule is approximated as an isotropic, and Redfield conditions are satisfied, the dipolar interaction gives rise to an additional spin relaxation characterized by the following T_{2dd}:

$$\frac{1}{T_{2dd}} = \gamma^4 \hbar^2 S(S+1) \frac{\tau_C}{r^6} \left[3 + \frac{5}{1+\omega^2 \tau_C^2} + \frac{2}{1+4\omega^2 \tau_C^2} \right]$$

Under this case the dipolar couplings would result in additional uniform Lorentzian broadening of CW-EPR spectra. McHaourab et al. developed the method in which such a broadening was utilized to quantify the distance between two nitroxide spin labels attached to a protein (McHaourab et al., 1997). The dipolar broadening was estimated by comparing CW-EPR line

widths of single and double-labeled mutants and relating the observed broadening $\Delta H_{dd} = 2\hbar\left(g\beta_e T_{2dd}\right)^{-1}$ with the interspin distance *r*.

Long distance measurement by pulsed EPR

For the long distance measurements larger than 2 nm the dipole-dipole coupling is much smaller than the inhomogeneous linewidth of the CW-EPR spectrum. The pulse sequence employed in the DEER experiment separates the dipolar coupling from those other interactions by exciting two subpopulations of spin A and spin B with two pulses at different frequencies as shown in Fig 20.

The microwave pulses which are not ideally rectangular on the timescale of dipolar evolution can overlap with the DEER signal and thus causes distortion of the signal at times $t < t_d$. The deadtime t_d is typically in the range of 30~100 ns (~80 ns). For broad distribution contributions with the mean distance shorter than 2.2 nm may decay completely within this time. In 4-pulsed DEER experiment deadtime is eliminated by refocusing the observer echo with an additional π pulse, which prolongs the experiment by a time span of at least $2t_d$. For short distances ($r < 2.2$ nm), the sensitivity loss due to decay factor $\exp(-2t_d/t_m)$ is compensated by recovering the most pronounced first oscillation of the signal. Longer distances with sufficiently long T_m can be determined without significant sensitivity loss.

For an isolated two-spin system (S_A = 1/2 and S_B = ½), the Hamiltonian in angular frequencies is

$$\mathsf{H} = \omega_A S_z^A + \omega_B S_z^B + \omega_{AB} S_z^A S_z^B$$

where ω_A and ω_B are the resonance frequency of the spin species A and B and ω_{AB} is the dipolar coupling between them, given as $\omega_{AB} = \frac{\mu_B^2 g_A g_B}{\hbar}\frac{3\cos^2\theta - 1}{r^3}$.

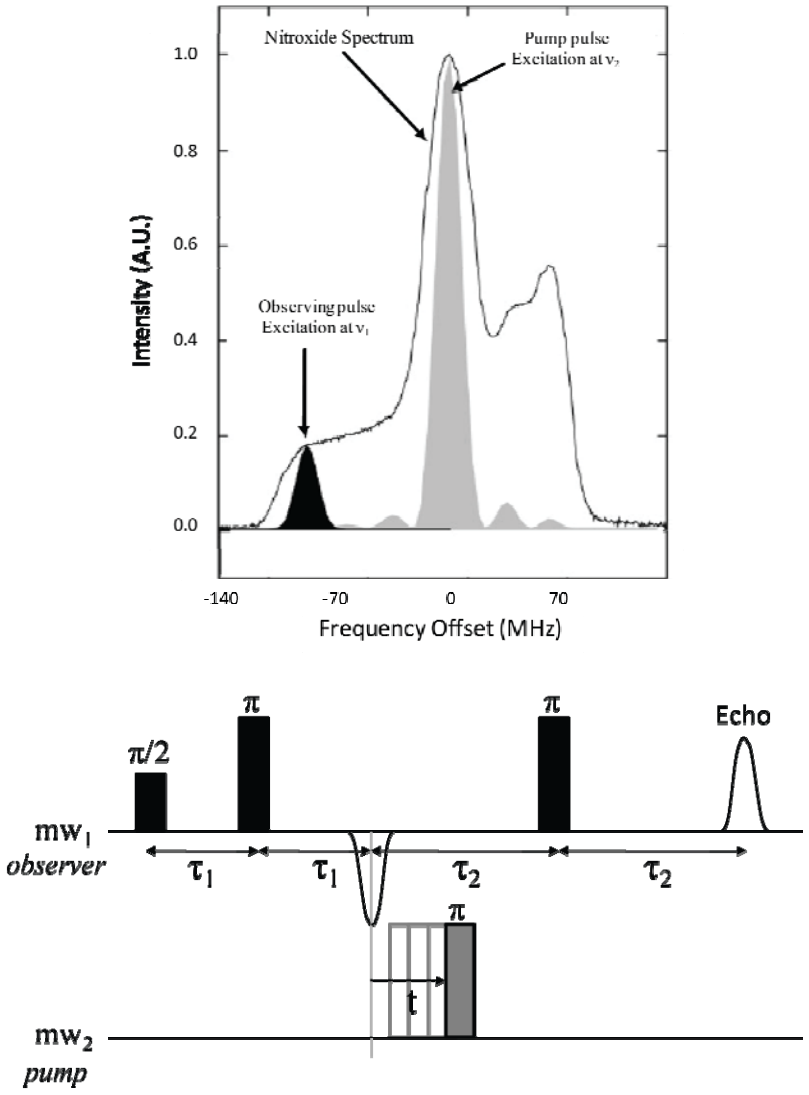

Figure 20. Excitation profiles of the mw pulses within the nitroxide spectrum (top) and the pulse sequence of the DEER experiment at two different microwave frequencies (bottom)

where g_A and g_B are the g factors of the respective electron, r is the electron-electron distance, and θ is the angle between the interspin vector and the magnetic field B_0.

The experiment can be explained by using the rotating frame picture, in which the Hamiltonian for spin A is written as

$$H'_A = \Delta\omega_A S_z^A + \omega_{AB} S_z^A S_z^B$$

where $\Delta\omega_A = \omega_A - \omega_{mw}$, and ω_{mw} is the microwave carrier frequency. Only the terms affecting A spins need to be considered, since any coherence of B spins generated during the pulse sequence does not contribute to the signal. The dipolar interaction leads to a splitting of each transition with the A spin frequencies $\omega_A^{\pm} = \Delta\omega_A \pm \frac{1}{2}\omega_{AB}$. The first π/2 pulse generates electron coherences evolving with ω_A^+ and ω_A^- and the following π pulse causes an inversion of the evolving electron coherence. An electron coherence transfer is then induced by the π pulse at the second (pump) mw frequency at the variable time *t*, which causes the electron coherence formerly evolving with ω_A^+ and ω_A^- to evolve after this pulse with ω_A^- and ω_A^+, respectively. The final pulse at the observer frequency induces again an inversion of the phase of the electron coherence resulting in an electron spin echo of which phase, Ψ, can be given by adding up all the phase changes induced by each pulse step:

$$\Psi(2\tau_1 + 2\tau_2) = \omega_A^{\pm}\tau - \omega_A^{\pm}(\tau_1 + t) - \omega_A^{\mp}(\tau_2 - t) + \omega_A^{\mp}\tau_2$$

$$= (\omega_A^{\mp} - \omega_A^{\pm})t$$

When normalized to the intensity at t = 0, the echo intensity is given by

$$I(t) = \cos(\omega_{AB} t)$$

Thus, the echo amplitude is modulated along the variable time *t*. Besides the dipolar couplings between two spins within nano-objects of interest (I_{intra}), the coupling between the observed spin and every other spin in the sample (I_{inter}) contribute to the DEER signal. For a homogeneous distribution of radicals, this contribution can be written as

$$I_{\text{int } er}(t) = \exp(-kCF_B t)$$

$$k = \frac{8\pi^2 \beta_e^2 g_A g_B}{9\sqrt{3}\hbar}$$

where C is the concentration of the unpaired electron spins and F_B is the fraction of electron spins excited by the mw pulse at frequency ν_{mw2}. This contribution to the decay, called instantaneous diffusion, can at least partially be suppressed by diluting the sample. The echo amplitude at evolution time t can then be expressed by the product of two factors:

$$I_{DEER}(t) = I_{intra}(t) I_{inter}(t)$$

$$= \cos(\omega_{AB} t) \exp(-kCF_B t)$$

In order to obtain the distance distribution from the observed DEER signal, the I_{intra} term responsible for echo modulation needs to be separated from the I_{inter} which represents background contributions. During the dipolar evolution of the echo signal along the evolution time t, $I_{DEER}(t)$ is damped with a factor of $\exp(-2t/T_m)$, where T_m is the phase memory time (transverse relaxation time, T_2), oscillating with a frequency that is proportional to r^{-3}. The decay of oscillation becomes faster with increasing distance distribution and can be characterized by an approximate time t_{decay} at which the oscillation is fully decayed. Due to the incomplete excitation of spins at the pump frequency, the signal decays to a $1-\lambda$, where λ is the modulation depth. For sufficiently long dipolar evolution times, the signal is described by $I_{DEER}(t > t_{decay}) = (1-\lambda) I_{inter}$.

Fourier transformation of the time-domain signal yields a Pake pattern. The distance can be computed either by fitting the time-domain DEER modulation or by measuring the frequency of singularity $\nu_{dd}(90^\circ)$ from the Pake pattern. However, asymmetric lineshape in the vicinity of singularity tend to shift the maximum to lower frequencies leading to an overestimate of the distance. Therefore, more precise distance distributions are obtained by fitting the time domain data with a set of parameters including the mean distance (r), distribution width (s), spin concentration (C), and modulation depth (λ).

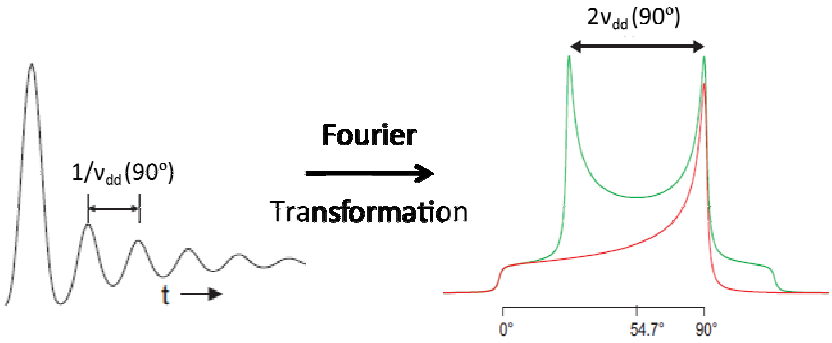

Figure 21. The relationship between time-domain DEER modulation and frequency-domain Pake patterns. The green line shows the Pake pattern and the red line indicates only one of the transitions in the Pake pattern showing the angular dependence.

Distance resolution depends on the maximum dipolar evolution time t_{max}. To obtain sufficient sensitivity, one should have $t_{max} < 1.5T_m$. For distances up to 2.5 nm, 1.5 μs of t_{max} is sufficient for determining a precise distance. Furthermore, sensitivity can be improved by increasing T_m, which can in turn be achieved by appropriate choice of temperature and matrix or solvent. The signal-to-noise (S/N) ratio in echo experiments varies with temperature T due to the temperature dependence of polarization of spin transitions, of transverse relaxation time, and of longitudinal relaxation time. In the high temperature limit, $h\nu_{mw} << k_BT$, polarizations of spin transitions are inversely proportional to T (Schweiger, 2001). Transverse relaxation with time constant T_2 damps echo modulation by a factor of $\exp(-2t/T_2)$. In general, T_2 in solids increases with decreasing temperature until it reaches its asymptotic limit. Thus, the temperature should be lowered to the point where transverse relaxation is dominated by spin diffusion of abundant nuclear spins in the system rather than by modulation of the hyperfine or g tensor by molecular reorientation. In addition, for a given measurement time, S/N ratio increases with the square root of the repetition rate of experiment that is inversely proportional to the longitudinal relaxation time T_1. The relation of S/N ratio with temperature can collectively expressed by

$$S/N(T) \propto \frac{1}{T}\exp\left(-2t/T_2(T)\right)\sqrt{\frac{1}{T_1(T)}}.$$

In the low-temperature limit, transverse relaxation is mainly mediated by the fluctuations of the hyperfine field at electron spin, which is induced by proton spin diffusion. Removal of those protons that contribute to the enhancement of transverse relaxation leads to elongation of relaxation time, which in turn improves the sensitivity and the range in DEER distance measurements. Perdeuteration of solvent or matrix reduces the fluctuations of hyperfine field due to the smaller magnetic moment of deuterons than that of protons by a factor of 6.5 and consequently expands the distance range that can be measured by DEER by slowing down the transverse relaxation rate ($1/T_M$). For example, in an attempt to measure the end-to-end distance distribution for a shape-persistent biradical with a length of approximately 7.5 nm, perdeuteration of the medium extended t_{max} from 4 μs to 24 μs, exhibiting three periods of full oscillation in dipolar modulation (Jeschke et al., 2004). In case of biomacromolecules, it is hard to expect such a huge extension in t_{max} due to more significant limitations imposed on many other factors, such as local structure of labeled position, sample concentrations, and the cost of deuterated matrices etc.; however, in some applications on proteins (Huber et al., 2001), perdeuteration of the solvent was successful in measuring long distances up to 7 nm with prolonged T_M. Alternatively, solvents without methyl groups are more favorable than those with methyl groups (Lindgren, 1997). Methyl group rotation is not fully repressed even at very low temperatures and causes a strong nuclear modulation.

Explicit modeling of spin labels in structural studies of proteins

The uncertainties given in DEER distance constraints by the flexible tether of the spin label set a substantial limitation in their application to structural studies on biomacromolecules. If the measured distance between the nitroxides is interpreted as a C_α-C_α distance ignoring the size and conformation of the spin label, errors of up to 1.2 nm may be introduced that result from conformational distributions of a single spin label (Borbat et al., 2002). Sales et al. have demonstrated the importance of explicit modeling of spin labels in EPR distance measurements

with regard to protein structures (Sale et al., 2005). When they compared dipolar-EPR distances with the corresponding C_β-C_β distances in the protein structures, the low correlation between two sets of distances with a mean error of 6 Å was substantially ameliorated by showing 2 fold increase in correlation (R^2) and a mean error of only 3 Å over the entire distance range (8-50 Å). Especially, the improvement in correlation was more remarkable in the shorter distance range (8-20 Å).

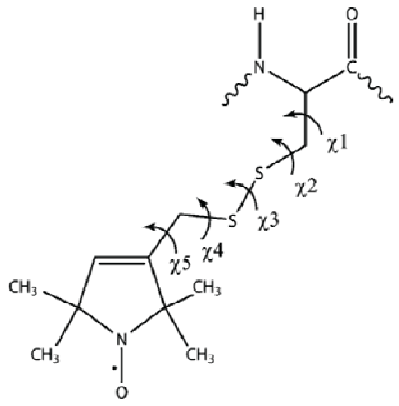

Figure 22. Structure of the R1 side chain.

A body of evidence from crystallographic analysis of spin-labeled T4 lysozymes (Guo et al., 2008; Langen et al., 2000), molecular modeling of spin labeled side chain based on MD simulation (DeSensi et al., 2008; Polyhach et al., 2010), and spin labeling with MTSSL analogues containing bulky substituents in the nitroxide ring (Columbus et al., 2001) have revealed that for the sites on an α-helix the flexibility of the spin labeled side chain is dominated by rotations about the two bonds (χ_4 and χ_5) closest to the nitroxide ring moiety. Crystal structures of spin labeled T4 lysozyme revealed that the formation of a hydrogen bond between the S_δ and C_α-hydrogen, and slow isomerization about the disulfide bond (χ_3) on the EPR timescale substantially restrict rotational motions about χ_1 and χ_2, allowing only a limited number of preferential conformers for a R1 side chain (Fig. 22) tethered on an solvent-exposed helical site. To date, {m,m}, {t,m}, and {t,p} rotamers are known to be preferred in spin labels residing on helical structures as shown in Fig. 23, where m = –60°, p = +60°, and t = 180° in Lovell's notation (Lovell et al., 2000). The

rotamers from the empirically constructed rotamer library are also supported by the quantum mechanical calculations (Tombolato et al., 2006) and MD simulations. Practically, spin label conformations can be approximated by simply taking preferential rotamers (typically χ_1=-60°, χ_2=60°) and then refining them with optimization processes such as energy minimization. This approach has been successfully employed in many applications to probe conformational changes using long DEER distance constraints (Altenbach et al., 2008; Kuo et al.; Oldham et al., 2007; Smirnova et al., 2007; Van Eps et al., 2006).

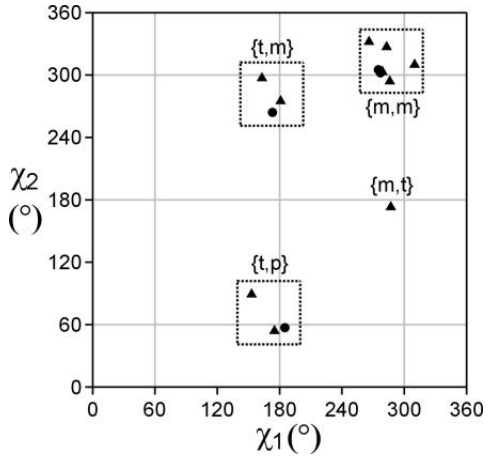

Figure 23. Rotamer preferences of R1 at solvent-exposed helical sites. Side chain dihedral angles χ_1 and χ_2 from the work by Guo et al.(Guo et al., 2008) are shown by circles, and those from Langen et al. (Langen et al., 2000) and Guo et al. (Guo et al., 2007) are shown by triangles.

CHAPTER III

STRUCTURE OF THE CDB3-ANKD34 COMPLEX

Introduction

Human erythrocytes exhibit an unusual biconcave disc shape and remarkable plasma membrane mechanical stability and deformability, all of which are necessary for their survival in the circulatory system. It is now well established that the unusual cell shape and membrane mechanical properties are due in large part to the presence of an extensive membrane skeleton, composed primarily of the proteins spectrin and actin, that lines the inner membrane surface and to specific bridging interactions between this membrane skeleton and intrinsic membrane proteins in the lipid bilayer. The spectrin-based cytoskeleton associates with the membrane bilayer via two types of contacts, one involving short actin protofilaments and protein 4.1 which interact with the cytoplasmic domain of glycophorin C, and the second involving the bridging protein ankyrin-R and protein 4.2 which interact with the cytoplasmic domain of the anion exchange protein (AE1) also known as band 3. Alterations in this second class of interactions often result in spherical erythrocytes with decreased cell size and increased fragility, a condition known clinically as hereditary spherocytosis (HS). HS is a spectrum of inherited diseases, occurring in one family out of 2,000 to 3,000, which presents clinically as varying degrees of hemolytic anemia resulting from hemolysis of the spherical erythrocytes as they flow through the microcirculation. Recent data have indicated that 15-20 % of HS cases are attributable to AE1 mutations and ~50 % of HS cases result from ankyrin-R mutations (Delaunay, 2002).

The ankyrin family of adaptor proteins, which includes the three isoforms ankyrin-R, ankyrin-G, and ankyrin-B in vertebrates, serve critical functions in cells by linking the lipid bilayer to the spectrin-based membrane skeleton as well as assembling proteins in specialized

membrane domains (Bennett and Baines, 2001; Nilsson and Bennett, 2009). Like the other two isoforms, ankyrin-R contains an N-terminal membrane binding domain, a central spectrin binding domain, and a C-terminal regulatory domain. The membrane binding domain is composed of 24 ankyrin-Repeat modules (ANK), each of which contains two anti-parallel α-helices and a long loop. The stacking of individual ANK repeats forms a superhelical spiral (Michaely et al., 2002). Proteolysis studies have shown that the 24 repeats in ankyrin-R, the isoform in human erythrocytes, can be subdivided into four groups of 6 repeats each (D1, D2, D3, and D4). This same study demonstrated that the full length membrane binding domain of ankyrin-R bound two dimeric cytoplasmic domains of AE1 with positive cooperativity. One binding site was located in domain 2 (AnkD2; repeats 7-12) and the second binding site was located in domains 3 and 4 (AnkD34; repeats 13-24) (Michaely and Bennett, 1995).

AE1 is the most abundant membrane protein in the erythrocyte with a population of one million copies per cell. While the transmembrane domain of AE1 plays a critical role in pH homeostasis of the body by exchanging two monovalent anions, bicarbonate and chloride across the plasma membrane, its cytosolic domain (cdb3) acts as an organizing center for a set of intracellular proteins to form a macromolecular complex. Cdb3 exclusively exists as a homodimer *in vitro*, where two dimerization arms from each monomer are tightly interlocked with each other and its N-terminal region, known to contain binding sites for many binding partners, is largely unstructured (Zhang et al., 2000; Zhou et al., 2005). A range of biochemical studies have implied that the β6/β7 hairpin loop of cdb3 (residues 175~185; also called 'critical ankyrin binding loop') and the disordered N-terminal region (residues 1~54) might be the major sites for interaction with the membrane binding domain of ankyrin-R.

Previous studies have indicated that a "tetramer" of AE1, rather than the fundamental dimer, is involved in binding ankyrin-R (Che et al., 1997). Interestingly, a stable sub-population of AE1 tetramers can be extracted by non-ionic detergents from erythrocyte ghost membrane preparations (e.g. (Blackman et al., 1998; Casey and Reithmeier, 1991b; Hanspal et al., 1998)).

What is not known is whether interaction of two cdb3 dimers with the two cooperative binding sites on ankyrin-R (Michaely and Bennett, 1995) drive the formation of a true tetramer of cdb3 or whether the structure is more accurately described as a dimer of dimers with no major structural rearrangements of the individual dimer units.

Now that crystal structures are available for isolated cdb3 (Zhang et al., 2000) and for isolated ankyrin-R repeats 13-24 (AnkD34; (Michaely et al., 2002)), it is possible to determine the structure of the complex formed between one cdb3 dimer and AnkD34 using modern protein docking algorithms in conjunction with structural constraints obtained from site directed spin labeling studies (e.g. (Bhatnagar et al., 2010; Hilger et al., 2007; Park et al., 2006)). In the present studies, site directed spin labeling and EPR have been employed to map the binding interfaces on cdb3 and on AnkD34 under conditions where the proteins form a stable complex. Distance measurements using double electron-electron resonance (DEER) between pairs of spin labels in cdb3 or AnkD34 have shown that the global structure of neither protein is significantly altered upon complex formation. Additional DEER measurements between pairs of spin labels, one in cdb3 and the other in AnkD34, have provided interprotein distance constraints. All of these data have been utilized to build a family of structural models using the ROSETTA suite of docking algorithms (reviewed in (Kauffman et al., 2010)) that are compatible with the experimental data. The models indicate that a large section of the peripheral domain of cdb3 interacts with ankyrin-Repeats 18-20 on the top loop region of AnkD34 primarily through hydrophobic interactions. The binding surface on AnkD34 is remote from the ankyrin groove which has been hypothesized to be involved in binding to a number of membrane proteins. In preliminary docking studies, the ankyrin groove of AnkD34 was hypothesized to be involved in binding to cdb3 (Michaely et al., 2002). The models presented in this work indicate that the ankyrin groove is not the binding interface and they also place restrictions on whether a second cdb3 dimer could bind to the D2 domain of ankyrin-R to form a true tetramer of cdb3.

Materials and Methods

Protein preparation and spin labeling

The preparation of wild-type and singly or doubly spin-labeled cdb3s has been described in previous work (Zhou et al., 2005). The cDNA encoding ankyrin-Repeats 13-24 plus 12 residues from the spectrin binding domain (AnkD34; residues 403-827) of ankyrin-R was provided by Dr. Peter Michaely (UT Southwestern). The DNA construct for wild-type AnkD34 was inserted into the pGEX-2T expression vector (GE Healthcare, Piscataway, NJ) wherein the two endogenous cysteines at positions 476 and 531 were converted to Ser and Ala, respectively. Cysless and single or double Cys mutants were constructed using the QuikChange Site-Directed Mutagenesis Kit (Stratagene, La Jolla, CA). The GST-fusion protein was overexpressed in BL21 Gold (DE3) competent cells by incubating the culture at 17 ºC for 3.5 to 4 hrs in the presence of 1 mM IPTG and purified using a GST affinity chromatography system (GE Healthcare, Piscataway, NJ) following the manufacturer's instructions. Before being cleaved from the resin, single or double Cys mutants of AnkD34 were reacted with a 10-fold molar excess of 1-oxyl-2,2,5,5,-tetramethyl-Δ3-pyrroline-3-methyl methanethiosulfonate spin label (MTSSL; Toronto Research Chemicals, North York, ON, Canada) in the binding buffer plus 0.1% (v/v) octaethylene glycol monododecyl ether (ANAPOE®-$C_{12}E_8$; Anatrace, Santa Clara, CA) at room temperature for 2 hrs and then at 4 ºC overnight. Unreacted spin label was removed by flowing excess washing buffer (50 mM sodium phosphate buffer containing 500 mM NaCl, 2 mM EDTA, pH 7.0) through the column until no spin label was detected in the flow through by EPR. Spin labeled AnkD34s were released from the immobilized GST-tag by thrombin cleavage in the binding buffer (50 mM sodium phosphate, 500 mM NaCl, 2 mM EDTA, and 10 % (w/v) glycerol, pH 7.0). Upon completion of the cleavage reaction, benzamidine sepharose (GE Healthcare Piscataway, NJ) was added to remove the residual thrombin from the protein solution. Protein purity was assessed by SDS-PAGE as described in previous work (Zhou et al., 2007). All samples used in the studies were >

95% pure as judged by coomassie blue staining intensity. Protein concentrations were determined either using the Bradford assay with bovine serum albumin as a standard or by measuring absorbance at 280nm with the calculated extinction coefficients for each protein construct (cdb3, 33,920 $M^{-1}cm^{-1}$; AnkD34, 15,930 $M^{-1}cm^{-1}$).

GST pull-down binding assay

In order to assess the effect of mutation and concomitant spin labeling on the binding affinity of singly labeled cdb3 mutants, a GST pull-down binding assay was performed. A known amount (0.5 to 1 nmole) of wt-AnkD34-GST fusion protein was immobilized on the GST resin. To each aliquot of 50 % (v/v) suspension, a 4-fold molar excess of a singly labeled cdb3 mutant was added. After overnight incubation at 4 ºC, the column was washed with washing buffer three times to remove unbound cdb3. The resultant resin was directly loaded onto a SDS-PAGE gel and the band intensities of each protein were analyzed using a UN-SCAN-IT gel digitizing system (Silk Scientific, Orem, UT). The amount of bound cdb3 was assessed from the band intensity ratio between bound cdb3 and normalized wt-AnkD34 fusion protein. The relative binding affinity of each spin-labeled cdb3 mutant was estimated by comparing the bound fraction of a mutant with that of wt-cdb3. Likewise, the binding affinities of singly labeled AnkD34 mutants to wt-cdb3 were evaluated in the same manner as described above using a series of singly labeled AnkD34-GST fusion proteins which were immobilized on the resin.

Complex Formation

Complexes between spin-labeled AnkD34s and cdb3s were prepared by incubating wild-type or specific spin-labeled proteins in the same binding buffer defined above at 4 ºC overnight. Both proteins were concentrated to the desired range using a centrifugal membrane filter device (30 kDa molecular weight cutoff; Millipore, Billerica, MA) before complex formation.

Circular dichroism (CD) measurements.

CD Spectra were recorded on a Jasco J-810 system (Easton, MD) at room temperature with a 0.1cm path length cell. All spectra were obtained from samples in 10 mM potassium phosphate buffer, pH 7.4. The data were collected from 190 to 260 nm at a scanning speed of 20 nm/min. The raw data, in millidegrees (θ), were converted to molar ellipticity [θ] using the relationship:

$$[\theta] = (100)\times[\text{signal}]/(ncl)$$

Where n is the number of amino acid residues, c is the protein concentration in mM, and l is the path length in cm.

CW-EPR measurements

CW-EPR spectra were collected at X-band (9.8 GHz) on a Bruker EMX spectrometer fitted with a TM_{110} cavity (BrukerBiospin, Billerica, MA) using 5mW microwave power and 1G field modulation at 100 kHz. Samples were prepared in the 80 to 120 μM concentration range and spectra were collected at room temperature in 50 μL glass capillaries (Kimble Glass, Inc., Vineland, NJ).

NiEDDA accessibility

For the measurement of spin label side chain accessibilities, a singly labeled protein was mixed with a 4 molar excess amount of its non-labeled binding partner. The 4-fold excess was used to ensure saturation of binding sites. NiEDDA accessibility of individual sites on each protein was measured using a gas permeable TPX capillary and an ER4123D resonator (BrukerBiospin, Billerica, MA) as previously described (Zhou et al., 2005). Accessibilities are expressed numerically as dimensionless Π values which were calculated from the following equation:

$$\Pi(NiEDDA) = \frac{P_{1/2}(NiEDDA) - P_{1/2}(N_2)}{\Delta H_0}$$

where $P_{1/2}$ is the half-saturation power in the presence of NiEDDA or N_2 and ΔH_0 is the field width of the central peak. Short inter-probe distances (<20Å) were measured on samples in binding buffer plus 50 % glycerol at 2 °C. The resulting EPR spectra were analyzed using the convolution method which assumes Gaussian distance distributions as described in previous work (Hustedt et al., 2006; Rabenstein and Shin, 1995).

Four-pulse DEER measurements and data analysis.

The four-pulse DEER experiment was performed at X-band (9.5 GHz) on a Bruker EleXsys 580 spectrometer equipped with a Bruker split ring resonator (ER 4118X-MD5). A standard 4-pulse sequence was employed with a 32 ns π pulse and a 16 ns π/2 pulse. All measurements were recorded at 80 °K. Samples were prepared in binding buffer containing 30% (w/w) glycerol in the 150 to 250 μM concentration range and loaded into 2.4 mm i.d. quartz capillaries (Wilmad LabGlass, Buena, NJ). While the interprotein distances were measured from a complex composed of two labeled proteins in an equimolar ratio, for the intraprotein distances, labeled proteins were allowed to form a complex with a 1.5 to 2 molar excess amount of its diamagnetic binding partner prior to the measurement. All DEER data were analyzed using software developed in house which simultaneously fits the background signal as a function of an effective spin concentration and radius of the molecule or complex while determining the specific interactions of interest using a distance distribution defined as a sum of Gaussians (manuscript in preparation). This approach, which takes into account the excluded volume of the molecule or complex, typically gave better fits to the data than those obtained using *a priori* background correction. The calculated average distances and distance distributions were similar to those obtained using the conventional Tikhonov regularization method (Chiang et al., 2005).

Chemical cross-linking of cdb3-AnkD34 complexes

Cross-linking of the complex between a pair of Cys residues from each protein was accomplished using the homo-bifunctional maleimide crosslinker, bismaleimidoethane (BMOE, Pierce Biotechnology, Rockford, IL) following the manufacturer's instructions. Briefly, each pair of single Cys mutants of cdb3 and AnkD34 was mixed at an equimolar ratio (10 μM final concentration of each protein) and allowed to form a complex in binding buffer containing 5mM EDTA. To 100 μL of protein mix, freshly prepared BMOE stock solution (20 mM in DMF) was added to give 30 μM final concentration. After 1 hr incubation at room temperature, the reaction was quenched with Laemmli sample buffer supplemented with 5 mM SDS and 10 mM DTT, and the formation of the cross-linked complex in the reaction mixture was visualized by SDS-PAGE as described in previous work (Zhou et al., 2007).

Molecular Modeling

The structure refinement process was carried out by first generating a large number of docked cdb3-AnkD34 complexes. The experimental results presented in Figs. 26-28, below, indicate that neither the cdb3 homodimer nor the AnkD34 fragment undergoes any major global conformational changes upon complex formation. Therefore, the RosettaDock program (Gray et al., 2003) was used to perform rigid docking calculations with the x-ray crystal structures for cdb3 (PDB code 1HYN) and AnkD34 (PDB code 1N11). 100,000 docked complexes were generated using unrestrained rigid body docking to explore all plausible docking orientations as shown in Fig. 37, upper panel, below. Next, a filtering protocol was devised to screen the 100,000 candidate complexes to eliminate all the models that were clearly inconsistent with the experimental DEER distance measurements. In the first-pass filter, the C_β-C_β distance was measured for a pair of spin labeled sites in cdb3 and AnkD34 from each docking model. In order to take the distance between the nitroxide electron and the C_β carbon (~7 Å) into account, the C_β-

C_β distance ± 14 Å cutoff was applied to select acceptable models in the first-pass filter process. Since cdb3 is a homo-dimer, spin label positions in each subunit were considered in the filtering process. Using this cutoff criterion and 20 experimental DEER distance measurements, it was determined that 811 docked poses from the RosettaDock calculations were compatible with the distance constraints as shown in Fig. 37, middle panel. All other docking poses had at least one (and generally many) pair distance violations that exceeded the C_β-C_β ± 14 Å tolerance value.

A second-stage filter was then implemented to select candidate structures that were consistent with experimental data for spin label side chain accessibility. Using MSMS software (Sanner et al., 1996), per-residue solvent-accessible surface areas were computed for five sites that caused large reductions in complex formation upon mutation (cdb3: 72, 129, 158 – AnkD34: 596 and 629) and nine sites that exhibited large changes in NiEDDA accessibility (i.e. changes in Π values of < -8; see Tables 1 and 2) upon formation of the complex (cdb3: 137, 148, 160, 166, 254 – AnkD34: 598, 631, 662, 664). Using canonical surface areas for fully-exposed side chains in G-X-G tripeptides (Chothia, 1975), the raw surface area computed for each of the wild-type residues was normalized to a value between 0 and 1, with 1 representing a fully-exposed residue and 0 representing a fully buried residue. The normalized values were summed together to form an accessibility score, where a small score corresponds to more buried surface and therefore better agreement with experiment. The top 100 structures were sorted based upon increasing accessibility score and every 10 structures were then binned cumulatively from the top. An overall backbone RMSD was then computed for all structures in each of the bins, and the RMSD values versus bin size were plotted. The larger bins, with 40 or more structures, contained structures with accessibility scores that were a minimum of 28 % larger than the best overall score of 1.96. In addition, the slope of the RMSD vs. bin size plot is much steeper beginning with a bin size of 40, indicating that besides significantly worse accessibility scores, the larger bins contain structures which look significantly different than the best-scoring structure (RMSD from

the mean of as high as 6.1 Å in the 40-structure bin, moving higher from there). Given these statistics, the top 30 structures were chosen as the final solution set, which spans a range of accessibility scores from 1.96-2.48, and has an average pairwise RMSD value of 2.68 Å. It should be noted that it is also possible to more precisely model the orientation of the R1 side chain thereby lowering the ±14 Å tolerance value used in this work (Bhatnagar et al., 2010; Borbat et al., 2002; Fajer et al., 2007; Herrick et al., 2009; Sale et al., 2005). However, having extensive interface mapping data from solvent accessibility measurements permitted the determination of structural models without the need for these approaches.

Results

Biophysical Characterization of AnkD34

Typically, structural studies using exogenous probes, such as the SDSL-EPR, require mutations which potentially can induce some structural alterations in the target protein. Hence, the mutant proteins to be studied should be stable enough to endure structural perturbations that can be induced by the mutations. AnkD34 contains two endogenous cysteine residues at positions 476 and 531, which were substituted with alanine and serine, respectively. The cysless form of AnkD34 was expressed with a good yield (more than 5 mg/L) and was stable in the presence of high salt (0.5 M NaCl) and 10 % (w/v) glycerol.

In order to assess the effect of point mutations on the global structure of AnkD34, CD spectroscopy was employed. As shown in Fig. 24, wild-type and cysless AnkD34 resulted in identical CD profiles showing that removal of two endogenous cysteins had no detectable effects on the secondary structure of the protein. Additionally, one single cysteine mutant of AnkD34 where a cysteine was introduced at position 656 on the cysless background also showed no difference in its CD profile. As predicted from the crystal structure of AnkD34, the spectra

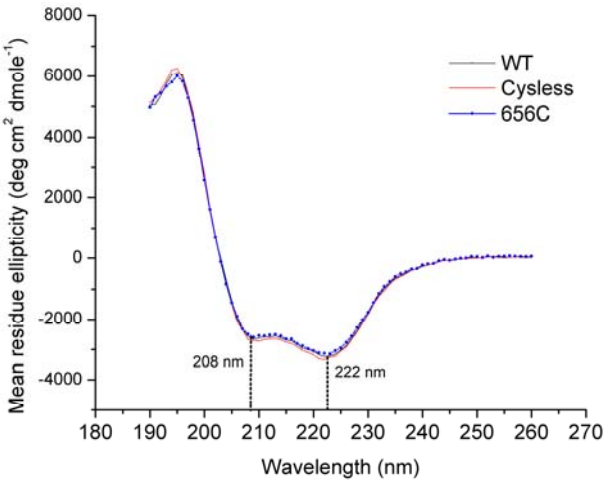

Figure 24. The CD spectra from three different AnkD34 constructs. Three spectra from wild-type (black), cysless (red), and S656C (blue) were superimposed for comparison.

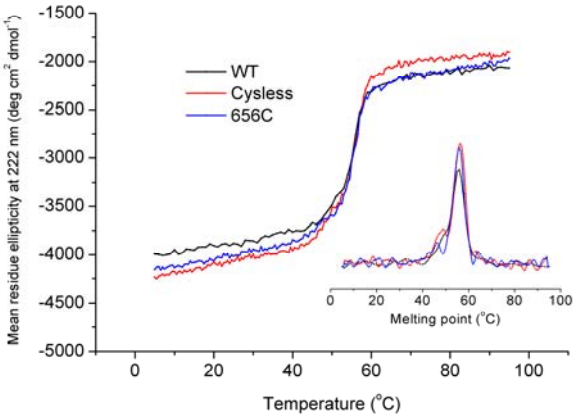

Figure 25. The thermal profiles obtained from CD measurements and its first derivatives (inset) for three different AnkD34 constructs. The three profiles from wild-type (black), cysless (red), and S656C (blue) were superimposed for comparison.

feature a typical pattern for α-helices with two local minima at 208 and 222 nm. Moreover, all three constructs showed identical thermal profiles in CD measurements with melting temperatures of approximately 56 °C. These data demonstrate that mutations to be utilized for SDSL cause no significant change in the secondary structure or the thermal stability of AnkD34.

Cdb3 and AnkD34 form a complex without any major changes in their global structures.

The first questions that were addressed were whether the global structures of either cdb3 or AnkD34 were significantly altered upon complex formation. This question was addressed for cdb3 by spin labeling selected sites on the cdb3 dimer and then observing dipolar coupling by CW-EPR for sites at the dimer interface or by DEER at selected sites remote from the dimer interface in the absence and then the presence of bound wt-AnkD34. Fig. 26 exhibits CW-EPR spectra obtained from four selected sites residing on the dimer interface. The dipolar couplings revealed by lineshape broadenings showed no significant changes upon binding AnkD34 in all the spectra with the exception of position 339. Given that the lineshape from the dipolar coupled spectrum is extremely sensitive to the inter-probe distance and their relative orientation, a slight change in the lineshape observed only in the mutant 339R1 appears to be the result of local structural perturbation associated with repacking of the R1 side chain upon binding AnkD34. These spectra show conclusively that binding of wt-AnkD34 to the peripheral domain of each cdb3 monomer does not lead to any observable changes in the structure of the dimer interface.

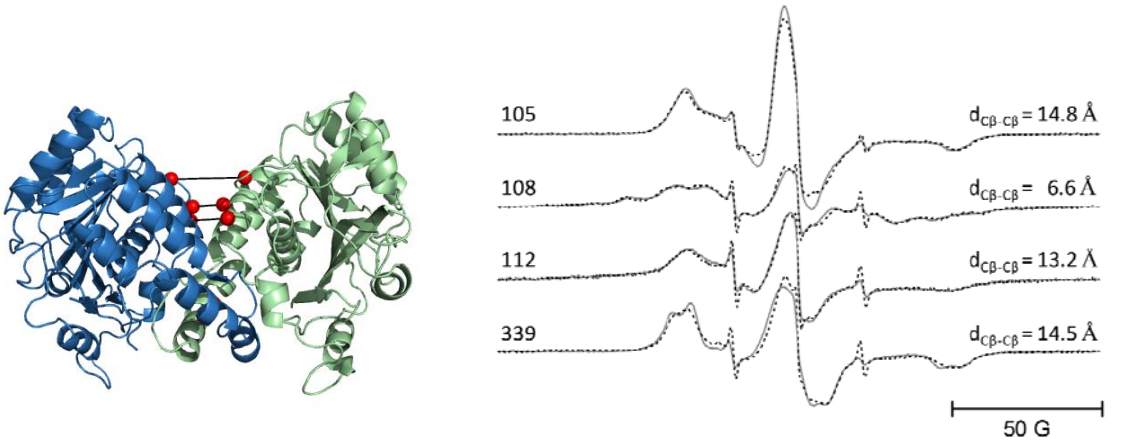

Figure 26. Dipolar coupled EPR spectra obtained from the sites at the dimer interface of cdb3 in the presence (grey solid line) or absence (black dashed line) of AnkD34. Sites 105, 108, 112, and 339 are all at the dimer interface and each gives rise to a dipolar coupled EPR spectrum due to their close proximity.

Likewise, there were no significant changes in inter-probe distances as a result of complex formation for three pairs of sites located in peripheral regions indicating that the global structure of the cdb3 dimer is not altered (Fig. 27 and Table 4).

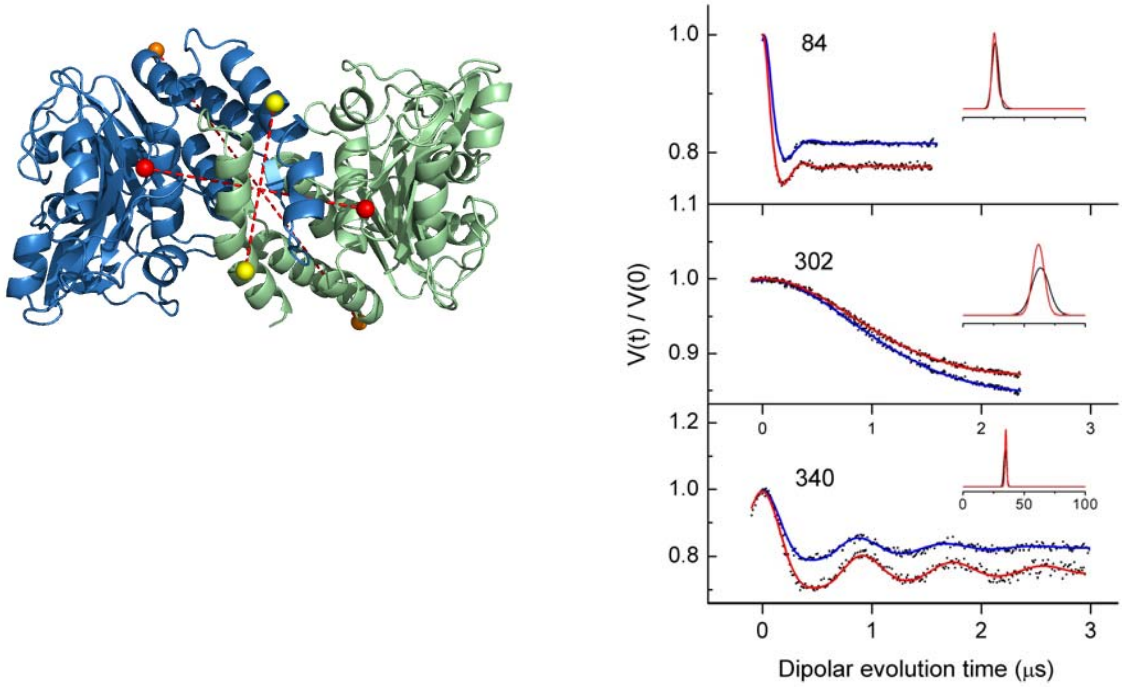

Figure 27. Inter-subunit distances between spin labeled side chains of cdb3 before and after complex formation with AnkD34 measured by DEER. Three pairs of surface sites consisting of identical positions from each monomer were selected as depicted by the spheres (84, red; 302, orange; 340, yellow) in the left panel. The DEER data (black dots) and fits to the data (blue, before complex formation; red, after complex formation) are shown as solid lines in the stacked plots in the right panel. The resultant average distances and distance distributions from fitting the data in Å is shown in the insets.

Table 4. Inter-subunit DEER distances analyzed from from the peripheral domains of a cdb3 dimer. The mean distances and their distributions (numbers in parentheses) are shown along with the corresponding C_β-C_β distances from the crystal structure.

Spin labeled sites on cdb3	Distance (Å)		C_β-C_β distance (Å) in crystal structure
	- AnkD34	+ AnkD34	
84	26.1 (0.4)	26.2 (0.3)	23.9
302	56.5 (0.2)	57.2 (6.8)	53.8
340	34.6 (0.8)	33.5 (0.5)	30.4

Again, when two cysteine residues were introduced into cysless AnkD34 at sites in the groove region or along the convex backbone and DEER measurements were made on the spin labeled proteins, there were no significant changes in inter-probe distances following complex formation with wt-cdb3 as shown in Fig. 28 and as given in tabular form in Table 5, indicating that binding to cdb3 does not induce any global structural change in AnkD34.

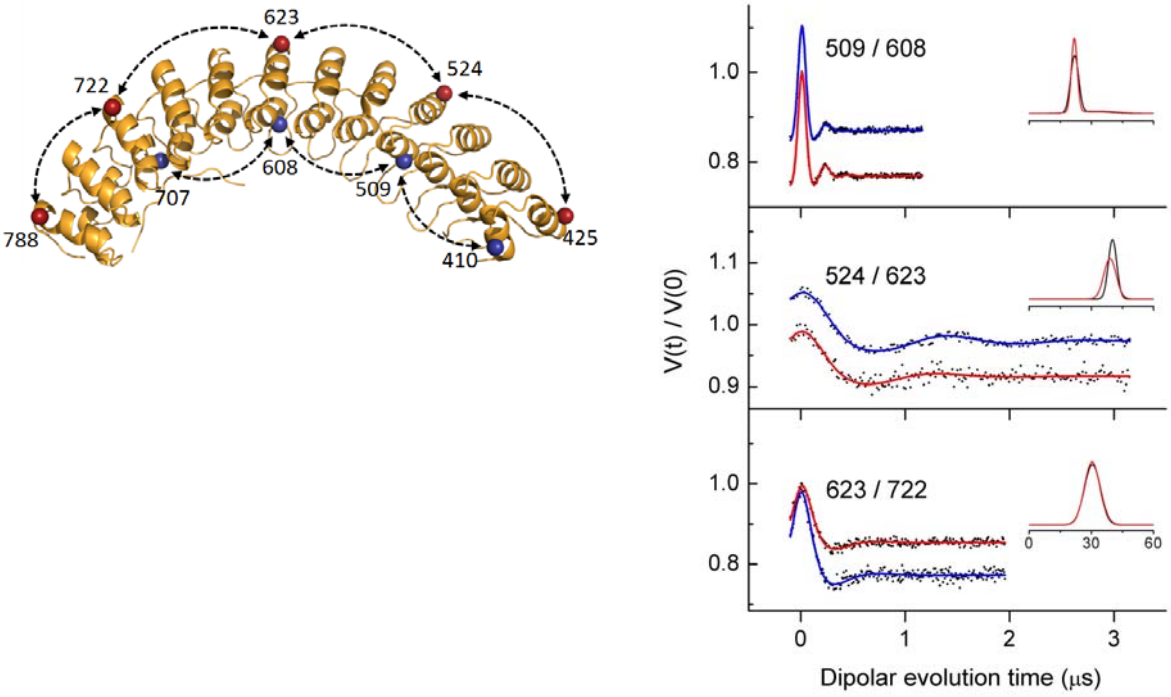

Figure 28. Intraprotein distances in AnkD34 measured by DEER. The residue pairs are defined by the structure in the upper panel and representative DEER data before and after complex formation with cdb3 are shown in the lower panel. The DEER data (black dots) and fits to the data (blue (before complex formation)) and red (after complex formation)) are shown as solid lines in the stacked plots in the lower panel. The resultant average distances and distance distributions from fitting the data (Å) is shown in the insets.

Table 5. Intraprotein DEER distances from both the concave groove and the convex backbone sides of AnkD34.For a set of doubly labeled mutants of AnkD34, DEER distances were measured in the absence and then in the presence of cdb3. The mean distances and their distance distributions (numbers in parentheses) are shown below along with the corresponding C_β-C_β distances from the crystal structure.

Spin-labeled sites		Distance (Å)		Cβ-Cβ distance (Å) in crystal structure
		- cdb3	+ cdb3	
Concave groove (Inner helices)	410/509	24.4 (2.7)	24.3 (3.0)	25.1
	509/608	22.1 (2.2)	22.0 (1.9)	26.2
	608/707	22.3 (2.3)	21.9 (2.0)	25.0
Convex backbone (Outer helices)	425/524	41.5 (8.6)	41.3 (6.8)	34.8
	524/623	35.3 (4.0)	32.0 (6.4)	33.9
	623/722	40.3 (1.5)	39.7 (2.3)	36.2
	722/788	30.7 (3.7)	30.6 (3.9)	25.5

Collectively, these data suggest that modeling of the structure of the complex formed between cdb3 and AnkD34 to a first approximation would only require rigid body docking of the two proteins using binding interface information obtained from EPR experiments (i.e. what surfaces of the two proteins are in close contact) and interprotein distance constraints obtained from EPR or DEER experiments (i.e. what is the relative spatial positioning of the two proteins). This basic approach has been described and successfully utilized in previous work on other protein complexes by other investigators (e.g. (Bhatnagar et al., 2010; Hilger et al., 2007; Park et al., 2006)).

Determination of the binding interface on cdb3.

Studies by a number of investigators (e.g. (Chang and Low, 2003; Davis et al., 1989; Stefanovic et al., 2007; Willardson et al., 1989)) as well as our own previous studies (Zhou, 2006) have indicated that residues on the peripheral domains of the cdb3 dimer are involved in binding

to ankyrin-R. Prior to CW-EPR scanning, a GST pull-down assay was performed for a series of singly spin labeled mutants of cdb3 where R1 side chains were attached at various surface sites on the peripheral domains to assess their binding affinity to wt-AnkD34. It was observed that most of the singly spin-labeled mutants had binding affinity that was > 80 % of that observed with wt-cdb3, indicating that spin labeling at these sites does not significantly disrupt the binding interface of the complex. When spin labeled side chains were introduced at residues 70, 72, 129, 155, and 158, binding affinity to wt-AnkD34 was reduced by greater than 60% (see binding data

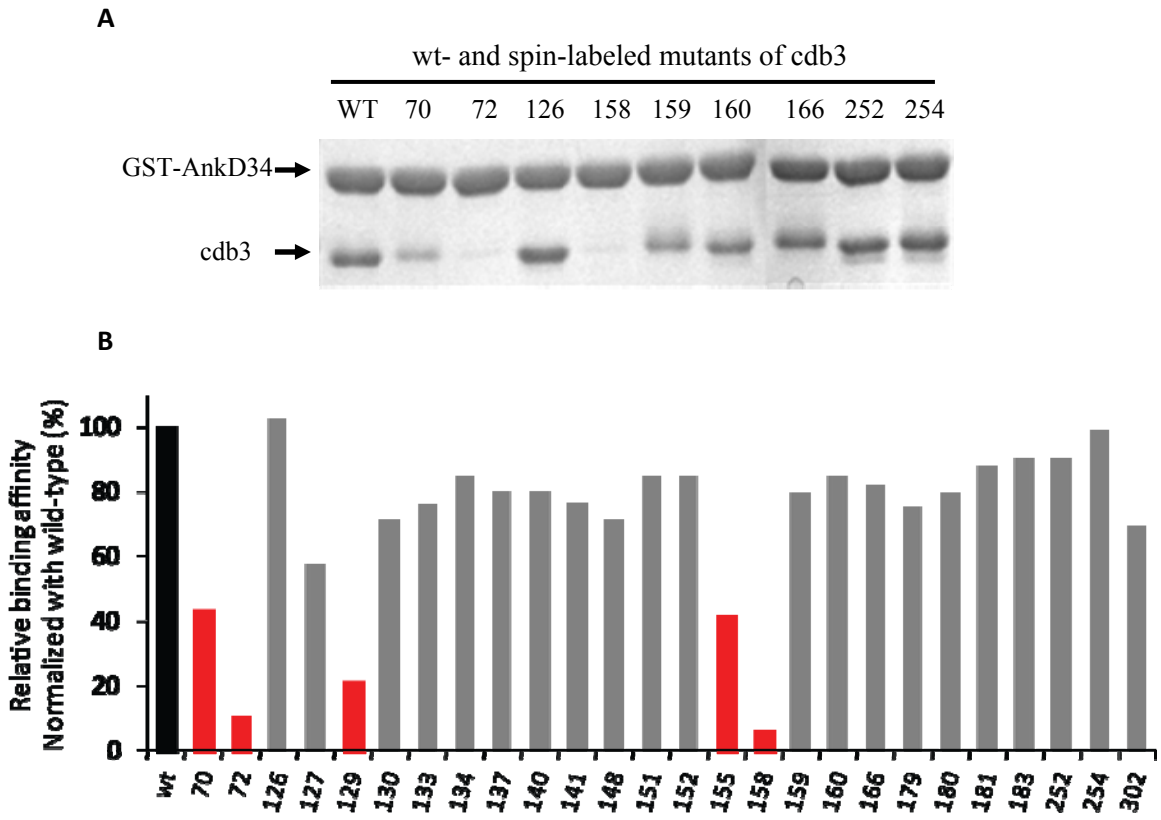

Figure 29. The effect of mutation and spin labeling at various sites of cdb3 on its binding affinity for AnkD34. Relative binding affinities for the selected spin labeled mutants of cdb3 with wt-AnkD34 were measured by the pull-down assay as described in the materials and methods section. The SDS-PAGE gel in the panel A (top) demonstrates the pull down assay results for sites 70, 72, 126, 158, 159, 160, 166, 252, and 254. The relative affinities of 26 sites are compared with binding of wt-cdb3 to wt-AnkD34 in panel B (bottom).

in Fig. 29) suggesting that these residues are in close contact with residues in AnkD34 in the complex and that a spin labeled side chain at these positions disrupts critical contacts between the two proteins.

The binding interface was further defined by the EPR data in Fig. 30, where specific sites on the α2-helix (residues 126, 127, and 130), on the α3-helix (residue 152), and on the β6/β7-hairpin loop (residues 179, 180, and 183) of cdb3 show significant changes in spin label side chain mobility when wt-AnkD34 is bound. In addition, spin labeled side chains at residues 160 and 254 also showed changes in mobility upon complex formation. These changes in side chain mobility are mapped onto the crystal structure of cdb3 in the right panel of Fig. 30, together with the sites that impair the binding affinity upon spin labeling. Spin labeled side chains at many other positions on the peripheral domains (sites 133, 134, 137, 140, and 141 in the α1 helix, at sites 148 and 151 in the α2 helix, and at sites 180 and 181 in the β6/β7 hairpin loop) showed no changes in mobility upon complex formation (marked in black in Fig. 30; (Zhou, 2006) and data not shown) consistent with the observation of no changes in global structure of cdb3 when it is bound to AnkD34.

The binding interface was further defined by measuring solvent accessibility of the same sites using NiEDDA as the paramagnetic broadening agent. As shown in Fig. 31 and in tabular form in Table 7, solvent accessibility mirrors the changes in spin labeled side chain mobility in general, providing further evidence for the surface on cdb3 that is involved in direct interaction with AnkD34. Consistent with mobility data, the most remarkable decreases in NiEDDA accessibility were observed in positions 160 and 254, which are located below the α2- and α3-helices. Collectively, a range of data collected from the surface sites on the peripheral domains of cdb3 well defines the putative binding interface mainly consisting of the N-terminal region of the α2-helix (residues 126, 127, 129, and 130), the C-terminal region of the α3-helix (residues 152, 155, and 158), and residues 70, 72, 160, and 254 on the loops. As predicted, spin labeling at

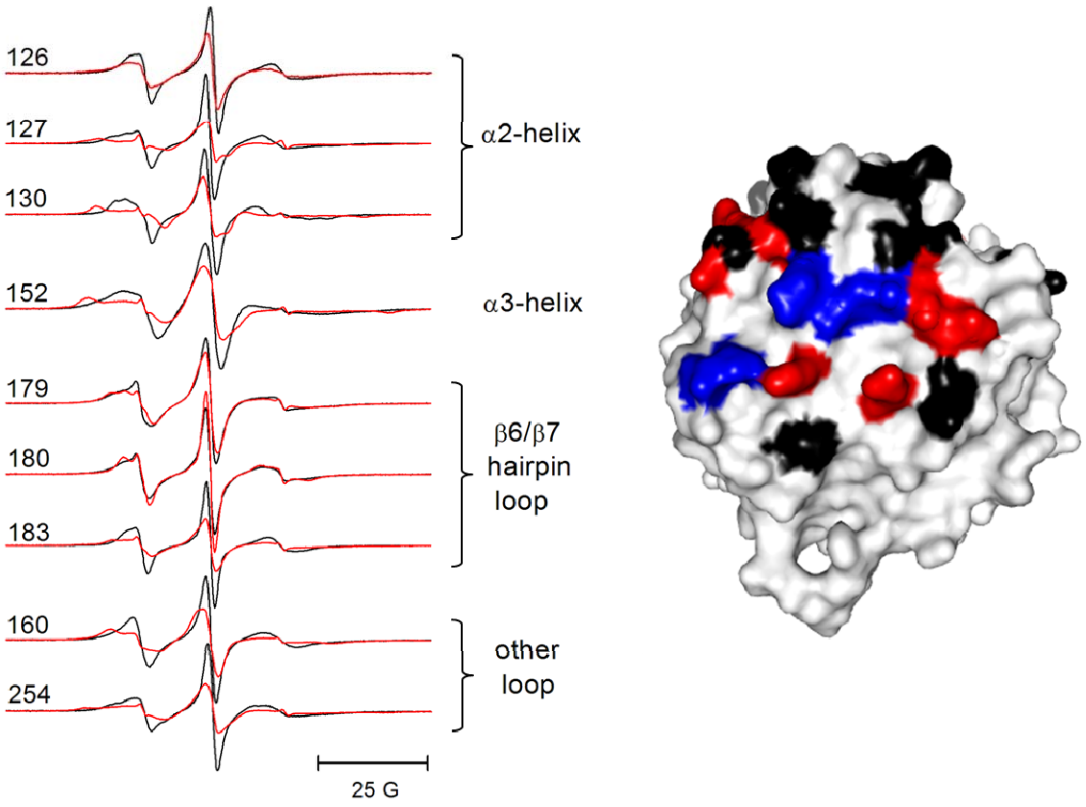

Figure 30. Changes in spin labeled side chain mobility in peripheral domain of cdb3 induced by complex formation. Left panel shows representative EPR spectra from spin labeled side chains incorporated into the α2-helix (126, 127, and 130), the α3-helix (152), and the β6/β7 hairpin loop (179, 181, and 183) in the peripheral domain of cdb3. The spectra in solid lines were recorded in the absence of wt-AnkD34. The superimposed spectra in dashed lines were recorded after complex formation with wt-AnkD34. Also shown are the data from sites 160 and 254 which lie outside these three structured domains but which showed significant changes upon binding of wt-AnkD34. There were no changes in EPR line-shapes upon complex formation at sites 133, 134, 137, 140, and 141 in the α2-helix, at sites 148 and 151 in the α3- helix, and at sites 180 and 181 in the β6/ β7 hairpin loop (data not shown). Changes in spin label side chain mobility (upper) assessed from EPR spectra were mapped onto the X-ray crystal structure of AnkD34 in the right panel. The red residues showed a decrease in side chain mobility upon complex formation, the black residues showed no change, and the blue residues significantly impaired complex formation when the wt residue was changed to cysteine and spin labeled with MTSSL.

positions 70 and 155, which exhibited partially impaired binding affinity (less than 50%), resulted in no decrease in NiEDDA accessibility. It is interesting to note that placing the R1 side chain at positions 137, 140, 141, and 148, which showed no change in mobility, gave rise to significant decreases in NiEDDA accessibility. While residue 137 is in close proximity with other residues contributing to the binding interface, residues 140, 141, and 148 forms a cluster at the top of the peripheral surface in Fig. 31. The long tether of the spin label and the spatial proximity of these residues to the binding interface revealed in the constructed structural models, which will be described later, suggest that local conformational changes or R1 side chain repacking are responsible for these observations.

Table 6 NiEDDA accessibility of surface sites on the peripheral domain of cdb3.

Labeled position	126	127	130	133	134	137	140	141	148	151	152
Π (- AnkD34)	20.5	22.5	15.8(1.4)	17.5(5.2)	14.9(1.9)	29.3(4.8)	24.8(2.1)	27.1(2.2)	29.7(2.5)	17.2	8.4(3.0)
Π (+ AnkD34)	12.8	17.1	16.0(2.7)	13.8(4.3)	12.6(3.3)	19.2(2.8)	21.5(1.8)	18.6(1.5)	16.3(0.8)	14.7	5.3(1.7)
Difference	-7.7	-5.4	0.2	-3.7	-2.2	-10.2	-3.3	-8.5	-13.4	-2.5	-3.1

Labeled position	155	179	180	181	183	70	160	166	216	254	293	302
Π (- AnkD34)	13.7	15.9(3.5)	21.2(2.9)	23.3(3.9)	19.8(2.2)	30.4	25.4	26.6	20.5	30	7.1	15
Π (+ AnkD34)	13.3	14.9(2.3)	17.4(2.2)	19.1(5.5)	17.4(1.8)	33	3.5	15.6	20.2	8.5	7.4	10.5
Difference	-0.4	-1.0	-3.8	-4.2	-2.4	2.6	-21.9	-11.0	-0.3	-21.5	0.3	-4.4

Standard deviations from triplicate measurements are shown in parentheses. Π values are dimensionless quantities as defined in experimental procedures. Residues 126 through 141 are in the α2 helix. Residues 148-155 are in the α3 helix. Residues 179-183 are in the β6-β7 hairpin loop. Residues 70, 160, 166, 216, 254, 293 and 302 are distributed over the peripheral domain of cdb3.

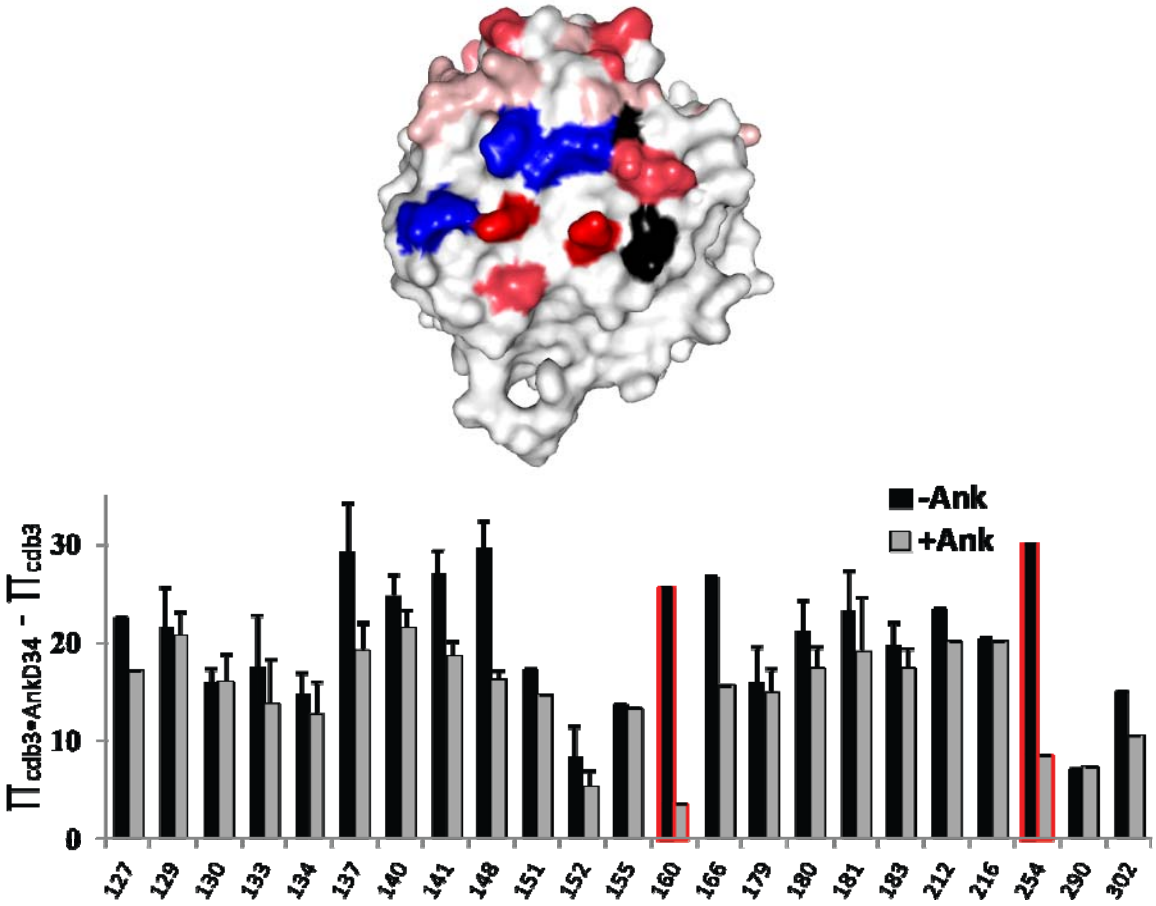

Figure 31. Changes in solvent accessibility as assessed by collision frequency with NiEDDA. Accessibility changes were mapped onto the X-ray crystal structure of AnkD34 in the top panel. The red residues showed a decrease in side chain mobility upon complex formation, the black residues showed no change, and the blue residues significantly impaired complex formation when the wt residue was changed to cysteine and spin labeled with MTSSL. The residues that showed changes in accessibility were displayed with three different colors based on their ΔΠ ($\Pi_{complex}$-Π_{AnkD34}) values (red, ΔΠ < -14.0; hot pink, -14.0 ≤ ΔΠ < -5.0; pale pink, -5.0 < ΔΠ ≤ -2.0). In the lower panel, ΔΠ values from each mutant in the presence (grey) and absence (black) of wt-AnkD34 were graphically displayed. Residues 160 and 254, showing the most dramatic decreases, are highlighted with red border lines.

Determination of the binding interface on AnkD34.

Early work by Michaely and Bennett showed that binding of cdb3 to ankyrin-Repeats 13–24 was salt independent, unlike the binding to ankyrin-Repeats 7–12 which was salt dependent (Michaely and Bennett, 1995b). This important observation provided evidence that the

binding of cdb3 to AnkD34 was likely to be dominated by hydrophobic interactions. In agreement with this hypothesis, the spin labeled side chains in the groove of ankyrin-Repeats of AnkD34, which contain a number of charged and polar residues, showed no changes in mobility upon complex formation (e.g., residues 599, 603, and 636; data not shown). However, as shown in Fig. 32, when spin labeled side chains were incorporated into the top linker surface of ankyrin-Repeats 18, 19, and 20 in AnkD34, there were significant changes in mobility when a complex

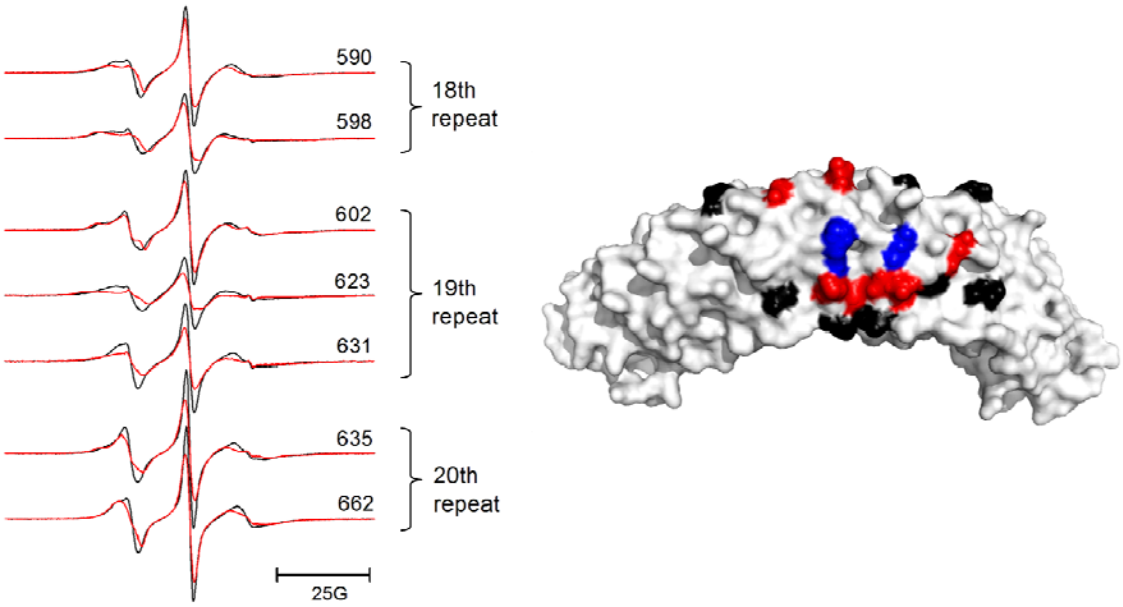

Figure 32. Binding-induced changes in spin label side chain mobility at the top liker surface sites of AnkD34. The left panel shows representative EPR spectra from spin labeled side chains incorporated into the β-hairpin loop regions of ankyrin-Repeat 18 (590 and 598), ankyrin-Repeat 19 (602, 623, and 631), and ankyrin-Repeat 20 (635 and 662) in AnkD34. The spectra in grey solid lines were recorded in the absence of wt-cdb3. The superimposed spectra in black dashed lines were recorded after complex formation with wt-cdb3. In the right panel, the mobility changes have been mapped onto the X-ray crystal structure of AnkD34. The red residues in the top panel showed a decrease in side chain mobility upon complex formation, the black residues showed no change, and the blue residues significantly impaired complex formation when the wt residue was changed to cysteine and spin labeled with MTSSL.

was formed with wt-cdb3. Introduction of spin labeled side chains at equivalent structural positions in repeats 17 and 21 showed no changes in mobility upon complex formation (e.g., residues 565 and 697; data not shown). Incorporation of a spin labeled side chain at residue 596 in ankyrin-Repeat 18 and at position 629 in ankyrin-Repeat 19 (blue residues in Fig. 32) inhibited binding affinity of wt-cdb3 by greater than 80% (Fig. 33) suggesting that these residues are critical for binding. The side chain mobility data are mapped onto the X-ray crystal structure of AnkD34 in Fig. 32, right panel.

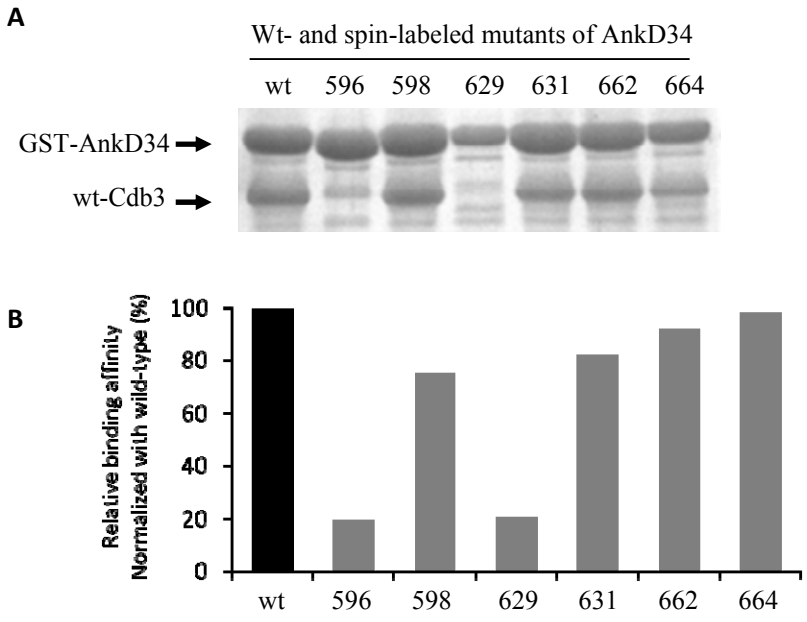

Figure 33. The effect of mutation and spin labeling at various sites of AnkD34 on its binding affinity for cdb3. Relative binding affinities for selected spin labeled mutants of AnkD34 with wt-cdb3 were also measured by the pull-down assay as described in the experimental procedures section. The relative affinities of 6 sites are compared with binding of wt-AnkD34 to wt-cdb3 in the panel B (bottom). Spin labeling at sites 598 on ankyrin-Repeat 18, 631 on ankyrin-Repeat 19, and sites 662 and 664 on ankyrin-Repeat 20 all resulted in relative binding affinities that were > 70 % of that observed with wt-AnkD34. However, labeling at site 596 in ankyrin-Repeat 18 and at site 629 in ankyrin-Repeat 19 resulted in less than 20 % of the binding relative to wt-AnkD34. The SDS-PAGE gel in panel A (top) demonstrates the dramatic reduction in relative binding affinity for AnkD34 mutations at sites 596 and 629 again indicating that spin labeling at these sites result in unfavorable steric and/or electrostatic interactions at the binding interface.

The binding interface was further defined by measuring the solvent accessibility of the same sites using NiEDDA as the paramagnetic broadening agent. Consistent with the mobility measurements, the residues that show most of the major changes in NiEDDA accessibility (Table 2; residues 590, 598, 623, 631, 662, 664) are clustered on the top linker surface together with residues 596 and 629. Note that the residues which reside on the same linkers, but whose side chains are facing the groove in the crystal structure (Table 8 and Fig. 32; residues 599, 603, and 636) showed no change in solvent accessibility. Overall, as shown in Fig. 34, top panel, solvent accessibility again mirrors the changes in spin labeled side chain mobility providing further evidence for the surface on AnkD34 that is involved in direct interaction with cdb3.

Table 7. NiEDDA accessibility of surface sites on AnkD34.

Labeled position	565	586	590	596	598	599	600	603	611	613	616
Π (- cdb3)	16.2	4.9	29.3	18.5	22.7	2.3	16.9	1.2	1.3	26.2	34.8
Π (+ cdb3)	14.2	3.1	19.6	15.3	6.8	1.3	15.0	0.9	1.8	18.8	23.3
	-2.0	-1.8	-9.7	-3.2	-15.9	-1	-1.9	-0.3	0.5	-7.4	-10.5

Labeled position	619	623	629	631	632	636	652	662	664	689	697
Π (- cdb3)	26.7	32.7	18.9	18.8	15.1	1.4	18.9	28.2	25.4	8.9	25.1
Π (+ cdb3)	13.9	20.7	16.2	3.9	7.1	0.9	6.8	13.5	16.9	13.2	19.8
	-12.8	-12.0	-2.7	-14.9	-8.0	-0.5	-12.1	-14.7	-8.5	4.3	-5.3

Π values are dimensionless quantities as defined in experimental procedures.

In addition to the sites on the top loop surface, spin labeling at another set of sites which reside on the outer helix (residues 616 and 619 from the 19th repeat and residue 652 from the 20th repeat) and the short linker (residue 613 from the 19th repeat) exhibited significant decreases in NiEDDA accessibility upon complex formation as shown in Table 8 and Fig. 34. The same set of spin labeled mutants also showed slight decreases in side chain mobility upon binding (data not shown). However, interprotein DEER distance constraints, which will be described in the next section, clearly excluded the outer helix surface from the binding interface. Observation of the

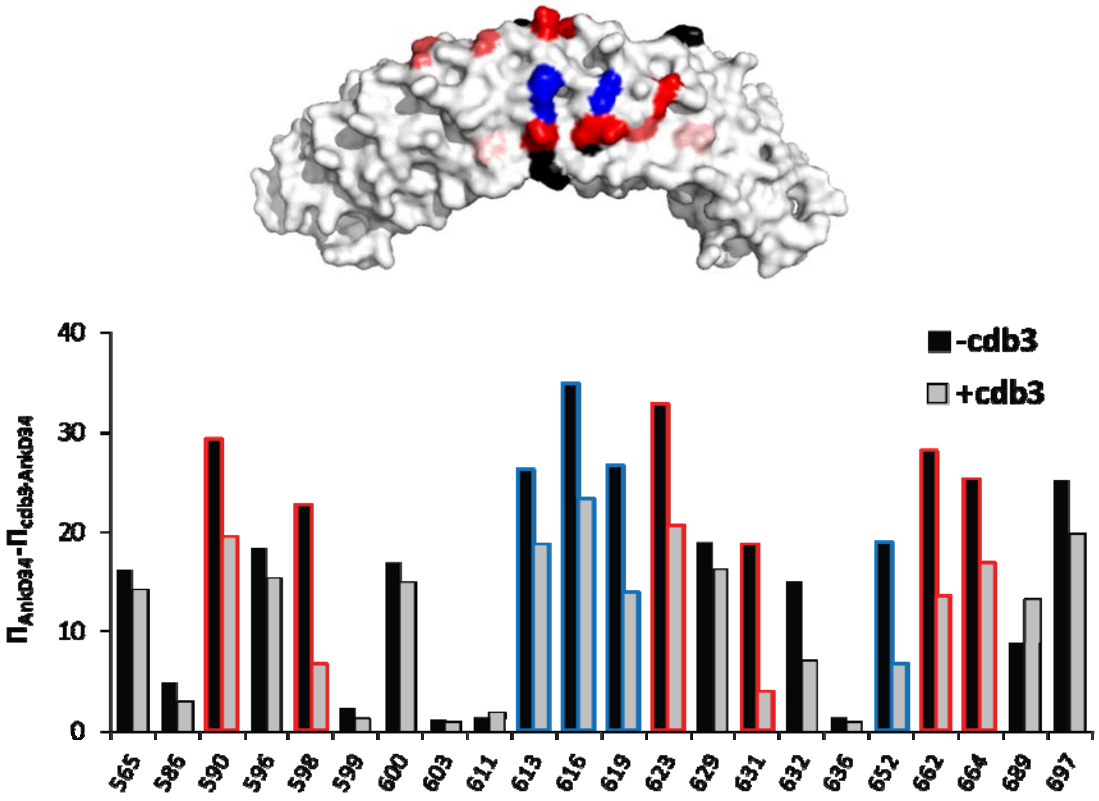

Figure 34. Changes in spin label side chain mobility (upper) and solvent accessibility as assessed by collision frequency with NiEDDA (lower) mapped onto the X-ray crystal structure of AnkD34. The red residues in the top panel showed a decrease in side chain mobility upon complex formation, the black residues showed no change, and the blue residues significantly impaired complex formation when the wt residue was changed to cysteine and spin labeled with MTSSL. The same color scheme is used for the NiEDDA accessibility data in the lower panel for the black and blue residues while the residues that showed changes in accessibility were displayed with three different colors based on their $\Delta\Pi$ ($\Pi_{complex}$-Π_{AnkD34}) values (red, $\Delta\Pi < -14.0$; hot pink, $-14.0 \leq \Delta\Pi < -5.0$; pale pink, $-5.0 < \Delta\Pi \leq -2.0$). The sites that showed significant decrease in accessibility at the top loop surface or outer helix are highlighted with red or blue border lines, respectively.

identical data from binding of these mutants to the N-terminal tail (residues 1–54)-truncated form of cdb3 and of no alteration in the R1 side chain mobility at the sites on C-terminal tail (residues 791–827) of AnkD34 upon complex formation demonstrated that these changes are not artifacts caused by interaction with those unstructured parts of the complex (data not shown). Based upon

the long range coupling observed in folding experiments and high sensitivity to the mutations, it is speculated that binding to cdb3 might induce some allosteric effects to be transmitted to the surface sites on the outer helix surface accompanying rearrangements of R1 side chain orientations at those sites.

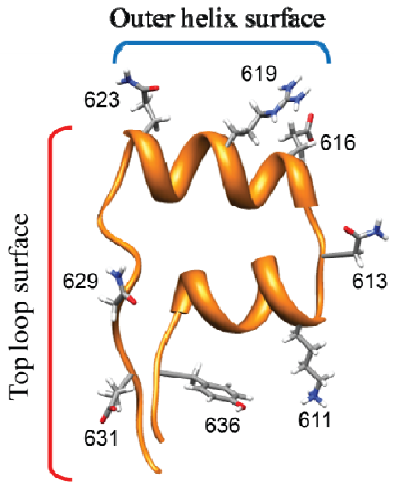

Figure 35. The ribbon presentation of 19th repeat of AnkD34 with the side chains of surface residues which were spin labeled for the binding interface mapping study.

Interprotein distance constraints from DEER measurements.

Having determined the surfaces on cdb3 and on AnkD34 located at the binding interface, it was possible to rationally choose residues on each protein for introduction of single Cys mutations, spin labeling, and making DEER measurements of interprotein distances. The interprotein distance data make it possible to spatially orient the two proteins relative to each other (Bhatnagar et al., 2010; Hilger et al., 2007; Park et al., 2006). Fig. 36 shows the 20 interprotein distances that were chosen along with the corresponding DEER data and analyses. The results of the analyses of DEER data from the 20 pairs are listed in Table 9. Most of the DEER data from these 20 pairs of sites (16 out of 20) gave rise to a single component without interference from the intra-dimer spin label on cdb3. However, analysis of data involving

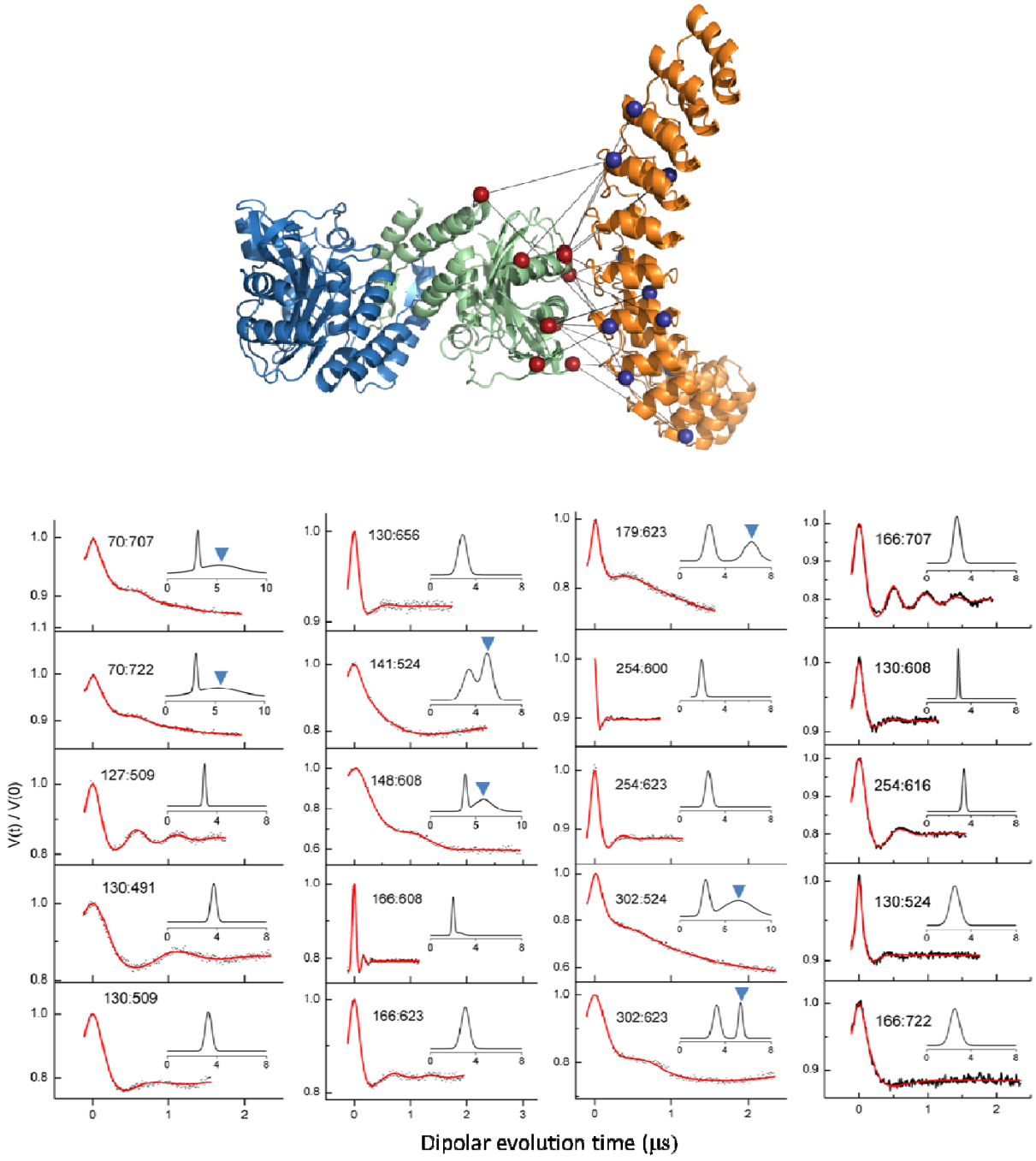

Figure 36. The 20 interprotein distances between selected sites on cdb3 and on AnkD34 that were used to refine the structural model for the complex. The distances measured by DEER are shown superimposed on a selected model for the complex in the upper panel. DEER data (dots) and the fits to these data (solid red lines) from 20 label pairs are shown in the lower panel. The insets in the lower panel show the average distances and distance distributions that were recovered from fitting the experimental data as described in experimental procedures.

Table 8. Interprotein DEER distances from 20 pairs of surface sites on cdb3 and AnkD34.

#	Sample		Interprotein DEER distance (Å)	Inter-subunit distance in cdb3 (Å)†
	cdb3	AnkD34		
1	70	707	30.6 (1.7)	76.2
2	70	722	27.1 (2.0)	76.2
3	127	509	29.9 (0.7)	70.0
4	130	491	37.4 (2.1)	67.9
5	130	509	34.5 (1.3)	67.9
6	130	524	24.7 (4.9)	67.9
7	130	608	28.6 (0.7)	67.9
8	130	656	28.2 (3.7)	67.9
9	141	524	33.9 (5.1)	46.5
10	148	608	38.1 (3.1)	53.0
11	166	608	20.2 (1.3)	67.8
12	166	623	30.3 (4.2)	67.8
13	166	707	26.9 (3.5)	67.8
14	166	722	31.9 (4.2)	67.8
15	179	623	25.7 (3.9)	59.6
16	254	600	19.6 (2.3)	72.3
17	254	616	30.0 (2.2)	72.3
18	254	623	24.8 (2.8)	72.3
19	302	524	28.9 (4.3)	53.8
20	302	623	32.1 (2.8)	53.8

†, C_β-C_β distance between two equivalent sites from each subunit obtained from the crystal structure of a cdb3 homodimer. The numbers in parentheses are the widths of the distance distributions recovered from fitting the experimental DEER data.

sites 141, 148, and 302 on cdb3 gave rise to two distance components, one from the intra-dimer dipolar coupling of spin labels on cdb3 and one from the interprotein dipolar interaction of spin labels on cdb3 and AnkD34. The intra-dimer distances were easily analyzed by extending the modulation time window in the DEER experiment and extraction of both inter-probe distances by a bimodal distance distribution as shown by the data presented in Fig. 36.

Molecular models of the complex based on long range distance constraints.

The unconstrained rigid docking calculations yielded 100,000 candidate complexes that span the full range of possible cdb3-ankyrin orientations, as shown in Fig. 37, upper. This result provides compelling evidence that no possible docking orientations were excluded in our modeling process. The first-pass distance filter reduced the solution set to 811 candidate structures, shown in Fig. 37, middle. When these candidate structures are superimposed on ankyrin, cdb3 dimers are localized in a radial band that extends from one side of the ankyrin molecule, across the convex surface and to the opposite side. This filter yielded a 99 % reduction in the solution set size, but as the fig. 37 shows, there is still considerable variability in this data set. The accessibility filter results exhibit a sharp increase in the model RMSD versus accessibility score when more than 30 best-scoring candidates are considered. As seen in Fig. 37, lower, the set of top 30 candidates forms a tightly clustered group on the side of the top loop surface of ankyrin, which agrees well with the empirically defined binding interface of AnkD34 from the mobility and accessibility measurements of spin labeled side chains. This collection of structures, which is shown in an expanded view in Fig. 38, upper panel, predicts an average buried surface area of 1103 $Å^2$ and represents the best current solution set. This set of structures will constitute the starting point for more detailed structural refinement in future work where both the spin labeled side chains will be explicitly modeled for interpretation of inter-probe distances and the local structures of cdb3 and AnkD34 at the binding interface will be allowed to relax.

Figure 37. Ensemble of structural models for the cdb3-AnkD34 complex superimposed on the crystal structure of AnkD34. The top panel shows 500 representative poses from the 100,000 generated by ROSETTA dock using no constraints to guide how the proteins could interact. The center panel shows how filtering these 100,000 poses using the 20 interprotein distance constraints from DEER measurements reduced the number of poses to 811 and gives a strong indication of the surfaces of the two proteins that form the binding interface, the potential orientations of cdb3 relative to AnkD34, and which ankyrin-Repeats were likely involved in binding. The bottom panel shows the top 30 structures that were obtained by filtering the 811 poses in the center panel with the solvent accessibility data as described in experimental procedures.

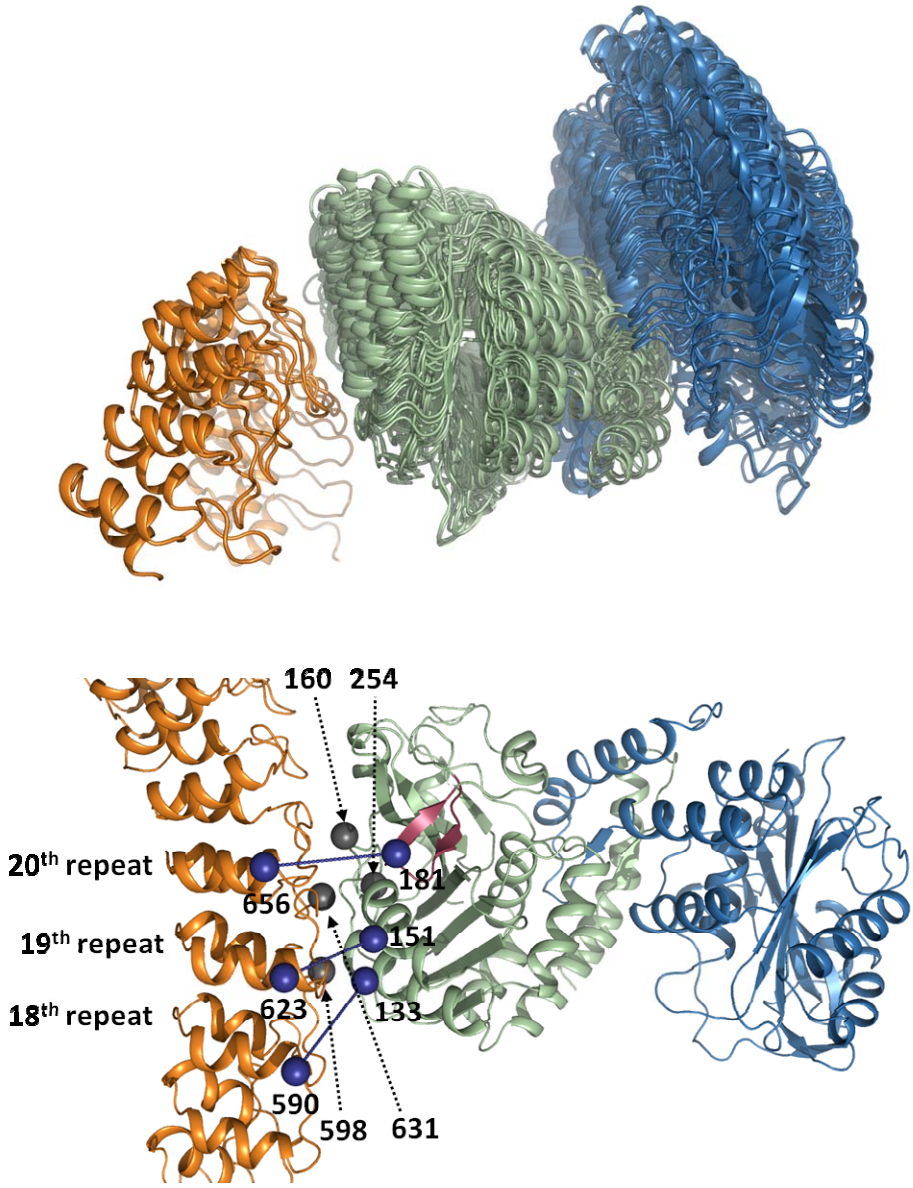

Figure 38. Color representation for the complex formed between cdb3 and AnkD34. In the upper panel, the set of poses for the α-carbon trace for AnkD34 (orange) has been held constant and the 30 poses of the cdb3 dimer (green/blue) are positioned relative to AnkD34. In the lower panel, the pose of AnkD34 that is closest to the mean of the 30 poses in the upper panel is shown docked with cdb3. The view in the lower panel is rotated ~90° from that shown in the upper panel in order to clearly see the positions of residues 160 and 254 on cdb3 and residues 598 and 631 on AnkD34 shown as silver balls at the binding interface. These residues showed high efficiency cross-linking with BMOE as shown in Fig. 41. Also shown as blue balls are residues 133, 151, and 181 on cdb3 and residues 590, 623, and 656 on AnkD34. These residues showed exchange and dipolar coupling upon complex formation as shown in Fig. 43. The β6/β7 hairpin loop is shown in red.

As shown in Fig. 39, the solution set of all top 30 models satisfies 20 DEER distances within the ±14 Å boundaries for the corresponding C_β-C_β distances with the mean violation of 7.4 Å. However, previously proposed Michaely model violated these boundaries for 4 distances, demonstrating that this model is not correct.

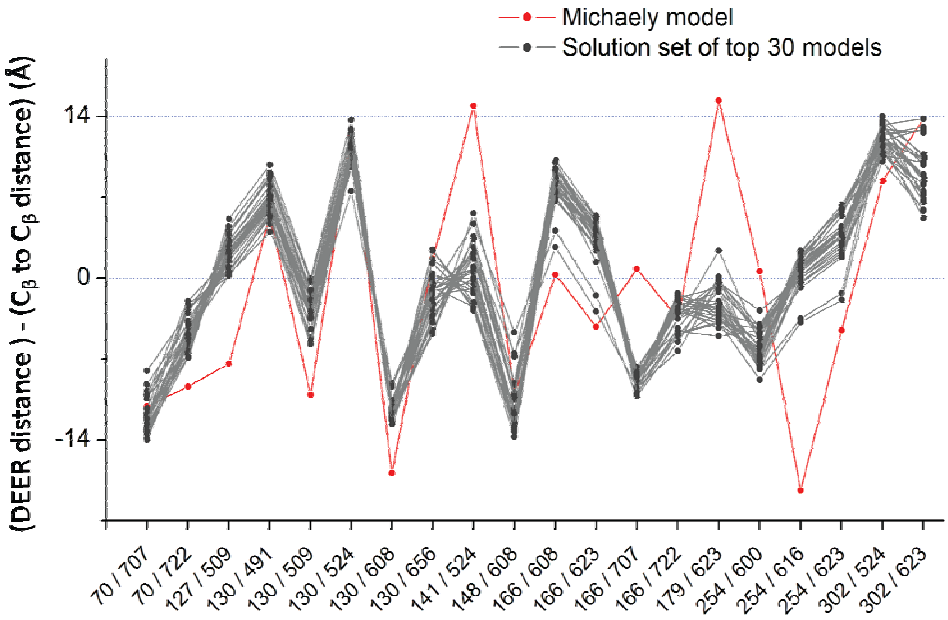

Figure 39. Distance differences between the DEER measurements and the corresponding C_β-C_β distances from the Michaely model (red) and the solution set of top 30 models (dark grey).

Surface electrostatic potentials of the binding interface

As mentioned earlier, observation of salt and pH independence of binding predicts that hydrophobic interactions might be the dominant forces associated with complex formation. The calculated surface electrostatic potential maps of the two proteins, as illustrated in Fig. 40, satisfies this hypothesis by showing approximately neutral electrostatic potentials on the predicted binding interface for both proteins. In particular, the concave groove region of AnkD34, which has been previously hypothesized to be the putative binding interface, exhibited the surface

with high density of electrostatic potentials and is unlikely to mediate the hydrophobic interaction. Likewise, the β6/β7 hairpin loop of cdb3, which presented considerable negative charges on its surface, appears not favorable for binding. These surface electrostatic potential maps further support the validity of the defined binding interfaces from each protein component and the solution set of structural models.

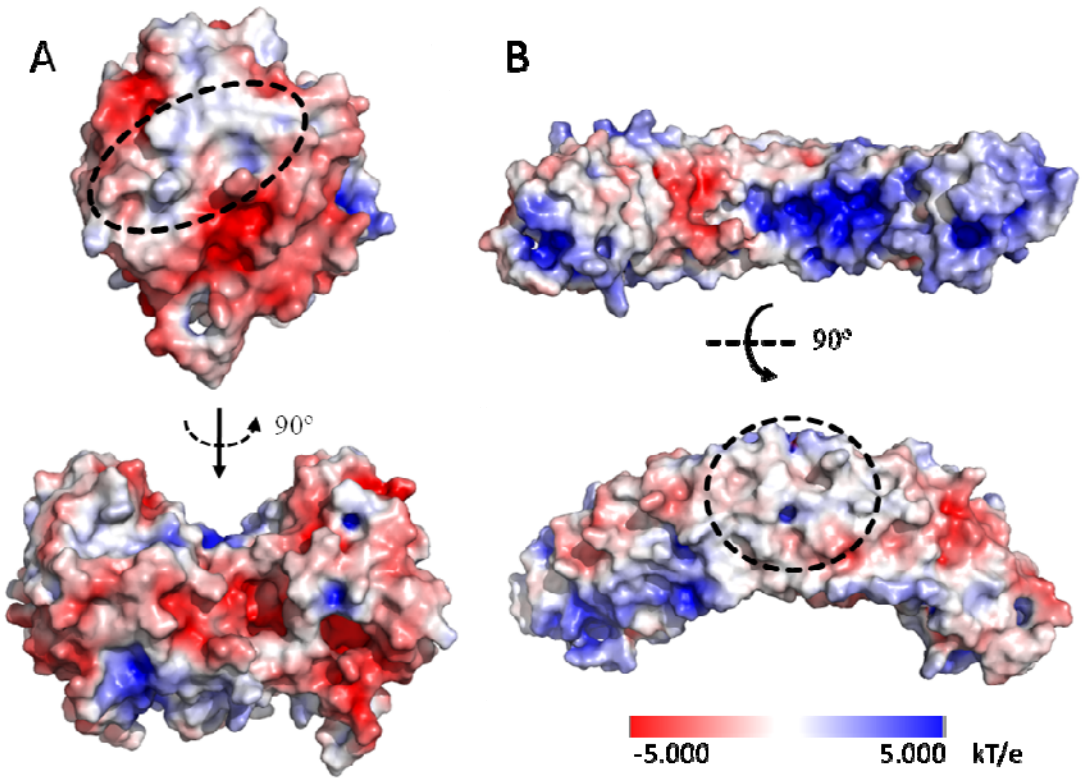

Figure 40. Surface electrostatic potentials mapped onto the crystal structures of cdb3 (panel A) and AnkD34 (panel B). The electrostatic potentials were calculated based upon the Poisson-Boltzmann equation using APBS (Adapted Poisson-Boltzmann Solver) software implemented on PyMol. The empirically defined binding interfaces are marked with black dashed lines.

Model validation.

The model of the complex in Fig. 38, bottom, predicts residues that are in close proximity at or near the binding interface. As a check on the validity of the models, two types of experiments were carried out. First, single Cys mutants of cdb3 at residues 160 and 254 were prepared. These residues are at the interface but do not inhibit complex formation as shown by the binding data in Fig. 38. Single Cys mutants of AnkD34 were made at residues 616, 619, and 623 on the back convex surface of repeat 19, at residue 613 on the short linker, and at residues 598 and 631 on the top convex surface. Residues 598 and 631, which are predicted by the model in Fig. 38, lower panel to be at the binding interface, do not interfere with complex formation as shown in Fig. 33. The model predicts that both residues 160 and 254 on cdb3 and residues 598

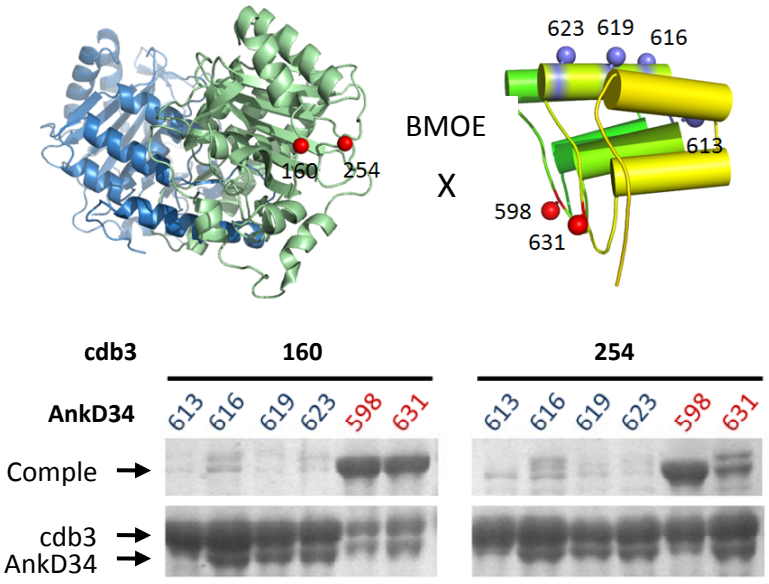

Figure 41. Chemical cross-linking of cysteine residues between single sites on cdb3 and at single sites on AnkD34. The models in Fig. 38 predict the residues that are at the protein-protein interface of the complex. These predictions were tested using the short cross-linking reagent BMOE. The SDS PAGE results confirm that residues 160 and 254 on cdb3 are in close proximity to residues 598 and 631 on AnkD34. However, residues 160 and 254 on cdb3 do not form cross-links with residue 613 in the linker region of AnkD34 or with residues 616, 619, or 623 on the back convex surface.

and 631 on AnkD34 are within 10 Å in the complex. It further predicts that residues 160 and 254 on cdb3 are greater than 20 Å from residues 613, 616, 619, and 623 on AnkD34. In order to test these predictions, the short cross-linking reagent bis-maleimidoethane (BMOE) was used to determine which pairs of cysteines could be cross linked and which could not. As shown by the SDS-PAGE gel in Fig. 29, residues 160 and 254 on cdb3 were efficiently cross-linked to residues 598 and 631 on AnkD34. However, no cross-links to residues 613, 616, 619, or 623 on AnkD34 were formed. The latter results not only agree with the model for the complex in Fig. 38, lower panel, but they also support the binding interface data for cdb3 and AnkD34. Fig. 42 illustrates that all top 30 models present relatively short C_β-C_β distances for four pairs of sites (indicated by red box in Fig. 42) that allowed the formation of BMOE-mediated cross-linked products. All those distances are in or close to the range of 4-12 Å, which are typical C_β-C_β distances that can

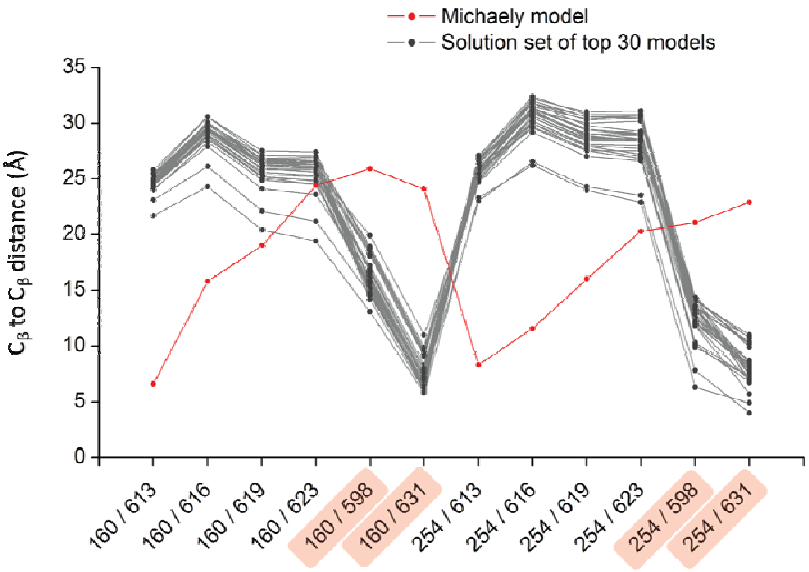

Figure 42. Comparison of C_β-C_β distances from the Michaely model (red line) and the solution set of top 30 models (grey lines) for the pairs of sites which have been used in cross-linking experiments.

afford BMOE-mediated cross-linking reactions. The same set of distances from the Michaely model shows that the observed cross-linked products cannot be formed in this model.

The second set of experiments involved measuring interprotein dipolar coupling between spin label pairs, one on cdb3 and the other on AnkD34. This was accomplished by placing a spin labeled side chain, one at a time, on cdb3 at residues 133, 151, and 181. All of these residues are near the binding interface based upon the model presented in Fig. 38, lower panel, introduction of a cysteine and spin labeling does not alter binding affinity (Fig. 29), and none shows significant changes in EPR lineshape upon complex formation. Similarly, spin labeled side chains were incorporated in AnkD34 at residue 590 on the 18^{th} ankyrin-Repeat, at residue 623 on the 19^{th} ankyrin-Repeat, and at residue 656 on the 20^{th} ankyrin-Repeat. Each of these residues is at structurally equivalent positions at the base of the outer helix of the respective ankyrin-Repeat motifs. The structural model for the complex presented in Fig. 38, lower panel, predict that a spin labeled side chain at residue 133 in cdb3 should be in close proximity (< 10 Å) to a spin labeled side chain at residue 590 in AnkD34, that a spin labeled side chain at residue 151 in cdb3 should be in close proximity to a spin labeled side chain at residue 623 in AnkD34, and a spin labeled side chain at residue 181 in cdb3 should be in close proximity to residue 656 in AnkD34. Fig. 43 shows that this is the case as strong exchange and dipolar coupling is observed for each of these three interprotein pairs. The models are also compatible with additional data which show weaker dipolar coupling between a spin labeled side chain at residue 133 on cdb3 and one at residue 623 on AnkD34 but no significant dipolar coupling to one on residue 656 on AnkD34. Similarly, the models predict weaker dipolar coupling between a spin labeled side chain at residue 151 on cdb3 and on residues 590 and 656 on AnkD34. Finally, the models predict very weak dipolar coupling between a spin labeled side chain at residue 181 in cdb3 and at residues 590 and 623 on AnkD34. The relevance of model prediction is more clearly illustrated in Fig. 44 where the C_β-C_β distances were compared between the Michaely model and the solution set of top 30 models for the pairs of sites which have been used in dipolar/exchange coupling experiments. All top 30 models show

relatively short C_β-C_β distances (approximately shorter than 20 Å) for the three pairs of sites which have shown strong dipolar/exchange coupled spectra; however, the Michaely model predicts that none of the pairs of sites are close to each other enough to present dipolar/exchange

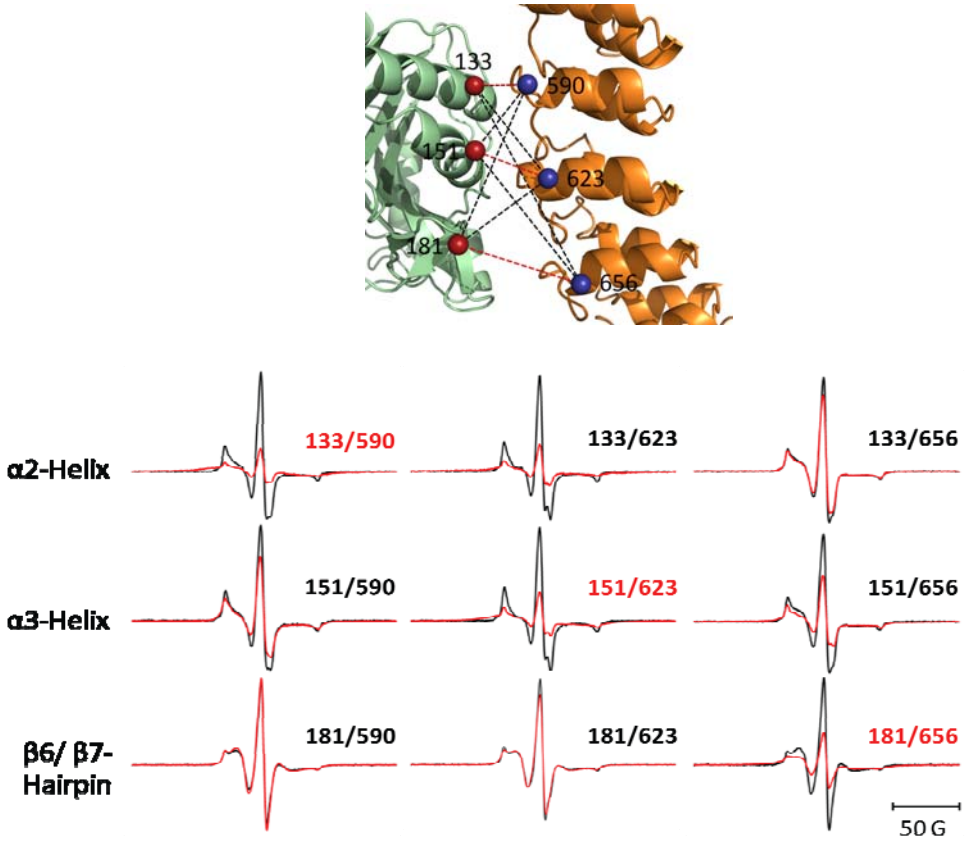

Figure 43. Exchange and dipolar coupling from pairs of labeled sites near the binding interface. The strong dipolar and exchange couplings were observed between spin label pairs in 133cdb3/590AnkD34, 151cdb3/623AnkD34, and 181cdb3/656AnkD34, all of which are predicted by the structural model in Fig. 38 to be at the binding interface between the two proteins. The models in Fig. 38 and in more detail, the lower panel, which presents one of those models with the pairs of sites for spin labeling, also predicts close proximity between two spin labels in 133cdb3/623AnkD34, 151cdb3/590AnkD34, and 151cdb3/656 AnkD34. However, it predicts much weaker dipolar interactions in 133cdb3/656AnkD34, 181cdb3/590 AnkD34, and 181cdb3/ 623AnkD34. The additional 6 EPR spectra confirm these predictions. Each EPR spectrum obtained from the complexes (red) was compared with the sum of spectra from the corresponding singly spin labeled constructs (black).

couplings reinstating that this model is not correct. Collectively, the cross-linking data and the dipolar coupling data verify that the models of the complex are able to correctly predict these experimental observations thereby adding confidence that many of the essential features of the models are correct.

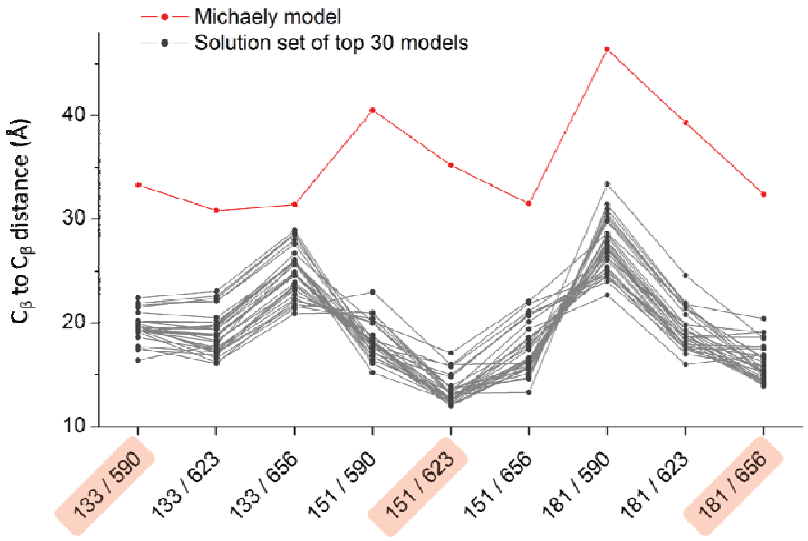

Figure 44. Comparison of C_β-C_β distances from the Michaely model and the solution set of top 30 models for the pairs of sites on or near the binding interface which have been used in the dipolar/exchange coupling experiments.

Local structural changes in the peripheral domain of cdb3

Dipolar couplings shown in CW-EPR and DEER distances, obtained from the pairs of spin labels attached at equivalent sites on the dimer interface confirmed that a cdb3 dimer undergoes no global structural change upon the complex formation. However, the possibility of local structural changes occurring on or near the peripheral binding interface cannot be excluded. In order to probe if binding to AnkD34 can induce such changes, multiple DEER distances were collected for pairs of sites residing around the binding interface as shown in Fig. 45 (top panel).

According to the constructed models, only residue 130 is on the binding interface while residues 166, 179, 302 are in proximity to, but not exactly on, the interface. In particular, a significant decrease in R1 side chain mobility observed in the EPR lineshpae of residue 130 suggests plausible changes in the conformation of the R1 side chain upon binding to AnkD34. Thus, the slight distance changes shown in 130/166 and 130/302 can be explained by repacking of the R1 side chain at residue 130. In accordance with the spin label mobility data and binding interface mapping, the DEER distance distribution from 166/302 was insensitive to binding. Collectively, these data indicate that a large peripheral area encompassing most of the binding interface is structurally stable to the binding reaction.

However, it is of particular interest to note the last three sets of DEER data in Fig. 45 which involve residue 179 on the β6/β7 hairpin loop. Though this loop is not at the binding interface, residue 179 exhibits some decrease in spin label mobility and NiEDDA accessibiltiy implying that the β6/β7 hairpin loop undergoes some local structural changes upon the complex formation. The substantial changes in distance distributions from the three doubly labeled mutants, 130/179, 166/179, and 179/302 demonstrate that there are the local conformational changes of the β6/β7 hairpin loop. Unlike the slight changes (less than 2 Å) from the DEER data involving residue 130, the DEER data from 130/179 and 166/179 presented more significant 4~5 Å alterations in the mean distances. Both internal conformational changes of the R1 side chain and backbone movement can contribute to the inter-spin DEER distances and they are typically not separable. Therefore, it is currently not clear if these distance changes involving residue 179 are associated with the backbone movement of the β6/β7 hairpin loop or just due to reorientation of spin label side chain at residue 179. In either case, the essential role of the β6/β7 hairpin loop in the complex formation, which was manifested by many lines of evidences (Chang and Low, 2003; Davis et al., 1989; Ding et al., 1996; Willardson et al., 1989) could be associated with the local structural changes of this loop observed in this study.

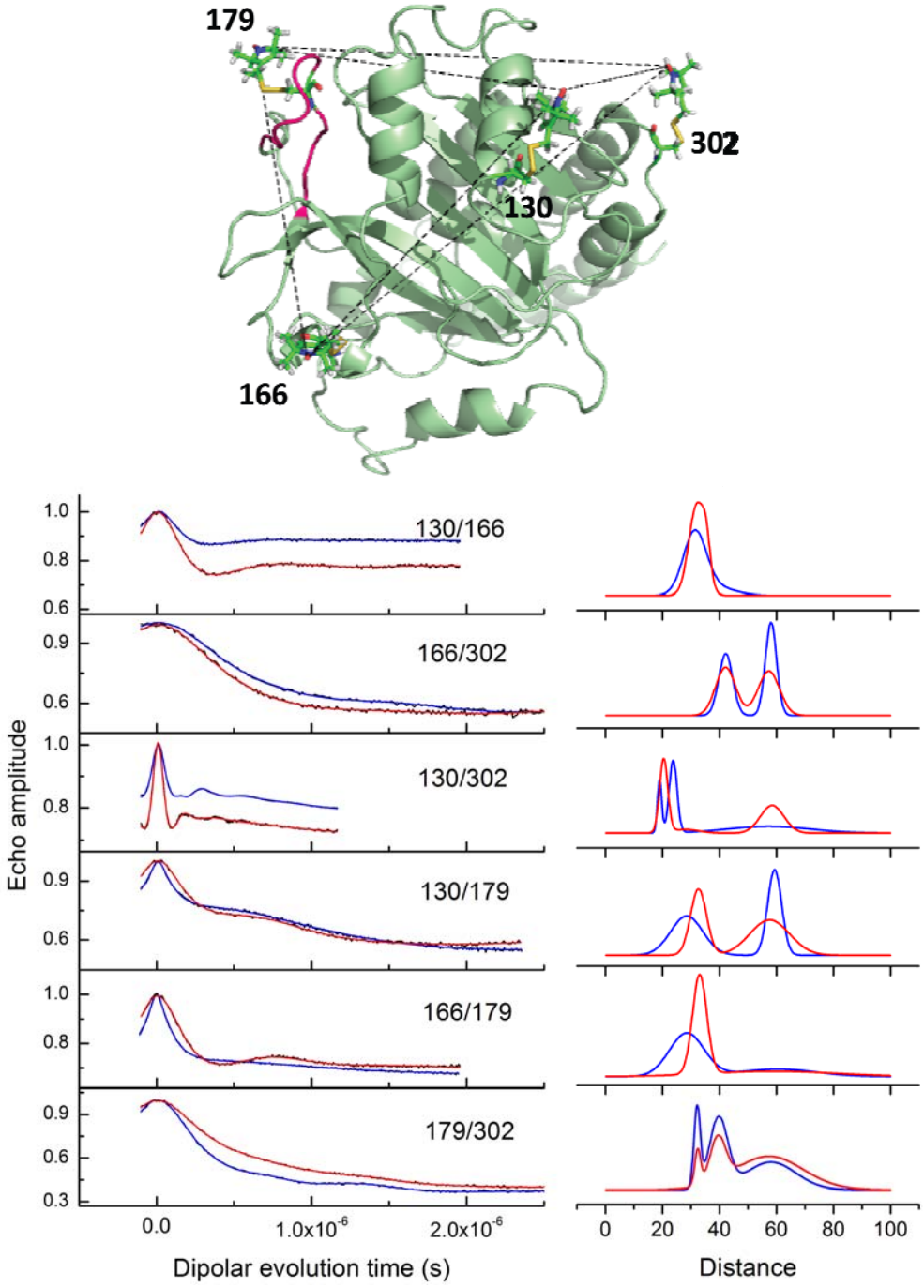

Figure 45. Intraprotein DEER distances around the binding interface of CDB3 with (red lines) and without (blue lines) molar excess of AnkD34. The top panel displays four sites used in DEER measurements with explicitly placed spin labels on them. The bottom panel exhibits DEER traces (left) and their corresponding distance distributions (right).

Discussion

Ankyrin as an adaptor protein that links the lipid bilayer to the cytoskeleton

The ankyrin family of adaptor proteins is able to recognize and bind to the cytoplasmic domains of a large number of intrinsic membrane proteins via their membrane binding domains (reviewed in (Bennett and Baines, 2001)) and thereby form a link between the cytosolic surface of the membrane and the underlying spectrin meshwork through binding of ankyrin to spectrin via its spectrin binding domain. Some of the ankyrin binding partners that have been reported include the Na^+/K^+-ATPases (Nelson and Veshnock, 1987), sodium channel β subunits (Malhotra et al., 2000), the cardiac Na^+/Ca^{2+} exchanger (Li et al., 1993), glycoprotein GP85 (Kalomiris and Bourguignon, 1988), nervous system cell adhesion molecules including neurofascin, L1, NrCAM, NgCAM, and neuroglian (Davis and Bennett, 1994), the InsP3 receptor (Bourguignon et al., 1993), clathrin (Michaely et al., 1999), and the ryanodine receptor (Bourguignon et al., 1995) in addition to the cytoplasmic domain of the anion exchange protein in erythrocytes (Michaely and Bennett, 1993). Interestingly, no clear patterns of which surfaces on ankyrin are involved in these many binding interactions and what structural elements on their target binding proteins serve for binding recognition have emerged (Mosavi et al., 2002). In fact, extensive data in the literature indicate that different surfaces of the ankyrin membrane binding domain can interact with different proteins. To date, there have been only a dozen structures determined at, or near, atomic resolution for many of the known complexes including those involving DARPins (Kohl et al., 2005; Kohl et al., 2003; Schweizer et al., 2007). Thus, it is of considerable interest to understand what the structures of representative members of these classes of complexes are and what drives the high affinity binding interactions which are essential to normal cellular function and organization.

AnkD34 binding interface of cdb3

The association of cdb3 with the AnkD34 region of the membrane binding domain of ankyrin-R has been examined in detail in previous biochemical and mutagenesis studies on cdb3 and on AnkD34. Studies on cdb3 have indicated that there are interactions of residues 1-75 in the unstructured N-terminal domain, and residues 118-141, 155-160, and 174-193 in the peripheral domain of cdb3 with AnkD34 (Davis et al., 1989; Davis et al., 1991; Ding et al., 1994; Ding et al., 1996; Wang et al., 1995; Willardson et al., 1989). The data in Figs. 30 and 31 and the binding data in Fig. 29 agree with these previous conclusions. The residues in and around α-helices 2 and 3 in the peripheral domain of cdb3 showed substantial changes in mobility and solvent accessibility upon complex formation as well as diminished binding affinity in pull-down assays. Also, spin labels at some positions in the β6-β7 hairpin loop showed spectral changes in agreement with previous work by site directed fluorescence labeling which showed modest changes in solvent accessibility when the complex with wt-AnkD34 was formed (Zhou, 2006). The collection of data presented clearly defined the binding interface as the horizontally extended area in the middle of the peripheral domain as presented in Figs.30 and 31, providing a relatively flat and hydrophobic surface (Fig. 40), which is highly complementary to the defined interface of ankD34 in terms of both shape and electrostatics. However, despite the spectral changes, the β6-β7 hairpin loop was excluded from the defined interface by the multiple interprotein DEER constraints, which will be discussed later.

In previous work, it has been shown that the N-terminal domain of cdb3, which is composed of residues 1-54, is dynamically disordered in solution with no observable interactions between this domain and the central folded domain of cdb3 (Zhou et al., 2005). However, when spin label side chains are placed at sequential positions along the central portion of the N-terminal domain, a signal with restricted motion is observed when cdb3 is bound to AnkD34 (data not shown). Previous studies have indicated a role for the N-terminal domain in the cdb3-AnkD34

interaction (Davis et al., 1989; Ding et al., 1994; Ding et al., 1996; Wang et al., 1995; Willardson et al., 1989). On the other hand, the models for the complex presented in Fig. 38 do not indicate any direct interactions between the peripheral domain of cdb3 and ankyrin-Repeats 22 and 23 even though previous studies have shown that these repeats are important for high affinity binding (Davis et al., 1991; Michaely and Bennett, 1995b). These results thus suggest that the N-terminal domain may be involved in interactions with ankyrin-Repeats 22 and 23. However, a cdb3 deletion mutant lacking the N-terminal domain was confirmed to retain the ability to bind AnkD34 in a previous study (Chang and Low, 2003) and in this study (data not shown), showing that the N-terminal domain is not necessary for binding AnkD34. Given that the N-terminal domain of cdb3 binds multiple intracellular proteins such as glycolytic enzymes to form a macromolecular complex in erythrocytes, stabilization of the N-terminal domain through its interaction with AnkD34 might have implications in organizing those binding partners. This working hypothesis needs to be tested in future studies.

Cdb3 binding interface of AnkD34 and structural models for cdb3-AnkD34 complex

Once the crystal structures for cdb3 (Zhang et al., 2000) and for AnkD34 (Michaely et al., 2002) became available, it was possible to construct docked structures for the complex using available rigid body docking software packages. Michaely and coworkers used FT-DOCK software (Gabb et al., 1997) to construct a model of the complex where the biochemical and mutagenesis data from previous studies served as a guide for orienting the two proteins relative to each other (Michaely et al., 2002). The proposed model showed extensive interactions of the peripheral domain of cdb3 including α-helices 2 and 3 with the ankyrin groove and bottom surfaces of ankyrin-Repeats 18-20 on the concave surface of AnkD34 and additional interactions between the β6-β7 hairpin loop with ankyrin-Repeats 22 and 23 (Michaely et al., 2002).

The models presented in Fig. 38 agree with the previous modeling work with regards to which ankyrin-Repeats in AnkD34 interact with the peripheral domain of cdb3. A previous study by Michaely and Bennett indicated that cdb3 binding to AnkD34 involves ankyrin-Repeats in the 13-18 range and in the 19-24 range (Michaely and Bennett, 1995). Specifically, this study showed that cdb3 did not bind to the separate domains of ankyrin-Repeats 13-18 (the AnkD3 domain) nor repeats 19-24 (the AnkD4 domain), both of which formed stable folded structural domains, suggesting the binding interface involved repeats that span the junction between the D3 and D4 domains. Consistent with this finding, the data in Figs. 32 and 34, indicate that ankyrin-Repeats 18-20, which span this junction, serve as primary sites of contact between cdb3 and AnkD34.

Indeed, many other proteins which contain ANK repeat-domains utilize the concave groove surfaces formed by inner helices and long linker to interact with their binding partners as revealed in co-crystal structures of the ankyrin complexes (e.g., (Katz et al., 2008; Nam et al., 2006; Truhlar et al., 2006)). Recently, the tips of the linker surface on the membrane binding domain of ankyrin-B, which contains many charged residues, has been shown by Mohler and coworkers to be involved in binding of the Na^+/Ca^{2+}-exchanger to the membrane binding domain of ankyrin-B in cardiomyocytes (Cunha et al., 2007).

However, the constructed models of the cdb3-AnkD34 complex do not agree with the interacting surface being located in the ankyrin groove and bottom surfaces of AnkD34 as seen in the previously proposed model (Michaely et al., 2002). By placing spin labeled side chains on all four surfaces of AnkD34 in the present work it was shown that the top linker surface of AnkD34 showed the most significant spectral changes as shown in Figs. 32 and 34 while the others did not. Moreover, spin labeled side chains incorporated into the tips of the loop regions in ankyrin-Repeats 16-21 (residues 600 and 633) showed no changes in side chain mobility or in solvent accessibility upon complex formation with wt-cdb3 (data not shown). Collectively, the present work provides direct new experimental evidence for a previously uncharacterized surface of AnkD34 being involved in binding to cdb3.

Construction of structural models of the complex

Site directed spin labeling, in conjunction with conventional CW-EPR and modern methods of pulsed dipolar EPR including DEER, has emerged as a powerful approach for determining the structures of protein complexes (e.g. Bhatnagar et al., 2010; Hilger et al., 2007; Park et al., 2006)). This methodology is applicable to determination of structural features of complexes of proteins in solution without the necessity of generating ordered single crystal samples of the complex as required by X-ray crystallography and is not limited by the size of the complex as NMR can be. Among several spectral observables, interspin distances are the most direct and powerful constraints that can be obtained from EPR for determination of the complex structures. However, the relatively long tether (approximately 6~7 Å) and the intrinsic flexibility of the spin label give rise to substantial uncertainty in its conformation relative to the protein backbone which complicates the application of inter-spin distances in model construction.

Recent work on the bacterial chemotaxis proteins CheA and CheW utilized long-range interprobe distance constraints obtained by pulsed EPR to guide the docking structure, avoiding explicit modeling of spin labels by adopting metric matrix distance geometry and a subsequent rigid body refinement process which is used in NMR studies (Borbat and Freed, 2007; Park et al., 2006). In another study where a similar site-directed spin-labeling approach has been used to determine the structure for the functional Na^+/H^+ antiporter dimer in a liposome, spin labels were modeled using a rotamer library and then the relative orientation of two monomers were determined by fitting the simulated DEER time traces to the experimental DEER data (Hilger et al., 2007).

In this study, solvent accessibility constraints were employed for the filtration of candidate models instead of explicit modeling of spin labels. As for the cdb3 dimer, the sites utilized in the interprotein DEER measurements were selected from the peripheral domain to minimize interference from the long intra-dimer DEER distances (generally longer than 60 Å). This selection led to the unavoidable inclusion of residues 70, 127, 130, and 254 from cdb3 and

residues 623 and 656 from AnkD34, which reside on the defined binding interface. R1 side chains attached at those sites are thus predicted to undergo significant changes in their local environment and concomitant rearrangement of R1 side chain conformation. The conformational spaces of the R1 side chain which can be explored by MD simulations from each crystal structure may not reflect the real conformation in the complex.

Previously, Perozo and his colleagues attempted direct incorporation of solvent accessibility constraints into the structure refinement of *Streptomyces lividans* potassium channel protein (KcsA) by calculating the interaction between a pseudoatom representation of the R1 side chain and solvent molecules using an empirical potential function (Sompornpisut et al., 2008). In terms of protein docking, however, it is notable that NiEDDA accessibility is considered as a relatively mild constraint since many factors such as the size effect of NiEDDA and the orientation of a spin label side chain will act as major determinants, especially for sites on the boundary of the binding interface. Under the basic assumption that solvent accessibility will be minimized for the sites on the binding interface, all the poses that passed the distance constraints were ranked with increasing sum of SAS (solvent accessible surface) area for the sites on the defined binding interface and top 20 models were represented as the solution set (described in Materials and Methods). However, despite these weaknesses, the solution set of models proves

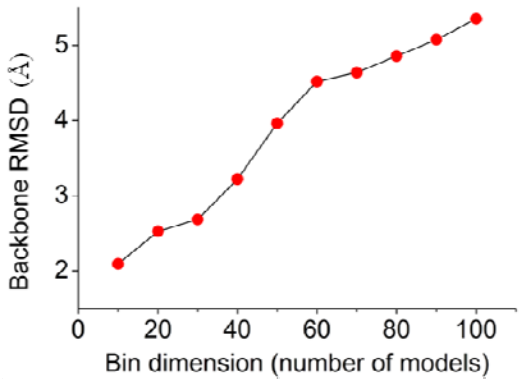

Figure 46. Mean backbone RMSDs of the models in bins with increasing bin dimension.

well justified by providing binding interfaces which are generally in a good agreement with interface mapping data and a considerably lower RMSD value.

Local structural changes induced by the complex formation and the β6-β7 hairpin loop of cdb3

Studies by Chang and Low (Chang and Low, 2003) indicated that the β6-β7 hairpin loop on cdb3 was essential for binding to AnkD34. Specifically, replacing the entire loop composed of residues 175-185 with a diglycine bridge greatly reduced binding affinity to levels essentially the same as reported for the kidney isoform of cdb3. Replacement of the loop with the diglycine bridge did not result in any significant global disruptions of the structure of cdb3 as judged by pH induced conformational changes, by binding to protein 4.1, and by binding of the N-terminus to glycolytic enzymes. The role of this loop was later tested in an *in vivo* mouse model (Stefanovic et al., 2007) where again results indicated a role for the β6-β7 hairpin loop in ankyrin binding.

The model in Fig. 38, lower panel, does not indicate a direct interaction between the β6/β7 hairpin loop of cdb3 and AnkD34 even though changes in spectroscopic observables suggest that this loop senses the binding interaction. None of the other 29 poses shown in Fig. 38, upper panel, indicate a direct interaction either. It is possible that this loop is necessary for structural rearrangements of residues on cdb3 that are at the protein-protein interface. It should be emphasized that even though the data in Figs. 27 and 28 demonstrate that there are no significant global structural changes in either cdb3 or AnkD34 upon complex formation, it is likely that there are side chain rearrangements and possibly small changes in positioning of secondary structural elements of both proteins at the binding interface. The changes in DEER distance distributions upon complex formation revealed in Fig. 45 also support this notion. Such localized changes could lead to additional interactions that are not revealed using rigid body docking as a first approximation for determining the major features of the structure of the complex. Thus, it will

require additional refinement of the rigid body docked structures using molecular dynamics approaches in order to draw final conclusions about the exact role of the β6-β7 hairpin loop in the binding interaction.

Insights into the structural models of Cdb3-AnkD34 complex in erythrocytes

Two cdb3 dimers may bind to ankyrin-R, one to AnkD2 and the other to AnkD34, either separately (Michaely and Bennett, 1995) or as a tetramer (Michaely et al., 2002). The models in Fig. 38 showing how one cdb3 dimer binds to AnkD34 likely preclude the possibility that the second cdb3 dimer could simultaneously bind to AnkD2 and the first cdb3 dimer in the orientation consistent with the previously proposed tetramer structure (Zhang et al., 2000) unless: 1) there is a significant structural rearrangement of the membrane binding domain as a result of binding two dimers of cdb3 or 2) the major binding interaction between cdb3 and the AnkD2 domain involves the extended N-terminus of cdb3. Further studies on the structure of the complex formed between cdb3 and the AnkD2 domain or studies on binding two dimers to the full length membrane binding domain will be required to discriminate between these two possibilities.

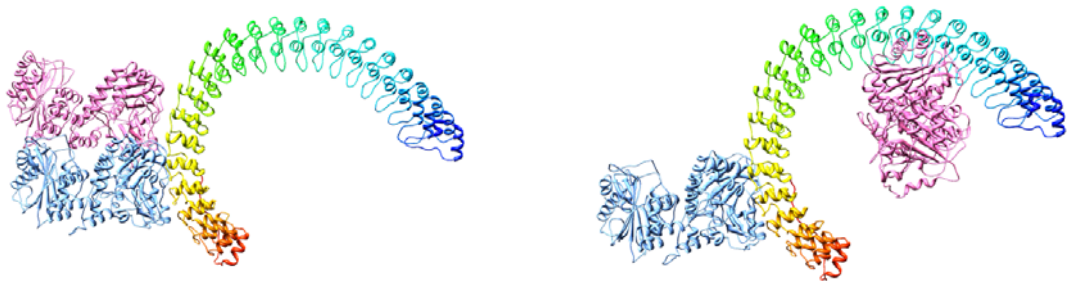

Figure 47. Two schematic cartoon presentations showing the possible arrangements of two cdb3 dimers that bind the membrane binding domain of ankyrin-R (D1–D4). Top model displays the formation of 'true tetramer' of cdb3 where two cdb3 dimers interact with each other and one of them (colored in blue) binds D34 region of ankyrin. In this model, the unstructured N-terminal region of the other cdb3 dimer, which is not shown in the figure, can be speculated to bind the D2 region of ankyrin-R. The bottom model features the 'dimer of dimer arrangement' of two cdb3 dimers in which one (colored in blue) binds to D34 and the other (colored in magenta) to D2.

APPENDIX

STRUCTURE OF THE CALCIUM BINDING DOMAIN OF NCX1.1

CHAPTER A1

Introduction

Excitation-Contraction Coupling in Cardiac Muscle Cells

Excitation-contraction (EC) coupling is the process whereby an action potential triggers myocytes to contract. It is well known that calcium ions play a pivotal role in cardiac EC coupling (reviewed in (Bers, 2002; Bers and Guo, 2005)). Upon membrane depolarization, Ca^{2+} ions enter the cell through L-type Ca^{2+} channels (or dihydropyrodine receptors [DHPRs]) located on the sarcolemma. The elevated level of intracellular Ca^{2+} concentration ($[Ca^{2+}]_{in}$) triggers a subsequent release of Ca^{2+} that is stored in the sarcoplasmic reticulum (SR) through Ca^{2+}-release channels, ryanodine receptors (RyRs), which increases local $[Ca^{2+}]_{in}$ from about 200–400 μM. The L-type Ca^{2+} channel and RyR are colocalized to form a local calcium signaling complex called a couplon that is specialized to enhance Ca^{2+} induced Ca^{2+} release by providing the RyR its maximum sensitivity for its ligand. The resultant rise in $[Ca^{2+}]_{in}$ binds to, and activates proteins in the myofilaments to produce cardiac contraction. First, the free Ca^{2+} binds to troponin-C that is a part of the regulatory complex attached to the thin filaments. Calcium binding induces a conformational change in the regulatory complex and troponin-I exposes a site on actin that is able to bind to the myosin ATPase located on the myosin head. The subsequent ATP hydrolysis provides the energy required for the conformational change which results in a movement

("ratcheting") between myosin heads and actin, so that the actin and myosin filaments slide past each other. Ratcheting cycles iterate as long as the $[Ca^{2+}]_{in}$ remains elevated. To allow cardiac muscle to relax, $[Ca^{2+}]_{in}$ must decline quickly to the basal level. This calcium removal process is performed mainly by the SR Ca^{2+}-ATPase (SERCA) which pumps cytosolic Ca^{2+} back into the SR, and the Na^{+}/Ca^{2+} exchanger (NCX) which extrudes Ca^{2+} out of myocytes. As $[Ca^{2+}]_{in}$ falls back to the basal level, the troponin complex undergoes conformational changes that render troponin-I able to inhibit actin-myosin binding. Replacement of ADP with a new ATP in the myosin head closes the cycle and the initial sarcomere length is restored.

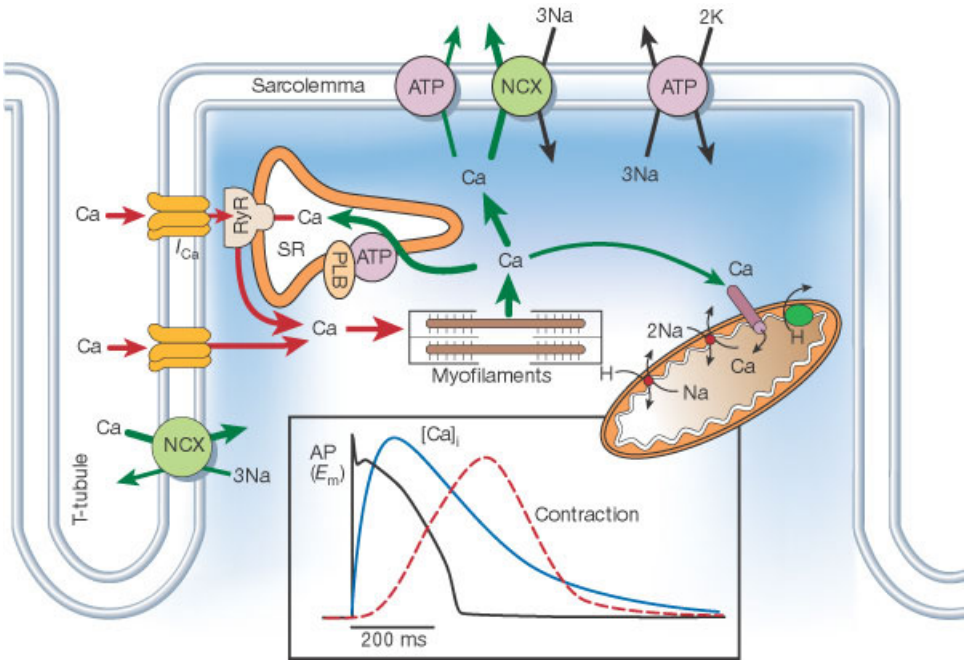

Figure 48. The mechanism of EC coupling and the involved Ca^{2+} pathway in myocytes. The inset shows the time-dependent changes in intracellular Ca^{2+} concentrations and contractions induced by the action potential. The flow of Ca^{2+} ions during the depolarization and relaxation of myocytes are indicated by red and green arrows, respectively.

The Na^+/Ca^{2+} exchanger family and NCX1 isoforms

NCX1 belongs to the SLC (solute carrier) 8 gene family, which is part of a larger superfamily of related Ca^{2+}/cation antiporter genes, known as the CaCA superfamily (Cai and Lytton, 2004). This superfamily comprises five major branches including NCX (SLC8) and NCKX (SLC24), both of which contain almost exclusively vertebrate members. The common structural feature of transporters from the CaCA superfamily reside in their membrane topology, where two clusters of five transmembrane helices are joined by a cytoplasmic loop of varying size. Importantly, each cluster contains a signature motif, the α-repeat (Schwarz and Benzer, 1997), which is known to be critical for the transport function of both NCX1 and NCKX2 transporters. Two α-repeats from each hydrophobic cluster are oppositely oriented in terms of the membrane and associate with each other, forming the ion-binding pocket of exchangers (Iwamoto et al., 2000; Kinjo et al., 2007).

Mammals express three members of the NCX (SLC8) family, NCX1, NCX2, and NCX3. NCX1 is predominantly expressed in heart, brain, and kidney, but also distributed in almost all other tissues at lower levels. The other members of the family show a much more restricted pattern of expression. NCX2 is almost exclusively found in neurons in brain while NCX3 is expressed in skeletal muscle and at lower levels in some brain regions.

The tissue-specific distribution of NCX1 isoforms is the consequence of alternative splicing where different combinations of 6 exons (denoted as exons A, B, C, D, E, and F) constitute the long cytoplasmic loop of NCX1 isoforms. Exons A and B are expressed in a mutually exclusive manner while the other 4 exon cassettes are randomly inserted (Kofuji et al., 1994). The splice variant of NCX1.1 (exons ACDEF) is the dominant form in heart, while the other variants NCX1.3 (exons BD) and NCX1.4 (exons AD) are typically found in kidney and brain, respectively. No difference was observed in regulatory property between heart and brain splice variants which show typical Ca^{2+} regulation. However, the kidney splice variant is

insensitive to regulatory Ca^{2+} which releases the exchanger from Na^{+}-dependent inactivation (Dyck et al., 1999).

Transport Function of NCX1 and its Regulation

Ion exchange function of NCX1

Na^{+}/Ca^{2+} exchange is the main Ca^{2+} efflux mechanism across the plasma membrane of cardiomyocytes that reestablishes resting levels of Ca^{2+} after muscle contraction. The transport function is fully reversible, so the direction of ion movement depends on the ion gradients and the number of ions that are transported. Under normal physiological conditions, NCX1 extrudes one Ca^{2+} ion for influx of 3 Na^{+} ions using the electrochemical Na^{+} gradient provided by Na^{+}/K^{+} ATPase (Kang and Hilgemann, 2004). The current model of the transport mechanism proposes a

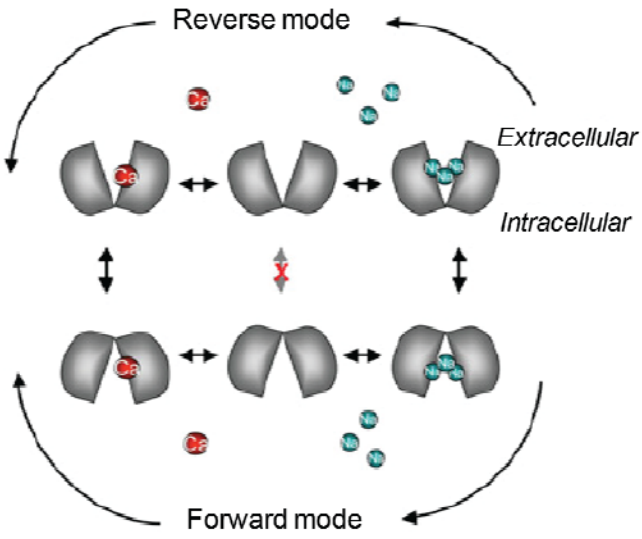

Figure 49. The transport cycle of NCX1. The empty exchanger is shown to bind either one Ca^{2+} ion or three Na^{+} ions, in a mutually exclusive manner. Either binding event allows a conformational change that reorients the accessibility of the ion-binding site across the membrane barrier.

cycle of sequential events that consists of binding, conformational changes, and release steps as shown below (Blaustein and Lederer, 1999). This model also involves a single ion-binding site that can bind either three Na^+ ions or one Ca^{2+} ion in a mutually exclusive manner.

Regulation of channel activity by ions

The transport site of NCX1 shows different binding affinities for intracellular and extracellular ion ligands. An apparent affinity in the low micromolar range for cytoplasmic Ca^{2+} prevents NCX1from being fully activated until $[Ca^{2+}]_{in}$ rises well above the resting level while an apparent affinity of 10-20 mM for Na^+ is close to or slightly higher than the resting $[Na^+]_{in}$. However, when the transport site faces outward, the apparent affinities for $[Ca^{2+}]_{ex}$ and $[Na^+]_{ex}$ become markedly higher, which are approximately 1 and 60-80 mM, respectively (Matsuoka and Hilgemann, 1992). Hence the overall kinetic rate of the exchanger under normal resting conditions is determined by occupancy of the cytoplasmic Ca^{2+}- binding sites.

Regulation of NCX1 activity by Ca^{2+} was first observed using dialyzed squid axon, and then in patch-clamped myocytes and giant excised patches. Several later studies have found that the long cytoplasmic loop is associated with regulation of exchange activity by $[Ca^{2+}]_{in}$. Treatment of the excised patches with chymotrypsin lead to removal of Ca^{2+} regulation (Hilgemann, 1990). Patch experiments using a series of mutant NCX1s revealed that acidic clusters within the central cytosolic loop are essential to Ca^{2+} regulation (Levitsky et al., 1994; Matsuoka et al., 1995).

The two major intrinsic regulatory properties of the Na^+/Ca^{2+} exchangers are Na^+-dependent inactivation and Ca^{2+} regulation. These are readily observable in the giant excised patch experiments (Hilgemann, 1990) as illustrated in Fig. 50. Unlike Ca^{2+} regulation, a high level of $[Na^+]_{in}$ has an inhibitory effect on exchange activity. This Na^+-dependent inactivation results in a characteristic pattern of outward Na^+/Ca^{2+} exchange current, which features a significant decline with time to a steady-state level following the rapidly developing current upon

the application of Na^+ in excised patches. Initially, this process was proposed to be triggered by Na^+-binding to the cytoplasmically oriented transport site. However, the current view supports an alternative model where Na^+ interacts with a regulatory site distinct from the transport site, called XIP (exchange inhibitory peptide) (DiPolo and Beauge, 2006). The XIP region is located on the N-terminal region of the cytosolic loop and consists of a 20 residue segment which is rich in hydrophobic and basic amino acids. The other regulatory mechanism, Ca^{2+} regulation, is mediated by the large intracellular loop. Binding of Ca^{2+} to distinct high-affinity sites on this loop activates the exchange activity in a concentration-dependent manner and also eliminates Na^+-dependent inactivation. However, these two different regulations by intracellular Ca^{2+} appear to be performed independently.

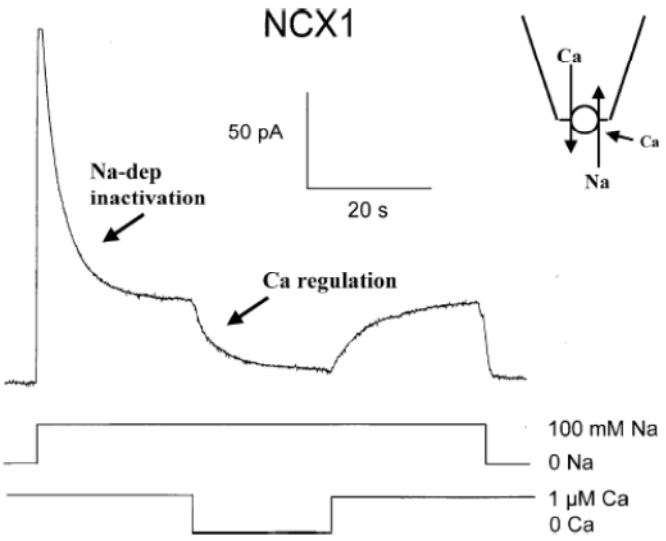

Figure 50. Regulation of the Na^+/Ca^{2+} exchanger by Na^+ and Ca^{2+} demonstrated by outward Na^+/Ca^{2+} currents generated across a giant patch excised from an oocyte expressing NCX1. The current is initiated by the rapid application of Na^+ into the bath at the intraculleular surface. Current peaks and then partially inactivates (Na^+-dependent inactivation). The Na^+/Ca^{2+} exchanger also requires submicromolar levels of regulatory Ca^{2+} in the bath for activation (Ca^{2+} regulation).

Regulation of channel activity by metabolites

During the early 90's, Hilgemann and co-workers found that ATP has an ability to activate exchange activity from giant excised patch preparations (Collins et al., 1992; Hilgemann et al., 1992). This ATP upregulation was observed to require the simultaneous presence of Mg^{2+} and also to be dependent on vanadate. The later studies have shown that this stimulation of NCX1 by Mg·ATP is predominantly mediated by the production of phosphatidyl inositol-4,5-bisphosphate (PIP_2) (Hilgemann and Ball, 1996). Thus the findings that ATPγS can upregulate the exchanger even in the absence of vanadate (Berberian et al., 1998) strongly suggest that vanadate may play a role in inhibiting the phosphatase associated with PIP_2 hydrolysis. Further experiments demonstrated that PIP_2 can directly bind to NCX1 (Asteggiano et al., 2001) and the XIP region of the intracellular loop is the binding site involved in PIP_2 upregulation, implying that the Mg·ATP and PIP_2 stimulation is mediated by alleviating Na^+-dependent inactivation (He et al., 2000). Consistent with this model, mutations of key residues in the XIP region showed reciprocal effects on Na^+-dependent inactivation and PIP_2 activation.

Regulation of channel activity by binding partners

Much evidence has been reported that interactions with other proteins are associated with modulation of NCX1 function. Recently, a study using ankyrin B-knockout heterozygous mice showed that ankyrin deficiency impaired stability, expression and localization of NCX1 (Cunha et al., 2007; Mohler et al., 2005).

Schulze *et al.* (Schulze et al., 2003) demonstrated an association between Na^+/Ca^{2+} exchanger and a macromolecular complex including protein kinase A, protein kinase C, protein phosphatase 1, protein phosphatase PP2A, and muscle protein kinase A-anchoring protein (mAKAP). Phospholemman (PLM), known as a modulator of Na^+/K^+-ATPase activity in various tissues, binds to the cytosolic loop of NCX1 through its C-terminal cytosolic tail upon being phosphorylated resulting in inhibition of NCX1 function (Wang et al., 2006; Zhang et al., 2006).

Another example of a protein-protein interaction that regulates NCX1 can be seen in Caveolin-3, an isoform of caveolins, which has been implicated in the regulation of normal cardiac function, and observed to be one of the proteins that associates with NCX1 (Bossuyt et al., 2002). Yeast two-hybrid screening approaches also identified calcineurin (Wang et al., 2006; Zhang et al., 2006) and protein 14-3-3 (Pulina et al., 2006) as other NCX1 binding partners, both of which have been observed to inhibit NCX1 upon binding.

Topology and structure of NCX1

Though the Na^+/Ca^{2+} exchanger was first described in squid axon and mammalian heart four decades ago, the canine cardiac Na^+/Ca^{2+} exchanger gene was cloned in 1990 and denoted as NCX1 (Nicoll et al., 1990). The translated polypeptide is matured by signal peptide (N-terminal hydrophobic segment of 32 amino acids) cleavage and glycosylation at the first extracellular segment at the N-terminus. A biochemically derived topology model of NCX1 predicts nine transmembrane α-helices, and a large cytosolic loop of about 500 residues (residues 217~705) between helices 5 and 6. This cytosolic loop consists of a tandem array of two CBDs (calcium binding domains) and the linker domain (residues 217–370 and 651–705) called the CLD (catenin-like domain). The CLD flanks the CBDs and link them to the transmembrane domain as shown in Fig. 51, below. The two structurally homologous Ca^{2+} binding domains, CBD1 and CBD2, are independently folded units, and connected by a short linker. They sense cytoplasmic Ca^{2+} levels by binding regulatory Ca^{2+} ions and account for the full Ca^{2+} regulation activity in the exchanger. The designation CLD is derived from its sequence homology with the cadherin adhesion molecule α-catenin (Hilge et al., 2006); however, any functional and structural information is not yet known for this domain. A segment of the N-terminal region of the CLD

forms the XIP domain which is responsible for Na^+-dependent inactivation and is predicted to be in proximity with the ion transport site of the transmembrane domain.

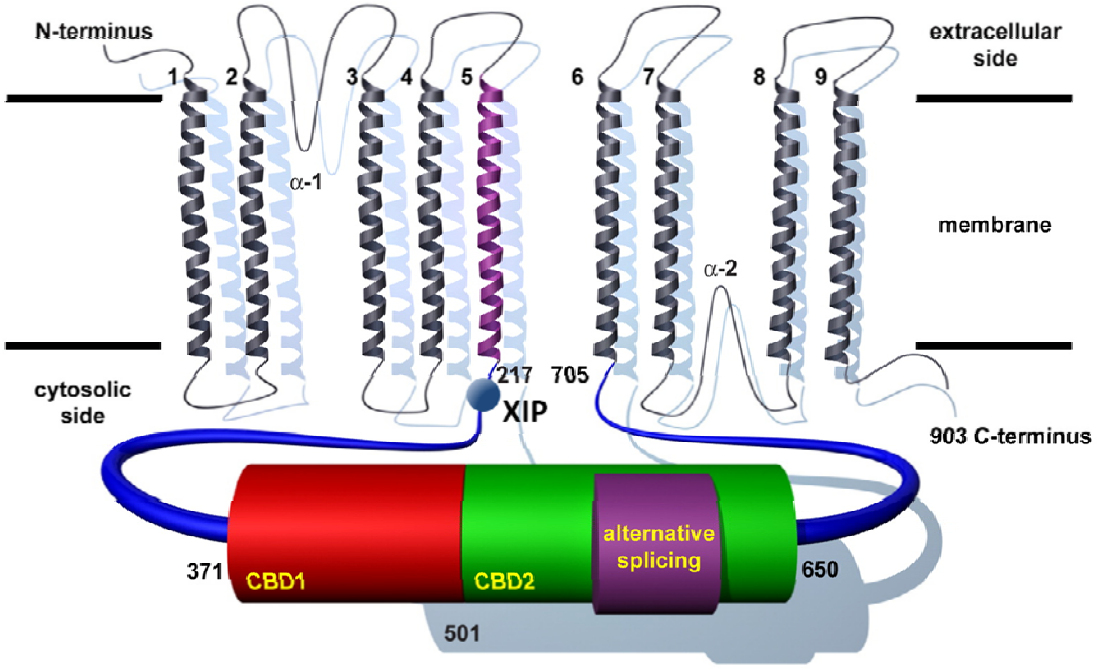

Figure 51. Topology model of NCX 1.4. The four NCX domains are depicted in unique colors: TM, gray; CLD, blue; CBD1, red; and CBD2, green. TM helix 5 and the region subjected to alternative splicing are displayed in violet. Boundaries of the domains are indicated by residue numbers and are based on the NCX1 AD-splice variant.

The membrane domain of NCX1

Despite a lack of structural information at the atomic level, a range of studies have determined the precise topology of the transmembrane domain of NCX1. Like other members of the CaCA superfamily, NCX1 comprises two hydrophobic clusters joined by a long intracellular loop which is encoded in a combination of 6 exons. The current model proposes 5 transmembrane helices in the N-terminal cluster and 4 in the C-terminal cluster (Iwamoto et al., 1999; Nicoll et al., 1999).

The two conserved α-repeats from each cluster are oriented in opposite directions with respect to the membrane, with their central regions between two transmembrane helices forming reentrant loops (Iwamoto et al., 2000; Nicoll et al., 1999). Cross-linking experiments have shown that helices 2, 3, 7, and 8, which are located in or around the α-repeats, are in proximity with one another (Qiu et al., 2001; Ren et al., 2006) as shown in Fig. 52. It has been suggested that the two α-repeats are near one another in the folded protein so that they can work in concert to form the ion conduction pathway. A study using NCX1 mutants where a set of residues on the α-repeats were mutated has confirmed that this region is pivotal to ion binding and transport. There are two critical acidic residues in each repeat (Iwamoto et al., 2000; Nicoll et al., 1996). In a subsequent mutational study on the α1 repeat, transmembrane helix 3, rather than the reentrant loop, was observed to be more directly involved in binding and transport of Na^+ ion (Ottolia et al., 2004). Taken together, it seems highly probable that the two highly conserved α-repeats form a pathway for the transport of ions across the membrane though its molecular mechanism still remains unknown.

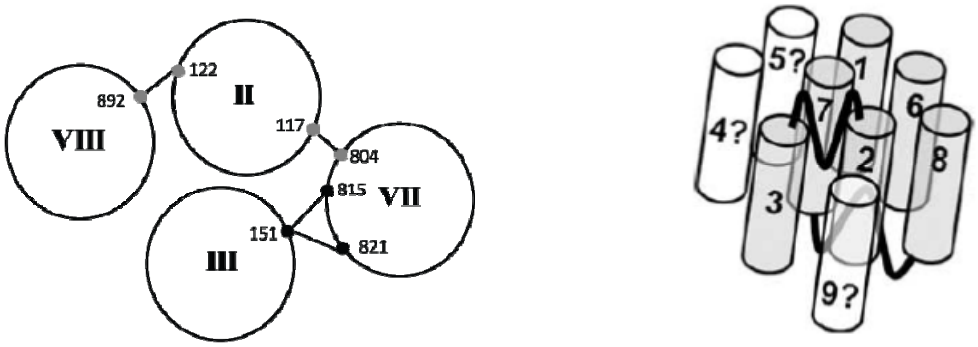

Figure 52. Helix packing of transmembrane segments in NCX1. The left panel is a diagram that shows a possible arrangement of transmembrane segments 2, 3, 7, and 8 with the pairs of sites that yielded disulfide bond formation in cross-linking experiments. Sites indicated by black-filled circles are modeled to be near the intracellular surface, whereas sites indicated by grey-filled circles are modeled to be in proximity with the extracellular surface. The right panel is the hypothetical topology of transmembrane domains that were examined for their intramolecular interactions are colored in grey.

The cytoplasmic domain of NCX1

Electrophysiological and mutational studies have indicated that the regulation of NCX1 function is primarily mediated by the long cytoplasmic loop region. More recent studies have identified the XIP and clusters of acidic residues as critical elements in the cytoplasmic loop. However, lack of structural information has slowed understanding of underlying molecular mechanisms of NCX1 function and its regulation. However, crystal and NMR structures of the isolated CBDs have been determined recently at atomic resolution as listed in Table 9, below. However, due to the large size of the two tandem Ca^{2+} binding domain (more than 500 amino acid residues), which makes NMR studies challenging, and the presence of flexible regions, which make crystallization difficult, currently available structures are limited to the two isolated fragments that can bind to regulatory Ca^{2+}, CBD1 (residues 357-500) and CBD2 (residues 501-650). The full length cytoplasmic loop of NCX1 contains not only the two Ca^{2+} binding domains

Table 9. Structures of CBDs determined at atomic resolution using X-ray crystallography or NMR

PDB code	Protein	Domain	Ca^{2+}	Source	Structure	References
3EAD	CALX	CBD1	+	Drosophila	X-ray	(Wu et al.)
3E9T	CALX	CBD1	-	Drosophila	X-ray	(Wu et al.)
3E9U	CALX	CBD2	-	Drosophila	X-ray	(Wu et al., 2009)
2KLT	NCX1.3	CBD2	-	Canis	NMR	(Hilge et al., 2009)
2FWS	NCX1.4	CBD1	+	Canis	NMR	(Hilge et al., 2006)
2FWU	NCX1.4	CBD2	+	Canis	NMR	(Hilge et al., 2006)
3GIN	NCX1.1	CBD1	+	Canis	X-ray	(Chaptal et al., 2009)
2DPK	NCX1.1	CBD1	+	Canis	X-ray	(Nicoll et al., 2006b)
2QVK	NCX1.4	CBD2	-	Canis	X-ray	(Besserer et al., 2007)
2QVM	NCX1.4	CBD2	+	Canis	X-ray	(Besserer et al., 2007)
2KLS	NCX1.4	CBD2	-	Canis	NMR	(Hilge et al., 2009)

but also the previously described XIP region, and N- and C-terminal loops. The function of the CLD ('catenin-like domain'(Hilge et al., 2006) described above, in particular, remains elusive.

Structure of CBD1 Atomic level (Crystal or NMR) structures of CBD1 have been obtained from three different isoforms, NCX1.1, NCX1.4 (canine), and CALX (Drosophila) to date. Even CALX, which has 60 % sequence homology with NCX1.1, exhibits practically identical crystal structure with the others (Wu et al., 2010), demonstrating that CBD1 is structurally well conserved throughout the different isoforms. CBD1 has a classical immuno-globulin fold, where two antiparallel β-sheets consisting of strands A-B-E and strands D-C-F-G forms a β-sandwich motif. Strands A and G are partly disrupted by a β-bulge and cis-proline, respectively, which appear to prevent them from forming intermolecular hydrogen bonding and then consequent interaction. The Ca^{2+}-bound from of the CBD1 crystal structure displays four Ca^{2+} ions positioned in a planar cluster where multiple acidic residues tightly coordinate Ca^{2+} ions. The binding region consists of multiple loops including the C-terminus (D498, D499, D500), A-B loop (E385), C-D loop (D421), and E-F loop (D446, D447, I449, E451, E454). Consistently, mutations in these residues lead to significant decreases in Ca^{2+} affinity (Hilge et al., 2006; Ottolia et al., 2004). Interestingly, the crystal structure of the E454K-CBD1 mutant showed that lysine substitution replaces a Ca^{2+} at position 1 resulting in full exchange activity in a charge compensation mechanism (Chaptal et al., 2009). Furthermore, mutations of key residues that coordinate Ca^{2+} at positions 1 and 2 failed to modulate exchange function in the same study, implying that Ca^{2+} ions at positions 3 and 4 are the primary Ca^{2+} ions that are responsible for Ca^{2+} regulation.

Two independent NMR studies revealed the structure of the apo form of CBD1 (Hilge et al., 2006; Johnson et al., 2008). In both studies, Ca^{2+} removal resulted in the most significant changes in the binding region, which were found to be unfolded due to the charge repulsion

between acidic residues. Based upon NMR parameters such as amide chemical shift change and residual dipolar coupling (RDC), the effect of Ca^{2+} removal was defined to be restricted to the binding region even though it appears that Ca^{2+} binding can be sensed by some distant residues away from the binding region. In addition, the long F-G loop and C-terminus were also observed to be in a more dynamic state in the apo form of CBD1 with low S^2 values.

Structure of CBD2 Due to the presence of the 35 residue-long, extra region of the F-G loop in CBD2 from NCX1.1 resulting from expression of 5 of the 6 possible splice variant exons, crystal or NMR structures of CBD2 have been determined only for the shorter NCX1.4 (Besserer et al., 2007) and CALX (Wu et al., 2009). The basic structural frame in CBD1 is well maintained in CBD2, which features an immunoglobulin fold with a β-sandwich motif formed by two antiparallel β-sheets. Even two β-bulges located in strand A and G are also seen in the CBD2 structure. The long F-G loop, which is located oppositely from the Ca^{2+} binding region, was not resolved in the crystal structure, suggesting this region is in a highly dynamic state. The main structural difference between the two domains is noted in the Ca^{2+} binding region, where the Ca^{2+} binding region of CBD2, unlike CBD1, coordinates only two Ca^{2+} ions. Based on Ca^{2+} binding affinity, coordination patterns, and mutational analysis, two Ca^{2+} binding sites were distinguished as primary and secondary sites (Besserer et al., 2007). While impaired Ca^{2+} binding at the secondary site did not influence NCX1 function, when the key residues that are involved in Ca^{2+} binding at the primary site were mutated, NCX1 entirely lost two characteristic Ca^{2+} regulatory functions, $[Ca^{2+}]_{in}$–dependence of exchange function and Na^{+}-dependent inactivation. Given that mutations that impaired primary Ca^{2+} binding in CBD1 just lowered the apparent Ca^{2+} affinity, but none of them was able to eliminate Ca^{2+} regulation, it is speculated that Ca^{2+} binding at the primary site in CBD2 presumably plays an essential role in Ca^{2+} regulation.

Another distinct feature seen in the crystal structure of CBD2 is that the effect of Ca^{2+} binding on the structure is much smaller than in CBD1. The only structural difference between

the bound and apo form of CBD2 is a small shift of the Ca^{2+} binding loop (Wu et al., 2009). However, in a more recent NMR study, chemical shift changes in response to Ca^{2+} binding were observed in multiple regions including residues up to 20Å away from the binding region, suggesting that Ca^{2+} binding can be sensed throughout the molecule (Breukels and Vuister, 2010). Moreover, significant changes in backbone dynamics in the F-G loop strongly suggest a critical role for this domain in transmitting the Ca^{2+} binding signal to other part of the Ca^{2+} regulation machinery involved in NCX1 function.

Current structural model of CBD12

The recent NMR and crystal structures from each isolated domain of CBD1 and CBD2 are contributing to our understanding of how the exchange function of NCX1 is regulated upon Ca^{2+} binding. Based upon the NMR structures of CBD1 and CBD2 from NCX1.4, Hilge and colleagues proposed a hypothetical model where the plane formed by two CBDs is approximately normal to the lipid bilayer so that the Ca^{2+}-binding sites of CBD1 are approximately 90 Å away from the transport Ca^{2+}-binding sites (Hilge et al., 2006). The model assumes that Ca^{2+}-dependent conformational changes in the relative orientation between two domains may trigger the Ca^{2+} regulation signal, which is transmitted to the transmembrane domain through the CLD domain. This model also supposes that the two separate Ca^{2+}-binding regions function as electrostatic switches that cause significant and global structural rearrangements in the whole cytoplasmic loop upon Ca^{2+}-binding as shown in Fig. 53 (Hilge et al., 2009). Consistent with this model, SAXS measurements of CBD12 constructs showed 25 Å and 15 Å of changes in D_{max} of scattering vectors from AD and ACDEF splice variants, respectively, though the low resolution of the technique prevents getting more information on molecular details of structural changes caused by Ca^{2+} -binding. However, a more recent NMR study using the CBD12 construct of the AD splice variant provided a different model (Salinas et al., 2011). The residual dipolar couplings indicated that the CBD12 adopts an elongated shape in the Ca^{2+}-bound state and the relative

arrangement of the two domains is not largely altered in the apo form. Instead, NMR ^{15}N relaxation data of the apo state showed a significant increase in interdomain flexibility compared with the bound form though it is not clear if the Ca^{2+}-dependence of CBD12 dynamics has any implication in the Ca^{2+} regulatory mechanism.

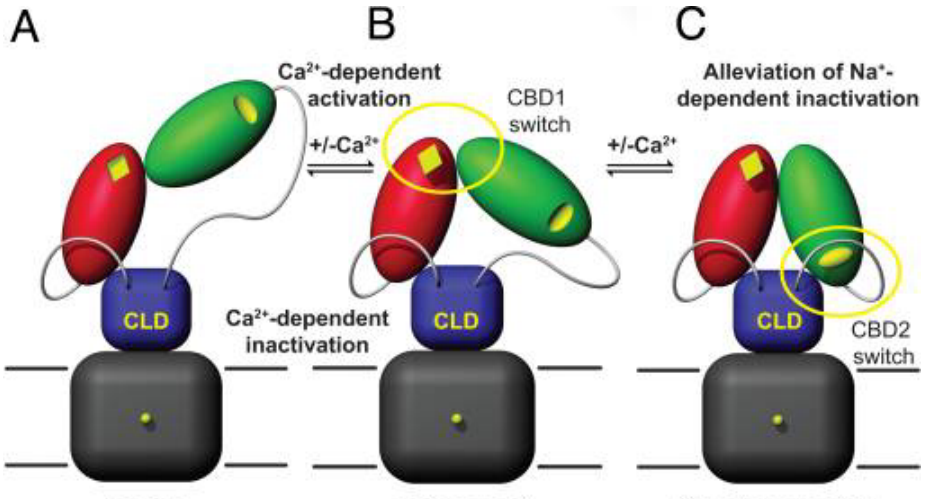

Figure 53. Hypothetical dual electrostatic switch mechanism in NCX regulation. (*A*) Inactive, Ca^{2+}-free NCX is in an extended conformation ($[Ca^{2+}] < 200$ nM). (*B*) Submicromolar Ca^{2+} concentrations induce a conformational change via the electrostatic switch in CBD1 that results in a compaction of the Ca^{2+}-binding domains probably reducing tension on the linker regions to the CLD ($[Ca^{2+}] \sim 200$ nM-1 μM). (*C*) Binding of Ca^{2+} to CBD2 allows for sustained Na^{+}/Ca^{2+} exchange and removes counteracting Na^{+}-dependent inactivation ($[Ca^{2+}] > 10\mu M$).

Another issue which should be considered with regards to the overall topology of NCX1 and the mechanism of Ca^{2+} regulation is the oligomeric state of NCX1 *in vivo* and *in vitro*. Evidence that a monomeric form of NCX1 is not sufficient for its appropriate trafficking to the plasma membrane came from the coexpression of two NCX1 proteins tagged with different fluorophores (Ottolia et al., 2007). While the two NCX1 constructs showed different localizations when they were separately expressed, coexpression of them exhibited homogeneous distribution of the two proteins, strongly suggesting that dimerization may be essential for the proper targeting of NCX1. Moreover, when FRET was monitored from fluorophores tagged at the long

intracellular loop regions of two NCX1s, Ca^{2+}-binding lead to an increase in FRET, which means that the long intracellular loops of two exchangers are in sufficiently close proximity to form a dimer and that the dimer undergoes Ca^{2+}-dependent conformational changes. FRET analysis of NCX1 mutants that lost their Ca^{2+}-binding affinity in either CBD1 or CBD2 revealed that the Ca^{2+}-induced conformational changes of NCX1 dimers arise from only the movement of CBD1 (John et al., 2011). In addition, cross-linking experiments also demonstrated that NCX1 can exist as a dimer *in vitro* (Ren et al., 2008). Taken together, evidence supporting dimer formation of NCX1 are accumulating from various approaches. Though any physiological relevance of dimer formation has not been implicated, it will be worth attempting to interpret structural aspects associated with Ca^{2+} regulation in the context of a dimer and to construct new structural models of NCX1.

CHAPTER A2

Determination of Structural Models of the Calcium Binding Domain of NCX1.1

Introduction

The cardiac Na^+/Ca^{2+} exchanger NCX.1.1 plays a major role in the contractile cycle via efflux of Ca^{2+} from the cardiomyocyte following its transient rise during systole. Under normal physiological conditions, the exchanger utilizes the electrochemical Na^+ gradient to extrude one Ca^{2+} ion for influx of 3 Na^+ ions (Kang and Hilgemann, 2004). This exchange process is vital to proper timing of the Ca^{2+} transient since studies have provided evidence that some cardiac arrhythmias are related to altered exchanger properties and that it has atypical function in heart failure (Piacentino et al., 2003; Pogwizd et al., 1999; Weisser-Thomas et al., 2003).

NCX1.1 is regulated by the same ions that it exchanges. Previous studies have shown that intracellular Na^+ can inactivate the exchanger (Hilgemann et al., 1992). Conversely, intracellular Ca^{2+} overcomes the Na^+-dependent inactivation and leads to the physiologically important increase in exchange activity (Hilgemann et al., 1992). This activation is vital to proper cardiac function. There are a number of splice variants of the NCX1 family of proteins with the ACDEF splice variant (NCX1.1) being expressed in cardiomyocytes (Hilge et al., 2006). Most current topological models for NCX1.1 predict nine trans-membrane α-helices and a large intracellular domain located between helices 5 and 6 (Nicoll et al., 1999; Ren et al., 2006). The intracellular domain can be subdivided into three separate structural elements. Current models include an α-catenin like domain which is proximal to the membrane surface and hence to the transmembrane domain of the exchanger and two Ca^{2+}-binding domains which are furthest from the membrane surface (Hilge et al., 2006). Numerous studies over the past decade have led to characterization of

two tandem regulatory Ca^{2+}-binding domains, denoted Ca^{2+}-binding domain 1 (CBD1) and Ca^{2+}-binding domain 2 (CBD2), which are located in the central portion of the large intracellular domain (e.g.(Hilge et al., 2006)). CBD1 binds four Ca^{2+} ions (Nicoll et al., 2006) while the CBD2-AD splice variant binds only two (Besserer et al., 2007).

Structural studies by NMR (Breukels and Vuister, 2010; Hilge et al., 2006; Johnson et al., 2008) and by X-ray crystallography (Besserer et al., 2007; Nicoll et al., 2006) on isolated CBD1 and on isolated CBD2-AD have shown that these domains adopt an immunoglobulin fold that is composed of a seven-stranded β-sandwich of two antiparallel β-sheets. Most structural studies to date have been carried out on the AD splice variant of CBD2 which has a shorter F-G loop between β-strands F and G than the ACDEF splice variant. Collectively, these studies have led to identification of the regions of the proteins that show changes in structure and dynamics upon Ca^{2+} binding to both isolated domains. Even though the atomic resolution structures of CBD1 and CBD2-AD are well established, it remains unknown how binding of Ca^{2+} is able to regulate exchanger activity. Recent studies by Hilge et al. have led to the proposal that Ca^{2+} regulation of the exchanger involves a dual electrostatic switch mechanism where binding of Ca^{2+} to both CBD1 and CBD2-AD are required for structural rearrangements within CBD12 and that this could be the basis for regulation of exchanger activity (Hilge et al., 2009). Small angle X-ray scattering data in this same extensive study suggested that such a structural rearrangement could also occur in the ACDEF splice variant found in heart.

In the present studies, site directed spin labeling has been employed in conjunction with conventional continuous wave electron paramagnetic resonance (CW-EPR) to determine how Ca^{2+} binding to the CBD12-ACDEF splice variant alters the dynamics of specific regions of the protein. The results from these studies agree well with the previous NMR studies on the isolated domains with regards to which regions of the Ca^{2+}-binding domains show the greatest changes upon Ca^{2+} binding. 4-Pulse DEER has been employed to construct a family of structural models

for CBD12-ACDEF in the Ca^{2+}-free and Ca^{2+}-bound forms. These latter studies show that CBD1 and CBD2 are not lengthwise antiparallel and in close proximity along the entire interface as hypothesized in early studies (Hilge et al., 2006) but rather are oriented in an almost linear arrangement as suggested by the more recent small angle X-ray scattering studies (Hilge et al., 2009) and an NMR study (Salinas et al., 2011). Most significantly, both EPR studies in solution and DEER measurements show that the relative orientations of the two Ca^{2+} binding domains are not significantly altered upon Ca^{2+} binding. This result strongly suggests that the allosteric signal that regulates the exchanger involves other types of changes in the structure and/or dynamics of CBD12 than rigid body reorientation of the two Ca^{2+}-binding domains. Additional studies indicated that binding of Ca^{2+} does lead to changes in the positioning of the α-helix and the structure/dynamics of the F-G loop of CBD2. These latter results, coupled with previous studies reported in the literature (Breukels and Vuister, 2010; Dyck et al., 1999; Hilge et al., 2009), suggest that further investigations of these regions of CBD2 are now warranted.

Materials and Methods

Protein preparation and spin labeling

The full length rat NCX1.1 cDNA, which was generously provided by Dr. J. Lytton at the University of Calgary, was used to produce the ACDEF splice variant of CBD12 (NCX1.1). The cDNA encompassing residues 360-685 was generated using QuikChange Site-Directed Mutagenesis Kit (Stratagene, La Jolla, CA). The PCR fragment was ligated into a pET19b+ expression vector (Stratagene, La Jolla, CA) using Nde I and Xho I restriction sites. All four endogenous cysteines were replaced with alanine to create a cysteine-less construct (ΔC-CBD12). Single or double cysteines were then introduced at desired sites in the ΔC-CBD12 construct. The

DNA sequences of all the mutants were confirmed by DNA sequencing. The mutant DNAs were then transformed into *Escherichia coli* competent cells (DE3, pLys-s, Stratagene, La Jolla, CA).

One liter of LB medium was inoculated with a 10 ml overnight culture and the culture was grown at 37° C to reach OD of 0.6-0.8. Protein expression was induced by adding 0.1 mM IPTG and then incubating the culture at 27° C for 4 hrs. After cells were harvested by centrifugation, the resultant cell pellet was re-suspended in 100 mL lysis buffer containing 20mM Tris-HCl, 300 mM NaCl, 0.2 mM DTT, 16 mM imidazole, 40 units/ml lysozyme and EDTA-free protease inhibitors (Roche, Indianapolis, IN), pH 8.0, and then quickly frozen in the ethanol bath cooled by dry ice. The frozen suspension was kept at -80 ºC before use.

After thawed, the cell suspension was sonicated on ice for two minutes and followed by incubation with 1 % (w/v) Triton X-100, 0.5 units/ml DNase and 0.5 units/ml RNase on ice for an additional 30 minutes. The lysates were centrifuged at 12,000 rpm (JA-20 Beckman rotor, Beckman Coulter, Inc., Indianapolis, IN) for 30 minutes. The cleared lysate was incubated with 2 mL of Ni-NTA resin (Qiagen, Valencia, CA) which had been preequilibrated with lysis buffer for one hour. The resin was washed with 100 column volumes of wash buffer containing 20 mM Tris-HCl, 150 mM NaCl, and 16 mM imidazole, pH 7.4. Single and double mutant proteins were then spin labeled overnight on the resin with a 10-fold molar excess of 1-Oxyl-2,2,5,5, tetramethyl-Δ 3-pyrroline-3- methyl methanethiosulfonate spin label (MTSSL: Toronto research chemicals, North York, ON, Canada) at 4° C. Labeled protein was first washed with wash buffer containing 20 mM Tris-HCl and 16 mM imidazole, pH 7.5, and then with buffer containing 20 mM Tris-HCl and 60 mM imidazole, pH 7.5. Protein was eluted with 20 mM Tris-HCl and 250 mM imidazole, pH 7.5. Partially purified protein was further purified using a DEAE anion exchange column (TSK DEAE 650M; Ace Scientific, Cherry Hill, NJ) with a linear 0-0.8 M NaCl gradient. The labeled proteins were collected from the main peak of the elution profile (detected at 280 nm) and then concentrated using an Amicon Ultra-4 centrifugal filter device (30 kDa cutoff, Millipore, Bedford, MA) to the desired protein concentration. The apparent molecular

weight and purity of each labeled protein was assessed by SDS-PAGE gel (Laemmli, 1970). All samples used for CW-EPR and DEER measurements were greater than 95 % pure according to the intensity of bands on gels.

Isothermal titration calorimetry (ITC) measurements

Wild type and ΔC-CBD12 protein samples were prepared as described above. The proteins were dialyzed against buffer containing 10mM EDTA, 20 mM Tris-HCl and 150 mM sodium chloride, pH 7.4. The samples were then thoroughly washed with 20 mM Tris-HCl and 150mM sodium chloride, pH 7.4. Protein concentrations were determined by the BCA assay according to the manufacturer's protocol (Themo Scientific, Rockford, IL). A 2 mM CaCl stock was prepared in the same buffer as the corresponding protein samples. ITC were carried out using a VP-isothermal titration calorimeter (Microcal, LLC, GE Healthcare, Piscataway, NJ) with protein concentrations of 50 μM. After equilibration at 25° C, a total of 55 5 μL serial injections of the CaCl stock were made at 3 minute intervals at a stirring speed of 300 rpm. To correct for background error, calcium chloride was titrated into the buffer in the absence of protein. All experiments were repeated three times.

CW-EPR measurements.

CW-EPR spectra were collected at X-band (9.8 GHz) on a Bruker EMX spectrometer fitted with a TM_{110} cavity (BrukerBiospin, Billerica, MA) using 5mW microwave power and 1Gauss field modulation (peak-to-peak) at 100 kHz. Samples were prepared in 20 mM Tris-HCl, 150 mM NaCl, pH 7.5, in the 80 to 120 μM concentration range and spectra were collected at room temperature in 50 μL glass capillaries (Kimble Glass, Inc., Vineland, NJ). Short inter-probe distances (< 20 Å) were measured on samples in 50 % glycerol at 2 °C. The resulting EPR spectra were analyzed using the convolution method which assumes Gaussian distance distributions as

described in previous work (e.g. (Hustedt et al., 2006; Rabenstein and Shin, 1995)). Samples with Ca^{2+} were incubated with 10 mM $CaCl_2$ and samples without Ca^{2+} were incubated with 10 mM EDTA for 10 minutes prior to EPR measurements.

Four-pulse DEER measurements and data analysis

The four-pulse DEER experiment was performed at X-band (9.5 GHz) on a Bruker EleXsys 580 spectrometer equipped with a Bruker split ring resonator (ER 4118X-MD5). A standard 4-pulse sequence was employed with a 32 ns π pulse and a 16 ns π/2 pulse. All measurements were recorded at 80 K as described in previous work (Kim et al., 2011; Zhou et al., 2007; Zhou et al., 2005). Samples were prepared in 20 mM Tris-HCl, 150 mM NaCl, pH 7.5, buffer containing 30% (w/w) glycerol in the 150 to 250 μM concentration range and loaded into 2.4 mm i.d. quartz capillaries (Wilmad LabGlass, Buena, NJ). All DEER data were analyzed using software developed in house which simultaneously fits the background signal as a function of an effective spin concentration and radius of the molecule or complex while determining the specific interactions of interest using a distance distribution defined as a sum of Gaussians (manuscript in preparation). This approach, which takes into account the excluded volume of the molecule or complex, typically gave better fits to the data than those obtained using *a priori* background correction. All of the DEER data shown in the Figs. 56, 58, and 59 are with the background removed subsequent to the analysis. The calculated average distances and distance distributions were similar to those obtained using the conventional Tikhonov regularization method (Chiang et al., 2005).

Molecular modeling

Explicit modeling of the spin label R1 side chains at each of the sites which were utilized for interdomain DEER distance measurements was carried out using the MMM program developed by Jeschke and coworkers (Polyhach et al., 2011). These modeling calculations were

performed on the MATLAB platform (The Mathworks, Inc., Natick, MA). Briefly, R1 side chains were modeled on the 7 sites in each structure of CBD1 (PDB code: 2DPK) and CBD2 (PDB code: 2QVM) and the resultant spatial distribution of MMM rotamers were calculated at 80 K. The average Cartesian coordinate of the nitroxide electron at the spin labeled site was taken from the probability-weighted sum of coordinates from each rotamer as shown in the following formula:

$$\overline{C}_{NO}(x,y,z)=\left(\sum_{i}^{n}x_i p_i,\sum_{i}^{n}y_i p_i,\sum_{i}^{n}z_i p_i\right)$$

where p_i is the probability of finding the i_{th} rotamer of the R_1 side chain at this set of coordinates and n is the number of allowed rotamers.

Two structures of CBD1 and CBD2 were covalently linked *in silico* by manually introducing a peptide bond between residue 500 in CBD1 and residue 501 in CBD2 using PyMOL software (www.pymol.org) to generate a CBD12 template structure. Inspection of two crystal structures from the isolated CBD1 and CBD2 indicates that the three consecutive residues 501-503 form a potentially flexible interdomain linker (Salinas et al.). Thus, a set of CDB12 structures having different configurations between the two domains was generated by systematically rotating the backbone bonds along the linker region using Chimera (www.cgl.ucsf.edu/chimera/) and in-house written python scripts. Three pairs of backbone bonds flanking two peptide bonds in residues 501 through 503 were subject to systematic rotations with a 30° interval while two

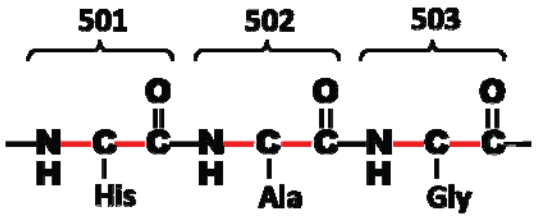

peptide bonds were fixed in the trans-configuration. The resultant conformers were first checked for backbone clashes in the absence of side chains and the conformers which contained any steric clash between backbone atoms were discarded. The remaining poses (569,520 out of 2,985,984 conformers; 19.1 %) were subsequently filtered with 17 interdomain DEER distance constraints (5 Å cutoff) and resulted in 1,356 poses. The generated models were ranked based upon the RMSD values for the distance violations. The overall scheme used for the molecular modeling is shown in Fig. 54.

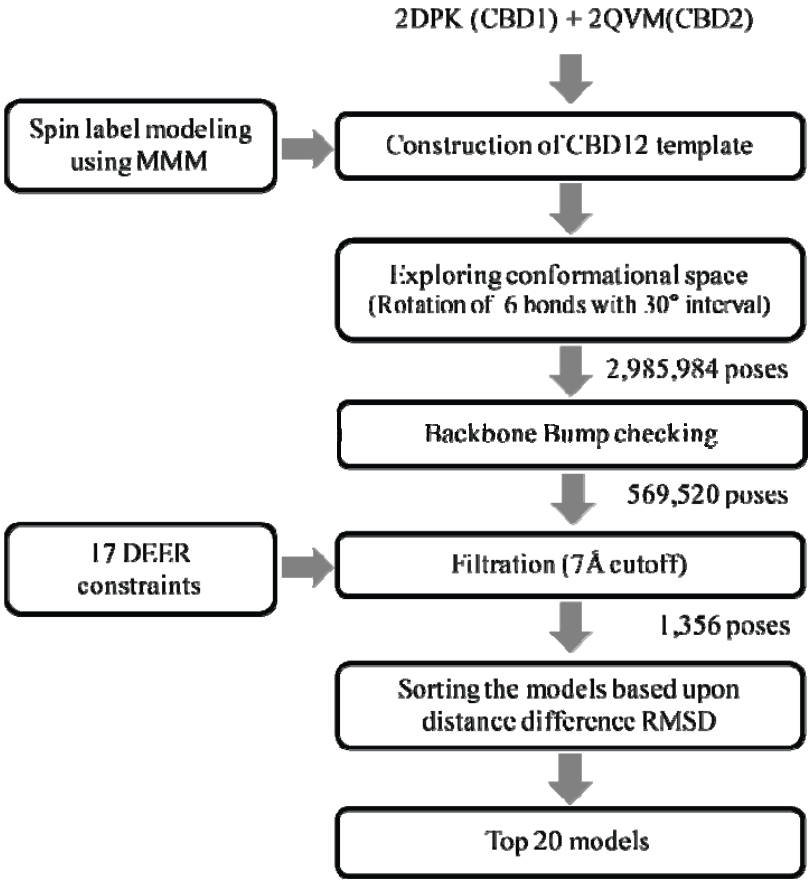

Figure 54. Schematic diagram of the method used to construct models of CBD12-ACDEF from experimental DEER data.

Results

Biophysical characterization of the CBD12 constructs

Wt-CBD12 from NCX1.1 contains four endogenous cysteine residues at positions 383, 387, 485, and 557. In order to carry out high quality site-directed spin labeling experiments, it was necessary to replace each of the endogenous cysteines with another amino acid that would not be chemically reactive with the MTSSL probe used for EPR detection. Alanine was chosen for this purpose and used to generate the ΔCys-CBD12 construct used in these studies. The first questions that were addressed were whether these substitutions disrupted Ca^{2+} binding properties or the secondary structure of the wt protein. Previously, a fragment of the long cytosolic loop of NCX1 encompassing CBD1 was reported to exhibit atypical mobility shift in SDS-PAGE between apo and Ca^{2+}-bound states (Levitsky et al., 1994). Consistent with this observation, the expressed recombinant protein of wt-CBD12 showed the mobility shift in a Ca^{2+} binding-dependent manner (data not shown), suggesting that the expressed protein is functional with regards to Ca^{2+} binding. The identical mobility shift was also seen in the ΔC-CBD12 construct.

To further examine the effect of removal of four endogenous cysteines from CBD12 on its global structure and Ca^{2+} binding affinity, CD and ITC measurements were performed for wt- and ΔC-CBD12. As shown in Fig. 55, the two proteins gave rise to identical spectra in the far-UV CD measurements for both Ca^{2+}-bound and unbound states, which means that the secondary structures in wt-CBD12 are well conserved in ΔC-CBD12. As predicted, the spectra are dominated by a characteristic pattern for β-sheets with the minimum and maximum ellipticity around 215 nm and 200nm, respectively.

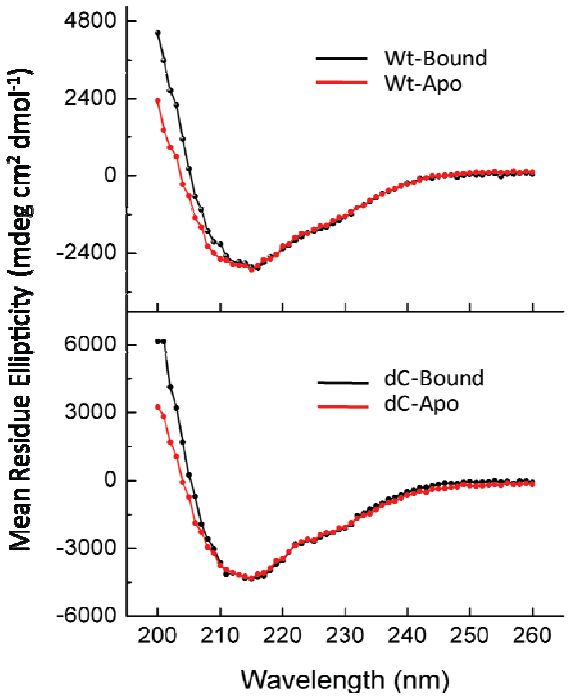

Figure 55. CD (circular dichroism) spectra from wild type and ΔC-CBD12-ACDEF.

Both the expressed wt- and ΔC-CBD12 exhibited essentially identical binding isotherms with that from wt-CBD12 as previously reported by Hilge et al. (Hilge et al., 2006), showing that two Ca^{2+} bind with medium affinity. They observed that the other 4 Ca^{2+} ions can be sequestered in the high binding affinity sites during titration under normal experimental conditions. Likewise, no significant difference was observed in binding isotherms between wt- and ΔC-CBD12 and the resultant ITC profiles were consistent with the one previously published which showed that 4 Ca^{2+} bind with high affinity. Although ΔC-CBD12 shows a slight decrease in binding affinity compared with wt-CBD12, this seems to be associated with low binding affinity sites in CBD2 based upon identical binding isotherms in CBD1. These results indicate that ΔCys-CBD12 displays critical wt-like properties and that it should provide a suitable background into which

single or double cysteine substitutions could be made in order to carry out site-directed spin labeling experiments.

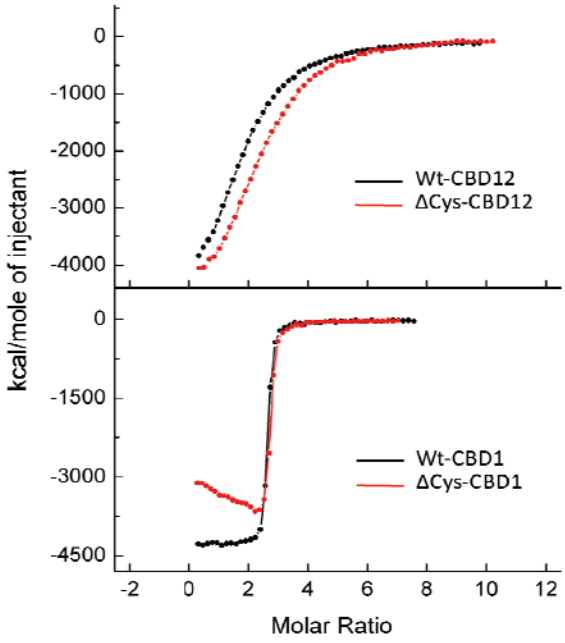

Figure 56. Calcium-binding isotherms of wild type and ΔC-CBD12-ACDEF measured by ITC (isothermal titration calorimetry).

The effects of calcium binding on the dynamics of selected spin-labeled sites in the CBD1 domain in CBD12

An initial NMR study suggested that almost a half of CBD1 unfolds in the apo form (Hilge et al., 2006). However, a later NMR study performed with a protein sample under more stabilizing conditions reported that the Ca^{2+}-dependent structural change is limited only to the Ca^{2+}-binding loop region. The cw-EPR spectra obtained from the surface sites residing on β-strands support the latter. Residues 380, 382, 384, 391, and 457 are proximal to the binding loop and initially regarded as unstructured in the apo state (Hilge et al., 2006). However,

none of them showed increases in R1 side chain motion in the absence of bound Ca^{2+}, which can be typically observed in unstructured regions of proteins. Many of the chosen sites in the highly structured β-sandwich region show no sensitivity to Ca^{2+} binding including sites 380 and 384 on the A' strand, site 395 on the B strand, site 443 on the E strand, and sites 457 and 461on the F strand. However, some sites in the β-strands do show sensitivity to Ca^{2+} binding including site 382 in the A' strand, 391 in the B strand, 441 in the E strand, and 464 in the F strand. The EPR spectra that demonstrate the spectral changes observed are shown in Fig. 57, right panel. These results, which are in qualitative agreement with previous NMR studies on isolated CBD1 (e.g. (Johnson et al., 2008)) and on isolated CBD2 (e.g. (Breukels and Vuister, 2010)), show that binding of Ca^{2+} (small yellow spheres in Figs. 54 and 57) to CBD12 is likewise sensed at positions distal from the Ca^{2+} binding loops.

The F-G loop of CBD1 forms a tip at the opposite side of the β-sheets from the Ca^{2+} binding loops and is known to be in a highly dynamic state based upon NMR studies (Hilge et al., 2006). Of two sites selected, spin labeling at residue 472 yielded a spectrum with fast motion, which is typical in flexible loops, and was not sensitive to Ca^{2+} binding. However, the other site in the F-G loop, residue 479, shows remarkably slow motion compared to residue 472 even in the apo state, and Ca^{2+} binding resulted in a significant increase in R1 side chain motion. This indicates that at least one region in the F-G loop including residue 479 may be locally structured or have tertiary interactions, which senses Ca^{2+}-binding occurring approximately 40 Å away across the β-sheets. Residue 370, located in the C-terminal region, but in proximity with the F-G loop, also showed a Ca^{2+}-dependent change in R1 side chain mobility. Unlike residue 479, however, this site showed a dramatic decrease in mobility upon Ca^{2+}-binding, which agrees well with the previous NMR studies. Taken together, spin labeling of the F-G loop (and N-terminal region)

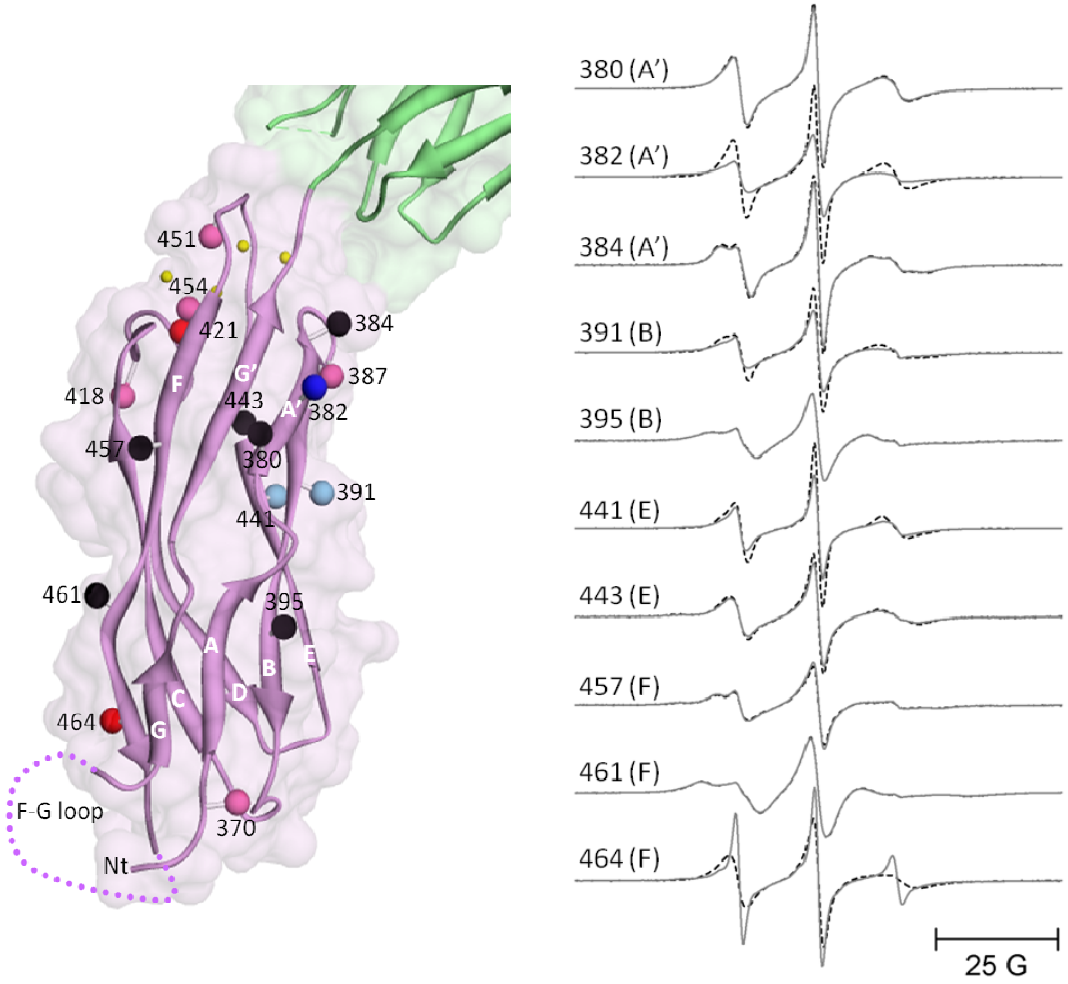

Figure 57. Sites selected for site directed spin labeling in the CBD1 domain of CBD12 and their corresponding EPR spectra. The ribbon diagram of CBD1 is shown in purple superimposed on the space filling model in the left panel (coordinates from PDB: 2DPK). The sites where single R_1 spin labeled side chains were incorporated are shown as solid spheres which are centered at the coordinates of the β-carbon of each residue. The spheres are color coded to indicate changes in spin labeled side chain mobility upon Ca^{2+} binding as follows: black, no change; bright red, substantial decrease; pale red, subtle decrease; bright blue, substantial increase; and pale blue, subtle increase. The positions of the four Ca^{2+} binding sites are shown as small yellow spheres. The position of the F-G loop is shown schematically in dots. The green ribbon diagram and space filling model at the top are the apical portion of the CBD2 domain. The EPR spectra in the right panel are from sites in the central β-sandwich region and are shown as solid lines (no bound Ca^{2+}) and dashed lines (saturating level of bound Ca^{2+}).

reveals that the structural effect of Ca^{2+}-binding on CBD1 can be transmitted throughout the whole molecule and results in heterogeneous dynamics in the F-G loop.

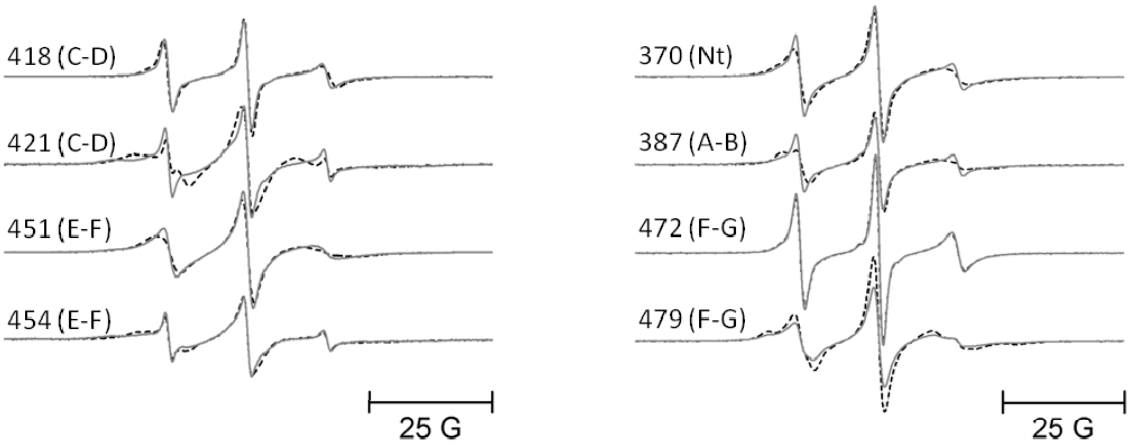

Figure 58. CW-EPR spectra from loop regions of the CBD1 domain of full length CBD12. The left panel shows the EPR spectra from four sites in the Ca^{2+} binding loops, and the right panel from the sites in the F-G loop and the N-terminus. The EPR spectra are shown as solid lines (no bound Ca^{2+}) and dashed lines (saturating level of bound Ca^{2+}) for each site.

In order to determine whether Ca^{2+}-binding to CBD12 produced any global structural changes in the CBD1 domain, five separate pairs of spin labeled R1 side chains were incorporated as shown by the black spheres in Fig. 59, left panel. DEER was employed to measure the average inter-probe distance and distribution of distances between each of these five pairs as described in experimental procedures and in detail in previous work (e.g. (Kim et al., 2011; Zhou et al., 2007; Zhou et al., 2005)). As shown by the DEER data in Fig. 59, right panel, the four inter-probe distances involving residues in the structured β-sandwich region of CBD1 showed no sensitivity to Ca^{2+} binding indicating that the β-sandwich region does not undergo any major global structural change even in some regions of the β-strands which are in proximity to the Ca^{2+}

binding loops (residues, 384, 387 and 391). These four distances agreed well with the previously determined structure of isolated CBD1.

However, both the average inter-probe distance and distribution of distances was highly sensitive to Ca^{2+} binding between probes at site 411 in the β-sandwich region and site 472 in the

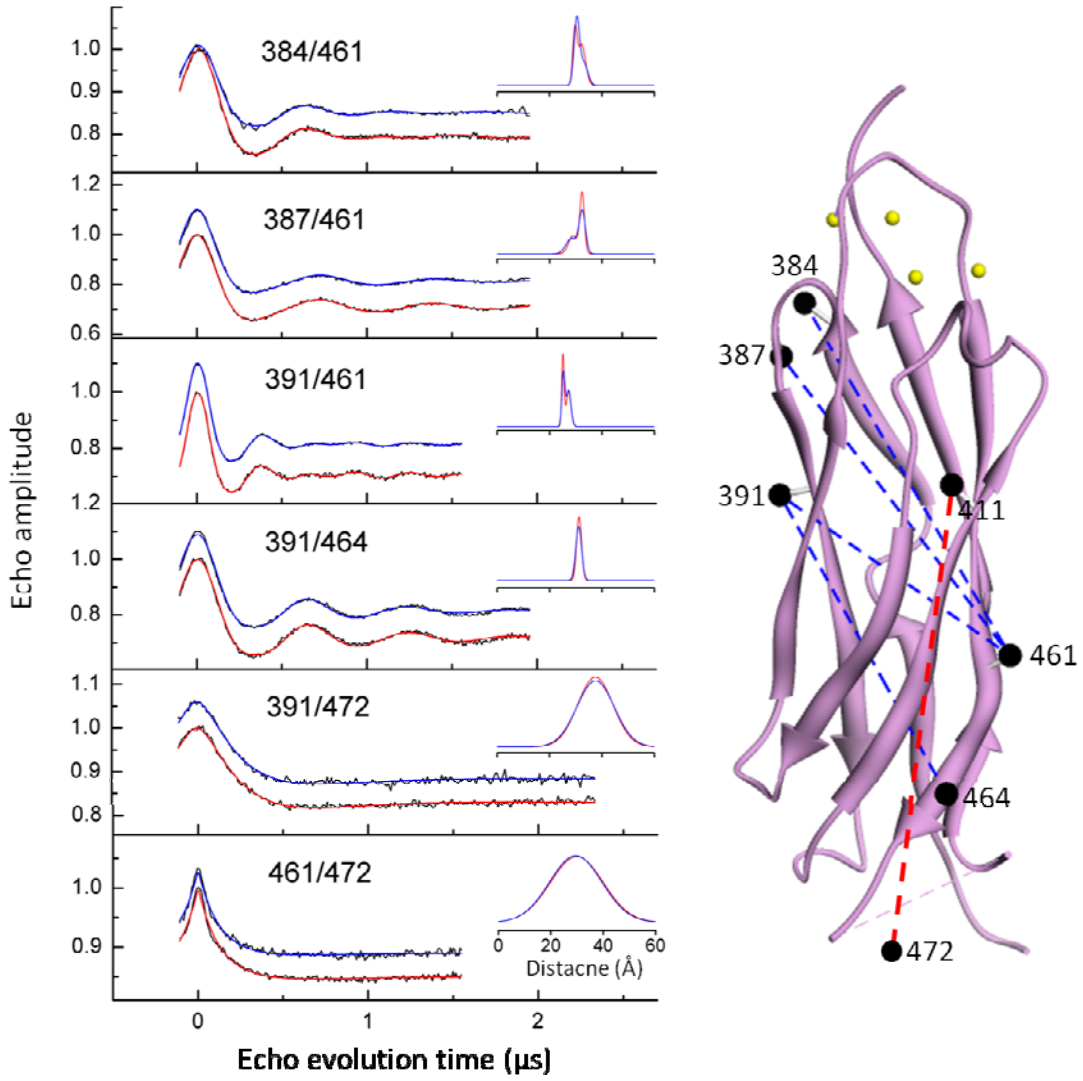

Figure 59. Pairs of sites selected for site directed spin labeling in the CBD1 domain of CBD12 and their corresponding DEER spectra. The ribbon diagram of CBD1 is shown in purple in the left panel (coordinates from PDB: 2DPK). The sites where pairs of R_1 spin labeled side chains were incorporated are shown as solid spheres connected by dashed lines. The spheres are centered at the coordinates of the β-carbon of each selected residue. The positions of the four Ca^{2+} binding sites are shown as small yellow spheres. The DEER data for each of the five pairs of sites are shown as solid black lines in the right panel.

The fits to the DEER data are shown as solid blue lines (no bound Ca^{2+}) and solid red lines (saturating level of bound Ca^{2+}). The average distances and widths of the distance distributions are shown in the insets to each DEER data set in Å.

flexible F-G loop. This latter result, in combination with the observation of changes in mobility of residues in the F-G loop as shown in Fig. 58., indicates that the localized changes in mobility of the Ca^{2+} binding loops are propagated over a long distance and affect the mobility and average position of the F-G loop. As shown in Fig. 65, the Ca^{2+} binding sites on CBD2 are far removed from the F-G loop of CBD1 in full length CBD12 and therefore, changes in the mobility of the Ca^{2+}-binding loops of CBD2 are unlikely to be directly responsible for the observed changes.

Effects of Ca^{2+}binding on the dynamics of selected spin-labeled sites in the CBD2 domain in CBD12.

Fig. 60, left panel shows the sites on CBD2 that were chosen for spin labeling in full length CBD12. In agreement with NMR and crystal structures from the isolated domain of CBD2, no sites examined in the β-sandwich region of CBD2 showed increased motion in the absence of bound Ca^{2+}. All but one of the chosen sites in the highly structured β-sandwich region showed no sensitivity to Ca^{2+} binding including sites 506 in the A strand, 515 in the A' strand, 520, 526, and 529 in the B strand, 557 and 559 in the D strand, and 673 in the break between the G and G' strands. The single exception occurred at site 680 which lies at the end of the G' strand near the Ca^{2+} binding sites (small yellow spheres). This site showed decreased motion upon saturation of the Ca^{2+} binding sites. Unlike CBD1, among the sites chosen, there were none that showed increased motion upon Ca^{2+} binding suggesting that CBD2 may exhibit a more rigid core structure than CBD1. Sites in loop regions including 565 and 567 in the D-E loop, 576 in the E-F loop, and 596 in the F-G loop as well as site 685 at the C-terminus all showed decreased motion upon Ca^{2+}-binding as indicated by the colored spheres in Fig. 60, left panel, and as demonstrated by the EPR spectra in the right panel.

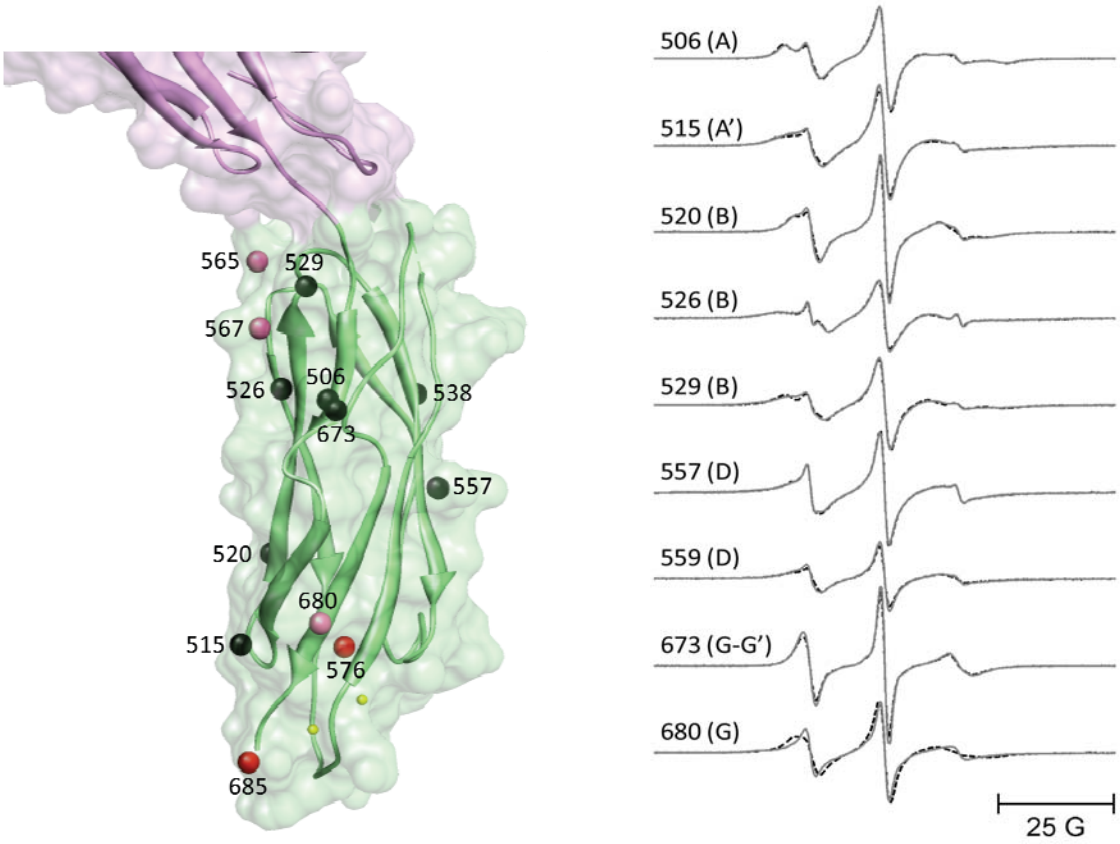

Figure 60. Sites selected for site directed spin labeling in the CBD2 domain of CBD12 and their corresponding EPR spectra. The ribbon diagram of CBD1 is shown in green superimposed on the space filling model in the left panel (coordinates from PDB: 2QVM). The sites where single R1 spin labeled side chains were incorporated are shown as solid spheres which are centered at the coordinates of the β-carbon of each residue. The spheres are color coded to indicate changes in spin labeled side chain mobility upon Ca^{2+} binding as follows: black, no change; bright red, substantial decrease; and pale red, subtle decrease. The positions of the two Ca^{2+}-binding sites are shown as small yellow spheres. The position of the F-G loop is shown schematically in dotted line. The purple ribbon diagram and space filling model at the top are the apical portion of the CBD1 domain. The EPR spectra in the right panel are from sites in the central β-sandwich region (top) and in the loops and C-terminal region (bottom), and are shown as solid lines (no bound Ca^{2+}) and dashed lines (saturating level of bound Ca^{2+}).

In order to determine whether Ca^{2+} binding to CBD12 produced any global structural changes in the CBD2 domain, five separate pairs of spin labeled R_1 side chains were incorporated as shown by the black spheres in Fig. 61, left panel. DEER was employed to measure the average inter-probe distance and distribution of distances between each of these five pairs as described in

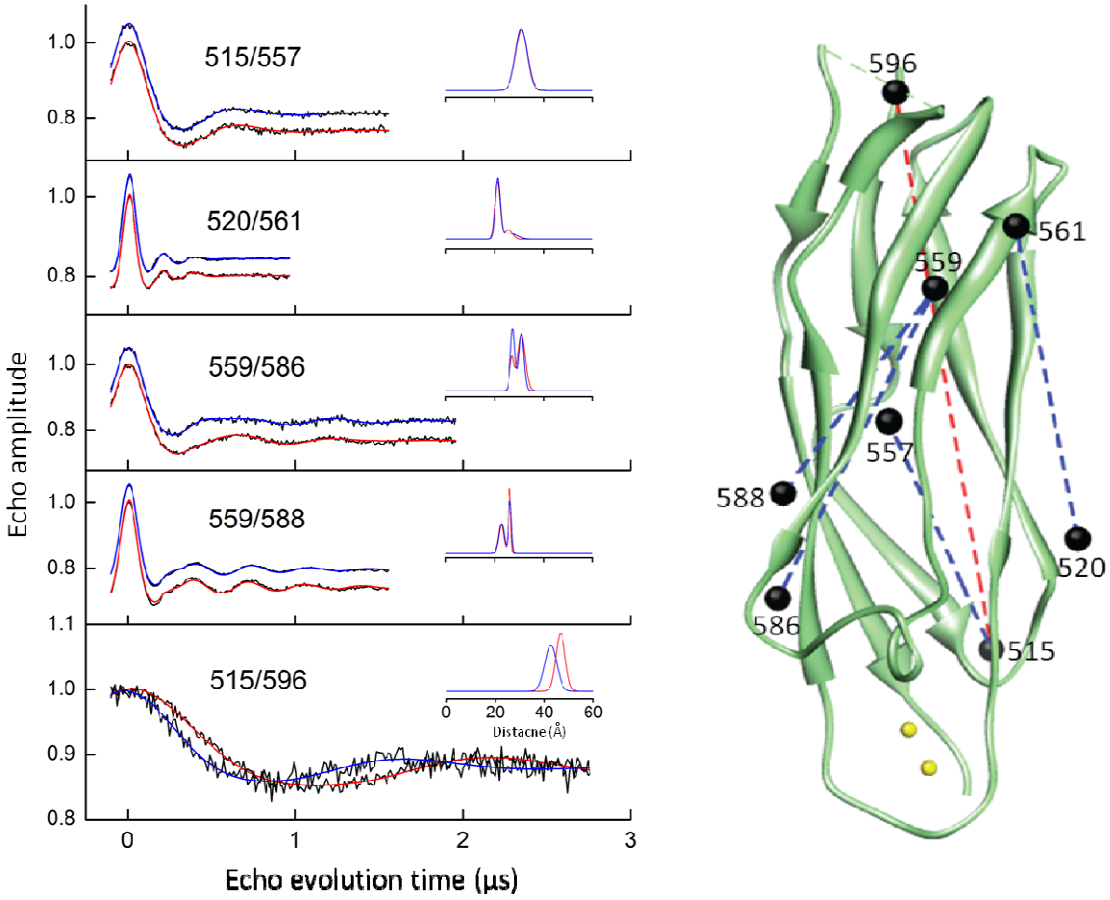

Figure 61. Pairs of sites selected for site directed spin labeling in the CBD2 domain of CBD12 and their corresponding DEER spectra. The ribbon diagram of CBD2 is shown in green in the left panel (coordinates from PDB: 2QVM). The sites where pairs of R_1 spin labeled side chains were incorporated are shown as solid spheres connected by dashed lines. The spheres are centered at the coordinates of the β-carbon of each selected residue. The positions of the two Ca^{2+} binding sites are shown as small yellow spheres. The position of the F-G loop is shown schematically in a dashed green line. The DEER data for each of the five pairs of sites are shown as solid black lines in the right panel. The fits to the DEER data are shown as solid blue lines (no bound Ca^{2+}) and solid red lines (saturating level of bound Ca^{2+}). The average distances and widths of the distance distributions are shown in the insets to each DEER data set in Å.

experimental procedures and in detail in previous work (e.g. (Kim et al., 2011; Zhou et al., 2007; Zhou et al., 2005)). As shown by the DEER data in Fig. 61, left panel, the four inter-probe distances involving residues in the structured β-sandwich region of CBD2 showed no sensitivity to Ca^{2+}-binding indicating that the β-sandwich region, like CBD1, does not undergo any major global structural change. However, a mutant 515/596, where the site 596 is located on the long F-G loop of CBD2, exhibited a 4 Å decrease in the mean inter-probe distance upon Ca^{2+} binding. This suggests that the binding of regulatory Ca^{2+} ions induce substantial changes in the conformation of the F-G loop in CBD2 and proposes a possible role of this region in Ca^{2+} regulation. Taken together, the presence of CBD1 does not alter the essential structural features of CBD2 which have been previously reported from the isolated domain. Like CBD1, Ca^{2+} binding in CBD2 appears to induce conformational changes mainly in Ca^{2+} binding loops and long F-G loop regions.

The effects of calcium binding on the structure of CBD12

Recently, Hilge et al. proposed a model describing how Ca^{2+}-binding occurring approximately 90 Å away from the intracellular surface of the membrane can be transmitted to the transport site of the transmembrane domain to regulate exchanger activity. This model assumes a conformational change which primarily includes alterations in the relative orientation between the two CBDs. In order to test this model, a set of 17 doubly labeled mutants of CBD12 where one spin label was placed in CBD1 and the other in CBD2 and interdomain DEER distances were collected in the presence and then absence of Ca^{2+}. The results are shown in Fig. 62. All the DEER measurements for the given set of double mutants resulted in well defined Gaussian distance distributions containing single or two components. Surprisingly, all of the collected DEER data exhibited no substantial differences in inter-probe distance between the Ca^{2+}-bound and apo forms of CBD12 with only a couple of exceptions. This strongly suggests a

model where the relative orientation of the two CBDs is not altered in a Ca^{2+} dependent manner. Significant changes in inter-probe distance between Ca^{2+}-bound and apo states were observed only in two pairs of sites, 380/506 and 441/506, with a 3.2 and 2.2 Å difference, respectively. Given that the rest of DEER distances are not affected by Ca^{2+} binding, these small differences may result from the changes in R1 side chain orientations or local movement of the protein backbone, and be assumed to be trivial in terms of the global structure of CBD12. Relatively narrow widths of distance distributions found in many of the DEER data sets also demonstrate that two CBD domains are tightly associated to maintain their relative orientations in a static state. Collectively, a body of interdomain DEER distances demonstrates that the relative orientation between the two CBDs is neither in a dynamic state nor significantly altered upon Ca^{2+}-binding.

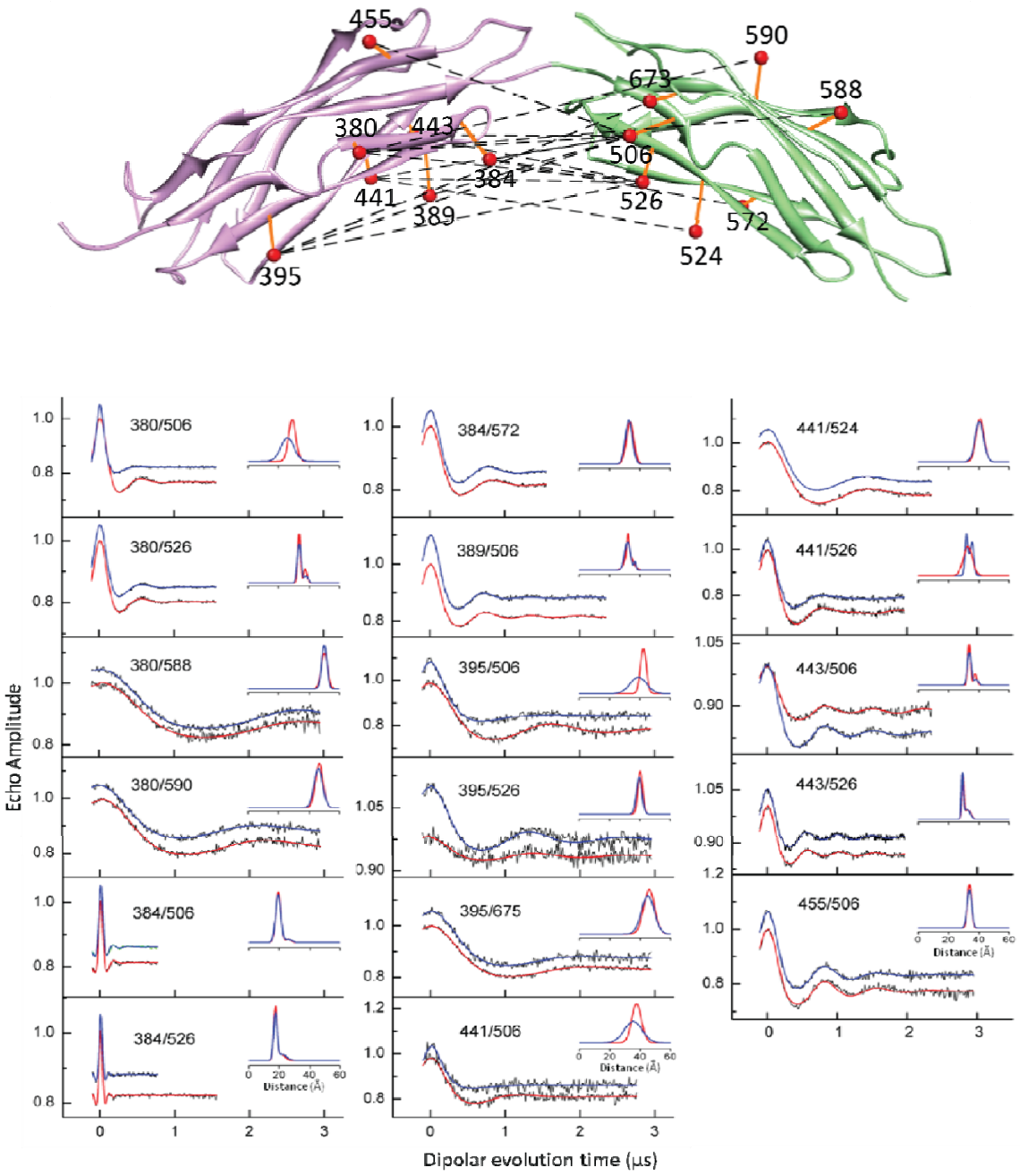

Figure 62. All 17 interdomain DEER data that were used for model construction

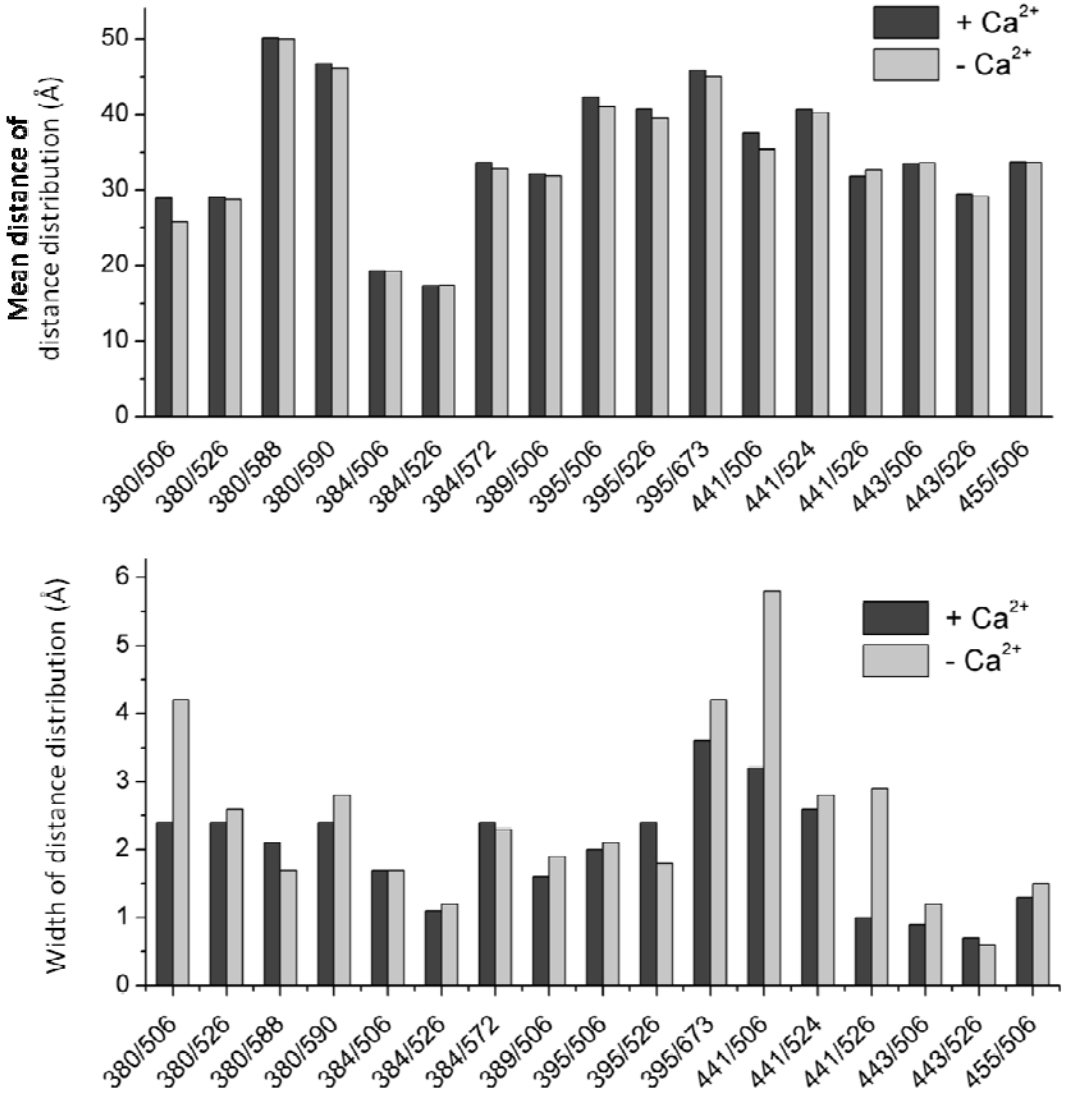

Figure 63. Mean distances (top panel) and distance distributions (bottom panel) of 17 interdomain DEER distances before (light grey) and after (dark grey) Ca^{2+} binding.

Construction of structural models of CBD12

The CBD12 template structure having an arbitrary orientation between the two CBDs was prepared by manually linking the crystal structures of CBD1 (PDB code, 2DPK) and CBD2 (PDB code, 2QVM). All possible conformational states were explored by systematic rotation of a set of backbone bonds forming a bridge linking the two domains as described in the methods

section. The scheme used for model construction is shown in Fig. 54 and the resultant sets of models from each filtration step are illustrated in Fig. 64. In the filtration step, the conformational space was sampled with the rotation of 6 bonds at 30° intervals while the two peptide bonds were fixed in the trans configuration. This generated about 3 million poses which were checked for steric clashes between backbone atoms of the two domains which left 569,520 bump-free poses (~ 19 %). The subsequent filtrations through the 17 interdomain DEER distance constraints using a 5.0 Å cutoff dramatically reduced the number of candidates to 1,356 poses (~ 0.2 % of the bump-free poses). The lowest mean distance difference RMSD of 1.6 Å in the best model suggests that a 5.0 Å cutoff is enough to safely include all the relevant models that represent the actual structure. The resultant poses were ranked with regards to the mean distance difference RMSD values. Surprisingly, the top 20 models exhibited a tight cluster with remarkably low distance difference RMSD (1.6~1.8 Å) (Fig. 65). Notably, the fact that all the sites involved in multiple DEER distance constraints (positions 380, 384, 395, 441, 443, 506, 526) simultaneously satisfy those distances in the solution set of models supports the reliability of the explicit modeling approach utilized in this study.

The solution set of models presented in Fig. 65 shows that CBD1 and CBD2 are not lengthwise antiparallel and in close proximity along the entire interface as hypothesized in early studies, but rather are oriented in an almost linear arrangement, which is consistent with the structural model constructed from residual dipolar couplings in a recent NMR study (Salinas et al., 2011). According to the constructed models, the N- and C-terminus of CBD12, which corresponds to the F-G loop of CBD1 and the Ca^{2+}-binding region of CBD2, respectively, are widely separated by approximately 90 Å. This topology of CBD12 is also corroborated by the observations of no DEER signals from a set of doubly labeled CBD12 mutants containing a pair of spin labels on those two regions (data not shown).

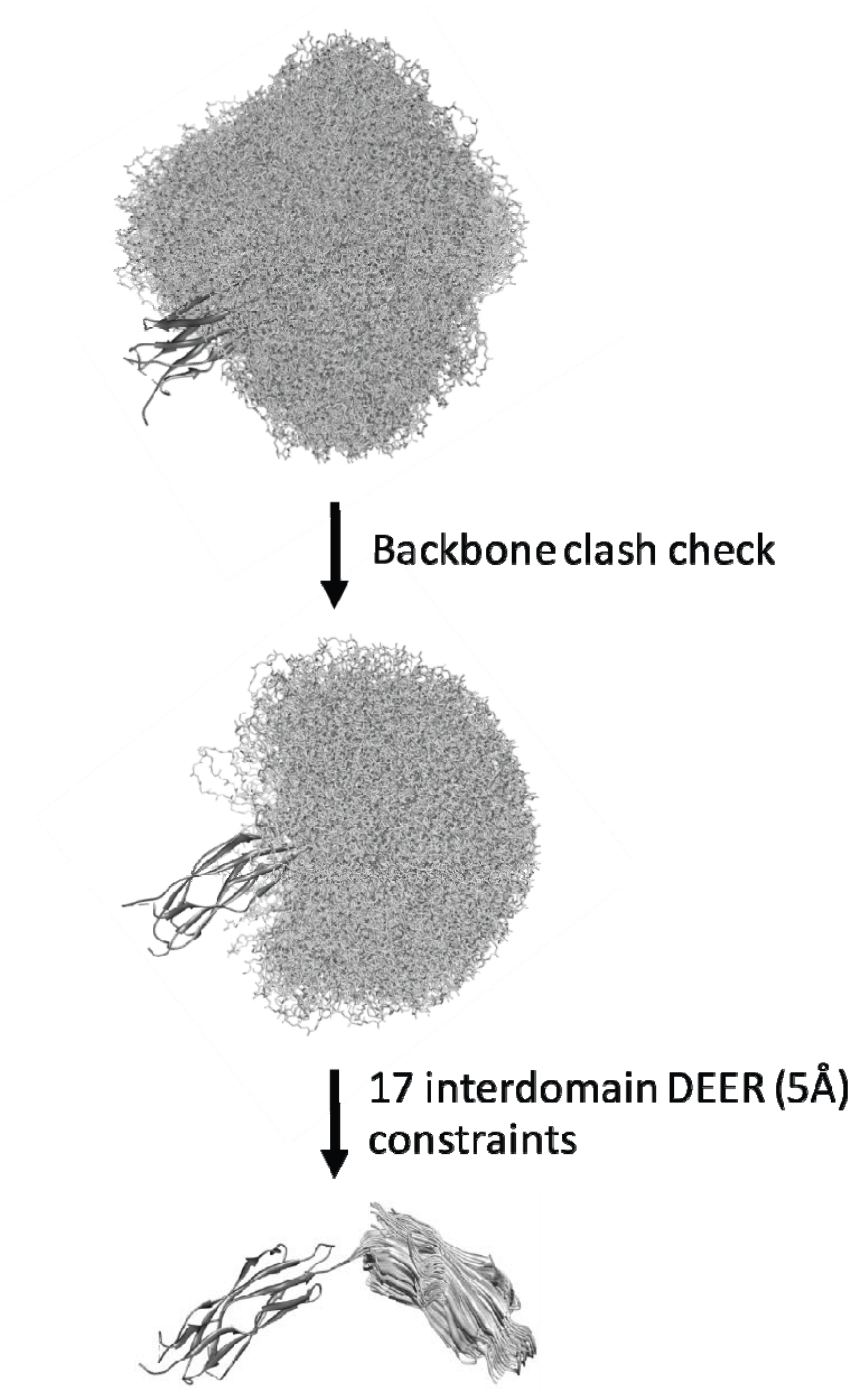

Figure 64. The scheme for the generation of solution models of CBD12. In each set of models, all the poses were displayed with fixed coordinates of CBD1.

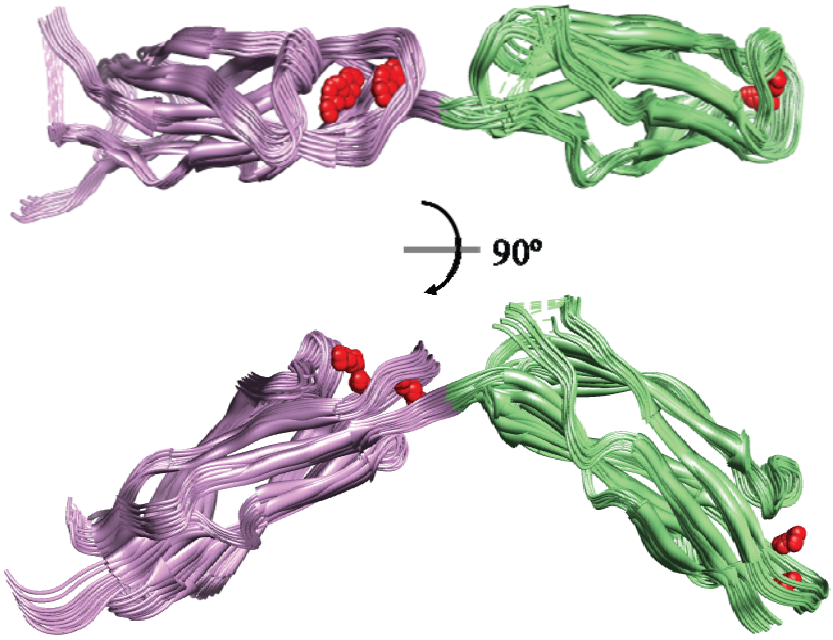

Figure 65. The top 20 solution set of structural models for the Ca^{2+}-bound form of CBD12 from the two different angles; CBD1, pink ; CBD2, green; Ca^{2+} ions, red sphere.

Model validation by short distance measurements

The interdomain DEER distances demonstrate that the two CBDs do not undergo any significant change in their relative orientation upon Ca^{2+} binding. These interdomain distances were used to generate structural models of CBD12 in the Ca^{2+} bound and apo forms. The structural models can be utilized to experimentally validate their accuracy by making additional model-guided distance constraints as described previously (Kim et al., 2011). In order to examine whether this observation is still valid under non-cryogenic conditions, and to confirm the solution set of structural models of CBD12, short inter-probe distance measurements were made along the bridge region that links the two domains. Guided by the constructed models in conjunction with MMM distance prediction, some pairs of sites with short inter-probe distances (5~15 Å) were chosen. However, the majority of the singly or doubly labeled mutants at selected sites resulted in cw-EPR spectra which exhibited dramatic changes in lineshapes upon Ca^{2+} binding or were

dominated by fast motional components, probably due to the partial denaturation of proteins (data not shown). These initial observations imply that the sites around the bridge

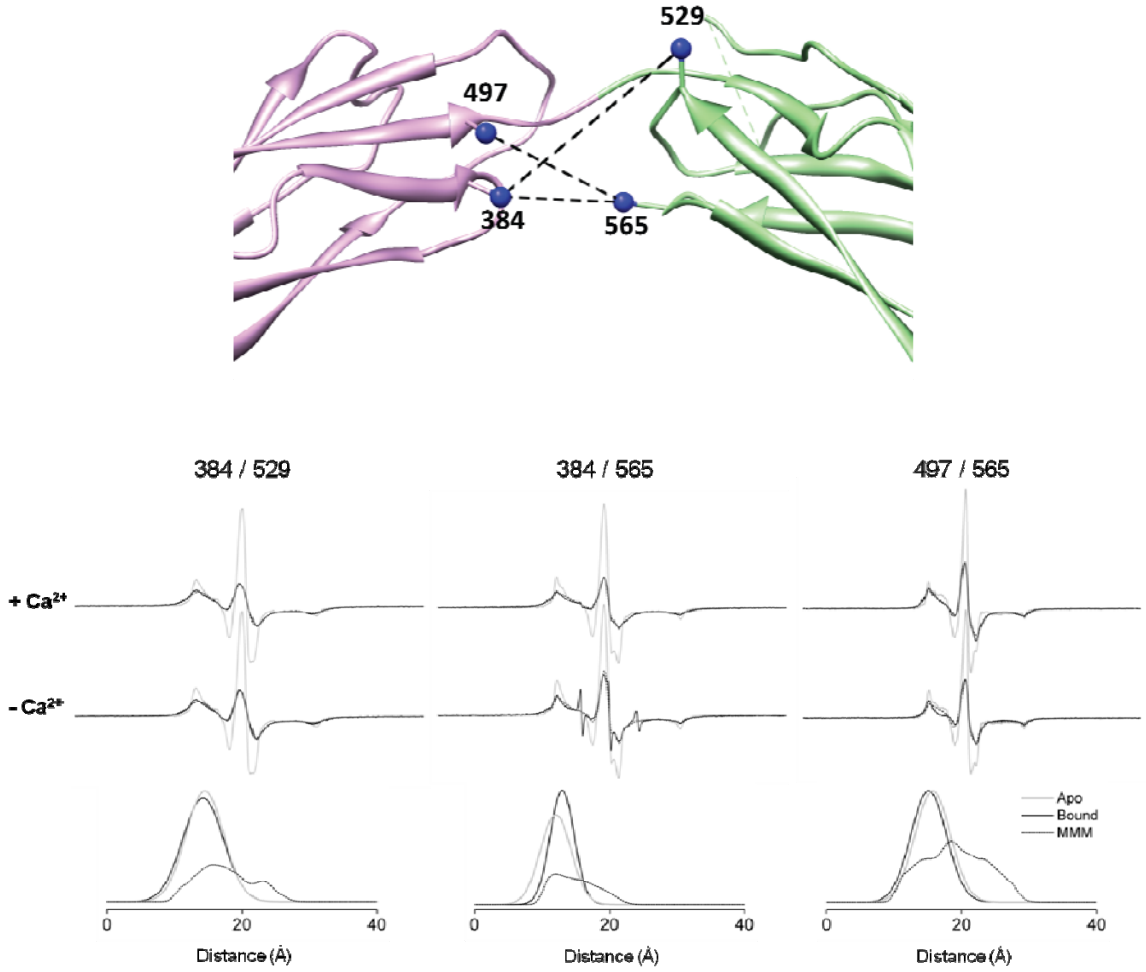

Figure 66. Exchange and dipolar couplings from doubly labeled mutants of CBD12 that have a pair of spin labels near the interdomain linker. In the top panel, three pairs of spin labeled sites that yielded strong exchange and dipolar couplings are marked as dashed lines with C_β atoms from the labeled sites as blue spheres. The model structure employed is one of the solution structures that best satisfy DEER distance constraints. The bottom panel shows CW-EPR spectra where the spectra from doubly labeled mutants (black solid line) and the sum of single spectra (grey solid line) were overlaid together with the resultant distance distributions calculated from deconvolution analysis (bound form, black solid line; apo form, grey solid line) and MMM program (dotted line).

region are critical in correct folding of CBD12. Fig. 66 displays cw-EPR spectra obtained from the three double mutants that give rise to significant lineshape broadening and their corresponding distance distributions analyzed by a conventional convolution method or the MMM program. Dipolar couplings from all three mutants were insensitive to Ca^{2+} binding, which is evident in the corresponding distance distributions, implying that there is no significant Ca^{2+}-dependent changes in the relative orientation between two CBDs at non-cryogenic conditions. Though a small population of unexpected fast motional component was observed in the cw-EPR spectrum from the Ca^{2+}-free form of the doubly labeled mutant, 384/565, the convolution method produced reasonably good fits to all dipolar coupled spectra. As shown in Fig. 66, the analyzed distance distributions from those fits agreed reasonably well with the ones from the MMM distance predictions calculated based on the constructed model.

Discussion

The effect of Ca^{2+} binding on the structure of CBD12

The Ca^{2+}-dependent modulation of NCX1 function is ascribed to the presence of the long intracellular loop of NCX1 containing a tandem array of two structurally homologous calcium binding domains. Despite the importance of this long loop region in understanding the mechanism of calcium regulation of NCX1, most structural information to date is limited to the NMR or crystal structures of two CBDs which were separately obtained from each isolated domain. However, incorporation of spin labels into the various surface sites of CBD1 and CBD2 within full length CBD12 produced dynamics information which is in good agreement with the atomic level structures of the isolated forms of CBD1 and CBD2 indicating structural features shown in the isolated domains are well conserved in CBD12. Together with intradomain DEER

distances, R1 spin labeled side chain mobility data collected from the central β-sandwich regions show that these regions undergo no significant changes upon Ca^{2+} binding, which provides a reasonable basis of treating the two CBDs as rigid bodies to a first approximation during the model construction.

In both domains, Ca^{2+} binding-induced structural changes appear to be localized to the Ca^{2+} binding loops and the F-G loop. In particular, it is interesting to note that the Ca^{2+} binding signal is transmitted to the F-G loop located at the opposite side of the β-sandwich domain as demonstrated by two intradomain DEER distances, 411-472 from CBD1 and 515-596 from CBD2, as well as spin label dynamics changes shown in residues 479 and 596.

The functional implications of the F-G loops from both CBDs are still elusive. Recently, a double deletion mutant of NCX1.1 which lacked both F-G loops was shown to retain normal Ca^{2+} regulation activity suggesting these loops are of no importance in Ca^{2+} regulation (Ottolia et al., 2009). However, several lines of evidences propose the biological relevance of F-G loops from both CBDs. The early study using a chimeric mutant of the Drosophila exchanger Calx1.1 (Dyck et al., 1998) implied the significance of the F-G loop in CBD1. Unlike other exchangers, Calx1.1, which lacks the F-G loop of CBD1, presents a negative regulatory response to Ca^{2+} (Hryshko et al., 1996). However, when the CBD1 F-G loop of cardiac NCX1 was introduced into the Calx1.1, the resultant chimeric construct restored normal calcium regulation. Additional evidence for the functional importance of the CBD1 F-G loop can be seen in proteolytic cleavage studies of this region of NCX1 and NCX3 isoforms that resulted in inactivation of exchanger function and subsequent cell death (Bano et al., 2005). Therefore, although this region was disordered in both NMR and crystal structures in both the Ca^{2+}-bound and apo states, it is probable that the CBD1 F-G loop may be stabilized in intact cells by its interaction with other parts of NCX1 or other binding partners, such as ankyrin B and thereby contribute to calcium regulation.

As in CBD1, the F-G loop in CBD2 is highly dynamic in NMR derived structures and unresolved in crystal structures. A recent NMR study using the isolated domain of CBD2 found that the F-G loop is in a highly dynamic state and its dynamics was not significantly altered by Ca^{2+} binding based upon the average S^2 values. However, R1 side chain mobility (residue 596, Fig. 59) and intradomain DEER distances (515/596 double mutant, Fig. 60) involving the F-G

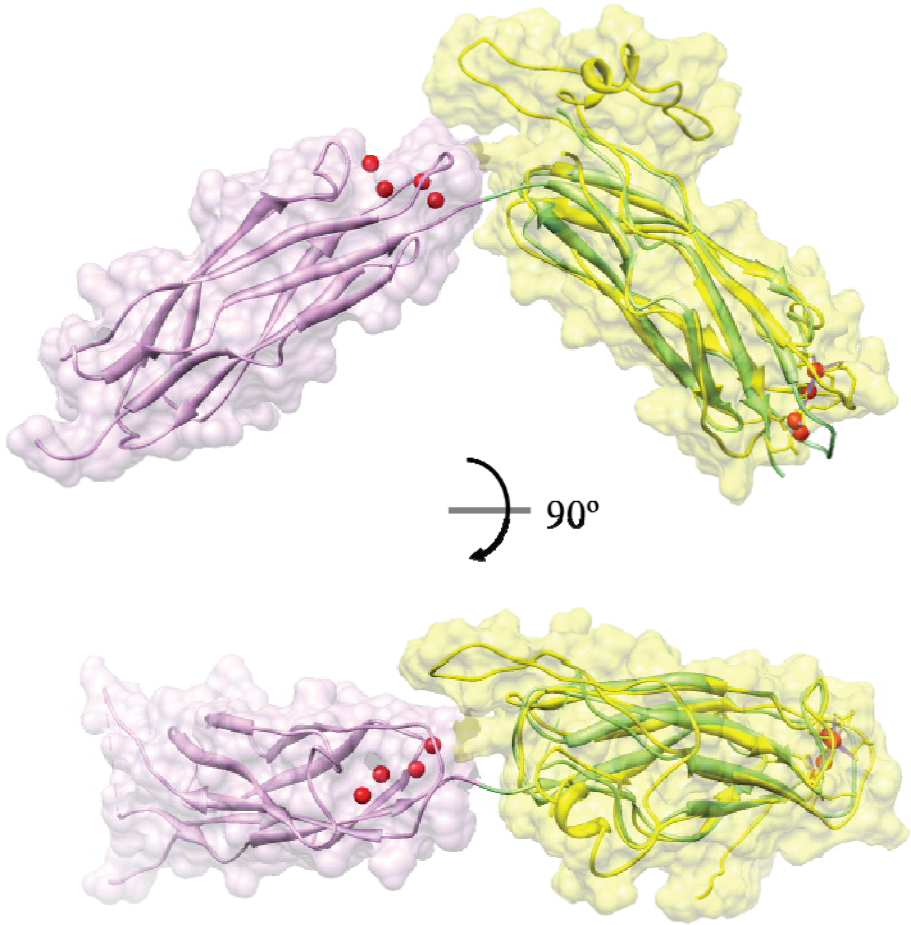

Figure 67. Structural model of CBD12 that predicts the spatial arrangement of F-G loop of CBD1. Space filling presentation was overlaid with ribbon diagram. One of structural models in the solution set that best fits the DEER distance constraints was adopted as CBD12 (CBD1, pink; CBD2, green). To explicitly model the F-G loop of CBD1, which is missing in the structural model of CBD12, NMR structure of CBD2 AD (PDB code: 2FWU) was superimposed (yellow). Calcium ions are shown in red spheres.

loop strongly imply that this region may undergo significant changes in its dynamics and conformation upon Ca^{2+} binding in the presence of nearby CBD1. These results are in line with possible functional relevance of F-G loop in CBD2. Given that the only difference between the ACDEF (NCX1.1) and AD (NCX1.4) splice variants is the presence of an additional 35 residues in the CBD2 F-G loop of the ACDEF form, the observations that the ACDEF splice variant exhibited much higher Ca^{2+} binding affinity (Hilge et al., 2009) *in vitro* and 10 times faster response of exchange function (Dyck et al., 1999) *in vivo* than the AD form indicate the involvement of the F-G loop in Ca^{2+} regulation of NCX1. Indeed, as shown in Fig. 66, when the NMR structure of CBD2 AD which contains the F-G loop is superimposed on one of the solution models, the F-G loop is placed in close proximity to the Ca^{2+} binding loops of CBD1 and there appears to be direct interactions between the two structural entities.

Construction of structural models of CBD12

One way of using sparse distance constraints to construct structural models of the complex consisting of CBD1 and CBD2 is to first generate all possible poses of the two domains using available docking algorithms or systematic grid search methods and then to filter them with the experimentally determined multiple distance constraints. One example of the successful applications of this approach has been described in Chapter III. The observations that the previously determined structures of isolated CBDs are well preserved in the CBD12 construct and that the two domains are contiguous without an intervention in primary sequence lead to the notion that CBD12 can be treated as two rigid bodies that are joined together at one end of each domain. Thus the systematic rotations of the consecutive backbone bonds linking the two domains were utilized to explore the conformational space and coarse structural models for CBD12 were generated by just determining the relative orientation between two rigid bodies using multiple DEER distance constraints with explicit spin label modeling.

To build a structural model using sparse DEER distance constraints is challenging mainly due to the uncertainty in association with the rotameric states of the R1 side chain at a given specific site. In this study, explicit modeling of the spin label was performed at each labeling site using the MMM program which determines the spatial distribution of rotamers from the rotamer library established based upon MD simulation of the R1 side chain (Polyhach et al., 2010). Even the initial versions of the rotamer library constructed on the basis of rough approximations on the sampling space and energy terms were successfully employed in the structural studies on various proteins such as the Na^+/H^+ antiporter (Hilger et al., 2007), Na^+/proline symporter PtuP (Hilger et al., 2009) of *E. coli*, and the maltose ATP-binding cassette importer $MalKGF_2$ (Grote et al., 2008).

The existence of solution models that simultaneously satisfy all the measured sparse DEER distances with high accuracy indicate that the spin label modeling work employed in this study is reasonable. In order to assess how accurately the MMM approach can predict the rotameric states of the R1 side chain which is attached on CBD1, distance distributions obtained from the collected intradomain DEER measurements were compared with those calculated from DEER simulations using MMM. As shown in Fig. 68, the two distance distributions almost overlap in the last five doubly labeled mutants of CBD12 where both spin labels reside on the β-sheet structure, indicating that explicit modeling of spin labels using MMM accurately predicts their rotameric states in CBD12. However, the first three DEER data show significant deviations from the corresponding simulations for the distance distributions. These discrepancies can be explained by the fact that one site involved in each of these DEER measurement is not located on the β-sheet. Indeed, residues 384 and 387 are on or near the linker region and residue 391 resides on the β-strand right next to the abnormal β-bulge of the A-strand. Typically, spin label modeling with MMM gives rise to better results with a site residing in β-sheet structure rather than in an α-helix or linker domain since the R1 side chain on the β-sheet is substantially restricted in its motion and orientation primarily due to steric hindrances from the residues at the i ± 2 positions and side

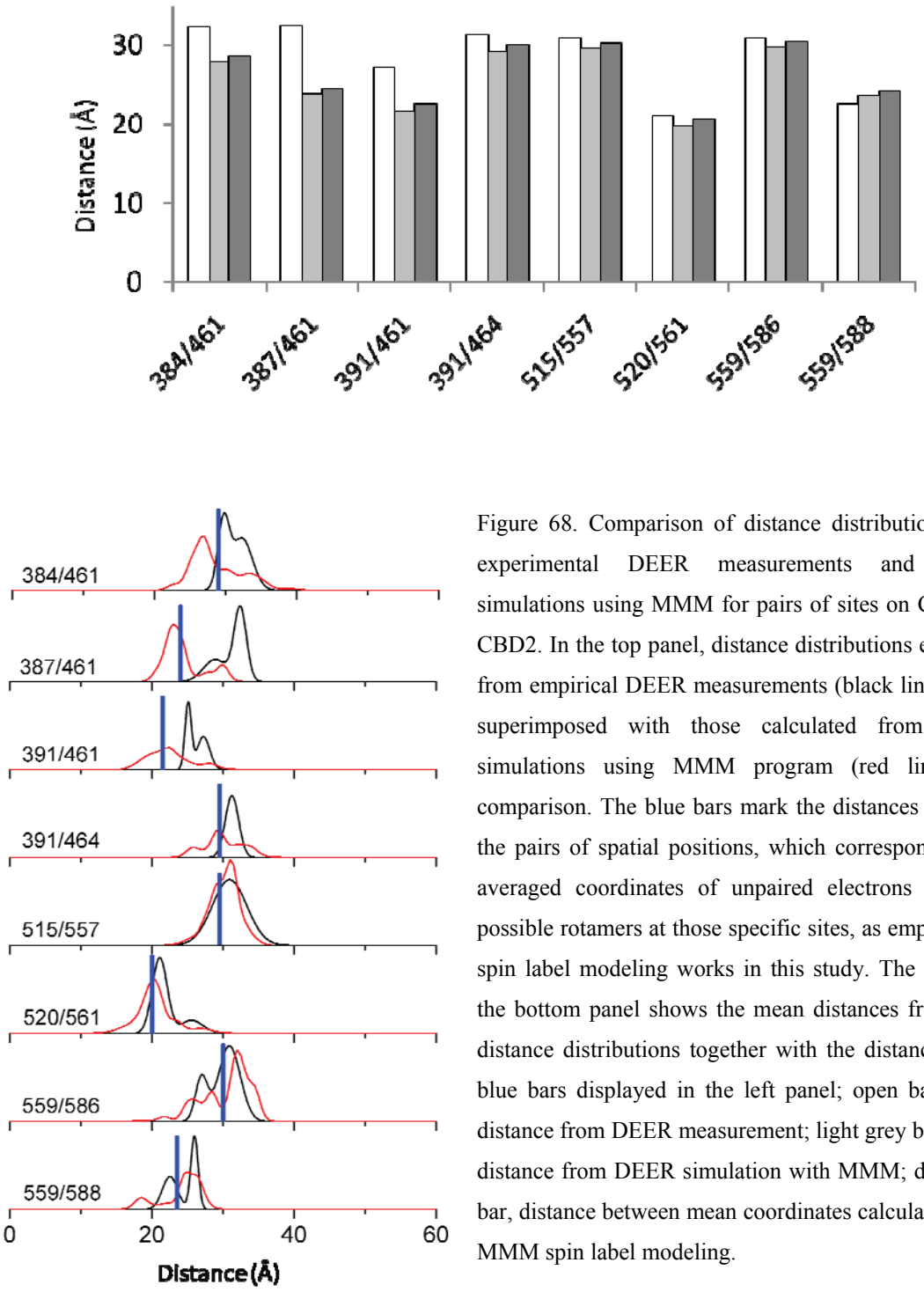

Figure 68. Comparison of distance distributions from experimental DEER measurements and DEER simulations using MMM for pairs of sites on CBD1 or CBD2. In the top panel, distance distributions extracted from empirical DEER measurements (black lines) were superimposed with those calculated from DEER simulations using MMM program (red lines) for comparison. The blue bars mark the distances between the pairs of spatial positions, which correspond to the averaged coordinates of unpaired electrons over all possible rotamers at those specific sites, as employed in spin label modeling works in this study. The graph in the bottom panel shows the mean distances from each distance distributions together with the distances from blue bars displayed in the left panel; open bar, mean distance from DEER measurement; light grey bar, mean distance from DEER simulation with MMM; dark grey bar, distance between mean coordinates calculated from MMM spin label modeling.

chains from the neighboring antiparallel β-strands. This insight suggests that the approach employed in this study can generate reliable structural models for proteins containing β-sheets.

Structural model of CBD12 and its implications in the Ca^{2+} regulation mechanism

Previously, Hilge and his colleagues proposed a model for the mechanism of Ca^{2+}-dependent NCX1 regulation with a novel topology of the long intracellular loop of NCX1, where the Ca^{2+} binding region of CBD1 is approximately 90Å away from the plasma membrane surface (Hilge et al., 2009). The essential feature of this model predicts a structural rearrangement in CBD12 involved in Ca^{2+} regulation, or more precisely, the change in the relative orientation between CBD1 and CBD2 induced by Ca^{2+} binding. Small angle X-ray scattering (SAXS) data from the same study supports this hypothesis by showing a significant decrease in maximal distance of the scattering vector upon Ca^{2+} binding in both the ACDEF and AD splice variants. However, multiple interdomain DEER distances collected from CBD12 (Fig. 62) indicate that there is no significant change in the relative orientation between the two domains, which is also supported by the recent NMR study where the structural model of CBD12 construct of AD splice variant has been generated from residual dipolar couplings (Salinas et al., 2011). These results indicate that the previously proposed mechanistic model involving rigid body movements between two CBDs is not correct. Hence, it is highly probable that the changes in SAXS data from the same construct that was used in the current study may result from conformational changes in the long F-G loop of CBD2 upon Ca^{2+} binding, rather than from the rigid body motions between the two CBDs.

In the context of its structural similarity with the CBDs in NCX1, C_2-domains provide insight into the implication of CBD12 in the mechanism of its Ca^{2+}-dependent regulation for NCX1 function. C_2-domains are one of the main Ca^{2+} binding motifs together with EF-hands and function in signal transduction or membrane trafficking in many proteins in a Ca^{2+}-dependent manner. Like CBDs, the structures of C_2-domains consist of a compact β-sandwich of two four-

stranded β-sheets with Ca^{2+} binding loops at the top of the domain. Importantly, none of the three-dimensional structures of C_2-domains determined so far showed a substantial Ca^{2+}-induced conformational change (Rizo and Sudhof, 1998). Instead, as exemplified in the binding of synaptotagmin I C_2A with syntaxin, Ca^{2+} binding to the C_2-domain was shown to result in changes in electrostatic potential of the Ca^{2+} binding region and is speculated to generate a binding surface for its binding partner (Shao et al., 1997). As seen in C_2-domains, Ca^{2+} binding to either CBD1 or CBD2 also caused substantial changes in the surface electrostatic potential of Ca^{2+} binding regions in both CBDs (Hilge et al., 2009). Taken together, these data strongly suggest that Ca^{2+} regulation on NCX1 function may be achieved through the electrostatic interactions of each Ca^{2+} binding region from CBDs with other structural elements.

The transport activity of NCX1 is modulated by integrated and differential regulation of CBD1 and CBD2. Under a low level of $[Na^+]_{in}$, the basal Ca^{2+} regulation associated with high Ca^{2+} binding affinity activate exchanger function. Functional studies using NCX1 mutants in which one or more key acidic residues on Ca^{2+} binding loops were mutated revealed that both CBD1 and CBD2 were involved in primary Ca^{2+} regulation (Besserer et al., 2007; Ottolia et al., 2009). However, the Na^+-dependent inactivation occurring with the rise of $[Na^+]_{in}$ (> 15mM) is overcome by the second Ca^{2+} regulation activity supposedly performed by CBD2 (Hilge et al., 2009). The strong correlation of the affinity and number of Ca^{2+} ions binding to CBD2 with the capability to overcome Na^+-dependent inactivation, which is evident in the comparison of NCX isoforms, indicates that the inactivation by XIP is primarily modulated by Ca^{2+} binding to CBD2 (Hilge et al., 2009).

Given that the multiple structural elements, which are distantly located within CBD12 communicate with one another to carry out differential Ca^{2+} regulation, this functional complexity in Ca^{2+} regulation is speculated to be achieved through the unique three-dimensional arrangements of CBD12 which may allow the critical interaction of CBD12 with other structural elements on their Ca^{2+} binding regions. Despite the paucity of information on the structure of the

CLD domain, it is predicted that the CLD domain may have a crucial role in the proper positioning of CBD12 or even in mediation of regulatory Ca^{2+} signals since it connects CBD12 to the transmembrane domain. NCX1 binding proteins such as Ankyrin B are other structural elements that can be considered as potentially important determinants for the correct spatial arrangement of CBD12. Previously, ankyrin B was shown to co-localize NCX1, Na^+/K^+ ATPase, and the $InsP_3$ receptor at the T-tubule microdomain of cardiomyocytes, forming a metabolon-like macro-molecular complex (Mohler et al., 2005). In particular, ankyrin B is essential in the targeting and stability of NCX1 and directly interacts with the membrane binding domain of ankyrin B (Cunha et al., 2007). Thus, the position and orientation of CBD12 will be restricted within the multi-protein complex by the interaction with ankyrin B and, potentially with other binding partners.

CHAPTER IV

CONCLUSION AND PERSPECTIVES

Structure of the cdb3-AnkD34 complex

In the current studies, site directed spin labeling, in combination with electron paramagnetic resonance (EPR) and double electron-electron resonance (DEER), has been utilized to map the binding interfaces of the two proteins in the complex and to obtain interprotein distance constraints. These data have been utilized to construct a family of structural models that are consistent with the full range of experimental data. These models indicate that an extensive area on the peripheral domain of cdb3 binds to ankyrin-Repeats 18-20 on the top loop surface of AnkD34 primarily through hydrophobic interactions. This is a previously uncharacterized surface for binding of cdb3 to AnkD34. Cross-linking experiments and a set of dipolar coupled spectra validated the binding interface that was predicted by the constructed structural models.

Since a second dimer of cdb3 is known to bind to ankyrin-Repeats 7-12 of the membrane binding domain of ankyrin-R, the current models have significant implications regarding the structural nature of a tetrameric form of AE1 that is hypothesized to be involved in binding to full-length ankyrin-R in the erythrocyte membrane.

A set of intraprotein DEER distances measured on the binding interface of cdb3 indicates that binding involves some local structural arrangement that can be accounted for local backbone movements and repacking of R1 side chains on the binding interface. The major change appears to occur in the β6/β7 hairpin loop and is predicted to have a crucial role in binding. These local structural changes on the binding interface prevented the construction of structural models at a higher resolution using explicit modeling of spin labels. These problems can be solved by molecular modeling approaches such as flexible docking in the near future.

In order to obtain insight into the whole picture of the structure of the complex containing an AE1 tetramer and the molecular mechanisms of the associated disorders, it is necessary to elucidate the structure of the complex formed by interaction of AnkD2 with the second cdb3 dimer. This will also provide a structural model of the central molecular frame in the ankyrin complex which involves a number of cytosolic proteins including a set of glycolytic enzymes and structural proteins such as protein 4.2.

Calcium binding domains of NCX1.1

Electron Paramagnetic Resonance (EPR) measurements on singly labeled constructs of CBD12 have identified the regions which undergo changes in dynamics as a result of Ca^{2+} binding. Double Electron Electron Resonance (DEER) measurements on doubly labeled constructs of CBD12 have shown that the β-sandwich regions of the CBD1 and CBD2 domains are largely insensitive to Ca^{2+} binding and that these two domains are not lengthwise anti-parallel and in close proximity as previously suggested but rather are widely separated at the N- and C-termini. Interdomain residues nearer to the apex of CBD12 are in close enough proximity to be measured by DEER. These interdomain distances have been employed to construct structural models for CBD12 in the presence and absence of Ca^{2+}. These models show that there is not a major change in the orientation of the two Ca^{2+}-binding domains relative to each other in full length CBD12 as a result of Ca^{2+} binding. Additional measurements have shown that there are changes in the structure and/or dynamics of the F-G loop regions of CBD1 and CBD2 which could potentially be involved in regulation of exchanger activity.

The current data strongly suggest that the transmission of Ca^{2+} binding signal to the transport site is mediated through the other structural elements. CLD, which links CBDs to the transmembrane domain, is predicted to contribute to Ca^{2+} regulation of exchanger activity.

Furthermore, previous studies showed that NCX1 has several binding partners including ankyrin-B and InsP3 receptors, implying the presence of macrocomplex accomplishing the complex and delicate Ca^{2+} regulation process. Thus, the molecular mechanism of the Ca^{2+} regulation by CBDs needs to be considered in the context of interactions with other domain or proteins. The changes in the conformation or dynamics of CBDs will need to be reevaluated in the full length NCX1 or in the presence of other binding proteins. Likewise, the role of the dual electrostatic switches formed by the surface of calcium binding loops needs to be examined in terms of the interactions with other structural elements.

REFERENCES

Altenbach, C., Greenhalgh, D.A., Khorana, H.G., and Hubbell, W.L. (1994). A collision gradient method to determine the immersion depth of nitroxides in lipid bilayers: application to spin-labeled mutants of bacteriorhodopsin. Proc Natl Acad Sci U S A *91*, 1667-1671.

Altenbach, C., Kusnetzow, A.K., Ernst, O.P., Hofmann, K.P., and Hubbell, W.L. (2008). High-resolution distance mapping in rhodopsin reveals the pattern of helix movement due to activation. Proc Natl Acad Sci U S A *105*, 7439-7444.

An, X., Debnath, G., Guo, X., Liu, S., Lux, S.E., Baines, A., Gratzer, W., and Mohandas, N. (2005). Identification and functional characterization of protein 4.1R and actin-binding sites in erythrocyte beta spectrin: regulation of the interactions by phosphatidylinositol-4,5-bisphosphate. Biochemistry *44*, 10681-10688.

An, X., Guo, X., Zhang, X., Baines, A.J., Debnath, G., Moyo, D., Salomao, M., Bhasin, N., Johnson, C., Discher, D*., et al.* (2006a). Conformational stabilities of the structural repeats of erythroid spectrin and their functional implications. J Biol Chem *281*, 10527-10532.

An, X., Lecomte, M.C., Chasis, J.A., Mohandas, N., and Gratzer, W. (2002). Shear-response of the spectrin dimer-tetramer equilibrium in the red blood cell membrane. J Biol Chem *277*, 31796-31800.

An, X., Zhang, X., Debnath, G., Baines, A.J., and Mohandas, N. (2006b). Phosphatidylinositol-4,5-biphosphate (PIP2) differentially regulates the interaction of human erythrocyte protein 4.1 (4.1R) with membrane proteins. Biochemistry *45*, 5725-5732.

Appell, K.C., and Low, P.S. (1981). Partial structural characterization of the cytoplasmic domain of the erythrocyte membrane protein, band 3. J Biol Chem *256*, 11104-11111.

Askin, D., Bloomberg, G.B., Chambers, E.J., and Tanner, M.J. (1998). NMR solution structure of a cytoplasmic surface loop of the human red cell anion transporter, band 3. Biochemistry *37*, 11670-11678.

Asteggiano, C., Berberian, G., and Beauge, L. (2001). Phosphatidyl inositol-4,5-bisphosphate bound to bovine cardiac Na^+/Ca^{2+} exchanger displays a MgATP regulation similar to that of the exchange fluxes. Eur J Biochem *268*, 437-442.

Bano, D., Young, K.W., Guerin, C.J., Lefeuvre, R., Rothwell, N.J., Naldini, L., Rizzuto, R., Carafoli, E., and Nicotera, P. (2005). Cleavage of the plasma membrane Na^+/Ca^{2+} exchanger in excitotoxicity. Cell *120*, 275-285.

Bennett, V., and Baines, A.J. (2001). Spectrin and ankyrin-based pathways: metazoan inventions for integrating cells into tissues. Physiol Rev *81*, 1353-1392.

Bennett, V., and Healy, J. (2009). Membrane domains based on ankyrin and spectrin associated with cell-cell interactions. Cold Spring Harb Perspect Biol *1*, a003012.

Berberian, G., Hidalgo, C., DiPolo, R., and Beauge, L. (1998). ATP stimulation of Na^+/Ca^{2+} exchange in cardiac sarcolemmal vesicles. Am J Physiol *274*, C724-733.

Berengian, A.R., Bova, M.P., and McHaourab, H.S. (1997). Structure and function of the conserved domain in alphaA-crystallin. Site-directed spin labeling identifies a beta-strand located near a subunit interface. Biochemistry *36*, 9951-9957.

Bers, D.M. (2002). Cardiac excitation-contraction coupling. Nature *415*, 198-205.

Bers, D.M., and Guo, T. (2005). Calcium signaling in cardiac ventricular myocytes. Ann N Y Acad Sci *1047*, 86-98.

Besserer, G.M., Ottolia, M., Nicoll, D.A., Chaptal, V., Cascio, D., Philipson, K.D., and Abramson, J. (2007). The second Ca^{2+}-binding domain of the Na^{+}/Ca^{2+} exchanger is essential for regulation: crystal structures and mutational analysis. Proc Natl Acad Sci U S A *104*, 18467-18472.

Bhatnagar, J., Borbat, P.P., Pollard, A.M., Bilwes, A.M., Freed, J.H., and Crane, B.R. (2010). Structure of the ternary complex formed by a chemotaxis receptor signaling domain, the CheA histidine kinase, and the coupling protein CheW as determined by pulsed dipolar spectroscopy. Biochemistry *49*, 3824-3841.

Bhattacharyya, R., Das, A.K., Moitra, P.K., Pal, B., Mandal, I., and Basu, J. (1999). Mapping of a palmitoylatable band 3-binding domain of human erythrocyte membrane protein 4.2. Biochem J *340 (Pt 2)*, 505-512.

Blackman, S.M., Piston, D.W., and Beth, A.H. (1998). Oligomeric state of human erythrocyte band 3 measured by fluorescence resonance energy homotransfer. Biophys J *75*, 1117-1130.

Blaustein, M.P., and Lederer, W.J. (1999). Sodium/calcium exchange: its physiological implications. Physiol Rev *79*, 763-854.

Borbat, P.P., and Freed, J.H. (2000). Distance Measurements in Biological Systems by EPR, Vol 19 (New York, Kluwer Academic).

Borbat, P.P., and Freed, J.H. (2007). Measuring distances by pulsed dipolar ESR spectroscopy: spin-labeled histidine kinases. Methods Enzymol *423*, 52-116.

Borbat, P.P., McHaourab, H.S., and Freed, J.H. (2002). Protein structure determination using long-distance constraints from double-quantum coherence ESR: study of T4 lysozyme. J Am Chem Soc *124*, 5304-5314.

Bossuyt, J., Taylor, B.E., James-Kracke, M., and Hale, C.C. (2002). Evidence for cardiac sodium-calcium exchanger association with caveolin-3. FEBS Lett *511*, 113-117.

Bourguignon, L.Y., Chu, A., Jin, H., and Brandt, N.R. (1995). Ryanodine receptor-ankyrin interaction regulates internal Ca^{2+} release in mouse T-lymphoma cells. J Biol Chem *270*, 17917-17922.

Bourguignon, L.Y., Jin, H., Iida, N., Brandt, N.R., and Zhang, S.H. (1993). The involvement of ankyrin in the regulation of inositol 1,4,5-trisphosphate receptor-mediated internal Ca^{2+} release from Ca^{2+} storage vesicles in mouse T-lymphoma cells. J Biol Chem *268*, 7290-7297.

Breukels, V., and Vuister, G.W. (2010). Binding of calcium is sensed structurally and dynamically throughout the second calcium-binding domain of the sodium/calcium exchanger. Proteins *78*, 1813-1824.

Budil, D.E., Earle, K.A., Freed, J.H. (1993). Full determination of teh rotational diffusion tensor by electron paramagnetic resonance at 250 GHz. J Phys Chem *97*, 1294-1303.

Budil, D.E., Sale, K.L., Khairy, K.A., and Fajer, P.G. (2006). Calculating slow-motional electron paramagnetic resonance spectra from molecular dynamics using a diffusion operator approach. J Phys Chem A *110*, 3703-3713.

Bustos, S.P., and Reithmeier, R.A. (2006). Structure and stability of hereditary spherocytosis mutants of the cytosolic domain of the erythrocyte anion exchanger 1 protein. Biochemistry *45*, 1026-1034.

Cabantchik, Z.I., and Rothstein, A. (1972). The nature of the membrane sites controlling anion permeability of human red blood cells as determined by studies with disulfonic stilbene derivatives. J Membr Biol *10*, 311-330.

Cai, X., and Lytton, J. (2004). The cation/Ca(2+) exchanger superfamily: phylogenetic analysis and structural implications. Mol Biol Evol *21*, 1692-1703.

Campanella, M.E., Chu, H., and Low, P.S. (2005). Assembly and regulation of a glycolytic enzyme complex on the human erythrocyte membrane. Proc Natl Acad Sci U S A *102*, 2402-2407.

Campanella, M.E., Chu, H., Wandersee, N.J., Peters, L.L., Mohandas, N., Gilligan, D.M., and Low, P.S. (2008). Characterization of glycolytic enzyme interactions with murine erythrocyte membranes in wild-type and membrane protein knockout mice. Blood *112*, 3900-3906.

Cartron, J.P. (2001). Rh-deficiency syndrome. Lancet *358 Suppl*, S57.

Casey, J.R., and Reithmeier, R.A. (1991). Analysis of the oligomeric state of Band 3, the anion transport protein of the human erythrocyte membrane, by size exclusion high performance liquid chromatography. Oligomeric stability and origin of heterogeneity. J Biol Chem *266*, 15726-15737.

Chang, S.H., and Low, P.S. (2003). Identification of a critical ankyrin-binding loop on the cytoplasmic domain of erythrocyte membrane band 3 by crystal structure analysis and site-directed mutagenesis. J Biol Chem *278*, 6879-6884.

Chaptal, V., Ottolia, M., Mercado-Besserer, G., Nicoll, D.A., Philipson, K.D., and Abramson, J. (2009). Structure and functional analysis of a Ca^{2+} sensor mutant of the Na^{+}/Ca^{2+} exchanger. J Biol Chem *284*, 14688-14692.

Che, A., Morrison, I.E., Pan, R., and Cherry, R.J. (1997). Restriction by ankyrin of band 3 rotational mobility in human erythrocyte membranes and reconstituted lipid vesicles. Biochemistry *36*, 9588-9595.

Chiang, Y.W., Borbat, P.P., and Freed, J.H. (2005). The determination of pair distance distributions by pulsed ESR using Tikhonov regularization. J Magn Reson *172*, 279-295.

Chothia, C. (1975). The nature of the accessible and buried surfaces in proteins. J Mol Biol *105*, 1-14.

Chu, H., Breite, A., Ciraolo, P., Franco, R.S., and Low, P.S. (2008). Characterization of the deoxyhemoglobin binding site on human erythrocyte band 3: implications for O2 regulation of erythrocyte properties. Blood *111*, 932-938.

Chu, H., and Low, P.S. (2006). Mapping of glycolytic enzyme-binding sites on human erythrocyte band 3. Biochem J *400*, 143-151.

Collins, A., Somlyo, A.V., and Hilgemann, D.W. (1992). The giant cardiac membrane patch method: stimulation of outward Na^{+}/Ca^{2+} exchange current by MgATP. J Physiol *454*, 27-57.

Columbus, L., and Hubbell, W.L. (2002). A new spin on protein dynamics. Trends Biochem Sci *27*, 288-295.

Columbus, L., and Hubbell, W.L. (2004). Mapping backbone dynamics in solution with site-directed spin labeling: GCN4-58 bZip free and bound to DNA. Biochemistry *43*, 7273-7287.

Columbus, L., Kalai, T., Jeko, J., Hideg, K., and Hubbell, W.L. (2001). Molecular motion of spin labeled side chains in alpha-helices: analysis by variation of side chain structure. Biochemistry *40*, 3828-3846.

Cuello, L.G., Cortes, D.M., and Perozo, E. (2004). Molecular architecture of the KvAP voltage-dependent K+ channel in a lipid bilayer. Science *306*, 491-495.

Cunha, S.R., Bhasin, N., and Mohler, P.J. (2007). Targeting and stability of Na/Ca exchanger 1 in cardiomyocytes requires direct interaction with the membrane adaptor ankyrin-B. J Biol Chem *282*, 4875-4883.

Davis, J.Q., and Bennett, V. (1994). Ankyrin binding activity shared by the neurofascin/L1/NrCAM family of nervous system cell adhesion molecules. J Biol Chem *269*, 27163-27166.

Davis, J.Q., Lambert, S., and Bennett, V. (1996). Molecular composition of the node of Ranvier: identification of ankyrin-binding cell adhesion molecules neurofascin (mucin+/third FNIII domain-) and NrCAM at nodal axon segments. J Cell Biol *135*, 1355-1367.

Davis, L., Lux, S.E., and Bennett, V. (1989). Mapping the ankyrin-binding site of the human erythrocyte anion exchanger. J Biol Chem *264*, 9665-9672.

Davis, L.H., Davis, J.Q., and Bennett, V. (1992). Ankyrin-Regulation: an alternatively spliced segment of the regulatory domain functions as an intramolecular modulator. J Biol Chem *267*, 18966-18972.

Davis, L.H., Otto, E., and Bennett, V. (1991). Specific 33-residue repeat(s) of erythrocyte ankyrin associate with the anion exchanger. J Biol Chem *266*, 11163-11169.

Delaunay, J. (2002). Molecular basis of red cell membrane disorders. Acta Haematol *108*, 210-218.

Delaunay, J. (2007). The molecular basis of hereditary red cell membrane disorders. Blood Rev *21*, 1-20.

DeSensi, S.C., Rangel, D.P., Beth, A.H., Lybrand, T.P., and Hustedt, E.J. (2008). Simulation of nitroxide electron paramagnetic resonance spectra from brownian trajectories and molecular dynamics simulations. Biophys J *94*, 3798-3809.

DeSilva, T.M., Peng, K.C., Speicher, K.D., and Speicher, D.W. (1992). Analysis of human red cell spectrin tetramer (head-to-head) assembly using complementary univalent peptides. Biochemistry *31*, 10872-10878.

Dhermy, D., Galand, C., Bournier, O., Boulanger, L., Cynober, T., Schismanoff, P.O., Bursaux, E., Tchernia, G., Boivin, P., and Garbarz, M. (1997). Heterogenous band 3 deficiency in hereditary spherocytosis related to different band 3 gene defects. Br J Haematol *98*, 32-40.

Ding, Y., Casey, J.R., and Kopito, R.R. (1994). The major kidney AE1 isoform does not bind ankyrin (Ank1) in vitro. An essential role for the 79 NH2-terminal amino acid residues of band 3. J Biol Chem *269*, 32201-32208.

Ding, Y., Kobayashi, S., and Kopito, R. (1996). Mapping of ankyrin binding determinants on the erythroid anion exchanger, AE1. J Biol Chem *271*, 22494-22498.

DiPolo, R., and Beauge, L. (2006). Sodium/calcium exchanger: influence of metabolic regulation on ion carrier interactions. Physiol Rev *86*, 155-203.

Dong, J., Yang, G., and McHaourab, H.S. (2005). Structural basis of energy transduction in the transport cycle of MsbA. Science *308*, 1023-1028.

Dyck, C., Maxwell, K., Buchko, J., Trac, M., Omelchenko, A., Hnatowich, M., and Hryshko, L.V. (1998). Structure-function analysis of CALX1.1, a Na^{+}/Ca^{2+} exchanger from Drosophila. Mutagenesis of ionic regulatory sites. J Biol Chem *273*, 12981-12987.

Dyck, C., Omelchenko, A., Elias, C.L., and Qudenau, B.D. (1999a). Ionic regulatory properties of brain and kidney splice variants of the NCX1 Na^{+}/Ca^{2+} exchanger. J Gen Physiol *114*, 701-711.

Dyck, C., Omelchenko, A., Elias, C.L., Quednau, B.D., Philipson, K.D., Hnatowich, M., and Hryshko, L.V. (1999b). Ionic regulatory properties of brain and kidney splice variants of the NCX1 Na(+)-Ca(2+) exchanger. J Gen Physiol *114*, 701-711.

Eaton, S.S., Eaton, G. R. (2000). Distance mearuements in biological systems by EPR, Vol 19 (New York, Kluwer Academic/Plenum Publishers Inc).

Eber, S., and Lux, S.E. (2004). Hereditary spherocytosis--defects in proteins that connect the membrane skeleton to the lipid bilayer. Semin Hematol *41*, 118-141.

Eber, S.W., Gonzalez, J.M., Lux, M.L., Scarpa, A.L., Tse, W.T., Dornwell, M., Herbers, J., Kugler, W., Ozcan, R., Pekrun, A.*, et al.* (1996). Ankyrin-1 mutations are a major cause of dominant and recessive hereditary spherocytosis. Nat Genet *13*, 214-218.

Endeward, V., Cartron, J.P., Ripoche, P., and Gros, G. (2008). RhAG protein of the Rhesus complex is a CO2 channel in the human red cell membrane. FASEB J *22*, 64-73.

Fajer, M.I., Li, H., Yang, W., and fajer, P.G. (2007). Mapping electron paramagnetic resonance spin label conformations by the simulated scaling method. J Amer Chem Soc *129*, 13840-13846.

Fajer, P. (2000). Electron spin resonance spectroscopy labeling in peptide and protein analysis (Jonh Wiley and Sons Ltd.).

Falke, J.J., and Chan, S.I. (1985). Evidence that anion transport by band 3 proceeds via a ping-pong mechanism involving a single transport site. A 35 Cl NMR study. J Biol Chem *260*, 9537-9544.

Fanucci, G.E., and Cafiso, D.S. (2006). Recent advances and applications of site-directed spin labeling. Curr Opin Struct Biol *16*, 644-653.

Farahbakhsh, Z.T., Altenbach, C., and Hubbell, W.L. (1992). Spin labeled cysteines as sensors for protein-lipid interaction and conformation in rhodopsin. Photochem Photobiol *56*, 1019-1033.

Farrens, D.L., Altenbach, C., Yang, K., Hubbell, W.L., and Khorana, H.G. (1996). Requirement of rigid-body motion of transmembrane helices for light activation of rhodopsin. Science *274*, 768-770.

Gabb, H.A., Jackson, R.M., and Sternberg, M.J. (1997). Modelling protein docking using shape complementarity, electrostatics and bioichemical information. J Mol Biol *272*, 106-120.

Gallagher, P.G. (2004). Hereditary elliptocytosis: spectrin and protein 4.1R. Semin Hematol *41*, 142-164.

Gallagher, P.G., and Forget, B.G. (1997). Hematologically important mutations: band 3 and protein 4.2 variants in hereditary spherocytosis. Blood Cells Mol Dis *23*, 417-421.

Gallagher, P.G., and Jarolim, P., eds. (2005). Red cell membrane disorders, 4th edn (WB Saunders, Philadelphia, PA).

Gargaro, A.R., Bloomberg, G.B., Dempsey, C.E., Murray, M., and Tanner, M.J. (1994). The solution structures of the first and second transmembrane-spanning segments of band 3. Eur J Biochem *221*, 445-454.

Gray, J.J., Moughon, S., Wang, C., Schueler-Furman, O., Kuhlman, B., Rohl, C.A., and Baker, D. (2003). Protein-protein docking with simultaneous optimization of rigid-body displacement and side-chain conformations. J Mol Biol *331*, 281-299.

Grinstein, S., Ship, S., and Rothstein, A. (1978). Anion transport in relation to proteolytic dissection of band 3 protein. Biochim Biophys Acta *507*, 294-304.

Grote, M., Bordignon, E., Polyhach, Y., Jeschke, G., Steinhoff, H.J., and Schneider, E. (2008). A comparative electron paramagnetic resonance study of the nucleotide-binding domains' catalytic cycle in the assembled maltose ATP-binding cassette importer. Biophys J *95*, 2924-2938.

Groves, J.D., and Tanner, M.J. (1995). Co-expressed complementary fragments of the human red cell anion exchanger (band 3, AE1) generate stilbene disulfonate-sensitive anion transport. J Biol Chem *270*, 9097-9105.

Gunn, R.B., and Frohlich, O. (1979). Asymmetry in the mechanism for anion exchange in human red blood cell membranes. Evidence for reciprocating sites that react with one transported anion at a time. J Gen Physiol *74*, 351-374.

Guo, Z., Cascio, D., Hideg, K., and Hubbell, W.L. (2008). Structural determinants of nitroxide motion in spin-labeled proteins: solvent-exposed sites in helix B of T4 lysozyme. Protein Sci *17*, 228-239.

Guo, Z., Cascio, D., Hideg, K., Kalai, T., and Hubbell, W.L. (2007). Structural determinants of nitroxide motion in spin-labeled proteins: tertiary contact and solvent-inaccessible sites in helix G of T4 lysozyme. Protein Sci *16*, 1069-1086.

Hall, T.G., and Bennett, V. (1987). Regulatory domains of erythrocyte ankyrin. J Biol Chem *262*, 10537-10545.

Hanspal, M., Golan, D.E., Smockova, Y., Yi, S.J., Cho, M.R., Liu, S.C., and Palek, J. (1998). Temporal synthesis of band 3 oligomers during terminal maturation of mouse erythroblasts. Dimers and tetramers exist in the membrane as preformed stable species. Blood *92*, 329-338.

Hanspal, M., Yoon, S.H., Yu, H., Hanspal, J.S., Lambert, S., Palek, J., and Prchal, J.T. (1991). Molecular basis of spectrin and ankyrin deficiencies in severe hereditary spherocytosis: evidence implicating a primary defect of ankyrin. Blood *77*, 165-173.

Harrison, M.L., Isaacson, C.C., Burg, D.L., Geahlen, R.L., and Low, P.S. (1994). Phosphorylation of human erythrocyte band 3 by endogenous p72syk. J Biol Chem *269*, 955-959.

He, Z., Feng, S., Tong, Q., Hilgemann, D.W., and Philipson, K.D. (2000). Interaction of PIP(2) with the XIP region of the cardiac Na/Ca exchanger. Am J Physiol Cell Physiol *278*, C661-666.

Herrick, D.Z., Kuo, W., Huang, H., Schwieters, C.D., Ellena, J.F., and Cafiso, D.S. (2009). Solution and membrane-bound conformations of the tandem C2A and C2B domains of synaptotagmin 1: Evidence for bilayer bridging. J Mol Biol *390*, 913-923.

Hilge, M., Aelen, J., Foarce, A., Perrakis, A., and Vuister, G.W. (2009). Ca^{2+} regulation in the Na^{+}/Ca^{2+} exchanger features a dual electrostatic switch mechanism. Proc Natl Acad Sci USA *106*, 14333-14338.

Hilge, M., Aelen, J., and Vuister, G.W. (2006). Ca^{2+} regulation in the Na^{+}/Ca^{2+} exchanger involves two markedly different Ca^{2+} sensors. Mol Cell *22*, 15-25.

Hilgemann, D.W. (1990). Regulation and deregulation of cardiac Na^{+}/Ca^{2+} exchange in giant excised sarcolemmal membrane patches. Nature *344*, 242-245.

Hilgemann, D.W., and Ball, R. (1996). Regulation of cardiac Na^{+}/Ca^{2+} exchange and KATP potassium channels by PIP2. Science *273*, 956-959.

Hilgemann, D.W., Collins, A., and Matsuoka, S. (1992). Steady-state and dynamic properties of cardiac sodium-calcium exchange. Secondary modulation by cytoplasmic calcium and ATP. J Gen Physiol *100*, 933-961.

Hilger, D., Polyhach, Y., Jung, H., and Jeschke, G. (2009). Backbone structure of transmembrane domain IX of the Na+/proline transporter PutP of Escherichia coli. Biophys J *96*, 217-225.

Hilger, D., Polyhach, Y., Padan, E., Jung, H., and Jeschke, G. (2007). High-resolution structure of a Na^+/H^+ antiporter dimer obtained by pulsed electron paramagnetic resonance distance measurements. Biophys J *93*, 3675-3683.

Hryshko, L.V., Matsuoka, S., Nicoll, D.A., Weiss, J.N., Schwarz, E.M., Benzer, S., and Philipson, K.D. (1996). Anomalous regulation of the Drosophila Na^+/Ca^{2+} exchanger by Ca^{2+}. J Gen Physiol *108*, 67-74.

Huang, C.H., Cheng, G., Liu, Z., Chen, Y., Reid, M.E., Halverson, G., and Okubo, Y. (1999). Molecular basis for Rh(null) syndrome: identification of three new missense mutations in the Rh50 glycoprotein gene. Am J Hematol *62*, 25-32.

Hubbell, W.L., Cafiso, D.S., and Altenbach, C. (2000). Identifying conformational changes with site-directed spin labeling. Nat Struct Biol *7*, 735-739.

Hubbell, W.L., Gross, A., Langen, R., and Lietzow, M.A. (1998). Recent advances in site-directed spin labeling of proteins. Curr Opin Struct Biol *8*, 649-656.

Hubbell, W.L., McHaourab, H.S., Altenbach, C., and Lietzow, M.A. (1996). Watching proteins move using site-directed spin labeling. Structure *4*, 779-783.

Huber, M., Lindgren, M., Hammarstrom, P., Martensson, L.G., Carlsson, U., Eaton, G.R., and Eaton, S.S. (2001). Phase memory relaxation times of spin labels in human carbonic anhydrase II: pulsed EPR to determine spin label location. Biophys Chem *94*, 245-256.

Hustedt, E.J., and Beth, A.H. (1999). Nitroxide spin-spin interactions: applications to protein structure and dynamics. Annu Rev Biophys Biomol Struct *28*, 129-153.

Hustedt, E.J., Stein, R.A., Sethaphong, L., Brandon, S., Zhou, Z., and Desensi, S.C. (2006). Dipolar coupling between nitroxide spin labels: the development and application of a tether-in-a-cone model. Biophys J *90*, 340-356.

Inoue, T., Kanzaki, A., Kaku, M., Yawata, A., Takezono, M., Okamoto, N., Wada, H., Sugihara, T., Yamada, O., Katayama, Y.*, et al.* (1998). Homozygous missense mutation (band 3 Fukuoka: G130R): a mild form of hereditary spherocytosis with near-normal band 3 content and minimal changes of membrane ultrastructure despite moderate protein 4.2 deficiency. Br J Haematol *102*, 932-939.

Ipsaro, J.J., and Mondragon, A. (2010). Structural basis for spectrin recognition by ankyrin. Blood *115*, 4093-4101.

Isas, J.M., Langen, R., Haigler, H.T., and Hubbell, W.L. (2002). Structure and dynamics of a helical hairpin and loop region in annexin 12: a site-directed spin labeling study. Biochemistry *41*, 1464-1473.

Iwamoto, T., Nakamura, T.Y., Pan, Y., Uehara, A., Imanaga, I., and Shigekawa, M. (1999). Unique topology of the internal repeats in the cardiac Na^+/Ca^{2+} exchanger. FEBS Lett *446*, 264-268.

Iwamoto, T., Uehara, A., Imanaga, I., and Shigekawa, M. (2000). The Na^+/Ca^{2+} exchanger NCX1 has oppositely oriented reentrant loop domains that contain conserved aspartic acids whose mutation alters its apparent Ca^{2+} affinity. J Biol Chem *275*, 38571-38580.

Jarolim, P., Murray, J.L., Rubin, H.L., Taylor, W.M., Prchal, J.T., Ballas, S.K., Snyder, L.M., Chrobak, L., Melrose, W.D., Brabec, V.*, et al.* (1996). Characterization of 13 novel band 3 gene defects in hereditary spherocytosis with band 3 deficiency. Blood *88*, 4366-4374.

Jarolim, P., Palek, J., Rubin, H.L., Prchal, J.T., Korsgren, C., and Cohen, C.M. (1992). Band 3 Tuscaloosa: Pro327----Arg327 substitution in the cytoplasmic domain of erythrocyte band 3 protein associated with spherocytic hemolytic anemia and partial deficiency of protein 4.2. Blood *80*, 523-529.

Jenkins, S.M., and Bennett, V. (2001). Ankyrin-G coordinates assembly of the spectrin-based membrane skeleton, voltage-gated sodium channels, and L1 CAMs at Purkinje neuron initial segments. J Cell Biol *155*, 739-746.

Jennings, M.L. (1982). Stoichiometry of a half-turnover of band 3, the chloride transport protein of human erythrocytes. J Gen Physiol *79*, 169-185.

Jeschke, G., Bender, A., Paulsen, H., Zimmermann, H., and Godt, A. (2004). Sensitivity enhancement in pulse EPR distance measurements. J Magn Reson *169*, 1-12.
John, S.A., Ribalet, B., Weiss, J.N., Philipson, K.D., and Ottolia, M. (2011). Ca^{2+}-dependent structural rearrangements within Na^{+}/Ca^{2+} exchanger dimers. Proc Natl Acad Sci U S A *108*, 1699-1704.

Johnson, C.P., Tang, H.Y., Carag, C., Speicher, D.W., and Discher, D.E. (2007). Forced unfolding of proteins within cells. Science *317*, 663-666.

Johnson, E., Bruschweiler-Li, L., Showalter, S.A., Vuister, G.W., Zhang, F., and Bruschweiler, R. (2008). Structure and dyanmics of Ca^{2+}-binding domain 1 of the Na^{+}/Ca^{2+} exchanger in the presence and absence of Ca^{2+}. J Mol Biol *377*, 945-955.

Kalomiris, E.L., and Bourguignon, L.Y. (1988). Mouse T lymphoma cells contain a transmembrane glycoprotein (GP85) that binds ankyrin. J Cell Biol *106*, 319-327.

Kang, T.M., and Hilgemann, D.W. (2004). Multiple transport modes of the cardiac Na^{+}/Ca^{2+} exchanger. Nature (London) *427*, 544-548.

Kanki, T., Young, M.T., Sakaguchi, M., Hamasaki, N., and Tanner, M.J. (2003). The N-terminal region of the transmembrane domain of human erythrocyte band 3. Residues critical for membrane insertion and transport activity. J Biol Chem *278*, 5564-5573.

Karinch, A.M., Zimmer, W.E., and Goodman, S.R. (1990). The identification and sequence of the actin-binding domain of human red blood cell beta-spectrin. J Biol Chem *265*, 11833-11840.

Katz, C., Benyamini, H., Rotem, S., Lebendiker, M., Danieli, T., Iosub, A., Refaely, H., Dines, M., Bronner, V., Bravman, T.*, et al.* (2008). Molecular basis of the interaction between the antiapoptotic Bcl-2 family proteins and the proapoptotic protein ASPP2. Proc Natl Acad Sci U S A *105*, 12277-12282.

Kauffman, K.W., Lemmon, G.H., DeLuca, S.L., Sheehan, J.H., and Meiler, J. (2010). Practically useful: What the Rosetta modeling suite can do for you. Biochemistry *49*, 2987-2998.

Khan, A.A., Hanada, T., Mohseni, M., Jeong, J.J., Zeng, L., Gaetani, M., Li, D., Reed, B.C., Speicher, D.W., and Chishti, A.H. (2008). Dematin and adducin provide a novel link between the spectrin cytoskeleton and human erythrocyte membrane by directly interacting with glucose transporter-1. J Biol Chem *283*, 14600-14609.

Kim, S., Brandon, S., Zhou, Z., Cobb, C.E., Edwards, S.J., Moth, C.W., Parry, C.S., Smith, J.A., Lybrand, T.P., Hustedt, E.J.*, et al.* (2011). Determination of structural models of the complex between the cytoplasmic domain of erythrocyte band 3 and ankyrin-R repeats 13-24. J Biol Chem *286*, 20746-20757.

Kinjo, T.G., Szerencsei, R.T., and Schnetkamp, P.P. (2007). Topologic investigation of the NCKX2 Na^+/Ca^{2+}-K+ exchanger alpha-repeats. Ann N Y Acad Sci *1099*, 34-39.

Kizhatil, K., Davis, J.Q., Davis, L., Hoffman, J., Hogan, B.L., and Bennett, V. (2007). Ankyrin-G is a molecular partner of E-cadherin in epithelial cells and early embryos. J Biol Chem *282*, 26552-26561.

Kofuji, P., Lederer, W.J., and Schulze, D.H. (1994). Mutually exclusive and cassette exons underlie alternatively spliced isoforms of the Na/Ca exchanger. J Biol Chem *269*, 5145-5149.

Kohl, A., Amstutz, P., Parizek, P., Binz, H.K., Briand, C., Capitani, G., Forrer, P., Pluckthun, A., and Grutter, M.G. (2005). Allosteric inhibition of aminoglycoside phosphotransferase by a designed ankyrin-Repeat protein. Structure *13*, 1131-1141.

Kohl, A., Binz, H.K., Forrer, P., Stumpp, M.T., Pluckthun, A., and Grutter, M.G. (2003). Designed to be stable: crystal structure of a consensus ankyrin-Repeat protein. Proc Natl Acad Sci U S A *100*, 1700-1705.

Korsgren, C., and Cohen, C.M. (1986). Purification and properties of human erythrocyte band 4.2. Association with the cytoplasmic domain of band 3. J Biol Chem *261*, 5536-5543.

Korsgren, C., and Cohen, C.M. (1988). Associations of human erythrocyte band 4.2. Binding to ankyrin and to the cytoplasmic domain of band 3. J Biol Chem *263*, 10212-10218.

Kuo, W., Herrick, D.Z., and Cafiso, D.S. Phosphatidylinositol 4,5-bisphosphate alters synaptotagmin 1 membrane docking and drives opposing bilayers closer together. Biochemistry *50*, 2633-2641.

Laemmli, U.K. (1970). Cleavage of structural proteins during the assembly of the head of bacteriophage T4. Nature *227*, 680-685.

Lakshmi, K.V., and Brudvig, G.W. (2001). Pulsed electron paramagnetic resonance methods for macromolecular structure determination. Curr Opin Struct Biol *11*, 523-531.

Lane, P.A., Shew, R.L., Iarocci, T.A., Mohandas, N., Hays, T., and Mentzer, W.C. (1987). Unique alpha-spectrin mutant in a kindred with common hereditary elliptocytosis. J Clin Invest *79*, 989-996.

Langen, R., Oh, K.J., Cascio, D., and Hubbell, W.L. (2000). Crystal structures of spin labeled T4 lysozyme mutants: implications for the interpretation of EPR spectra in terms of structure. Biochemistry *39*, 8396-8405.

Lemaillet, G., Walker, B., and Lambert, S. (2003). Identification of a conserved ankyrin-binding motif in the family of sodium channel alpha subunits. J Biol Chem *278*, 27333-27339.

Lepke, S., Becker, A., and Passow, H. (1992). Mediation of inorganic anion transport by the hydrophobic domain of mouse erythroid band 3 protein expressed in oocytes of Xenopus laevis. Biochim Biophys Acta *1106*, 13-16.

Levitsky, D.O., Nicoll, D.A., and Philipson, K.D. (1994). Identification of the high affinity Ca(2+)-binding domain of the cardiac Na^+/Ca^{2+} exchanger. J Biol Chem *269*, 22847-22852.

Li, J., Mahajan, A., and Tsai, M.D. (2006). Ankyrin-Repeat: a unique motif mediating protein-protein interactions. Biochemistry *45*, 15168-15178.

Li, Z.P., Burke, E.P., Frank, J.S., Bennett, V., and Philipson, K.D. (1993). The cardiac Na^+/Ca^{2+} exchanger binds to the cytoskeletal protein ankyrin. J Biol Chem *268*, 11489-11491.

Lietzow, M.A., and Hubbell, W.L. (2004). Motion of spin label side chains in cellular retinol-binding protein: correlation with structure and nearest-neighbor interactions in an antiparallel beta-sheet. Biochemistry *43*, 3137-3151.

Lindgren, M., Eaton, G. R., Eaton, S. S., Jonsson, B. -H., Hammarstrom, P., Svensson, M, Carlsson, U. (1997). Electron spin echo as a probe of nitroxide environment in spin labeled mutants of human carbonic anhydrase II. J Chem Soc Perkin Trans *2*, 2549-2554.

Liu, S.C., and Palek, J. (1980). Spectrin tetramer-dimer equilibrium and the stability of erythrocyte membrane skeletons. Nature *285*, 586-588.

Lovell, S.C., Word, J.M., Richardson, J.S., and Richardson, D.C. (2000). The penultimate rotamer library. Proteins *40*, 389-408.

Low, P.S. (1986). Structure and function of the cytoplasmic domain of band 3: center of erythrocyte membrane-peripheral protein interactions. Biochim Biophys Acta *864*, 145-167.

Low, P.S., Westfall, M.A., Allen, D.P., and Appell, K.C. (1984). Characterization of the reversible conformational equilibrium of the cytoplasmic domain of erythrocyte membrane band 3. J Biol Chem *259*, 13070-13076.

Luckhurst, G.R. (1976). Biradicals as spin probes (New York, Academic).

Main, E.R., Jackson, S.E., and Regan, L. (2003). The folding and design of repeat proteins: reaching a consensus. Curr Opin Struct Biol *13*, 482-489.

Malhotra, J.D., Kazen-Gillespie, K., Hortsch, M., and Isom, L.L. (2000). Sodium channel beta subunits mediate homophilic cell adhesion and recruit ankyrin to points of cell-cell contact. J Biol Chem *275*, 11383-11388.

Manno, S., Takakuwa, Y., and Mohandas, N. (2002). Identification of a functional role for lipid asymmetry in biological membranes: Phosphatidylserine-skeletal protein interactions modulate membrane stability. Proc Natl Acad Sci U S A *99*, 1943-1948.

Marcotte, E.M., Pellegrini, M., Yeates, T.O., and Eisenberg, D. (1999). A census of protein repeats. J Mol Biol *293*, 151-160.

Marfatia, S.M., Lue, R.A., Branton, D., and Chishti, A.H. (1994). In vitro binding studies suggest a membrane-associated complex between erythroid p55, protein 4.1, and glycophorin C. J Biol Chem *269*, 8631-8634.

Matsuoka, S., and Hilgemann, D.W. (1992). Steady-state and dynamic properties of cardiac sodium-calcium exchange. Ion and voltage dependencies of the transport cycle. J Gen Physiol *100*, 963-1001.

Matsuoka, S., Nicoll, D.A., Hryshko, L.V., Levitsky, D.O., Weiss, J.N., and Philipson, K.D. (1995). Regulation of the cardiac Na^+/Ca^{2+} exchanger by Ca^{2+}. Mutational analysis of the Ca^{2+}-binding domain. J Gen Physiol *105*, 403-420.

McHaourab, H.S., Lietzow, M.A., Hideg, K., and Hubbell, W.L. (1996). Motion of spin-labeled side chains in T4 lysozyme. Correlation with protein structure and dynamics. Biochemistry *35*, 7692-7704.

McHaourab, H.S., Oh, K.J., Fang, C.J., and Hubbell, W.L. (1997). Conformation of T4 lysozyme in solution. Hinge-bending motion and the substrate-induced conformational transition studied by site-directed spin labeling. Biochemistry *36*, 307-316.

Mello, C.C., Bradley, C.M., Tripp, K.W., and Barrick, D. (2005). Experimental characterization of the folding kinetics of the notch ankyrin domain. J Mol Biol *352*, 266-281.

Michaely, P., and Bennett, V. (1993). The membrane-binding domain of ankyrin contains four independently folded subdomains, each comprised of six ankyrin-Repeats. J Biol Chem *268*, 22703-22709.

Michaely, P., and Bennett, V. (1995). The ANK repeats of erythrocyte ankyrin form two distinct but cooperative binding sites for the erythrocyte anion exchanger. J Biol Chem *270*, 22050-22057.

Michaely, P., Kamal, A., Anderson, R.G., and Bennett, V. (1999). A requirement for ankyrin binding to clathrin during coated pit budding. J Biol Chem *274*, 35908-35913.

Michaely, P., Tomchick, D.R., Machius, M., and Anderson, R.G. (2002). Crystal structure of a 12 ANK repeat stack from human ankyrinR. EMBO J *21*, 6387-6396.

Michel, F., Soler-Lopez, M., Petosa, C., Cramer, P., Siebenlist, U., and Muller, C.W. (2001). Crystal structure of the ankyrin-Repeat domain of Bcl-3: a unique member of the IkappaB protein family. EMBO J *20*, 6180-6190.

Mohandas, N., and Gallagher, P.G. (2008). Red cell membrane: past, present, and future. Blood *112*, 3939-3948.

Mohler, P.J., Davis, J.Q., and Bennett, V. (2005). Ankyrin-B coordinates the Na/K ATPase, Na/Ca exchanger, and InsP3 receptor in a cardiac T-tubule/SR microdomain. PLoS Biol *3*, e423.

Mohler, P.J., Rivolta, I., Napolitano, C., LeMaillet, G., Lambert, S., Priori, S.G., and Bennett, V. (2004). Nav1.5 E1053K mutation causing Brugada syndrome blocks binding to ankyrin-G and expression of Nav1.5 on the surface of cardiomyocytes. Proc Natl Acad Sci U S A *101*, 17533-17538.

Mohler, P.J., Schott, J.J., Gramolini, A.O., Dilly, K.W., Guatimosim, S., duBell, W.H., Song, L.S., Haurogne, K., Kyndt, F., Ali, M.E.*, et al.* (2003). Ankyrin-B mutation causes type 4 long-QT cardiac arrhythmia and sudden cardiac death. Nature *421*, 634-639.

Morris, M.B., and Lux, S.E. (1995). Characterization of the binary interaction between human erythrocyte protein 4.1 and actin. Eur J Biochem *231*, 644-650.

Mosavi, L.K., Cammett, T.J., Desrosiers, D.C., and Peng, Z.Y. (2004). The ankyrin-Repeat as molecular architecture for protein recognition. Protein Sci *13*, 1435-1448.

Mosavi, L.K., Minor, D.L., Jr., and Peng, Z.Y. (2002). Consensus-derived structural determinants of the ankyrin-Repeat motif. Proc Natl Acad Sci U S A *99*, 16029-16034.

Nam, Y., Sliz, P., Song, L., Aster, J.C., and Blacklow, S.C. (2006). Structural basis for cooperativity in recruitment of MAML coactivators to Notch transcription complexes. Cell *124*, 973-983.

Nelson, W.J., and Veshnock, P.J. (1987). Ankyrin binding to (Na^+/K^+) ATPase and implications for the organization of membrane domains in polarized cells. Nature *328*, 533-536.

Nicolas, V., Le Van Kim, C., Gane, P., Birkenmeier, C., Cartron, J.P., Colin, Y., and Mouro-Chanteloup, I. (2003). Rh-RhAG/ankyrin-R, a new interaction site between the membrane bilayer and the red cell skeleton, is impaired by Rh(null)-associated mutation. J Biol Chem *278*, 25526-25533.

Nicoll, D.A., Hryshko, L.V., Matsuoka, S., Frank, J.S., and Philipson, K.D. (1996). Mutation of amino acid residues in the putative transmembrane segments of the cardiac sarcolemmal Na^+/Ca^{2+} exchanger. J Biol Chem *271*, 13385-13391.

Nicoll, D.A., Longoni, S., and Philipson, K.D. (1990). Molecular cloning and functional expression of the cardiac sarcolemmal Na^+/Ca^{2+} exchanger. Science *250*, 562-565.

Nicoll, D.A., Ottolia, M., Lu, L., Lu, Y., and Philipson, K.D. (1999). A new topological model of the cardiac sarcolemmal Na^+/Ca^{2+} exchanger. J Biol Chem *274*, 910-917.

Nicoll, D.A., Sawaya, M.R., Kwon, S., Cascio, D., Philipson, K.D., and Abramson, J. (2006). The crystal strcuture of the primary Ca^{2+} sensor of the Na^+/Ca^{2+} exchanger reveals a novel Ca^{2+} binding motif. J Biol Chem *281*, 21577-21581.

Nilsson, K.R., Jr., and Bennett, V. (2009). Ankyrin-based patterning of membrane microdomains: new insights into a novel class of cardiovascular diseases. J Cardiovasc Pharmacol *54*, 106-115.

Okubo, K., Kang, D., and Hamasaki, N., eds. (1997). The carboxy terminal region of the human AE1 (erythrocyte band 3 protein) (Basel, Karger).

Oldham, W.M., Van Eps, N., Preininger, A.M., Hubbell, W.L., and Hamm, H.E. (2007). Mapping allosteric connections from the receptor to the nucleotide-binding pocket of heterotrimeric G proteins. Proc Natl Acad Sci U S A *104*, 7927-7932.

Ottolia, M., John, S., Xie, Y., Ren, X., and Philipson, K.D. (2007). Shedding light on the Na^+/Ca^{2+} exchanger. Ann N Y Acad Sci *1099*, 78-85.

Ottolia, M., Nicoll, D.A., and Philipson, K.D. (2009). Roles of two Ca^{2+}-binding domains in regulation of the cardiac Na^+/Ca^{2+} exchanger. J Biol Chem *284*, 32735-32741.

Ottolia, M., Philipson, K.D., and John, S. (2004). Conformational changes of the Ca^{2+} regulatory site of the Na^+/Ca^{2+} exchanger detected by FRET. Biophys J *87*, 899-906.

Pake, G.E. (1948). Nuclear resonance absroption in hydrated crystals: Fine structure of the proton line. J Chem Phys *16*, 327-336.

Pan, Z., Kao, T., Horvath, Z., Lemos, J., Sul, J.Y., Cranstoun, S.D., Bennett, V., Scherer, S.S., and Cooper, E.C. (2006). A common ankyrin-G-based mechanism retains KCNQ and NaV channels at electrically active domains of the axon. J Neurosci *26*, 2599-2613.

Pantaleo, A., Ferru, E., Giribaldi, G., Mannu, F., Carta, F., Matte, A., de Franceschi, L., and Turrini, F. (2009). Oxidized and poorly glycosylated band 3 is selectively phosphorylated by Syk kinase to form large membrane clusters in normal and G6PD-deficient red blood cells. Biochem J *418*, 359-367.

Park, S.-Y., Borbat, P.P., Gonzalez-Bonet, G., Bhatnagar, J., Pollard, A.M., Freed, J.H., Bilwes, A.M., and Crane, B.R. (2006). Reconstruction of the chemotaxis receptor-kinase assembly. Nature Structural and Molecular Biology *13*, 400-407.

Passow, H. (1986). Molecular aspects of band 3 protein-mediated anion transport across the red blood cell membrane. Rev Physiol Biochem Pharmacol *103*, 61-203.

Perozo, E., Cortes, D.M., and Cuello, L.G. (1999). Structural rearrangements underlying K+-channel activation gating. Science *285*, 73-78.

Perozo, E., Cortes, D.M., Sompornpisut, P., Kloda, A., and Martinac, B. (2002). Open channel structure of MscL and the gating mechanism of mechanosensitive channels. Nature *418*, 942-948.

Perozo, E., Kloda, A., Cortes, D.M., and Martinac, B. (2001). Site-directed spin-labeling analysis of reconstituted Mscl in the closed state. J Gen Physiol *118*, 193-206.

Perrotta, S., Gallagher, P.G., and Mohandas, N. (2008). Hereditary spherocytosis. Lancet *372*, 1411-1426.

Piacentino, V., Weber, C.R., Chen, X., Weisser-Thomas, J., Margulies, K.B., Bers, D.M., and Houser, S.R. (2003). Cellular basis of abnormal calcium transients of failing human ventricular myocytes. Circ Res *92*, 651-658.

Pinder, J.C., Pekrun, A., Maggs, A.M., Brain, A.P., and Gratzer, W.B. (1995). Association state of human red blood cell band 3 and its interaction with ankyrin. Blood *85*, 2951-2961.

Pogwizd, S.M., Qi, M., Yuan, W., Samarel, A.M., and Bers, D.M. (1999). Upregulation of Na(+)/Ca(2+) exchanger expression and function in an arrhythmogenic rabbit model of heart failure. Circ Res *85*, 1009-1019.

Polyhach, Y., Bordignon, E., and Jeschke, G. (2011). Rotamer libraries of spin labelled cysteines for protein studies. Phys Chem Chem Phys *13*, 2356-2366.

Popov, M., Tam, L.Y., Li, J., and Reithmeier, R.A. (1997). Mapping the ends of transmembrane segments in a polytopic membrane protein. Scanning N-glycosylation mutagenesis of extracytosolic loops in the anion exchanger, band 3. J Biol Chem *272*, 18325-18332.

Prisner, T., Rohrer, M., and MacMillan, F. (2001). Pulsed EPR spectroscopy: biological applications. Annu Rev Phys Chem *52*, 279-313.

Pulina, M.V., Rizzuto, R., Brini, M., and Carafoli, E. (2006). Inhibitory interaction of the plasma membrane Na^+/Ca^{2+} exchangers with the 14-3-3 proteins. J Biol Chem *281*, 19645-19654.

Qiu, Z., Nicoll, D.A., and Philipson, K.D. (2001). Helix packing of functionally important regions of the cardiac Na(+)-Ca(2+) exchanger. J Biol Chem *276*, 194-199.

Rabenstein, M.D., and Shin, Y.K. (1995). Determination of the distance between two spin labels attached to a macromolecule. Proc Natl Acad Sci U S A *92*, 8239-8243.

Rasmussen, H.B., Frokjaer-Jensen, C., Jensen, C.S., Jensen, H.S., Jorgensen, N.K., Misonou, H., Trimmer, J.S., Olesen, S.P., and Schmitt, N. (2007). Requirement of subunit co-assembly and ankyrin-G for M-channel localization at the axon initial segment. J Cell Sci *120*, 953-963.

Reid, M.E., Takakuwa, Y., Conboy, J., Tchernia, G., and Mohandas, N. (1990). Glycophorin C content of human erythrocyte membrane is regulated by protein 4.1. Blood *75*, 2229-2234.

Reithmeier, R.A. (2001). A membrane metabolon linking carbonic anhydrase with chloride/bicarbonate anion exchangers. Blood Cells Mol Dis *27*, 85-89.

Ren, X., Nicoll, D.A., Galang, G., and Philipson, K.D. (2008). Intermolecular cross-linking of Na^+/Ca^{2+} exchanger proteins: evidence for dimer formation. Biochemistry *47*, 6081-6087.

Ren, X., Nicoll, D.A., and Philipson, K.D. (2006). Helix packing of the cardiac Na^+/Ca^{2+} exchanger: proximity of transmembrane segments 1, 2, and 6. J Biol Chem *281*, 22808-22814.

Rief, M., Pascual, J., Saraste, M., and Gaub, H.E. (1999). Single molecule force spectroscopy of spectrin repeats: low unfolding forces in helix bundles. J Mol Biol *286*, 553-561.

Rizo, J., and Sudhof, T.C. (1998). C2-domains, structure and function of a universal Ca^{2+}-binding domain. J Biol Chem *273*, 15879-15882.

Rybicki, A.C., Qiu, J.J., Musto, S., Rosen, N.L., Nagel, R.L., and Schwartz, R.S. (1993). Human erythrocyte protein 4.2 deficiency associated with hemolytic anemia and a homozygous 40glutamic acid-->lysine substitution in the cytoplasmic domain of band 3 (band 3Montefiore). Blood *81*, 2155-2165.

Rybicki, A.C., Schwartz, R.S., Hustedt, E.J., and Cobb, C.E. (1996). Increased rotational mobility and extractability of band 3 from protein 4.2-deficient erythrocyte membranes: evidence of a role for protein 4.2 in strengthening the band 3-cytoskeleton linkage. Blood *88*, 2745-2753.

Sale, K., Song, L., Liu, Y.S., Perozo, E., and Fajer, P. (2005). Explicit treatment of spin labels in modeling of distance constraints from dipolar EPR and DEER. J Am Chem Soc *127*, 9334-9335.

Salinas, R.K., Bruschweiler-Li, L., Johnson, E., and Bruschweiler, R. (2011). Ca^{2+} Binding Alters the Interdomain Flexibility between the Two Cytoplasmic Calcium-binding Domains in the Na^{+}/Ca^{2+} Exchanger. J Biol Chem *286*, 32123-32131.

Salomao, M., Zhang, X., Yang, Y., Lee, S., Hartwig, J.H., Chasis, J.A., Mohandas, N., and An, X. (2008). Protein 4.1R-dependent multiprotein complex: new insights into the structural organization of the red blood cell membrane. Proc Natl Acad Sci U S A *105*, 8026-8031.

Sanner, M.F., Spehner, J.-C., and Olson, A.J. (1996). Reduced surface: an efficient way to compute molecular surfaces. Biopolymers *38*, 305-320.

Schneider, E., Freed, J. H. (1989). Calculating slow motional magnetic resonance spectra: a user's guide. Biol Magn Reson *10*, 1-76.

Schulze, D.H., Muqhal, M., Lederer, W.J., and Ruknudin, A.M. (2003). Sodium/calcium exchanger (NCX1) macromolecular complex. J Biol Chem *278*, 28849-28855.

Schwarz, E.M., and Benzer, S. (1997). Calx, a Na-Ca exchanger gene of Drosophila melanogaster. Proc Natl Acad Sci U S A *94*, 10249-10254.

Schweiger, A., Jeschke, G. (2001). Principles of pulse electron paramagnetic resonance (Oxford, Oxford university press).

Schweizer, A., Roschitzki-Voser, H., Amstutz, P., Briand, C., Gulotti-Georgieva, M., Prenosil, E., Binz, H.K., Capitani, G., Baici, A., Pluckthun, A.*, et al.* (2007). Inhibition of caspase-2 by a designed ankyrin-Repeat protein: specificity, structure, and inhibition mechanism. Structure *15*, 625-636.

Setty, B.N., Kulkarni, S., and Stuart, M.J. (2002). Role of erythrocyte phosphatidylserine in sickle red cell-endothelial adhesion. Blood *99*, 1564-1571.

Shao, X., Li, C., Fernandez, I., Zhang, X., Sudhof, T.C., and Rizo, J. (1997). Synaptotagmin-syntaxin interaction: the C2 domain as a Ca^{2+}-dependent electrostatic switch. Neuron *18*, 133-142.

Shi, Z.T., Afzal, V., Coller, B., Patel, D., Chasis, J.A., Parra, M., Lee, G., Paszty, C., Stevens, M., Walensky, L.*, et al.* (1999). Protein 4.1R-deficient mice are viable but have erythroid membrane skeleton abnormalities. J Clin Invest *103*, 331-340.

Sipido, K.R., Volders, P.G., de Groot, S.H., Verdonck, F., Van de Werf, F., Wellens, H.J., and Vos, M.A. (2000). Enhanced Ca(2+) release and Na/Ca exchange activity in hypertrophied canine ventricular myocytes: potential link between contractile adaptation and arrhythmogenesis. Circulation *102*, 2137-2144.

Skalak, R., and Branemark, P.I. (1969). Deformation of red blood cells in capillaries. Science *164*, 717-719.

Slichter, C.P. (1980). Principles of Magnetic Resonance (Berlin, Heidelberg, New York, Springer-Verlag).

Smirnova, I., Kasho, V., Choe, J.Y., Altenbach, C., Hubbell, W.L., and Kaback, H.R. (2007). Sugar binding induces an outward facing conformation of LacY. Proc Natl Acad Sci U S A *104*, 16504-16509.

Sompornpisut, P., Roux, B., and Perozo, E. (2008). Structural refinement of membrane proteins by restrained molecular dynamics and solvent accessibility data. Biophys J *95*, 5349-5361.

Speicher, D.W., DeSilva, T.M., Speicher, K.D., Ursitti, J.A., Hembach, P., and Weglarz, L. (1993). Location of the human red cell spectrin tetramer binding site and detection of a related "closed" hairpin loop dimer using proteolytic footprinting. J Biol Chem *268*, 4227-4235.

Stabach, P.R., Simonovic, I., Ranieri, M.A., Aboodi, M.S., Steitz, T.A., Simonovic, M., and Morrow, J.S. (2009). The structure of the ankyrin-binding site of beta-spectrin reveals how tandem spectrin-repeats generate unique ligand-binding properties. Blood *113*, 5377-5384.

Stefanovic, M., Markham, N.O., E.M., P., Garrett-Beal, L.J., Cline, A.P., Gallagher, P.G., Low, P.S., and Bodine, D.M. (2007). An 11-amino acid B-hairpin loop in the cytoplasmic domain of band 3 is responsible for ankyrin binding in mouse erythrocytes. Proc Natl Acad Sci USA *104*, 13972-13977.

Steinhoff, H.J., Radzwill, N., Thevis, W., Lenz, V., Brandenburg, D., Antson, A., Dodson, G., and Wollmer, A. (1997). Determination of interspin distances between spin labels attached to insulin: comparison of electron paramagnetic resonance data with the X-ray structure. Biophys J *73*, 3287-3298.

Stoll, S.S., A. (2003). An adaptive method for computing resonance fields for continuous-wave EPR spectra. Chem Phys Lett *380*, 464-470.

Tang, K.S., Guralnick, B.J., Wang, W.K., Fersht, A.R., and Itzhaki, L.S. (1999). Stability and folding of the tumour suppressor protein p16. J Mol Biol *285*, 1869-1886.

Tanner, M.J. (1993). Molecular and cellular biology of the erythrocyte anion exchanger (AE1). Semin Hematol *30*, 34-57.

Tchernia, G., Mohandas, N., and Shohet, S.B. (1981). Deficiency of skeletal membrane protein band 4.1 in homozygous hereditary elliptocytosis. Implications for erythrocyte membrane stability. J Clin Invest *68*, 454-460.

Thevananther, S., Kolli, A.H., and Devarajan, P. (1998). Identification of a novel ankyrin isoform (AnkG190) in kidney and lung that associates with the plasma membrane and binds alpha-Na, K-ATPase. J Biol Chem *273*, 23952-23958.

Thevenin, B.J., and Low, P.S. (1990). Kinetics and regulation of the ankyrin-band 3 interaction of the human red blood cell membrane. J Biol Chem *265*, 16166-16172.

Thevenin, B.J., Periasamy, N., Shohet, S.B., and Verkman, A.S. (1994). Segmental dynamics of the cytoplasmic domain of erythrocyte band 3 determined by time-resolved fluorescence anisotropy: sensitivity to pH and ligand binding. Proc Natl Acad Sci U S A *91*, 1741-1745.

Tombolato, F., Ferrarini, A., and Freed, J.H. (2006). Dynamics of the nitroxide side chain in spin-labeled proteins. J Phys Chem B *110*, 26248-26259.

Toye, A.M., Ghosh, S., Young, M.T., Jones, G.K., Sessions, R.B., Ramauge, M., Leclerc, P., Basu, J., Delaunay, J., and Tanner, M.J. (2005). Protein-4.2 association with band 3 (AE1, SLCA4) in Xenopus oocytes: effects of three natural protein-4.2 mutations associated with hemolytic anemia. Blood *105*, 4088-4095.

Truhlar, S.M., Torpey, J.W., and Komives, E.A. (2006). Regions of IkappaBalpha that are critical for its inhibition of NF-kappaB.DNA interaction fold upon binding to NF-kappaB. Proc Natl Acad Sci U S A *103*, 18951-18956.

Van Dort, H.M., Moriyama, R., and Low, P.S. (1998). Effect of band 3 subunit equilibrium on the kinetics and affinity of ankyrin binding to erythrocyte membrane vesicles. J Biol Chem *273*, 14819-14826.

Van Eps, N., Oldham, W.M., Hamm, H.E., and Hubbell, W.L. (2006). Structural and dynamical changes in an alpha-subunit of a heterotrimeric G protein along the activation pathway. Proc Natl Acad Sci U S A *103*, 16194-16199.

Vince, J.W., and Reithmeier, R.A. (1996). Structure of the band 3 transmembrane domain. Cell Mol Biol (Noisy-le-grand) *42*, 1041-1051.

Vince, J.W., and Reithmeier, R.A. (2000). Identification of the carbonic anhydrase II binding site in the Cl(-)/HCO(3)(-) anion exchanger AE1. Biochemistry *39*, 5527-5533.

Walder, J.A., Chatterjee, R., Steck, T.L., Low, P.S., Musso, G.F., Kaiser, E.T., Rogers, P.H., and Arnone, A. (1984). The interaction of hemoglobin with the cytoplasmic domain of band 3 of the human erythrocyte membrane. J Biol Chem *259*, 10238-10246.

Wang, C.C., Moriyama, R., Lombardo, C.R., and Low, P.S. (1995). Partial characterization of the cytoplasmic domain of human kidney band 3. J Biol Chem *270*, 17892-17897.

Wang, D.N., Kuhlbrandt, W., Sarabia, V.E., and Reithmeier, R.A. (1993). Two-dimensional structure of the membrane domain of human band 3, the anion transport protein of the erythrocyte membrane. EMBO J *12*, 2233-2239.

Wang, D.N., Sarabia, V.E., Reithmeier, R.A., and Kuhlbrandt, W. (1994). Three-dimensional map of the dimeric membrane domain of the human erythrocyte anion exchanger, Band 3. EMBO J *13*, 3230-3235.
Wang, J., Zhang, X.Q., Ahlers, B.A., Carl, L.L., Song, J., Rothblum, L.I., Stahl, R.C., Carey, D.J., and Cheung, J.Y. (2006). Cytoplasmic tail of phospholemman interacts with the intracellular loop of the cardiac Na^{+}/Ca^{2+} exchanger. J Biol Chem *281*, 32004-32014.

Wang, Z., Nolan, B., Kutschke, W., and Hill, J.A. (2001). Na^{+}/Ca^{2+} exchanger remodeling in pressure overload cardiac hypertrophy. J Biol Chem *276*, 17706-17711.

Ward, R., Bowman, A., El-Mkami, H., Owen-Hughes, T., and Norman, D.G. (2009). Long distance PELDOR measurements on the histone core particle. J Am Chem Soc *131*, 1348-1349.

Waugh, S.M., and Low, P.S. (1985). Hemichrome binding to band 3: nucleation of Heinz bodies on the erythrocyte membrane. Biochemistry *24*, 34-39.

Weil, J. (1971). The analysis of large hyperfine splittings in paramagnetic resonance spectroscopy. J Magn Reson *4*, 394-399.

Weisser-Thomas, J., Piacentino, V., Gaughan, J.P., Margulies, K., and Houser, S.R. (2003). Calcium entry via Na/Ca exchange during the action potential directly contributes to contraction of failing human ventricular myocytes. Cardiovasc Res *57*, 974-985.

Willardson, B.M., Thevenin, B.J., Harrison, M.L., Kuster, W.M., Benson, M.D., and Low, P.S. (1989). Localization of the ankyrin-binding site on erythrocyte membrane protein, band 3. J Biol Chem *264*, 15893-15899.

Wong, E.Y., Lin, J., Forget, B.G., Bodine, D.M., and Gallagher, P.G. (2004). Sequences downstream of the erythroid promoter are required for high level expression of the human alpha-spectrin gene. J Biol Chem *279*, 55024-55033.

Wrong, O., Bruce, L.J., Unwin, R.J., Toye, A.M., and Tanner, M.J. (2002). Band 3 mutations, distal renal tubular acidosis, and Southeast Asian ovalocytosis. Kidney Int *62*, 10-19.

Wu, M., Le, H.D., Wang, M., Yurkov, V., Omelchenko, A., Hnatowich, M., Nix, J., Hryshko, L.V., and Zheng, L. (2010). Crystal structures of progressive Ca^{2+} binding states of the Ca^{2+} sensor Ca^{2+} binding domain 1 (CBD1) from the CALX Na^{+}/Ca^{2+} exchanger reveal incremental conformational transitions. J Biol Chem *285*, 2554-2561.

Wu, M., Wang, M., Nix, J., Hryshko, L.V., and Zheng, L. (2009). Crystal structure of CBD2 from the Drosophila Na(+)/Ca(2+) exchanger: diversity of Ca(2+) regulation and its alternative splicing modification. J Mol Biol *387*, 104-112.

Yamaguchi, T., Fujii, T., Abe, Y., Hirai, T., Kang, D., Namba, K., Hamasaki, N., and Mitsuoka, K. (2010). Helical image reconstruction of the outward-open human erythrocyte band 3 membrane domain in tubular crystals. J Struct Biol *169*, 406-412.
Yang, Y., Ogawa, Y., Hedstrom, K.L., and Rasband, M.N. (2007). betaIV spectrin is recruited to axon initial segments and nodes of Ranvier by ankyrinG. J Cell Biol *176*, 509-519.

Yasin, Z., Witting, S., Palascak, M.B., Joiner, C.H., Rucknagel, D.L., and Franco, R.S. (2003). Phosphatidylserine externalization in sickle red blood cells: associations with cell age, density, and hemoglobin F. Blood *102*, 365-370.

Yawata, Y., Kanzaki, A., Yawata, A., Doerfler, W., Ozcan, R., and Eber, S.W. (2000). Characteristic features of the genotype and phenotype of hereditary spherocytosis in the Japanese population. Int J Hematol *71*, 118-135.

Zeeb, M., Rosner, H., Zeslawski, W., Canet, D., Holak, T.A., and Balbach, J. (2002). Protein folding and stability of human CDK inhibitor p19(INK4d). J Mol Biol *315*, 447-457.

Zhang, B., and Peng, Z. (2000). A minimum folding unit in the ankyrin-Repeat protein p16(INK4). J Mol Biol *299*, 1121-1132.

Zhang, D., Kiyatkin, A., Bolin, J.T., and Low, P.S. (2000). Crystallographic structure and functional interpretation of the cytoplasmic domain of erythrocyte membrane band 3. Blood *96*, 2925-2933.

Zhang, X.Q., Ahlers, B.A., Tucker, A.L., Song, J., Wang, J., Moorman, J.R., Mounsey, J.P., Carl, L.L., Rothblum, L.I., and Cheung, J.Y. (2006). Phospholemman inhibition of the cardiac Na^{+}/Ca^{2+} exchanger. Role of phosphorylation. J Biol Chem *281*, 7784-7792.

Zhou, J., and Low, P.S. (2001). Characterization of the reversible conformational equilibrium in the cytoplasmic domain of human erythrocyte membrane band 3. J Biol Chem *276*, 38147-38151.

Zhou, Z. (2006). EPR and fluorescence studies on erythrocyte membrane skeletal proteins: cdb3 and ankyrin. In Molecular Physiology and Biophysics (Nashville, Vanderbilt University), pp. 1-213.

Zhou, Z., DeSensi, S., Stein, R.A., Brandon, S., Song, L., Cobb, C.E., Hustedt, E.J., and Beth, A.H. (2007). Structure of the Cytoplasmic Domain of Erythrocyte Band 3 Hereditary Spherocytosis Variant P327R: Band 3 Tuscaloosa. Biochemistry *46*, 10248-10257.

Zhou, Z., DeSensi, S.C., Stein, R.A., Brandon, S., Dixit, M., McArdle, E.J., Warren, E.M., Kroh, H.K., Song, L., Cobb, C.E*., et al.* (2005). Solution structure of the cytoplasmic domain of erythrocyte membrane band 3 determined by site-directed spin labeling. Biochemistry *44*, 15115-15128.

Zhu, Q., Lee, D.W., and Casey, J.R. (2003). Novel topology in C-terminal region of the human plasma membrane anion exchanger, AE1. J Biol Chem *278*, 3112-3120.

Zwaal, R.F., and Schroit, A.J. (1997). Pathophysiologic implications of membrane phospholipid asymmetry in blood cells. Blood *89*, 1121-1132.

Zweifel, M.E., and Barrick, D. (2001). Studies of the ankyrin-Repeats of the Drosophila melanogaster Notch receptor. 1. Solution conformational and hydrodynamic properties. Biochemistry *40*, 14344-14356.

Zweifel, M.E., Leahy, D.J., Hughson, F.M., and Barrick, D. (2003). Structure and stability of the ankyrin domain of the Drosophila Notch receptor. Protein Sci *12*, 2622-2632.